High Throughput Bioprinting of Colorectal Cancer Tumour Spheroids

Peter Johnson

Brasenose College

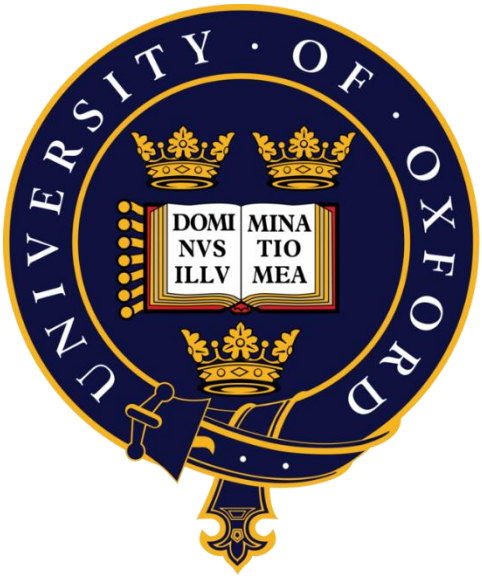

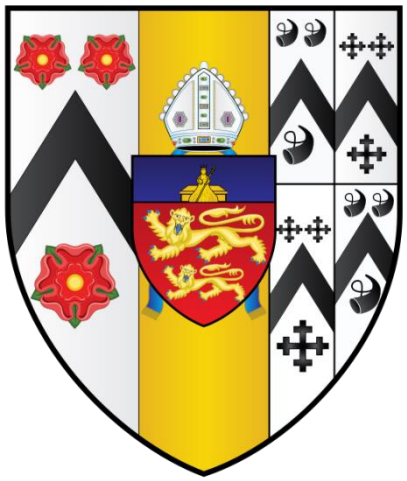

A dissertation presented in partial fulfilment of the requirements for the degree of Doctor of Philosophy

Hilary Term 2021

University of Oxford

Declaration:

This thesis describes work carried out in the Chemistry Research Laboratory, University of Oxford, between October 2016 and April 2021 under the supervision of Prof. Hagan Bayley and Prof. Adam Perriman. This thesis is a result of my own work, except when otherwise stated, and has not been submitted for any other degree at this or any other university.

Signed:

Peter Johnson 23/4/2021

To my parents, for believing in me, to my brother for keeping me sane, to my girlfriend for looking after me and to my grandfather who still supports the wrong team…

(Word Count: ~44000 words)

Acknowledgements

There are a number of people who have my sincere gratitude for their help and support these past 4 years. First and foremost, I would like to thank my parents and siblings for their endless encouragement throughout this process. Thank you for making time to see me around my frantic schedule. To Phil, who's mind is a complex mix of edgy jokes and half-baked plans, thank you for distracting me when the workload was a bit much. Asha, thanks for your infinite patience and unwavering support, I couldn't have done it without you.

Sam, Henry, George and Jack, thanks for making the Synbio CDT a much more enjoyable experience. I will always admire your reckless disregard for clear-headed thinking. G, I still believe the rains will come. Wathen, thanks for staying in touch all these years and visiting every now and then. Lottie, thank you for making Oxford feel like home.

To my supervisors, Prof. Hagan Bayley and Prof. Adam Perriman, thank you for your support and helping me see the big picture. Adam, thanks for the royal welcome. Likewise, a huge thanks goes out to the Bayley and Perriman research groups, who welcomed an engineer into their mix of biologists, chemists, and biochemists. To our collaborators, Prof. Ann Williams, and Dr. Adam Chambers, thank you for your insight into all things cancer. Tracey, thank you for teaching me to become a 'biologist'.

A special thanks is also required for Elspeth, who is undoubtably one of the most inspiring, kind, and generous professors Brasenose College has ever seen. Thank you for all your support and innumerable lunch and dinner invites.

To the staff at the Wolfson Bioimaging Facility: Chris Neal, Dominic Alibhai and Judith Mantell, thank you for all your hard work in making image analysis and electron microscopy possible with our complicated system.

Finally, I would like to thank the SynBio CDT and its funding bodies, the EPSRC and BBSRC for enabling and supporting this project.

Abstract

There is a significant unmet need for the development of complex and scalable 3D colorectal cancer (CRC) models. Presently, there is no known method for predicting patient-response to chemotherapy, and many nonresponding patients undergo this treatment which has no therapeutic value and significant negative impacts on health and wellbeing.

It has been recently demonstrated that patient-specific microtumours, known as tumour spheroids, can be cultured *in vitro* from patient biopsy's and are predictive of chemotherapy-response in CRC. However, current approaches are low throughput and cannot be readily scaled to address the large clinical need. Bioprinting, the controlled 3D patterning of cell-laden biocompatible materials known as 'bioinks', has untapped potential to reproduce the CRC tumour spheroid model in a robust, high throughput manner.

At this time, no scalable bioprinted CRC tumour spheroid model has been reported in the literature. Consequently, this thesis addresses this space, outlining the development of a high throughput bioprinting assay for CRC tumour spheroid chemotherapy-response. In Chapter 3, a bioink was formulated which ubiquitously supports spontaneous spheroid self-assembly in every tested CRC line. In Chapter 4, the characteristics of these tumour spheroids are explored, and found to exhibit important characteristic features of tumours *in vivo*, such as zonal hypoxia and necrosis.

Finally, in Chapter 5, work from the previous two chapters is used to develop a high throughput, bioprinted chemotherapy and radiotherapy-response assay, using non-invasive high content microscopy to measure the growth of spheroids challenged by therapy. Here, the throughput and utility of the system is validated through the accurate measurement of many thousands of tumour spheroids simultaneously, paving the way for future use of scalable bioprinted CRC spheroid assays as a clinical tool.

(276 words)

List of Abbreviations

5FU	Fluorouracil
AFM	Atomic Force Microscopy
BSA	Bovine Serum Albumin
CAD	Computer Aided Design
CMC	Critical Micelle Concentration
CoSC	Colon Stem Cell
CPD	Critical Point Drying
CRC	Colorectal Cancer
CSC	Colorectal Cancer Stem Cells
CryoEM	Cryogenic Electron Microscopy
DAC	Dual Asymmetric Centrifuge
DMEM	Dulbecco's Modified Eagle Medium
ECM	Extracellular Matrix
EDTA	Ethylenediaminetetraacetic Acid
EGF	Epidermal Growth Factor
EM	Electron Microscopy
EMT	Epithelial-Mesenchymal Transition
F127	Pluronic F127
FACS	Fluorescence Activated Cell Sorting
FAP	Familial Adenomatous Polyposis
FCS	Fetal Calf Serum
FDM	Fused Deposition Modelling
FGF	Fibroblast Growth Factor
FGF	Fibroblast Growth Factor
FITC	Fluorescein isothiocyanate
FOLFOX	Fluorouracil, Leucovorin & Oxaliplatin
GAG	Glycosaminoglycan
GBM	Glioblastoma
GelMA	Gelatin Methacrylate
GI50	50% Inhibition of Growth
H&E	Haematoxylin and Eosin
HA	Hyaluronic Acid

HA	Hydroxyapatite
HIF1α	Hypoxia-Inducible Factor 1 Alpha
HUVEC	Primary Human Umbilical Vein Endothelial Cells
LAB	Laser-Assisted Bioprinting
MMP	Matrix Metalloproteinase
MSC	Mesenchymal Stem Cell
MSI	Microsatellite Instability
MSS	Microsatellite Stable
MW	Molecular Weight
NR	Non-response
OS	Overall Survival
PBS	Phosphate Buffered Saline
PEG	Poly(Ethylene Glycol)
Pen/strep	Penicillin/Streptomycin
PFA	Paraformaldehyde
PFS	Progression-Free Survival
PLA	Poly(Lactic Acid)
PROM1	Prominin-1
qPCR	quantitative Polymerase Chain Reaction
RDG	Arg-Gly-Asp {integrin-binding peptide}.
ROS	Reactive Oxygen Species
RR	Response Rate
SCID	Severe Combined Immunodeficient {mice}
SD	Standard Deviation
SEM	Standard Error of the Mean
SEM	Scanning Electron Microscopy
TEM	Transmission Electron Microscopy
TGF β	Transforming Growth Factor β
TRITC	Tetramethylrhodamine
TS	Thymidine Synthase
UV	Ultraviolet
VEGF	Vascular Endothelial Growth Factor

Table of Contents

List of Figures

List of Tables

Chapter 1: Introduction

1.1 Colorectal cancer

Colorectal cancer (CRC) is the third-most prevalent cancer worldwide, and the fourth-most common cause of cancer related death[1]. In the United Kingdom, despite improvements in screening and treatment, CRC remains the 2nd most common cause of cancer death, and its incidence increases every year[2].

CRC occurrence is predominantly linked to age, with around 90% of CRC patients being above the age of 50[3,4]. Hereditary and familial links exist but are uncommon, with around 10% of patients having a family history of CRC[5,6], and 2-5% of cases arising in the context of well-understood inherited syndromes, such as familial adenomatous polyposis (FAP)[7]. A number of environmental risk factors for CRC have been suggested in response to the measured change in diet and lifestyle in Western countries where CRC incidence is increasing. Specifically, obesity[8,9], high-meat high-fat low-fibre diets[9,10], alcohol consumption[11,12] and smoking[13] have been identified as significantly increasing risk of CRC occurrence.

5-year survival rates for CRC have been steadily increasing for a number of years but vary drastically with staging at diagnosis, decreasing from 93.2% in stage I CRC to 8.1% in stage IV[14]. Consequently, historical increase in survival rates has been driven primarily by emphasis on screening and early diagnosis[15,16], where treatments are more effective. Curative treatment for CRC is surgical, with chemotherapy and radiotherapy typically taking adjunctive, or supporting, roles to shrink tumour size and prevent recurrence; greater than 90% of Stage I-III CRCs are treated with surgery[17]. Surgical options for CRC vary in invasiveness, from local excision in early or benign cancers to total colectomy (removal of the entire colon).

Chemotherapy forms an important part of the multimodal approach for the treatment and management of CRC. Its origin stems from the development of the thymidine-synthase (TS) inhibitor fluorouracil (5FU) in 1957[18], which is still the frontline chemotherapy agent for CRC today. 5FU alone is effective in around 20% of cases[19,20], but was found to be improved in combination with other drugs, like leucovorin, which improves the inhibition TS by 5FU[21], and oxaliplatin, which when combined with 5FU/leucovorin significantly increases overall-survival

(OS), progression-free survival (PFS) and response rate (RR) in clinical trials, in a combination now known as FOLFOX[22–24]. The supporting role of chemotherapy was explicated in the late 1980s and early 1990s, where its use both pre- (neoadjuvant therapy) and post-surgery (adjuvant therapy) significantly reduced recurrence[25–27]. Consequently, today, neoadjuvant 5FU-based chemotherapy regimens, like FOLFOX, are the mainstay of multimodal CRC treatment.

Despite these improvements, patient non-response (NR) to chemotherapy remains an issue, with a large fraction of patients not benefiting from chemotherapy whilst still suffering the toxic side effects[28,29]. Moreover, the ability to predict patient chemotherapy response is still nascent, with no recognised screening approach for preventing the assignment of chemotherapy to nonresponding patients. However, there have been two recent and promising studies using patient-derived cancer spheroids to measure personalized chemotherapy response, in which these 3D models were found to be predictive of patient response[30,31].

As such, this work will explore the robust generation of tumour spheroids as a model for chemotherapy and radiotherapy response. Bioprinting, an emerging biotechnology for the patterning of live cells and biomaterials, is used to establish spheroid cultures, and combined with other high-throughput systems to produce a semi-automated pipeline for the screening of different therapies on thousands of tumour spheroids.

1.2 The colon

The colon, also known as the large intestine or large bowel, is a complex organ which is a part of the digestive system. Structurally, the wall of the intestine is composed of different layers of specialised tissue (**Figure 1-1**, **A**). The outermost layers, the serosa and muscularis, support peristalsis of the gut and impels food through the gastrointestinal tract. The innermost layers, the submucosa and mucosa, surround the lumen and perform the necessary functions of digestion,

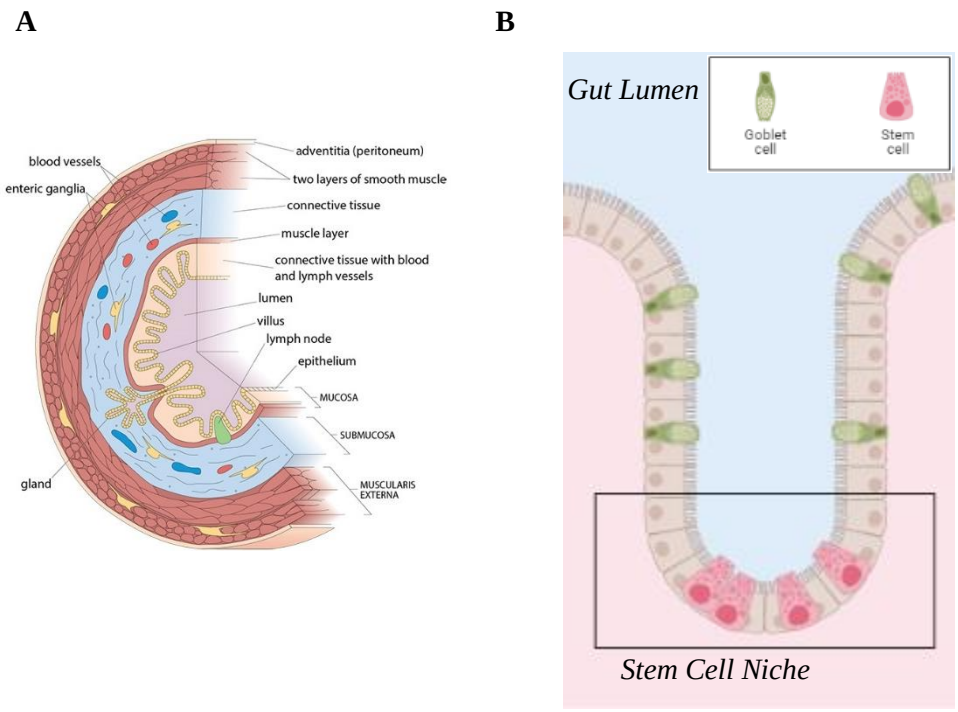

*Figure 1-1 Structure of the gut wall (**A**) and colonic crypts (**B**). **A** Layers of the gut wall of the intestine, adapted from the open university. **B** Simplified diagram of colonic crypt structure within the colonic epithelium, produced with BioRender.com*

such as water absorption. Unlike the small intestine, the epithelium of the colon contains no villi and is instead punctuated by colonic crypts, invaginations with a central lumen. These crypts exist in a dynamic state of constant cell-flux, whereby apoptotic epithelial cells are shed into the lumen are renewed in crypts by resident colonic stem cells (CoSCs). CoSCs have the ability to self-renew and are multipotent, generating differentiated cells specialised to the gut epithelium, such as columnar goblet cells. CoSCs are thought to residue in a dispersed manner in the stem cell niche at the base of colonic crypts (**Figure 1-1**, **B**). An estimate for the mean prevalence of CoSCs is that there are approximately 2,000 cells in a colonic crypt, of which 19 are CoSCs[32].

1.3 Colorectal cancer pathology

Most cases of CRC arise from pre-malignant adenomatous polyps, which have a neoplastic conversion rate of approximately 2.5 per 1000[33]. The progression of adenomatous polyps to dysplastic polyps and finally colorectal carcinoma is often an asymptomatic process. As such, a

variety of screening programmes exists across health services, in the UK consisting of occult blood faecal sampling with follow-up endoscopic examination, but exhibit variable adherence rates (~60%)[34]; if not discovered through routine screening, colorectal carcinomas can invade neighbouring tissue and metastasize.

From here the classification of CRC stages is founded, with a number of different classification systems existing, the most common in the UK being TNM (primary tumour [T], regional lymph nodes [N] and distant metastasis [M]), AJCC (American Joint Committee on Cancer), and Duke's staging. However, in all cases, more severe cancer is indicated by invasion through the layers of the gut wall, a risk factor for metastasis *via* the lymphatic system which is the leading cause of death in CRC[35]. In the UK 48% of all CRC diagnoses are in the final two AJCC stages of the disease[2]. Earlier stages of CRC are curative entirely through surgery without the need for chemotherapy[17]. However, the frequency of late-presentation drives the use of chemotherapy in treatment to increase the operability of tumours and decrease the risk of recurrence.

1.4 Cancer stem cells

There are two prominent models of cancer development and progression. The clonal evolution model was first published by Peter Nowell[36] in 1976, which proposes that as mutations acquire in somatic cells, some mutations cause growth advantages under selective pressures. As a tumour mass forms, additional pressures arise such as pH changes, nutrient deprivation and hypoxia which shape the evolutionary trajectory of the tumour and clonal lineages[37]. More recently, the cancer stem cell (CSC) model has gained popularity for CRC. Here, CoSCs, which are thought to be immortal[38], are the origin of colorectal tumours. CoSCs can acquire mutations over their long life, including oncogenic mutations, which do not necessarily initiate tumour formation, but may trigger cancer transformation at a certain mutational load. Once transformed, these cancer stem cells (CSCs) divide both symmetrically and asymmetrically, resulting in a population of CSCs and progenitors inside a tumour bulk.

The CSC model for CRC predicts a population of CSCs inside a tumour. A number of studies have tried to determine which cells are CSCs by analysis of cell surface markers which are conserved in CoSCs. Here, a number of putative markers have since been identified from clinical data, including: CD133[39], CD44[40], CD166[41], CD24[42], CD29[41], EpCAM[43] and Lgr5[44]. CD133 in particular has been extensively studied and found to be an independent prognostic marker for lower overall survival in CRC[45,46]. CD44 has been studied both alone and combination with CD133 in CRC. Alone, $CD44^+$ primary CRC cells have been reported to be highly tumorigenic in mice, and able to form tumour spheres *in vitro* from a single cell[47]. Combined with CD133, the double positive population, $CD133^+/CD44^+$, is often studied and is linked with increased metastasis[48], worse disease-free survival and recurrence[49].

1.4.1 CD133 and CD44

The most studied and reliable biomarker in CRC is CD133, also known as prominin-1 (PROM1). This cell surface antigen is known to be expressed in hematopoietic[50], neural[51], and prostate stem cells[52]. In cancer, CD133 expression was first reported in brain cancer[39], but has since been reported in colorectal tumours[53], and tumours of the pancreas[54], lung[55], and prostate[52]. CD133 is a 97kDa transmembrane glycoprotein comprising three extracellular domains, three intracellular domains, and five transmembrane domains[56]. Transcription of the chromosome 4 gene, PROM1, is linked to five separate promoters, three of which exist in CpG islands[56] and therefore subject to regulation by hypermethylation which is a commonly upregulated epigenetic process in cancer.

The exact relationship of CD133 to cancer is still unknown. Localisation of CD133 at plasma membrane protrusions suggests it has a role in cell polarity and migration[57]. Association with various signalling pathways related to cancer has also been reported. A reduction in Wnt signalling and loss of β-catenin nuclear localisation has been linked with CD133 suppression[58]. Moreover, CD133 can be upregulated in hypoxic conditions by hypoxia inducible factor-1α (HIF1A)[59].

Experimentally, $CD133^+$ cells have been linked with increased tumorigenic or metastatic potential in prostate cancer[60], liver cancer[61] and colorectal cancer[62], demonstrated by implantation

of $CD133^+$ cells into mice and measuring tumour size or number of distal metastases relative to $CD133^-$ cells, which may not form tumours at all.

CD133 has been most studied in CRC in combination with CD44, also known as HCAM (homing cell adhesion molecule), is a single-span transmembrane glycoprotein which is expressed in embryonic stem cells[63]. CD44 binds to a variety of components of the extracellular matrix (ECM), including collagen, fibronectin, and osteopontin, but most specifically to hyaluronic acid (HA)[64]. Conformational changes follow from this interaction which facilitate participation in various cell-signalling pathways, including Ras, MAPK and PI3K[65].

In cancer, the results of CD44 activation are dependent on the ligand. For example, CD44 binding with low molecular weight HA has been shown to promote cell motility and angiogenesis in breast cancer cells[66] and CD44-osteopontin binding is linked with resistance to radiation for non-small cell lung cancer[67]. For CRC specifically, CD44v6 facilitates CSC colonization, invasion, and metastasis[68].

CD44 and CD133 are often studied together as the double-positive population, $CD133^+/CD44^+$, seems to be a more powerful indicators of disease-free survival. Experimentally, $CD133^+/CD44^+$ have been studied *in vitro* and *in vivo*. $CD133^+/CD44^+$ HCT-116 CRC cells have been reported to grow faster both *in vitro* and when implanted into severe combined immunodeficient (SCID) mice[69]. $CD133^+/CD44^+$ DLD-1 CRC cells grow into more colonies in low adherent conditions and are more resistant to 5FU[70].

Not all CRC cell lines express CD133 and CD44, demonstrating that there exists a variety of pathways to tumour formation for CoSCs, and highlighting the need for a multiplicity of CSC markers for accurate models. In this work the CRC cell line, SW620, was commonly used as it is known to express both markers and was therefore selected as a model for evaluating the role of these critical CSC markers in cell monolayers and tumour spheroids.

1.5 Tumour structure and the tumour microenvironment

Tumours have long been recognised as a complex tissue. Tumours *in vivo* are a collection of cancer, immune and stromal cell types, as well as extracellular matrix (ECM) components and blood vessels. Consequently, the tumour structure is characterized by increased stiffness due to recruitment of cancer associated fibroblasts (CAFs)[71], nutrient and oxygen gradients[72] due to poor vascularization[73] and pH gradients due to increased lactic acid production via the Warburg effect[74].

The tumour microenvironment (TME) has important implications for therapy. Most tumours exhibit hypoxic regions[72], a condition which regulates apoptosis[75], decreases pH[76] and upregulates expression of drug-efflux genes via HIF1A activation[77]. Experimentally, many common chemotherapies, including both 5FU and OX, have been shown to be impaired under hypoxic conditions for CRC cells[78]. For radiotherapy, hypoxia is of particular importance, as reduction of local oxygen inhibits the formation of reactive oxygen species (ROS), which is the primary mechanism by which ionizing radiation (IR) damages DNA and kills cancer cells. Poor nutrient diffusion is commensurate with hypoxia as both arise from abnormal vasculature and angiogenesis in the TME. Reduced nutrient availability causes regions of slowly dividing or senescent cells[79], which are less effected by cytotoxic drugs like oxaliplatin that target proliferating cells.

Recruitment of CAFs by tumour cells results in fibrosis and desmoplasia which are characteristic features of tumours *in* vivo. Consequently, increased ECM concentration results in increased local mechanical stiffness about the tumour relative to comparable healthy tissue. Here, cells experience the stiffness of their environment *via* mechanotransduction, which is the process by which mechanical cues are translated into biochemical signals. Through this mechanism, increased stiffness contributes to tumour pathogenesis. For instance, matrix stiffness can induce epithelial-mesenchymal-transition (EMT), a cancer phenotype involved in metastasis[80]. Substrate stiffness has been reported to increase chemoresistance in MDA-MB-231 breast cancer cells[81],

and matrix stiffness has likewise been reported to increase chemoresistance in MDA-MB-231 spheroids[82].

As such, it is now clear that successful recapitulation of the TME *in vitro* is necessary for more representative cancer models beyond simple cell monolayers. Accurate representation of this microenvironment is broadly recognised as being the next crucial step in the progression of cancer models[83–85], with the potential to drastically improve discovery of powerful new or repurposed anti-cancer drugs, or to personalize chemotherapy regimens to prevent patient non-response and optimise treatment.

1.6 Cancer Models

The most established *in vitro* cancer model is the cell monolayer. In this model cancer cells are seeded onto plastic or glass substrates and cultured, whereby they grow into 2D colonies, forming cell-cell junctions in the X-Y plane. The advantage of this model is its simplicity. Experiments typically have short setup and turn-around times, are highly scalable with multiwell plates and trivial to interrogate with high-content measurement and analysis systems. However, the poor complexity of this model is especially apparent in the context of cancer. Nutrient, oxygen and pH gradients, invasion of immune cells or blood vessels are not only absent in this model, but cannot be incorporated in principle. As such, there has been an increasing popularity of 3D cancer models, which can be fabricated in different ways and thus exist in different forms to more accurately reflect the TME.

Tumour spheroids, tumour organoids and tumour spheres are terms which describe 3D collections of cancer cells but are not strictly defined. To avoid confusion, three definitions will be stated here for consistency:

- **Organoid**: A 3D collection of cells formed from the growth of stem cells in 3D. For CRC, organoids refer to structures arising from the growth of CoSCs in a biocompatible

matrix. Patient-derived organoids (PDOs) use patient stem cells to generate personalized organoids.

- **Tumour Aggregate**: A 3D collection of cancer cells generated by forced aggregation. The hanging drop method[86], rotating bioreactors[87] and low attachment plates[88] are common methods of producing tumour aggregates.
- **Tumour Spheroid**: A 3D collection of cancer cells formed through division of cancer cells in a biocompatible matrix. Mixing cancer cell suspensions into commercial gels like Matrigel and GelTrex are common approaches to producing tumour spheroids.

The difference between these 3D models is cell-type and method of production. Organoids are comprised of stem cells which differentiate in 3D culture, producing a structure which contains different cell types. Relevant to this work, Sato *et al.* pioneered the growth and expansion of murine and human colonic organoids from Lgr5+ CoSCs in Matrigel[89,90]. The optimised culture conditions put forward were adapted for this work and described in section **2.5**.

Tumour aggregates are the simplest form of 3D cancer culture. Here, hundreds or thousands of cells are forcibly aggregated into colonies, typically through gravity or low adherent conditions. This approach is not specific to cancer as many somatic cell lines will similarly aggregate under these conditions. As the simplest form of 3D culture, tumour aggregates exhibit many practical benefits. First, the size of the aggregate can be reliably controlled by the quantity of cells used, with little dispersity in aggregate size. Second, many scalable solutions exist for the production of aggregates, for instance, Corning© produce 384-well, aggregate-forming, low adherent microplates, in which typically a single aggregate is cultured per well. Third and finally, the uniformity of aggregate production enables simpler analysis. For instance, bespoke imaging solutions are available for aggregates[91], accompanied with standardized assays and inbuilt software for aggregate detection and measurement. Although an improvement on the complexity of cell monolayers, tumour aggregates do not fully recapitulate the TME. Notably, ECM-analogues are typically absent from these approaches, which are ordinarily matrix-free. As such,

cell-matrix interactions are not represented. Furthermore, aggregate heterogeneity is enforced by the mixing of a population directly into a structure, which is unlike tumours *in vivo* which arise from a single cell and where heterogeneity evolves clonally.

Tumour spheroids represent a step forward in complexity from tumour aggregates. Tumour spheroids each grow from a single cell over time in a biocompatible matrix, thus recapitulating important cell-matrix interactions. The composition of the matrix can be fine-tuned to the cell line, to optimise its growth and behaviour in 3D. Heterogeneity within spheroids arises purely from the culture conditions and spheroid microenvironment, however, a heterogeneity will also exist between spheroids due to differences in the parent cells. The disadvantages to the tumour spheroid approach are entirely practical. Scalability is poor due to matrix component, which may be expensive, temperature or light sensitive and therefore requires significant manual-labour. Experiments take longer as spheroids are not pre-formed, but rather grow over time from individual cells, a process which can take several weeks. Direct measurements are impeded by the matrix component, which may not be optically transparent. Assays which require whole spheroids, cell suspensions, or cell lysates now involve a spheroid-retrieval step, whereby non-toxic degradation of the surrounding matrix is required to harvest viable spheroids.

Consequently, there presently exists potential to improve the practicality of the tumour spheroid model. Methods to increase scalability and improve measurement are required to increase throughput and enhance reliability. With these factors optimised, tumour spheroids could represent a significant step forward in 3D cancer models and represent a more accurate *in vitro* environment for chemotherapeutic agent study. Therefore, in this thesis, selection of the 3D culture environment and method of fabrication are important factors.

1.7 3D Cell Culture

A variety of approaches exist toward fabricating 3D culture systems. Broadly, fabricated 3D architectures for cell culture are referred to as “scaffolds”. Scaffolds can be defined as ordered,

acellular, biocompatible 3D structures which can be cellularized by mixing or seeding cells into or onto the structure. Rigid scaffolds requiring post-fabrication cell seeding can be produced by electrospinning[92], freeze-drying[93] and phase-separation[94]. Generally, these approaches result in a porous material, which are typically composed of synthetic polymers, such as poly(lactic acid) (PLA)[95], or polysaccharides, such as dextran[96]. Modification of synthetic polymers has given rise to a wide range of scaffold materials with different biochemical enhancements, like surface treatments for increased cell-adhesion[97], adsorption of biochemical molecules for improved differentiation of seeded stem cells[98] and degradation *in vivo* for eventual substitution of the scaffold by natural tissue[94].

Scaffolds are of particular relevance to regenerative medicine applications, whereby damaged tissue can be either replaced by an implanted acellular scaffold, into which cells migrate, adhere and proliferate, or by an implanted, cellularized scaffold, into which cells are pre-seeded. For instance, autologous therapies involving the harvesting and expansion of patient cells, such as mesenchymal stem cells (MSCs), could be used to avoid the need for immunosuppressants in implanted scaffolds. Examples of scaffolds technology are numerous, particularly in the field of artificial cartilage, which is avascular and therefore simpler to fabricate. However, rigid scaffold technology is not prominent in 3D cancer models, which generally benefit from a soft receiving substrate. Some examples do exist at the interface of cancer and bone, for instance, Bassi *et al.* produced a porous, hydroxyapatite (HA) foam as a model of the osteosarcoma stem cell niche[99].

For 3D cancer spheroid culture, hydrogels are the most promising scaffold technology. Hydrogels are water-swollen networks of crosslinked polymers, which are approximately 99% water by mass of water to dry weight of monomer[100]. Polymer chains can be ionically or covalently crosslinked in the presence of water to form such networks. Here, the ability to absorb water is due to the presence of hydrophilic functional groups within the polymer backbone, and the resistance to dissolution in aqueous environments arises from the crosslinks between chains. Hydrogels can be both synthetic or natural, with examples of both in the literature. The advantage of synthetic hydrogels is their reproducible and customisable physical and chemical properties.

The most abundantly reported synthetic hydrogel is poly(ethylene glycol) (PEG), is biocompatible and exhibits a versatile macromer chemistry suited to functionalisation with relevant biological peptides, such as the integrin binding peptide Arg-Gly-Asp (RGD)[101]. PEG hydrogels have been used extensively for controlled drug delivery and release[102], but also for cell encapsulation in regenerative tissue applications[101,103]. Natural hydrogels include alginate, collagen, gelatin, chitosan and hyaluronic acid, and the widely used commercial hydrogel, Matrigel. Many natural hydrogels are derived from mammalian proteins, such as collagen or fibrin, and are therefore bioactive, containing moieties recognizable to cells. Other natural hydrogels are biocompatible but not bioactive for human cells due to their non-mammalian source, such as cellulose and alginate, but may be further functionalised similarly to synthetic hydrogels.

Formation of hydrogels involves the critical cross-linking step, which can be a limiting factor in cell culture as it may be cytotoxic. Gelation methods of hydrogels broadly includes physical and chemical crosslinking. Physically, polymer chain interactions can form transient network junctions *via* entanglements. Collagen hydrogels are an example of a common hydrogel which can crosslink through entanglement, whereby collagen molecules can self-assemble into collagen fibrils which entangle to form hydrogels around 37°C and near neutral pH[104]. Matrigel behaves similarly, being comprised of a variable protein mixture secreted by Engelbreth-Holm-Swarm (EHS) mouse sarcoma cells[105], crosslinking *via* physical gelation at physiological temperatures. Gelatin, a hydrolyzed form of collagen, also gelates via physical entanglement in the presence of water. Here, gelatin solution solidifies thermally roughly below room temperature, however, a gelatin gel will dissolve in aqueous conditions, rapidly if heated. Consequently, gelatin gels for tissue culture are crosslinked either enzymatically by the transglutaminase enzyme, or chemically methacrylated to form gelatin methacrylate (GelMA)[106], which can be photocrosslinked using a radical initiator.

Photocrosslinking is a common crosslinking approach for a number of hydrogels and is advantageous due to its simplicity. Hyaluronic acid[107], gelatin[108], chitosan[109] and collagen[110] have

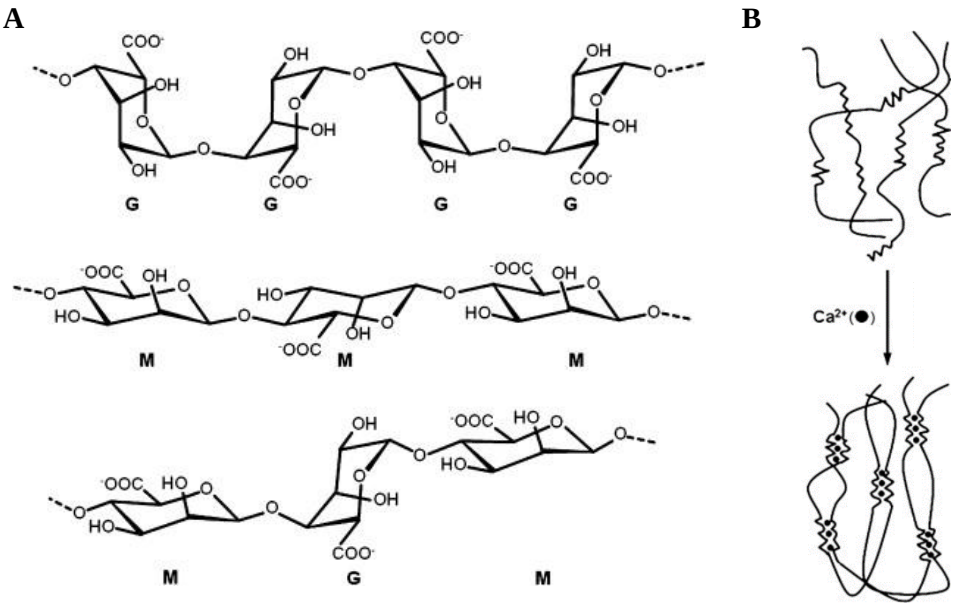

Figure 1-2 *Structure and ionic crosslinking of alginate.* ***A*** *G-blocks, formed of repeating G residues, M-blocks, formed of repeating M-residues and mixed blocks, formed from both residues, of alginate.* ***B*** *Egg-box model of ionic alginate crosslinking, using calcium^{2+} as the crosslinking ion. Calcium ions rest interstitially between adjacent G blocks.*

been successfully chemically altered and photocrosslinked, whilst preserving biocompatibility for various cell types. Methacrylated monomers can be purchased directly, only requiring the addition of water, a radical initiator and UV light to gelate. Here, concerns around the use of UV light arise due to its role in DNA damage, which could influence experimental results and limits *in vivo* applications due to the links between UV light and cancer[111]. A range of blue-light crosslinkers has arisen in response[112–114], but are still emergent in use.

Alginate gels are derived from the naturally occurring polysaccharide, alginic acid, which is extracted from algae[115]. The soluble sodium salt, sodium alginate, is the primary hydrogel component, which forms a gel when mixed with water. Alginate contains two residues, (1,4)-linked β-D-mannuronic acid (M-residue) and α-L-guluronic acid (G-residue), which link together and form blocks in the polymer chain (**Figure 1-2**, **A**)[116]. Consequently, alginate from difference sources have different M/G ratios and therefore exhibit different physical properties when formed into gels. The G blocks (blocks containing only G residues) of alginate can be crosslinked ionically with multivalent cations to form robust hydrogels[116]. The egg-box model depicts the crosslinking of alginate, whereby the G blocks form interstitial structures within which cations

can bind to multiple monomers (**Figure 1-2**, **B**). It is sometimes erroneously suggested that divalent cations are the only suitable crosslinkers for alginate, however, Idota *et al.* have reported metal trivalent cations with high binding affinity to alginate, such as Tb^{3+} and Dy^{3+} [117]. Of the metal ions with high binding affinity, calcium is the most suitable for biological culture, as other high-binding affinity crosslinkers are cytotoxic, such as Pb^{2+}. Calcium chloride is water soluble and therefore can be simply added to solution to crosslink immersed alginate gels, dissociating readily into the crosslinking cation. Consequently, $CaCl_2$ crosslinking of alginate gels is most commonly reported in the literature.

Alginate gels are bioorthogonal for mammalian cell culture, not possessing any binding sites for cell adhesion proteins such as integrins. However, cells can still readily divide in unmodified calcium-crosslinked alginate gels, which are a mainstay of cell-encapsulating microfluidic systems[118,119]. Alginate gels can be modified to increase cell adhesion, with RDG-alginate being the most common modification[120], or combined with other gels where it acts as a structural component. Alginate-gelatin[121], alginate-collagen[122], alginate-gelMA[123] and alginate-fibrin[124] gels have all been used in 3D cell culture. The ionic nature of alginate crosslinking is both advantageous and disadvantageous. On the one hand, in experimental conditions, calcium ions will be released gradually over time into the surrounding media post-crosslinking, deforming the hydrogel structure before causing it to dissolve fully. As such, culture media must be supplemented with $CaCl_2$ to prevent hydrogel dissolution. For most cell lines, low-level $CaCl_2$ supplementation has no negative consequences, however, some cells are sensitive to calcium signalling and therefore not suited to this culture setup[125].

The advantage of the weak nature of the ionic bond is not often discussed but is a practical aspect of 3D culture which may be overlooked. Metal ions like Ca^{2+} may be chelated by chelating agents such as Ethylenediaminetetraacetic acid (EDTA), triggering rapid dissolution of alginate gels and liberating encapsulated cells. Many functional assays involve viable whole cells or cell lysates, such western blots, flow cytometry and quantitative polymerase chain reaction (qPCR), and therefore the ability to control hydrogel degradation and harvest viable cells has enormous utility.

Moreover, hydrogels interfere in various common assays, and so in many cases their removal is preferable, though not strictly necessary. For instance, alginate is stained by prevalent histological stains, and hydrogels limit diffusion of stains for microscopy.

1.8 Hydrogels for 3D cancer culture

More specific to this work, 3D cultures for tumour spheroids have been reported in the literature, predominantly using biocompatible hydrogels. The most common hydrogel for cancer culture is the Corning product, Matrigel. Matrigel, as discussed, is the product of EHS cell secretions and primarily contains laminin (~60%), collagen IV (~30%), enactin (~8%) and perlecan (~3%)[126], and is thus reminiscent of human basement membrane. As EHS cells are cancerous, Matrigel includes a number tumour-derived proteins, such as transforming growth factor β (TGF β), fibroblast growth factors (FGFs), and matrix metalloproteinases (MMPs)[127]. As an encapsulating gel, various cancer lines grow into spheroids when dispersed as single cells throughout the gel[128–130].

Matrigel has a unique history with CRC. Sato *et al.* first discovered that CoSCs could grow into organoids in Matrigel, forming crypt-like structures with resident stem cells in each crypt[89]. The culture conditions established in this landmark study have since been adapted for use in tumour spheroid culture with cancer cell lines[131]. Indeed, in this work, culture conditions are adapted from Sato *et al.* for tumour spheroid growth.

Unfortunately, Matrigel has a number of downsides. Matrigel is variable in composition between batches, leading to authors exercising caution in the reliability of results. Practically, Matrigel is expensive and challenging to work with. Matrigel is amongst the weakest hydrogels, and does not support its own self weight[132], and so cannot be readily be patterned into shapes. Matrigel gelates thermally at temperatures above 4°C, and so must be worked with on-ice, and the addition of cell suspension, or pipetting with warm pipette tips, can trigger early gelation. Consequently,

studies have attempted to either mix Matrigel into other gels[133] to make it more practicable or find a suitable alternative.

Here, the workability of hydrogels is only a factor in the patterning of gels to construct more complex culture systems. Matrigel is ruled out due to its poor mechanical properties, but many other gels, like agarose, alginate and gelMA can be formulated such that they are structurally robust and therefore patternable. For instance, models of human ears and noses have been produced with alginate hydrogels[134]; The 3D patterning of such cell-laden gels is known as bioprinting.

1.9 Bioprinting

Bioprinting refers to the spatiotemporal control of the deposition of biomaterials, including acellular and cell-laden hydrogels. Bioprinting as a technology emerged from the recent advances in conventional 3D printing with thermoplastics. Indeed, early bioprinters in the literature are simply modified 3D printers[124,134] and have since become more advanced, bespoke and commercialised. Bioprinting, like 3D printing, involves the creation of digital models *in silico*, then the conversion of this model into step-by-step, layer-by-layer commands ('slicing') and finally printing. A variety of computer aided design (CAD) programs exist for designing digital models, many of which are free, and the print commands are outputted in GCODE, which is a universal language for 3D printers. Consequently, bioprinting, like 3D printing, is reasonably accessible to the end user.

In bioprinting, patterning of living cells is typically achieved by blending cells into the print material, usually a hydrogel, then printing the combined cell-laden hydrogel. The term 'bioink', was coined by Vladimir Mironov[135] and originally meant the direct positioning of cells or tissues onto a 'biopaper'. However, this term has since expanded to generally encompass cell-laden, biocompatible materials which are deposited with a biofabrication technique. This is functionally

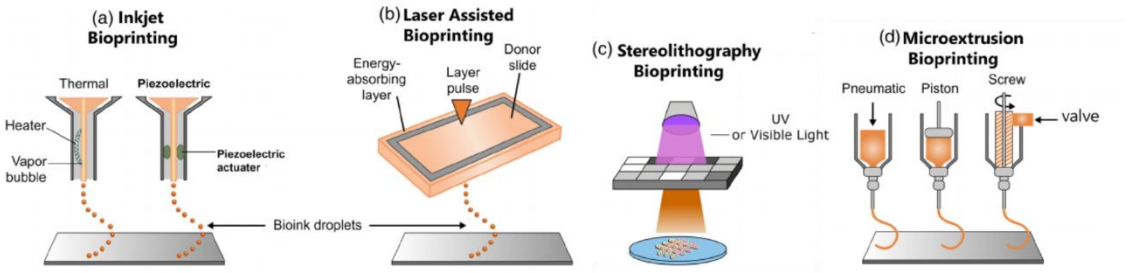

Figure 1-3 *Overview of different bioprinting approaches, reprinted from Midha et al.* [136]

distinct from an acellular biomaterial which acts as a scaffold onto which cells are deposited ('seeding').

A plurality of printing approaches exist for 3D printing, and the same is true for bioprinting. The four prevailing technologies are: inkjet (**Figure 1-3**, **A**), laser-assisted (**Figure 1-3**, **B**), extrusion (**Figure 1-3**, **C**) and stereolithography (**Figure 1-3**, **D**). Each technology has its own advantages and disadvantages, and exhibits various subtypes.

1.9.1 Inkjet bioprinting

Inkjet bioprinters produce high resolution 3D structures through the controlled deposition of small droplets. Inkjet bioprinters can use thermal printheads to produce vapour bubbles which drive droplets through a nozzle, however, the high operating temperatures prevent use with live cells, thus limiting its application to the patterning of non thermally-degrading biomaterials. Consequently, piezoelectric inkjet bioprinters are therefore the prevailing variant, reported in a number of studies. Graham *et al.* use an inkjet bioprinter to produce cell-laden agarose/collagen droplets approximately 40μm in size for MSC culture[137]. Zhou *et al*. go on to use the same printing technology to pattern Matrigel-encapsulated human neural stem cells in complex droplet structures[138]. Functional and connected neural networks emerged from these printed neural tissues over 44 days.

Through the patterning of small droplets, inkjet printers are able to produce high-resolution structures. For instance, Villar *et al.* were able to produce folding and shape-changing structures

using droplet of differing osmolarity[139], and Alcinesio *et al.* produced droplet structures containing conductive single-droplet channels for controlled signal propagation[140].

The advantages of the inkjet approach are the unparalleled high-resolution of printed droplet-structures, and the ability to manipulate low-viscosity fluids like Matrigel, which cannot be printed with other methods. However, these advantages with associated costs. High-resolution droplet patterning precludes rapid fabrication of many large structures, and the sensitive piezo actuation, whilst suited to low viscosity fluids, cannot work with high-viscosity gels (>100 mPas[141]).

1.9.2 Laser-assisted bioprinting

Laser-assisted bioprinting (LAB) is derived from the laser-induced forward transfer (LIFT) process which exists in industry. Here, a donor layer of material is energised by laser pulses, ejecting donor material to a receiving substrate[142]. For bioprinting, the donor material is a cell-laden hydrogel arranged on a laser-transparent carrier substrate, such as quartz. Laser pulses travel through the carrier substrate and produce vapour pockets which expel small volumes of bioink onto the receiving substrate, which could be a multi-well plate for convenience. Gudapati *et al.* use this process to eject 20μL droplets of cell-laden alginate into a 24 well plate[143], demonstrating a lower resolution than inkjet printing, but with improved throughput and using more viscous gels.

LAB is not a common bioprinting approach and has a number of disadvantages. The high cost and lack of commercial options for laser-assisted bioprinters is prohibitive for basic research[144]. Moreover, there are concerns as to the toxicity of the laser pulses on living cells. Cell viability was found to be lower in LAB than in inkjet bioprinting, with the primary cause of cytotoxicity being thermal damage from nano- and femto-second laser pulses[145].

1.9.3 Stereolithography bioprinting

Stereolithography has been realized by the development of photocurable biocompatible polymers, such as GelMA. Using a projector, patterned light can be projected onto a photocurable

bioink, resulting in selective covalent crosslinking of the bioink into different patterns. A key advantage of this approach is the ability to pattern entire layers simultaneously with the projected shape. For instance, Wang *et al.* patterned cm-scale logos and grids with 50μm resolution in less than 2 minutes a layer, using a photocurable PEG/GelMA bioink[146].

As most photocurable polymers use UV-light there has been some concern about UV-induced DNA damage in experimental samples. As Stereolithography is a layer-by-layer approach, UV exposure times increase with larger structures. For instance, although Wang *et al.* only required 2 minutes to photocure a single layer, entire structures took more than 15 minutes to cure, as a result of additive UV exposure for each layer. Some studies have addressed this concern by introducing blue-light crosslinkers. However, these studies produce acellular scaffolds which are seeded later and therefore UV exposure was not a concern in these instances[147,148].

Practical considerations with this approach are apparent. Large structures using blue light exposure would encounter focal plane limitations due to light scattering in the hydrogel structure[149]. Experimental setups are often large and expensive, requiring powerful lamps and arrays of lenses to pattern light effectively[150].

1.9.4 Extrusion bioprinting

Extrusion bioprinting is the most popular method of bioprinting and is derived from conventional fused deposition modelling (FDM) 3D printing technologies. Here, prepared bioinks are extruded through a nozzle pneumatically, or using a piston or screw, onto a print surface. Often, bioinks are simply loaded into syringes for piston printing, or syringe barrels for pneumatic and screw printing.

The accessibility of extrusion bioprinting is currently the highest of all approaches. Innovations in desktop FDM printers has drastically reduced the price of such systems[151], translating directly to extrusion bioprinters. Moreover, open source FDM print software, such as CAD programs and slicers is abundant and can be readily adapted for use with bioprinters. Consequently, there is

increasing use of custom, modified 3D printers used as extrusion bioprinters in academic institutions for tissue engineering research[152–157].

Extrusion-based systems come with important limitations. As material moves through the print nozzle, shear forces are imposed on the bioink and cells within. As such, rheological material properties are significant, as some materials become more viscous ("dilatant materials") in response to applied shear whereas others become less viscous ("pseudoplastic materials"). Shear-thinning, pseudoplastic, materials are necessary for accurate extrusion, as the fluid behaviour of shear-thinning materials enables smooth and continuous flow through the print nozzle. However, many appropriate natural materials are shear thinning, such as alginate[158] and gelatin[159]. Shear-forces can be a concern for the viability of encapsulated cells in bioinks, limiting print forces and therefore extrusion rate from these systems, however, typical printing conditions have not been reported to be significantly harmful to most cell lines[160].

The advantages of the extrusion bioprinting approach lie in its accessibility and scale. Similarly to FDM 3D printers, extrusion bioprinters can print large structures on the mm-scale, such as ear-[161], nose-[134] and bone-analogues[161], which can be implanted for regenerative medicine applications. Consequently, this approach has been of particular interest due to its potential to print functional tissues and organs, an ongoing, long-term goal of bioprinting[144].

An underutilised advantage of extrusion bioprinting is its potential to be exploited for high throughput systems. The same ability to produce large and detailed structures also permits for the rapid fabrication of many simpler structures. Contextually, the emphasis in the high-throughput approach shifts from the biofabrication of large tissue analogues for regenerative medicine applications, to development of high throughput 3D models for the rapid screening of different conditions. The need for such systems is clear for drug discovery, drug repurposing, and personalised medicine, whereby high throughput testing is the norm for 2D models, but an established, complex, high throughput 3D model does not exist. The foundation of such a model rests on the bioink selection, as this encompasses both the practical elements, *e.g.* printability, cost, scalability, *etc.* and the model complexity, *e.g.* cell-matrix interactions.

1.10 Bioinks for bioprinting

Many of the most common bioink components were discussed in section **1.8**. Recently, Sánchez *et al.* performed a meta-analysis measuring the frequency of bioinks appearing in different journals; The 10-most common materials in cellular bioinks were as follows[162]:

1. Alginate (38%)
2. Gelatin (18%)
3. GelMA (15%)
4. Hyaluronic Acid (10%)
5. Cellulose (10%)
6. Collagen (6%)
7. PEG-derivatives (6%)
8. Agarose (5%)
9. PEG (4%)
10. Chitosan (2%)

These components can exist independently or as complex mixtures to form different bioinks. For instance, the two most common bioink components, gelatin and alginate, are often blended to form alginate/gelatin bioinks. For instance, a 3% alginate, 7% gelatin gel and a 1% alginate, 7% gelatin gel have both been used to culture breast cancer cells[121,163]. Blending different bioink components is often used to increase mechanical performance. For instance, Matrigel and collagen, which cannot be typically be extrusion bioprinted due to poor mechanical properties, have been blended with agarose and alginate to produce printable bioinks[122,133]. Here, the alginate component acts as a structural element, as the strength of alginate gels is tuneable with alginate concentration, crosslinker concentration or crosslinking time, whereas collagen and Matrigel act as ECM analogues supporting binding sites for cell-matrix interactions.

Bioink components can be blended with sacrificial elements, which can act as viscosifiers for printing[164], supporting layers for complex geometries like overhangs[165], or dispersers for the fabrication of porous structures[134]. Pluronic F127, a tri-block co-polymer with a hydrophobic core

flanked by two hydrophilic blocks, gelates thermally and is highly printable, resulting in its frequent use as a sacrificial, or fugitive ink[134,165]. The combination of fugitive, active, and structural has given rise to a range of different bioprinted models spanning multiple tissue types.

1.11 Bioprinted 3D culture models

Bioprinting has been used in a number of tissue engineering applications, using blends of bioink components listed in section **1.10**, as well as other bioactive compounds. Generally, attempts have been made to reproduce any complex tissue with a stratified structure. Bone, kidney, and skin tissue are all examples of tissues with zonal histologies, which have been bioprinted in the literature. For instance, Chimene *et al.* recently developed an osteoinductive GelMA/Nanosilicate bioink for either injection or engraftment into bone[166]. This bioink was porous and demonstrated high toughness and compressive stiffness (up to 150kPa). MSCs dispersed in this bioink remained viable for 90 days of culture, exhibited genetic hallmarks of osteogenic differentiation and mineralised the bioink by calcium deposition. Homan *et al.* developed perfusable renal proximable tube models using bioprinting to template a sacrificial, or fugitive, Pluronic F127 ink[165]. Flowing cells through the vacant channels resulting from the removal of the sacrificial ink produced highly organised cellular structures which remained viable for at least 60 days. *In vivo* characteristics of the model included superior albumin uptake relative to cell monolayers and more accurate response to nephrotoxic compounds. Derr *et al.* produced a bioprinted skin model which accurately mimicked the stratified structure of the skin[167]. Patterning of different bioinks, containing gelatin/collagen/fibrinogen was used to produce a skin model with 4 stratum, using a coculture of dermal fibroblasts and epithelial keratinocytes.

Collectively, these studies and others demonstrate the emerging role of bioprinting as a foundation for 3D culture, providing reliable data and producing models which are otherwise not possible with standard monolayer approaches. Cancer models have similarly benefitted from bioprinting-mediated 3D cultures, and although still in their infancy, are summarized below.

1.12 Bioprinted cancer models and the current state of the art

Bioprinted cancer models have been used for the generation of tumour spheroids and subsequent exposure to chemotherapy. Sun *et al.* produced an alginate/fibrin/gelatin hydrogel in which the cervical cancer line, HeLa, was highly viable and self-assembled into spheroids[124]. Paclitaxel treatment on these spheroids was less effective than for cell monolayers, although the effect was not explicitly quantified. Swaminatham *et al*. bioprinted MDA-MB-231 and MCF-7 breast cancer cells in alginate/gelatin and alginate/collagen bioinks[122]. However, Swaminatham *et al.* report that these cancer lines do not spontaneously proliferate and self-assemble in the aforementioned bioinks, and therefore Matrigel is used to culture spheroids, which are harvested and dispersed into bioinks for printing. MDA-MB-231 and MCF-7 breast cancer spheroids maintained their structure in the alginate bioinks for 72 hours, after which cells migrated into the surrounding bioink. Compared to monolayer culture, these spheroids were more resistant to paclitaxel.

Studies such as these are the most common for bioprinted cancer models, representing low throughput bioprinted 3D cancer monoculture with immortalized cancer cell lines. The important gel-matrix interaction is preserved, and drug resistance is reported to increase. However, throughput is low, with both studies using 6-well plates as their culture platform. Moreover, quantification of drug effect is minimal, with no dose-response curves or inhibitory concentrations calculated. Spheroid chemoresistance is reported, however no assays were performed to attempt to explain this increased resistance, for example, it is unknown if spheroids are hypoxic or acidic, express CSC markers, or exhibit changes in expression of resistance-related drugs.

More complex bioprinting studies do exist, for instance, Jiang *et al.* used an alginate/gelatin bioink to culture MDA-MB-231 breast cancer cells in coculture with IMR-90 stromal fibroblasts[121]. These fibroblasts were found to preferentially migrate towards MDA-MB-231 cells, migrating through an acellular zone. Yi *et al.* recently produced one of the most complex cancer models to-date[168]. Here, a bioprinted perfusable, personalised glioblastoma (GBM) model was generated, using decellularized brain ECM as the basis of their bioinks. Patient-derived GBM

cells were cocultured with human umbilical vein endothelial cells (HUVECs) and treated with chemotherapy and radiotherapy. Yi *et al*. found that GBM patient samples from patients with high, medium and low survival rates aligned with resistance *in vitro* in the bioprinted model. This study represents the current state-of-the-art for bioprinted cancer models, incorporating primary cells, stromal cells, tissue-specific ECM, and microfluidic perfusion. However, a drawback still lies in its low-throughput approach, as each technical replicate was printed on a standard microscope slide, and a complex pump system required for the continual perfusion of multiple samples.

There are remarkably few studies involving bioprinted CRC models, with one recent cancer bioprinting review summarizing 29 bioprinted cancer models across 6 different cancer types, none of which were CRC[83]. However, studies on CRC spheroid aggregates have demonstrated time and time again that drug resistance, gene expression and CSC markers are regulated by the 3D environment, even in this simple form[169–171]. Scaffold-based approaches have used for CRC, with Chen *et al.* printing a poly(caprolactone)/collagen I scaffold, cellularized by seeding with HCT116 CRC cells. HCT116 cells in 3D scaffold-culture exhibited increased CD133 expression, increased resistance to 5FU, cisplatin and doxorubicin and caused larger tumour formation in SCID mice compared to cells harvested from ordinary monolayer culture[172]. HCT116 cells have also been encapsulated in alginate, growing into spheroids over 21 days and exhibiting increased resistance to 5FU[173]. Although not bioprinted CRC models, these works again highlight the importance of the 3D environment on chemoresistance in CRC cells.

1.12.1 Patient-derived colorectal cancer spheroids

In the case of CRC specifically, there exists powerful clinical evidence surrounding the utility of CRC spheroids and their relevance in mirroring patient-response. Two recent landmark studies exist, comparing *in vitro* chemoresistance data from patient-derived spheroids to patient chemotherapy response. Vlachiogiannis *et al.*[31] and Ooft *et al.*[30] both report co-clinical studies to analyse the predictive performance of patient-derived cancer spheroids (PDSs). In both studies, patient

cancer cells were harvested *via* biopsy and seeded into Matrigel, forming spheroids with reasonable efficiencies (70%, and 63%, respectively).

Vlachiogiannis *et al.* harvested patient cells pre- and post- treatment, from primary tumours and distal metastases. A number of important clinical links were determined. First, comparison of PDSs from patients who were resistant and sensitive showed ~10-fold differences in drug response. Second, PDSs cultured from primary cells harvested before and after treatment mirrored acquired resistance in the patient population, exhibiting mutant oncogenes responsible for such resistance. Third, PDSs harvested prior to treatment predicted non-response in all cases. Ooft *et al.* report similar observations. PDSs in their study were predictive of patient response to the topoisomerase inhibitor, irinotecan, and the combined therapies irinotecan/5FU and 5FU/OX, identifying a patient population in advanced CRC who would not benefit from palliative chemotherapy.

Collectively, these studies demonstrate the predictive potential of patient-specific 3D cultures for identifying responsive and nonresponsive CRC patients, and thereby optimising their treatment with available therapies. However, the success of these studies cannot be pursued without innovation in the spheroid model, as these works required intense manual labour for the establishment of PDS cultures and drug screening. Automation of the PDS approach would greatly benefit the advancement of personalised medicine in CRC.

1.13 Thesis aims and structure

In CRC, a unique case exists whereby an urgent need for predicting patient response to therapy has an apparent solution in emerging tumour spheroid models, which are currently limited to small scale assays. Consequently, automated, high-throughput assays using proven spheroid models could provide a powerful solution, having obvious utility in the future of cancer care.

In this work, the overall aim is to use nascent bioprinting technology and high content microscopy to produce such a high-throughput CRC spheroid assay. Bioink selection, induction of spheroid

self-assembly and chemotherapy assay design must be optimised to produce a holistic and robust system for the analysis of spheroids at scale.

As this author is not aware of any previous bioprinted models for CRC, chapter 3 explores bioink options for different CRC cell lines. Spheroid culture in different bioinks is attempted, and the links between bioink structure and spontaneous spheroid formation are explored. Chapter 4 describes the application of an optimised bioink developed in chapter 3 for the development of a spheroid-formation assay with a range of different CRC cell lines. The properties of the resulting spheroids are investigated, including morphology, internal structure, oxygen, and glucose consumption. Finally, in Chapter 5, a high-throughput bioprinting pipeline is established for the simultaneous measurement of thousands of tumour spheroids, using bespoke image analysis code. The efficacy of chemotherapy, radiotherapy and combination therapies is measured for both tumour spheroids and conventional monolayers.

Chapter 2: Materials and Methods

2.1 Introduction

This chapter contains an overview of the theory and protocols behind the experimental techniques used in this research. Frist, general protocols are summarised, followed by detailed descriptions for how different analyses were performed. Finally, an in-depth overview and explanation of image analysis code developed is given.

2.2 Cell culture

A variety of cancer cell lines were used in this research, most of colorectal origin. Colorectal cancer cell lines were kindly provided by Professor Ann Williams and initially purchased from American Type Culture Collection; breast cancer cell lines were kindly provided by Dr. Claire Perks. All cancer lines used are listed in **Table 2-1**, below:

Table 2-1 *Cell lines used in this research. Cancer origin and staging included where known.*

Cell Line	***Tissue of Origin***	***Cancer Stage***	***Primary/(Metastasis)***
SW480	Colon	Dukes' B	Primary
SW620	Colon (lymph node: liver)	Dukes' C	Metastasis
SW837	Rectum	*Not known*	Primary
SW1463	Rectum	Dukes' C	Primary
LS174T	Colon	Dukes' B	*Not known*
LOVO	Colon (lymph node: neck)	Dukes' C	Metastasis
HT29	Colon	Dukes' C	Primary
HCT116	Colon	Dukes' D	Primary
CACO2	Colon	*Not known*	Primary
MCF7	Breast	(Early)	Primary
MDA-MB-231	Breast (lung)	(Late)	Metastasis

2.2.1 Culture conditions

All cell lines used are adherent and therefore grown in adherent culture conditions. Cells were grown in 12.5cm^2, tissue-culture treated flasks with 4mL of culture media and incubated in humidified incubators at 37˚C, 5% CO2. Culture media for all lines except HCT116 consisted of

high-glucose Dulbecco's Modified Eagle Medium (DMEM) supplemented with 10% fetal calf serum (FCS), 100 U/mL penicillin, 100 µg/mL streptomycin and 2mM glutamine (all Gibco; Thermo Fisher Scientific). Culture media for HCT116 consisted of McCoy's 5A modified medium supplemented with 10% FCS, 100 U/mL penicillin, 100 µg/mL streptomycin and 2mM glutamine (all Gibco; Thermo Fisher Scientific). All cell work was performed in class II laminar flow cabinets; media was exchanged every 2-3 days.

2.2.2 Passaging, Harvesting and Cell Counting

Cells were harvested around 80% confluence and either re-seeded into new flasks, cryopreserved, or used experimentally. Media was aspirated from flasks before washing with 5mL pre-warmed Phosphate Buffered Saline (PBS; Sigma Aldrich, UK) before incubating with 2mL pre-warmed trypsin/EDTA solution for 3-5minutes at 37˚C. Flasks were gently agitated and cell detachment confirmed with a brightfield microscope. 8mL media was added to the detached cells, forming a 10mL cell suspension which was transferred to a 30mL universal tube and centrifuged at 3000RPM (500xg) for 3minutes with a Sorvall Legend RT centrifuge (Thermo Fisher Scientific, UK).

After centrifugation, the resulting cell pellet was resuspended in high glucose DMEM and a 10uL volume counted either with a Neubauer Improved Haemocytometer Counting Chamber (Sigma Aldrich, UK) or a Countess II automated cell counter (Invitrogen, Thermo Fisher Scientific, UK). Cells were optionally stained with 0.4% Trypan Blue solution (Thermo Fisher Scientific, UK) to confirm high viability in the cell suspension.

For cryopreservation, $4x10^6$ cells were suspended in freezing medium, comprised of 50% 10%(v/v) dimethyl sulfoxide (DMSO) in FCS and 50% DMEM, then transferred to a 1.5mL cryovial (Thermo Fisher Scientific, UK). Cryovials were slowly cooled overnight in a Mr. Frosty Freezing Container filled with neat isopropyl alcohol (Thermo Fisher Scientific, UK), after which vials were moved to storage containers in liquid nitrogen dewars.

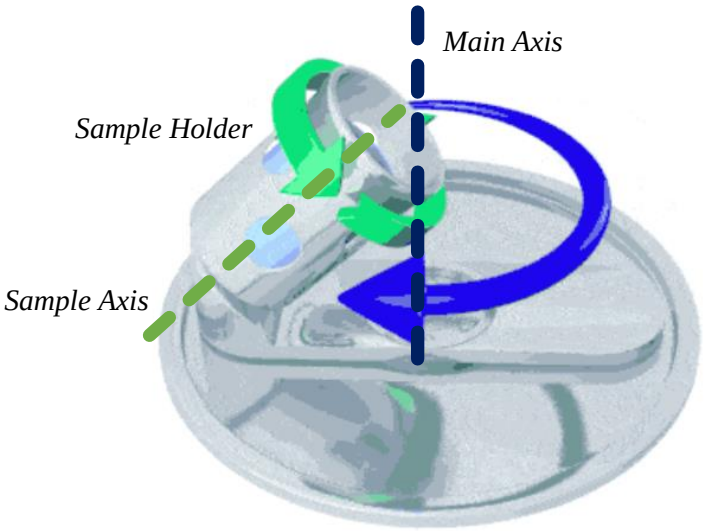

Figure 2-1 *Dual asymmetric centrifuge with the two axes of rotation shown. Rotating the sample about both axes ensures through mixing of viscous fluids. Figure adapted from Speedmixer.com.*

2.3 Bioink Preparation

2.3.1 Alginate-Pluronic F127 Bioinks

This bioink was first developed and published by Armstrong *et al.* as a stiff, microporous, printable bioink supportive of the growth of human mesenchymal stem cells (hMSCs) in 3D and therefore suited to engineered cartilage applications[134]. The protocol established by Armstrong *et al.*was as follows: First, a 40%(w/v) Pluronic F127 (Sigma Aldrich, UK) solution was prepared by mixing F127 powder with serum-free culture media and autoclaving at 121˚C, with a 15-minute hold time. Here, autoclaving fully dissolves the F127 and sterilizes the solution, forming a viscous gel which can be stored at 4˚C until needed. Second, a 10%(w/v) sodium alginate solution was prepared by adding sodium alginate powder (Sigma Aldrich, UK) to culture media and mixing at 500RPM with an overhead stirrer until dissolved and a gel formed. Alginate gels undergo irreversible physical changes when autoclaved which alter their mechanical properties[174], consequently, this gel was sterilized by exposure to ultraviolet (UV) light for 1 hour in a laminar flow hood immediately prior to use. The two gels were mixed by hand to form the final 6%(w/v) alginate, 13%(w/v) Pluronic F127 bioink; a small volume of cell suspension was added and similarly mixed-in by hand prior to bioprinting. Cell densities varied between 10^4-10^6 cells/mL.

To reduce variability in the bioink produced with this protocol, a dual asymmetric centrifuge (DAC) was incorporated into the mixing steps. Dual asymmetric centrifuges rotate samples about their own vertical axis in addition to a main axis as with ordinary centrifuges (**Figure 2-1**), resulting in greater homogeneity and smaller air bubbles when mixing viscous liquids. In this adjusted protocol, the 10% alginate gel was prepared through mixing sodium alginate powder and media in a DAC (Speedmixer, UK) at 3500RPM for 5 minutes, followed by UV exposure for at least 1 hour. The F127 gel was prepared by autoclaving as before but blended with the alginate gel using the DAC at 1500RPM for 30 seconds; cell suspension, typically 50,000 cells/mL of bioink, was added in the same way.

2.3.2 Gelatin-Alginate Bioinks

10%(w/v) gelatin gel was prepared by dissolving gelatin powder (Sigma Aldrich, UK) in serum-free media at 60˚C on a hotplate while stirred, then stored at 4˚C until use. Sodium alginate powder was added to pre-warmed gelatin gel then mixed using the DAC at 3500RPM for 5 minutes. Alginate concentration varied between 0.5-5% (w/v). The resulting gelatin-alginate bioink was UV exposed for at least an hour in a laminar flow hood before use. Sterile gelatin-alginate bioink was then prewarmed to 37°C with a water bath, then 50uL/mL cell suspension was added with a DAC at 1500RPM for 20 seconds, for a total of 50,000 cells/mL of bioink.

2.3.3 Commercial Bioinks and Gels

Cellink Bioink, a proprietary blend of alginate and nanofibrillar cellulose, was purchased from CELLINK (CELLINK, Sweden). SW620 cells were blended into this gel as specified by CELLINK: A 3ml syringe containing 300uL of cell suspension, typically 50-100,000 cells/mL was connected to a syringe containing the Cellink bioink using a male-to-male luer-lok connector. The cell suspension and bioink were passed repeatedly back and forth between the two syringes, slowly mixing them together.

Matrigel is a commercial biocompatible hydrogel with extensive use reported in the literature. Matrigel is basement-membrane matrix derived from Engelbreth–Holm–Swarm (EHS) mouse

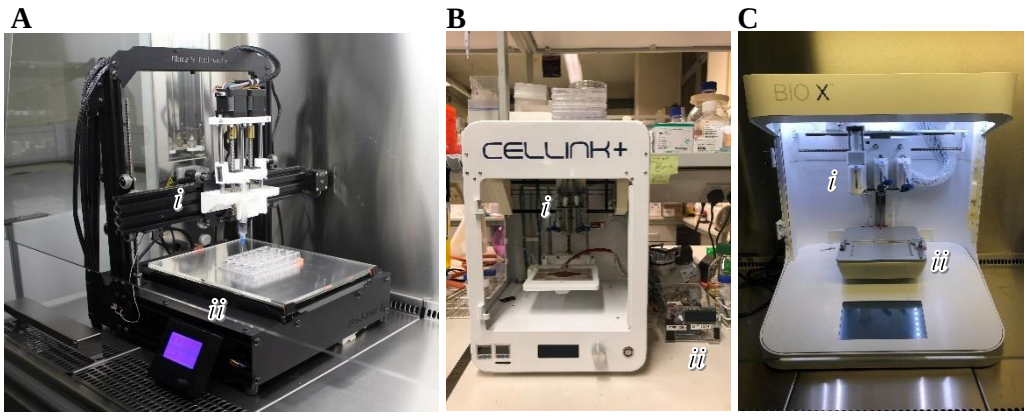

Figure 2-2 *Different bioprinters used in this research.* ***A*** *Modified Mendelmax3 3D printer with a custom dual extrusion system* ***(i)*** *and mount for conventional well-plates* ***(ii)****.* ***B*** *Cellink INKREDIBLE+ bioprinter with pneumatic print heads* ***(i)*** *and control box for the custom-made heated bed* ***(ii)****.* ***C*** *Cellink BIO-X bioprinter with syringe-pump print heads alongside pneumatic print heads* ***(i)*** *and a fully temperature-controlled print bed* ***(ii)****.*

sarcoma cells and therefore contains common extra-cellular matrix (ECM) components, growth factors and other biological compounds. Matrigel is known to support the growth of colorectal tumour spheroids and organoids[89,90,175] from single cells suspended in the gel. Growth factor reduced Matrigel (Corning, UK) was purchased, then aliquoted into 1mL Eppendorf tubes and stored at -20˚C. Matrigel aliquots were thawed at 4˚C overnight, ready for use the next day. Cell suspension, at a 1:20 ratio of cell suspension:Matrigel, was pipetted into cold Matrigel on ice and mixed by pipetting gently up and down. Final cell density was 10,000 cells/mL. 25µL/well of cell-laden Matrigel was added to wells in a 24-well plate (Costar, Corning), then incubated at 37˚C for 5 minutes to thermally set the gel. Finally, 500µL culture media was added to each well.

2.4 Bioprinting

Three different bioprinters were used for this research, each representing an improvement over the previous system (**Figure 2-2**). As a result, three separate printing protocols were developed:

2.4.1 Bioprinting with the modified MendelMax3 3D printer

Following the published work of Armstrong *et al.*[134], in which a simple bioprinting system was developed, a more sophisticated, dual extrusion printer was designed by Dr Thomas Richardson. This bioprinter was the basis of the initial research outlined here and was only used in conjunction

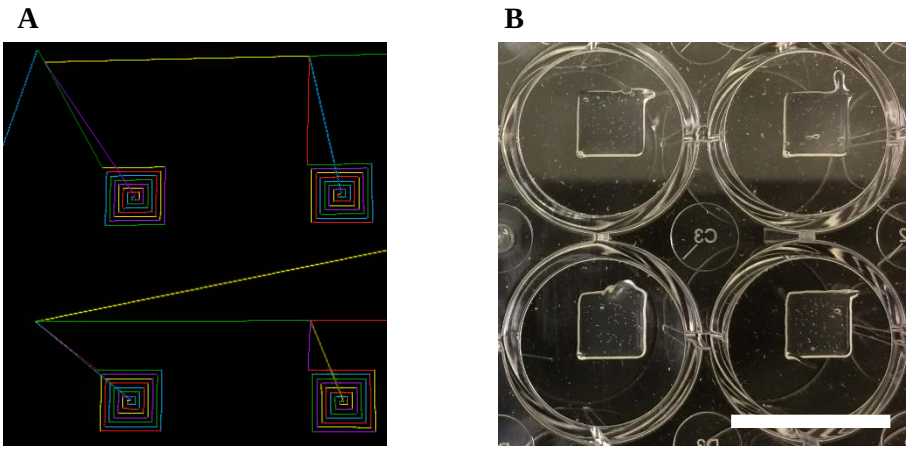

Figure 2-3 *Visualized GCODE, and bioprint with the modified MendelMax system.* ***A*** *GCODE commands visualized where coloured lines show the path of the print nozzle.* ***B*** *Magnified view of bioprints in a 24 well plate, from the GCODE commands visualized in* ***A****. Scale bar = 15mm*

with alginate-F127 bioinks. The printer was further altered to include a mount compatible with multi-well plates designed in *SOLIDWORKS* (Dassault Systèmes, France) and fabricated from laser-cut acrylic. After loading a bioink-containing syringe into the bioprinter, print command files were uploaded to the printer with an SD card, and the printing controlled *via* MatterControl (Matterhackers, USA), an open-source 3D printing software for slicing and managing print files. Print commands took the form of .GCODE files, which contain lists of instructions such as changing the print bed temperature, moving the extruder, and extruding bioink (through stepper-motor commands which in turn drive the syringe plunger downwards). As GCODE files can contain hundreds or thousands of lines of code, python scripts were written in Microsoft visual studio (Microsoft, USA) to generate GCODE files for printing. GCODE files could be checked for errors before printing with simple online GCODE visualisers (**Figure 2-3**).

To sterilise the MendelMax system, the bioprinter was first wiped down with 70% ethanol and left exposed to UV light for at least 1 hour. Nozzles or needles of different gauges were autoclaved before use and syringes and well-plates used were all sterile and individually wrapped. The alginate-F127 bioink was prepared according to section **2.3.1** and loaded into a 5mL syringe with a luer fitting (Terumo, UK). A GCODE print file was written and stored on an SD card, then uploaded to the printer. Print speed was set to 25mm/s, infill to 100% and the layer height equal

to the diameter of the nozzle used, which was typically 0.514mm, corresponding to 21-gauge blunt needles (Metcal, USA). As the first layer of any form of extrusion 3D printing can determine the success of the print, the bioprinter needed to be calibrated before the print could start. Specifically, the initial height of the needle from the print surface must be precise to ensure prints of good quality. As such, this height was determined manually by gradually increasing the height of the needle from the print surface to an appropriate level. Finally, the print bed was heated to 37˚C immediately prior to printing to activate the gelation of the F127 phase in the bioink once extruded.

2.4.2 Bioprinting with the Cellink INKREDIBLE+ bioprinter

Two Cellink (Gothenburg, Sweden) bioprinted systems were purchased which represented significant improvements over the MendelMax design. The INKREDIBLE+ bioprinter is a self-contained unit with its own High Efficiency Particulate Air (HEPA) filters and UV lamps for sterile work. It features high precision (XY: 10μm, Z: 2.5μm, cellink.com), pneumatic printheads which can be heated up to 130˚C. However, while the printheads may be heated, the print bed itself is not temperature controlled, which is required to ensure gelation of the F127 component of the alginate-F127 bioink after printing. Consequently, a heated print bed was designed, built, and retrofitted to the INKREDIBLE+ by this author.

The design of the heated print bed focused on simple compatibility with the INKREDIBLE+ and low temperature variance when holding at 37˚C. The bed itself was milled from sheet copper, with a small lip to allow fitting of heating elements and sensors; copper was chosen over aluminium or steel due to its higher thermal conductivity. Two adhesive heating elements and digital sensors were adhered to the underside of the heated bed, and electrically insulated with Kapton tape (DuPont, USA). Digital sensors were wired to an Arduino UNO (Arduino, USA) which recorded the temperature measurements in real-time. Heating elements were wired to a relay, toggleable by a control signal from the Arduino, and connected to an independent power

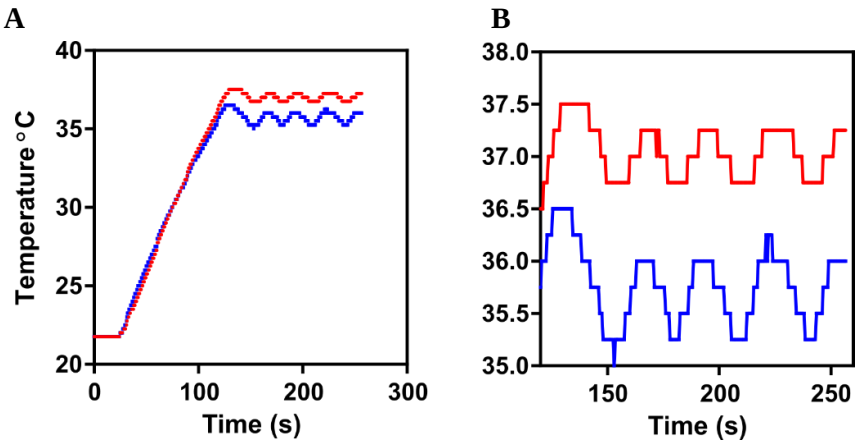

Figure 2-4 *Temperature response of the heated bed designed for use with the INKREDIBLE+.* ***A*** *Initial response of bed to heating commands.* ***B*** *Steady-state response when holding a temperature of 37˚C. The waveform behaviour is due to repeated toggling of power to the heating elements. Red line = Central sensor nearest the heating elements. Blue line = Outer sensor nearest the edge of the*

supply. When temperature readings were below a threshold temperature (typically 37˚C), the relay was toggled into its open state, powering the heating elements on the print bed. The temperature threshold could be changed by the user with a simple Infrared (IR) remote control. The print bed was found to heat quickly to the typical operating temperature of 37˚C and hold the temperature indefinitely to a margin of ±0.5˚C (**Figure 2-4 A**). Temperature variance across the bed was observed due to the additional copper in the riser and the central location of the heating elements, but on average only varied by 1.25˚C (**Figure 2-4 B**).

To print with the INKREDIBLE+, GCODE files were edited from templates in Celink's proprietary printing software, Heartware, and stored on an SD card for upload to the printer. Alginate-F127 bioink was loaded into a sterile 5mL syringe, then transferred into autoclaved, specialised 3mL syringe barrels (Nordson EFD, USA) *via* male-to-male luer lok connectors. These syringe barrels contain tight-fitting caps which are depressed into the bioink pneumatically, causing controlled extrusion of the bioink. After loading the bioink, an autoclaved nozzle was attached the syringe barrel, typically a 22-gauge tapered nozzle (Metcal, USA). Similarly to the MendelMax printer, manual calibration of print height was needed before each print, as well as manually selecting the centre point of the first printed object.

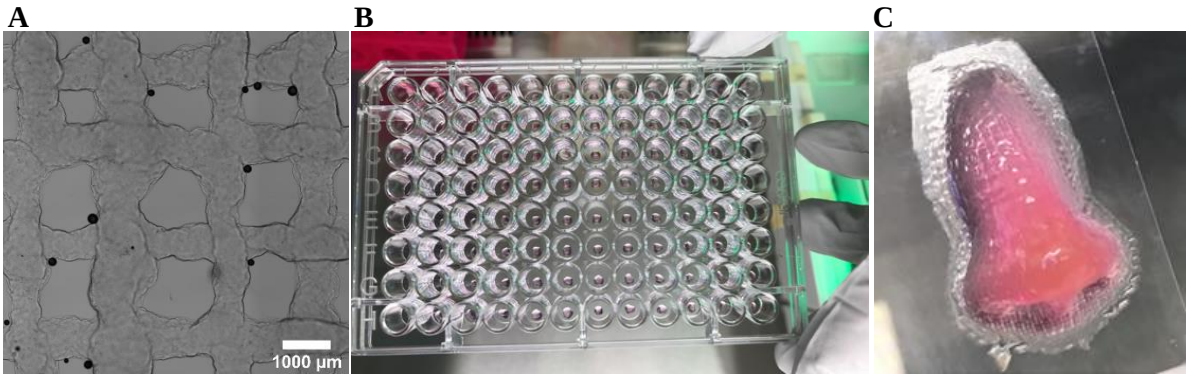

Figure 2-5 *Different print approaches with the BIOX.* ***A*** *Simple crosshatch print from a custom GCODE file with the gelatin-alginate bioink.* ***B*** *Droplet-printing protocol into a poly-d-lysine treated 96-well plate with the gelatin-alginate bioink.* ***C*** *Printing from a 3D model file (.STL file) of a human nose with the alginate-F127 bioink, which the printer has automatically sliced and generated GCODE for printing (adapted image from Dr. Thomas Richardson, with permission)*

2.4.3 Bioprinting with the Cellink BIOX bioprinter

The Cellink BIOX bioprinter (Cellink, Gothenburg, Sweden) when purchased was the newest Cellink bioprinter released and one of the most advanced commercial desktop bioprinters on the market (**Figure 2-2**, **C**). Additional features compared to the INKREDIBLE+ include a fully temperature-controlled print bed (heating and cooling) an additional print head, and interchangeable print heads of different designs. Critically, the syringe pump print-head and cooled print bed enabled the bioprinting of gelatin-based gels, which must be printed below their melting temperature of ~ 25˚C. The syringe pump printhead includes retraction parameters for automated syringe retraction after each print, preventing unintended continued extrusion after finishing a print command, one of the most common issues with bioprinting.

Bioprinting with the BIOX could be done through three approaches. First, GCODE files could be uploaded for direct control over print commands (**Figure 2-5A**). Second, the "droplet-printing" protocol could be used for high-throughput applications, which simply extrudes a pre-set bioink volume into the centre of each well in a multi-well plate (**Figure 2-5B**). Last, 3D model files (.STL files) could be sliced by the printer itself, automatically generating a GCODE file from the 3D model (**Figure 2-5C**). For automated imaging, it was desirable to prevent movement of gel samples within wells over time, such that the relative positions of samples remained constant during an experiment and therefore could be imaged repeatedly. As alginate-based bioinks would

detach from culture plastic over time and float in the surrounding culture media, a protocol was developed to keep samples adhered to wells in 96 well plates for up to 21 days. Poly-d-lysine hydrobromide (MW 70,00-150,000, Sigma Aldrich, UK), a crystalline, water soluble from of poly-d-lysine, was dissolved in sterile, deionized water at a concentration of 1mg/mL. 200µL/well was added to each well of a 96 plate and left at room temperature for at least an hour then aspirated prior to printing. The recovered poly-lysine solution was filter sterilized and reused 5 times before discarding. This formed a long-lasting poly-lysine coating, electrostatically binding to both the negatively charged alginate and the negatively charged tissue-culture plastic, keeping samples static over time.

Printing with the BIOX was typically done in conjunction with gelatin-alginate bioinks. Gelatin-alginate bioinks were prepared according to section **2.3.2**, then poured into a 3mL syringe (Becton Dickinson, USA) with a stopper plug attached. Then, the syringe plunger was gently partially inserted and the syringe placed upright, causing the liquid bioink to settle atop the plunger. Finally, the stopper plug was removed, and the plunger driven until all remaining air evacuated. The stopper plug was reattached, and the syringe left in the fridge for 3 minutes to solidify the gelatin component of the bioink.

Next, the syringe was inserted into the syringe-pump printhead and the piston driven until a small amount of gel had been extruded from the nozzle. Then, either a GCODE file or the droplet-printing protocol selected for printing. When printing from GCODE files the print settings were: 10mm/s extrusion speed, 5mm/s move speed. When printing using the droplet printing protocol, the print settings were: 5µL extrusion volume, 10µL retraction volume. The printer was calibrated automatically, using three points of contact to determine if the print bed was level and adjusting it accordingly. The print bed was cooled to 10˚C for printing.

2.4.4 Crosslinking

Crosslinking for all bioinks used, with the exception of Matrigel, was typically done with 100mM calcium chloride solution. Anhydrous calcium chloride powder (Fischer Scientific, UK) was dissolved in sterile, deionized water to form a 1M stock solution which was stored at -20˚C and

thawed for use. High-glucose DMEM was mixed with 1 molar $CaCl_2$ to form a 100mM crosslinking solution, in which bioprints were immersed for 10 minutes at room temperature. After crosslinking, crosslinking solution was exchanged for culture media containing 1.25 mM $CaCl_2$. This maintained the structural fidelity of bioprinted constructs and prevented bioprinted constructs from dissolving into the surrounding culture media over time.

2.5 Spheroid-Formation Assay

Cells were harvested from flasks, counted, blended into bioink and printed and crosslinked (see sections **2.2, 2.3** and **2.4**). Typical seeding densities were $5x10^4$ in the bioinks, and $1x10^4$ in Matrigel. For spheroid-formation, cells were grown in spheroid-expansion media (spheroid media), which is different in composition to expansion media used to grow cells in culture flasks.

2.5.1 Spheroid-expansion media

Spheroid media formulation is derived from the seminal work of Sato *et al.* who first described the isolation and expansion of colorectal stem cells into colorectal organoids in Matrigel[89,90]. Spheroid media listed here is the basal media formulation outlined by Sato *et al.* without addition of hormones and growth factors added to induce stem cell differentiation. 1.25 mM $CaCl_2$ was added to maintain the crosslinked structure of the alginate-based bioinks as stated in section **2.4.4**.

Single cells dispersed in bioinks or Matrigel would grow into rounded colonies, "spheroids" over time when cultured in the media described in **Table 2-2**. Typically, viable cells would grow into spheroids visible by microscopy 3-5 days after seeding; spheroid size was routinely measured with microscopy, as stated in sections **2.8** and **2.15**. Spheroid cultures did not usually exceed 18 days due to spheroids outgrowing the surrounding bioink.

Table 2-2 *Composition of spheroid-expansion media, derived from Sato et al.*

Component	***Quantity***
Advanced DMEM/F12	(Base Media)
Penicillin/streptomycin	100U/mL
HEPES	10mM
Glutamax	1%
Bovine Serum Albumin	0.1%
N2	1%
B27	2%
N-acetylcysteine	1mM
$CaCl_2$	1.25mM

2.5.2 Harvesting spheroids from bioink

Spheroids were routinely harvested from bioinks for cell counting for use in other procedures, such as histological staining, imaging with confocal microscopy, or flow cytometry. An advantage to alginate-based gels is that the ionic nature of the bonds between alginate residues allows for chelating agents to bind to metal ions (e.g., Ca^{2+}) and disrupt ionic bridges and dissolve the gel. This process can be much quicker and milder than published enzymatic gel degradation protocols, which typically take 1-2hours for Matrigel or collagen gels.

Ethylenediaminetetraacetic acid (EDTA) is a widely used chelator of metal ions, commonly applied with trypsin to enhance its activity. For alginate gels, EDTA chelates Ca^{2+} ions, triggering the dissolution of the gel. To dissolve the bioink, bioprinted constructs collected into 15mL falcon tubes and immersed in 200mM EDTA in PBS at 37°C for 3-5 minutes, liberating embedded spheroids into suspension. Spheroid-solution was gently centrifuged at 500RPM for 5 minutes to aggregate the spheroids into a pellet. If a single cell-suspension was required, spheroid pellets were incubated in 1.5mL trypsin/EDTA for 5 minutes at 37°C, then passed repeatedly through an 18-gauge needle to break apart remaining aggregates. 8.5mL DMEM was added to the falcon tubes to inactivate the trypsin and the suspension centrifuged again at 3000RPM for 3 minutes. The resulting cell pellet was resuspended in PBS and passed through a 40μm filter, then counted with a countess II automated cell counter.

2.6 Electron Microscopy

Electron microscopy uses accelerated electron beams to illuminate specimens. Due to the low wavelength of electron beams in the picometre range, the resolution of this approach is much higher than light microscopy, with resolvable feature size in the single nanometre range compared to hundreds of nanometres for light microscopy. As electron microscopy is dependent on the absorption and scattering of electrons, organic materials require coating or staining with heavy atoms such as palladium, gold, platinum, or chromium for adequate image contrast. Osmium tetroxide is an example of such a heavy-metal stain, binding strongly to lipids in cell membranes. However, on unfixed samples, osmium tetroxide has poor penetration rates and is therefore generally used after aldehyde fixation, which crosslinks proteins within biological samples to preserve them. Alternatively to heavy-metal staining, sputter coating may also be used to image biological samples by depositing a thin layer (2-20nm) of conductive material onto the surface of a sample. Here, samples are contained in a vacuum chamber where inert gas is injected into an electric field and ionized, bombarding a target material (*e.g.*, gold) which is subsequently eroded and deposited as a film onto the samples themselves.

Hydrogels are a challenging material to image with electron microscopy due to their high-water content and the associated propensity to generate artifacts due to ice crystallisation. Approaches to imaging hydrogels necessarily include a dehydration step to remove bound water and reveal the internal structure. A common approach is to vitrify samples using a cryogen with a high cooling rate, such as liquid nitrogen slush, liquid ethane or liquid propane[176]. Here, the frozen samples are exposed to low-temperature vacuum conditions causing sublimation of vitrified water and exposing underlying structures. Once a sample is dehydrated in this way, it can then be sputter coated and imaged. Both freeze-drying and Cryo-Electron Microscopy techniques use this approach to coating dehydrated samples.

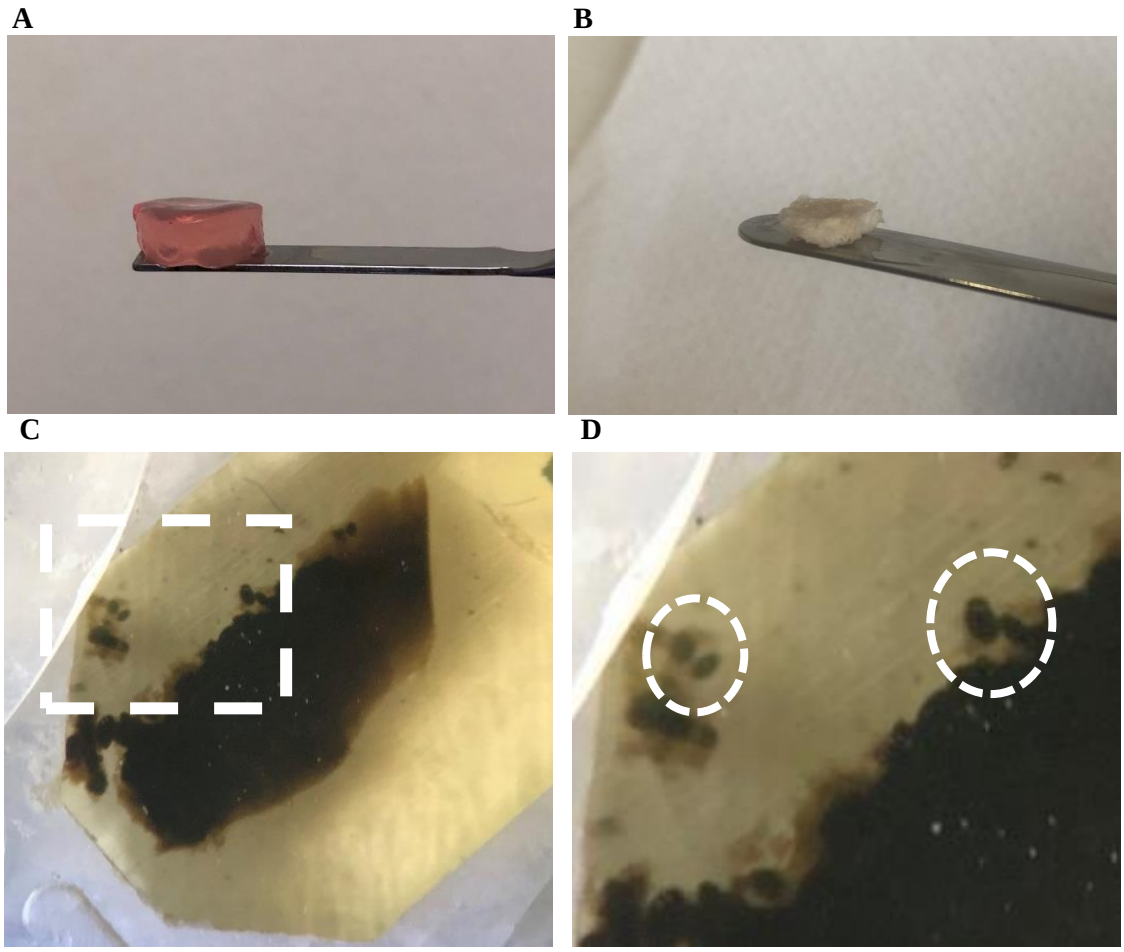

Figure 2-6 *Acellular gelatin-alginate bioink before (**A**) and after (**B**) freeze-drying. **C** fixed, osmium stained SW620 spheroids embedded in a BSA gel for sectioning and visualizing with TEM. **D** Enlarged view of region highlighted in **C**, individual spheroids are visible and circled. Spheroids appear as rounded black shapes due to the osmium staining. Some free osmium stain is also embedded.*

2.6.1 Scanning Electron Microscopy of freeze-dried hydrogels

Bioinks were prepared according to section **2.3**, crosslinked and incubated overnight at 37°C in culture media. Samples were moved to glass flasks, then lyophilized with a ModulyoD freeze-drier (Fisher Scientific, UK) at -60°C under low pressure (<0.05mBar) for 5 days (**Figure 2-6 A-B**). Some samples were first plunged into liquid nitrogen immediately prior to freeze-drying in order to more rapidly freeze the sample and thus better preserve its true structure. Regardless, after lyophilization samples were fractured by hand, then adhered to aluminium specimen stubs with conductive carbon tape and the fracture surfaces sputter coated with a Quorum Q150RES (Quorum Technologies, UK), forming 15nm gold/palladium coating. SEM was performed with

a FEI Quanta 200 field emission gun-SEM (ThermoFisher Scientific, USA), with an 8.0kV beam energy.

2.6.2 Scanning Electron Microscopy of embedded spheroids

Gelatin-Alginate bioinks were seeded with $5x10^5$ cells/mL of SW620 cells and cultured as described in sections **2.2-2.5**. After 11-14 days of culture, samples were fixed overnight with 2% glutaraldehyde in 100mM sodium cacodylate buffer at 4°C. Then, samples were freeze-dried, fractured, sputter coated and imaged as described in section **2.6.1**.

2.6.3 Scanning Electron Microscopy of liberated spheroids

Whole spheroids were harvested from bioink after 11-14 days of culture, as described in section **2.5.2**. After harvesting, spheroids were fixed overnight with 2% glutaraldehyde in 100mM sodium cacodylate buffer at 4°C. Spheroids were then carefully pipetted onto a poly-lysine coated aluminium stub, prepared by treating the stub with 1mg/mL poly-lysine solution overnight at 4°C, and stained with osmium tetroxide for 1 hour at room temperature. Next, spheroids were dehydrated with increasing concentrations of ethanol in water (10,30,50,70,90,100% w/w) for 5 minutes at each concentration. Finally, samples were transferred to a Leica EM CPD300 (Leica Microsystems, Germany) critical point dryer (CPD), which exchanged ethanol in the samples with liquid CO_2 before reaching the critical point of CO_2 at 31°C and 74bar, causing conversion of the CO_2 to its gaseous phase. The fully dehydrated samples were then sputter coated and imaged as described in section **2.6.1.**

2.6.4 Cryo-Electron Microscopy

Cryo-Electron Microscopy (Cryo-EM) is a technique where samples are vitrified, coated, and imaged all *in situ* with a high degree of control over temperature and pressure. Ethanol dehydration, aldehyde fixation, heavy metal staining and CPD are not required for cryo-EM. Consequently, Cryo-EM is regarded as one of the least invasive EM techniques, accurately preserving native structures of organic materials[176].

Samples for cryo-EM are prepared by first freezing with a cryogen, then gradually sublimated and cryo-coated with carbon. Cryogen selection and sublimation protocols can impact the final imaged structure due to differences in cooling rate and therefore ice nucleation and form within the sample[177]. Cryogens used in this research were liquid nitrogen slurry (LNS) and liquid ethane (LE); sublimation times were either 3 minutes or 1 hour. Imaging was performed with a Tecnai G^2 20 electron microscope (FEI, USA).

2.6.5 Transmission Electron Microscopy of spheroids

Whole spheroids were harvested and fixed overnight with 2% glutaraldehyde in 100mM sodium cacodylate buffer identically to section **2.6.3**. Samples were then stained with osmium tetroxide at room temperature for 1 hour before being transferred to a 15% bovine serum albumin (BSA) gel for processing (**Figure 2-6 C-D**). Embedded samples were dehydrated and sectioned using an ultramicrotome before imaging.

2.7 Mechanical Testing

The mechanical properties of biocompatible scaffolds, hydrogels and substrates is known to influence cellular behaviour, with research indicating that cells behave more naturally in environments where mechanical stimuli mimic *in vivo* conditions. As such, mechanical properties of bioinks are often rationally designed to approximate the tissue that is most relevant to the cell types used when bioprinting.

There exist multiple mechanisms for mechanical characterization of materials. Compression and tensile testing outline material behaviour under both compressive and tensile loading; stiffness, modes of failure, maximum elongation and yield stresses can be determined through these tests, which are staples in the literature for evaluating biomaterials[163]. Rheology is the study of the flow behaviour of materials and is of particular importance for bioprinting. As bioinks are extruded during the printing process, shear forces act on the bioink and cells within. Consequently, most bioinks are shear thinning, becoming less viscous as they are extruded, easily flowing from the

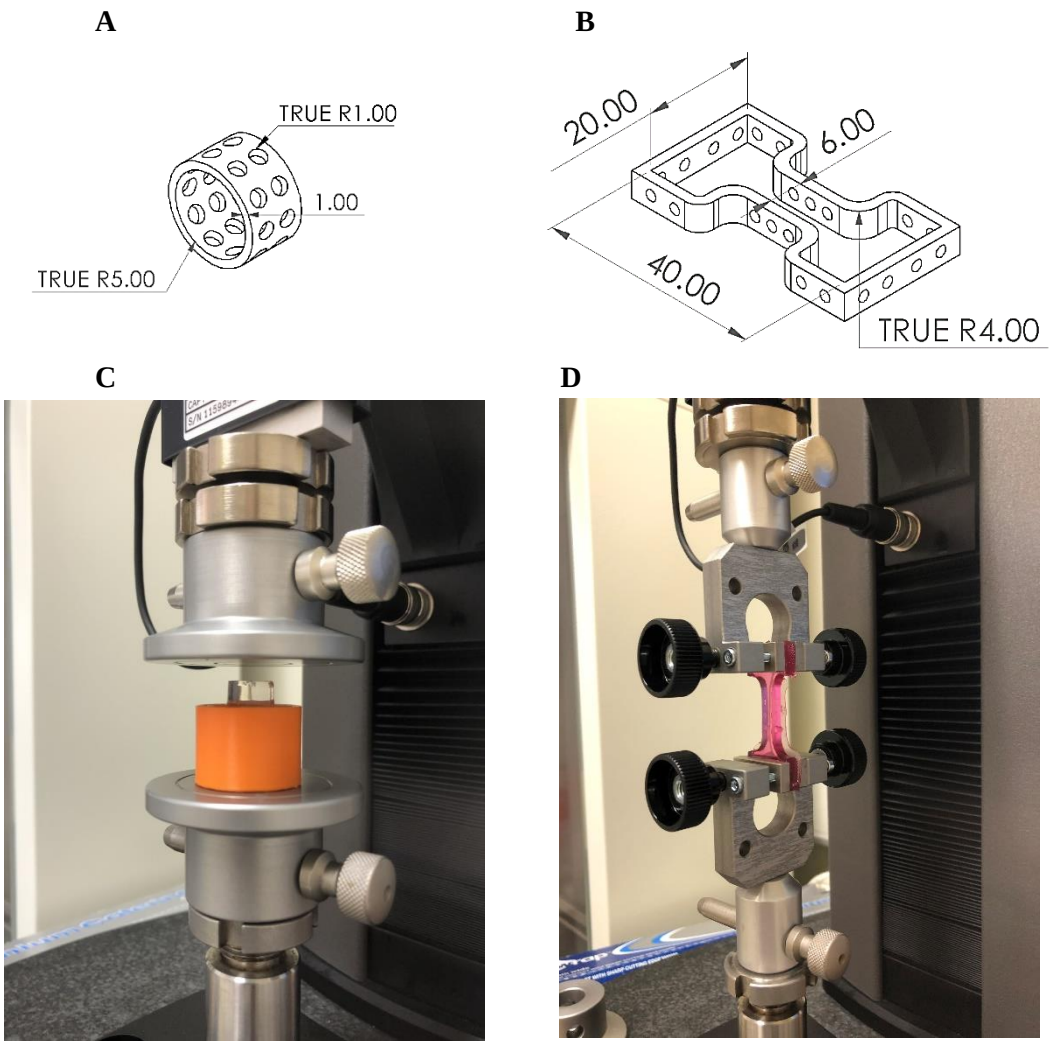

Figure 2-7 *Mechanical testing procedure for cast hydrogels.* ***A-B*** *Hydrogels were cast into porous, 3D printed moulds, which allowed better diffusion of the crosslinker into the gel structure.* ***C-D*** *Compression & tensile testing of hydrogel samples cast into moulds show in* ***A,B****. Units are in mm.*

print nozzle and therefore easily deposited and patterned. Such shear-thinning behaviour can be characterized by rheometry.

2.7.1 Compression testing of hydrogels

Compression testing is one of the most common approaches to characterising biomaterials, calculating a characteristic value used to compare materials: The Young's modulus. The value of the Young's modulus values is calculated with the following equation:

Equation 1: *Young's modulus of a material*

$$E = \frac{\sigma}{\varepsilon} = \frac{(F/A)}{\Delta L}$$

Where E is the Young's Modulus in pascals (Pa), σ is the stress on the sample in Pa, ε is the strain or change in length of the sample. F is the force acting on the sample, A is the sample cross-sectional area and ΔL is the change in length caused by the applied force. When the force applied is compressive, E can be referred to as the compressive stiffness of the sample, and when the force applied is tensile, E can be referred to as the modulus of elasticity. Critically, these two loading cases typically result in different values of E due to anisotropic material properties and therefore cannot be directly compared. Moreover, different methods of calculating E exist, even where the type of loading is the same. For instance, indentation and unconfined compression testing both apply compressive loading to the sample, but generally output different values of E for the same material. Consequently, when stating or comparing values of E, the methods used should be clearly defined.

Unconfined compression testing of hydrogels was carried out with an Instron 3343 universal testing machine (Instron, UK). At least 6 samples were prepared by casting hydrogels into 3D printed moulds, designed in *SOLIDWORKS* and printed with a Form 2 (Formlabs, USA) stereolithography (SLA) printer in clear resin (**Figure 2-7 A**). The moulds were designed to fit inside 24-well plates; after casting samples were inserted into wells and crosslinked with 1.5mL of crosslinking solution.

After crosslinking, samples were removed from their moulds and placed between parallel, impermeable plates, and the uppermost plate lowered such that sample surface was flush with the plate (**Figure 2-7 C**). Then, the upper plate destructively compressed the sample at a rate of 1mm/s with a 10N load cell. Force and displacement readings were recorded in real time and saved in .csv files. A custom Excel macro aggregated .csv files and calculated the compressive stiffness using linear regression. As hydrogels generally do not have a well-characterized linear-elastic region, stresses corresponding to the 0-10% strain region were used to calculate compressive stiffness.

2.7.2 Tensile testing of hydrogels

Tensile testing is another common approach to characterising biomaterials, particularly those designed to mimic to dynamic biological systems, *e.g.*, skin, muscle, and intestinal models. Tensile testing can be used to determine the modulus of elasticity of a material, E, the equation for which is given in section **2.7.1** (**Equation 1**). In addition, yield stresses and strain at failure can also be calculated.

Tensile tests were performed with an Instron 3343 universal testing machine (Instron, UK). Samples were cast into 3D printed moulds (**Figure 2-7 B**), crosslinked in petri dishes then mounted with two holding clamps (**Figure 2-7 D**). The upper clamp was driven upwards at a rate of 1mm/min while measuring force and displacement readings in real time. Similarly to section **2.7.1,** 0-10% strain regions were used to calculate the modulus of elasticity.

2.7.3 Rheological measurements of hydrogels

Bioprintable hydrogels commonly exhibit shear-thinning properties, which enable precision extrusion printing. Rheometers contain samples between two surfaces which can rotate relative to one another. Rotation of the top surface relative to the bottom causes shear forces in the specimen being measured. Shear-thinning materials will decrease in viscosity in response to the applied shear, whereas shear thickening materials will increase in viscosity. This viscosity responsive can be explicitly characterized with the fluid power-law model, mathematically relating viscosity and shear rate:

Equation 2 *Fluid power-law model (Also known as the Ostwald-de Waele relationship)*

$$\mu(\dot{\gamma}) = K\dot{\gamma}^{n-1}$$

Where μ is the generalized viscosity, $\dot{\gamma}$ is the shear rate, K is the viscosity when $\dot{\gamma} = 1$, and n is the dimensionless 'flow behaviour index'. In this model, materials with values of $n = 1$ are ordinary Newtonian fluids. Values of $n < 1$ are pseudoplastic (shear thinning) and values of $n > 1$ are dilatant (shear thickening).

Rheology can also be used to determine the melting points of viscous fluids. Here, shear-strain, shear-stress and frequency of the rheometer are kept constant during the test, but the temperature varied with a constant gradient. Using an oscillatory motion, shear strain in induced in the material, which, due to its viscous nature, is offset from the associated shear stress by an angle, δ, known as the phase lag or phase shift. The complex shear modulus, storage modulus, and loss modulus of the material, G^*,G' and G'', are calculated from the phase lag and describe the viscoelastic nature of the material. G^* expresses the viscoelastic nature of the fluid whereas G' and G'' describe the elastic, and viscous components, respectively.

G' and G'' typically vary with temperature, corresponding to physical changes in the material at those temperatures. During a temperature-sweep oscillatory test, the point where $G' = G''$ is defined as the melting temperature of the fluid, T_m.

Small amplitude oscillatory measurements of uncrosslinked gels were carried out with a Kinexsus Pro+ Rheometer (Malvern Instruments, UK). Samples were placed on the rheometer plate and the test geometry lowered to 500μM between the plates and excess gel removed. For viscosity-response measurements, a strain sweep from 0.1-10% strain, at an oscillation frequency of 1 Hz was used to determine the flow index, n. For melting temperature measurements, temperature was varied from 25°C-45°C at a rate of 1°C/minute and T_m calculated as the crossover point of G', G''.

2.8 Epifluorescence (Widefield) Microscopy

Fluorescence microscopy uses the properties of fluorophores for imaging. Fluorophores are chemical compounds which absorb light at a specific wavelength and re-emit light at a longer wavelength due to excited orbital electrons in the fluorophore releasing photons as they undergo relaxation. Fluorophores are components of biological stains; for instance, phalloidin, a phallotoxin which binds to F-actin in cells, can be conjugated with Tetramethylrhodamine (TRITC), an orange-fluorescent dye, for visualization of actin structure in cells.

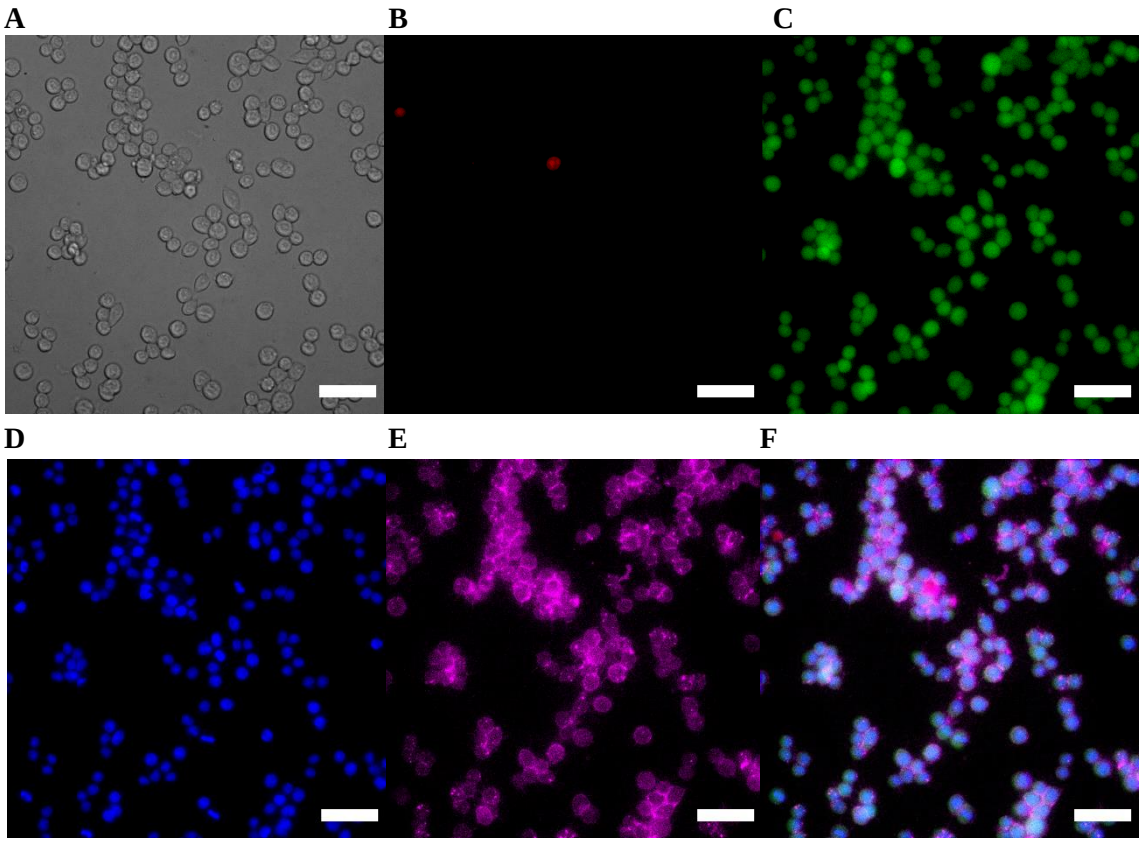

Figure 2-8 *Widefield microscopy of SW620 cells with the stains listed in* ***Table 2-3****.* ***A*** *Brightfield image.* ***B*** *Dead stain, Ethidium Homodimer III.* ***C*** *Live stain, CalceinAM green.* ***D*** *Nuclear stain, Hoechst 33342.* ***E*** *Membrane stain, CellMask.* ***F*** *Composite image, overlaying* ***B-E****. All scale bars = 50μm*

Epifluorescence microscopes pass a beam of light directly through a sample and into an objective lens, maximizing illumination at the cost of higher background signals when compared other illumination arrangements[178]. Imaging in 3D is possible by taking images at different layers of a sample, known as a z-stack, which can be rendered as a 3D image or a 2D image where all the layers are combined (A "projection"). Multiple optical filters allow the transmission of light with specific wavelengths ranges, permitting the imaging of samples stained with multiple fluorophores (**Figure 2-8**).

Table 2-3 *Fluorescent stains used for widefield microscopy*

Fluorescent Stain	***Staining Target***
CalceinAM Green	Cytoplasm (live cells)
CalceinAM Blue	Cytoplasm (live cells)
Ethidium Homodimer III	Nucleus (dead cells)
Propidium Iodide	Nucleus (dead cells)
DAPI	Nucleus (fixed cells)
Hoechst 33342	Nucleus (live cells)
CellTracker Red	Cytoplasm (live cells)
CellMask Green	Cell Membranes
Image-iT Green	Low Oxygen Activated

In this research, a Leica DMI6000 inverted epifluorescence microscope (Leica Microsystems, Germany) was used for widefield imaging for both brightfield and fluorescence imaging. The fluorescent stains used in this research and staining target are listed in **Table 2-3**, and example staining shown in **Figure 2-8**.

2.8.1 Automation of the microscope

Leica DMI6000 microscopes do not come with automated multi-well imaging features either as standard or with purchasable software add-ons as of the time of this writing. Therefore, an automation approach was designed around the "Mark-And-Find" feature within the microscope software ("LASX"). This feature allows users to manually save the current position of the microscope stage and return to it later; an .XML file could be exported containing these locations, which could be loaded to return the saved positions.

A program was written in MATLAB (MathWorks, USA) by this author to generate an .XML file with "Mark-And-Find" coordinates for 24,48 or 96 well plates. Because the "zero" position of the microscope drifts with repeated use, the program requires the user to input coordinates for the centre of the first well to be imaged. The output .XML file can then be loaded by the microscope and used as if the user had manually selected these points in an imaging session. Because the BIOX bioprinter accurately prints into the same location in each well, this approach aligns imaging positions and sample locations with precision. Unfortunately, this approach is not

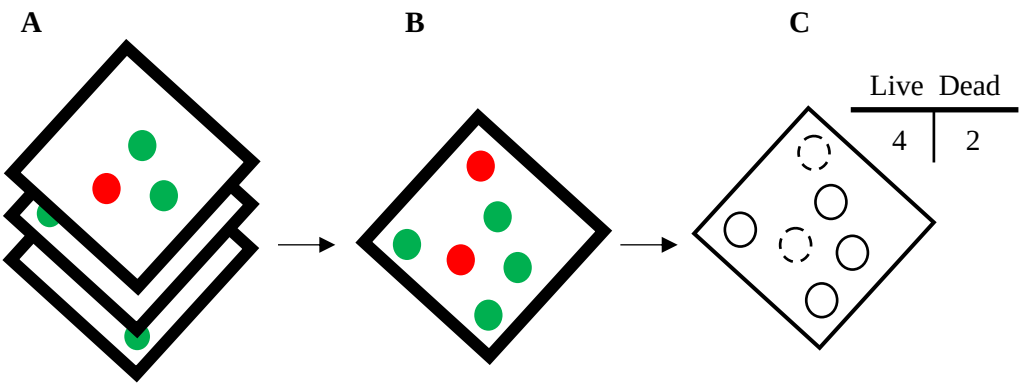

Figure 2-9 *Image analysis procedure for cell viability determination.* ***A*** *Samples were imaged with z-stack widefield microscopy of live/dead channels.* ***B*** *projections of z-stack images were automatically generated with an ImageJ macro which also reduced background noise.* ***C*** *Live (green) and dead (red) cells were counted with a custom CellProfiler pipeline which output results as .csv files.*

immediately applicable to any LEICA widefield microscope, because the .XML position files require microscope-specific fields to be input. A new entry containing the relevant microscope fields must be added to the program for each new microscope used.

2.8.2 Live/Dead staining and cell viability calculations

Cell viability in 3D was calculated using widefield microscopy, typically 24 hours after crosslinking of bioprints seeded with $1x10^5$ cells/mL of bioink. CalceinAM and Ethidium Homodimer III were used to stain live and dead cells, respectively, then Z-stack images were taken of stained samples at 10µm intervals in each channel. Cell viability was calculated as:

Equation 3: *Cell viability calculation*

$$Cell\ Viability = \frac{live\ cells}{live\ cells + dead\ cells}$$

Where it was assumed that the sum of live and dead cells is equal to the total number of cells in the image. A minimum of 3 z-stacks from an experiment, for 3 experiments, was used to calculate final cell viability and perform statistical analysis.

Calculating cell viability through imaging requires robust mechanisms for counting the number of stained cells in each channel. *CellProfiler* (Broad Institute, MIT, USA) is a free, bespoke image analysis software for analysing images of cells. *CellProfiler* is a modular tool, whereby the user creates their own "pipeline" of modules, each performing a step in the analysis. A custom pipeline

was created for cell viability calculations, counting the number of cells in the live and dead channels of projections from the z-stack images. This pipeline used adaptive thresholding, size exclusion and shape exclusion to detect objects in each channel. Z-stack images could not be directly measured in *CellProfiler* due to limitations in the software. As such, a macro for *ImageJ* (National Institutes of Health, USA), another free and open-source image analysis program, was written to generate 2D image projections and remove background noise from z-stacks. Therefore, the procedure for analysing images was first to image live/dead-stained samples with z-stack imaging, then to create projections containing all the cells in the stacks with ImageJ, then to count the numbers of live and dead cells in *CellProfiler*, generating a .csv results file (**Figure 2-9**).

2.8.3 Hypoxia staining with Image-iT

To determine whether oxygen concentration was reduced in spheroids relative to cell monolayers, both cells and spheroids were stained with Image-iT green, a sensitive hypoxia stain which is stated by the manufacturer to fluoresce when oxygen concentration drops below 5%. SW620 cells were seeded into 96 well plates with a seeding density of $9x10^3$ cells/well and cultured for 24 hours before staining. SW620 spheroids were grown in bioink for 11 days before staining. Staining was carried out according to the manufacturer's recommendations: 1µL/mL of media of Image-iT green was added to each well and incubated for an hour. Then, media was aspirated, samples washed with PBS and imaged in PBS.

2.9 Confocal Microscopy

The principal advantages of confocal microscopy when compared to widefield microscopy are the reduction of out-of-plane light in forming the image (increasing signal-to-noise ratio), and the fine-tuning of filters for wavelength selection of emitted light, typically to within 5nm. Confocal microscopes also use laser-light which is tightly monochromatic and therefore less likely to excite multiple fluorophores simultaneously. However, confocal microscopy is typically more time consuming, expensive, and lower throughput than widefield microscopy. Consequently, confocal

microscopes are often used for high-detail imaging with antibody stains, for improved resolution of antibody localisation and finer control over excitation power and wavelength selection.

In this work, confocal microscopy was used for cell monolayers, whole spheroids, and stained spheroid sections from paraffin-embedded spheroids. All imaging was performed with a Leica SP5-AOBS confocal laser scanning microscope (Leica Microsystems, Germany), and the stains used are listed in **Table 2-4**, below:

Table 2-4 *Stains used in confocal microscopy*

Stains	***Type***	***Staining Target***
DAPI	Fluorescent chemical stain	Nucleus
TRITC-Phalloidin	Fluorescent phallotoxin	F-actin
Collagen I	Primary antibody	Collagen I
FITC-anti Mouse	Secondary antibody	Mouse antibody
HypoxyProbe	(Mouse) antibody-conjugated, pimonidazole binding	Pimonidazole adducts

2.9.1 Staining cell monolayers

Cell monolayers were cultured in 35mm confocal imaging dishes (Nunc, Thermo Fisher Scientific, UK) until ready for imaging. Media was removed and cell monolayers fixed with 4% paraformaldehyde (PFA) solution in PBS overnight at 4°C. Then, fixative was removed, and samples washed three times with PBS, for 5 minutes each. Cell membranes were permeabilised with 0.5%(v/v) Triton X-100 in PBS for 15 minutes at room temperature, then washed three times with PBS as before. Unspecific antibody binding was blocked with 3% BSA solution in PBS for one hour at room temperature, then stains were added in low-light conditions. After stains were removed, samples were washed with PBS and imaged in PBS.

2.9.2 Staining whole spheroids

Staining dense tissue structures, such as spheroids, is difficult due to poor permeabilization depth of stains, particularly antibodies, and scattering of light inside the structure. Consequently, common staining protocols for cell monolayers, such as the protocol listed in section **2.9.1**, are

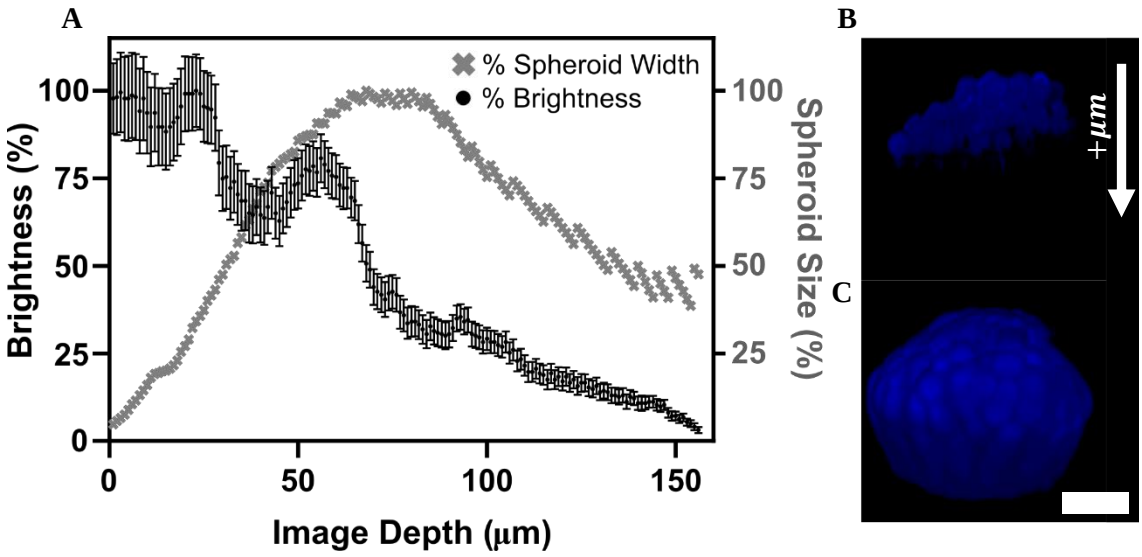

Figure 2-10 *Loss of signal of DAPI through a tumour spheroid.* ***A*** *Average brightness of stained pixels and an estimate of the width of the spheroid, at each layer of imaging from confocal microscopy. Black circles show signal losses through the spheroid, stated as a proportion of the maximum signal from the brightest layer; Error bars are the standard deviation of pixel values in each layer. Gray crosses represent an estimate of the spheroid cross-sectional area at each layer, represented as a proportion of the maximum spheroid cross sectional area.* ***B*** *Unaltered confocal image showing a drastic loss of signal within 100μm of the uppermost surface of the spheroid.* ***C*** *Reconstructed spheroid from MATLAB. Signal intensity was scaled at each layer to increase visibility of deeper sections of the spheroid. Scale bar = 50μm*

ineffective for staining whole spheroids. Simply increasing permeabilization time or concentration has not been found to be effective at increasing staining depth[179]. Weiswald *et al.* developed a staining protocol specifically for tumour spheroids up to 150μm in size. Unlike ordinary staining approaches, fixation and permeabilization were synchronous, and blocking and antibody staining times were increased up to 48 hours at 4°C. A methanol dehydration-rehydration step was also included, corresponding with earlier studies finding success with this approach for permeabilising large tissues[178,180].

This protocol was adapted to remove the dehydration step due to the repeated washing causing large losses in harvested spheroids. Otherwise, the protocol was the same. Specifically, the protocol used is as follows: Spheroids were harvested from the bioink as described in section **2.5.2**. Spheroids were fixed and permeabilised synchronously with 0.1% Triton X-100 in PBS (PBS-T) overnight at 4°C. Then, after three washes in PBS for 10 minutes each, blocking was performed with 3%BSA in PBS-T for 24 hours at 4°C. Blocking solution was removed, and the

sample washed with PBST twice. For collagen I staining, samples were incubated with primary antibody in PBST for 48 hours at 4°C. Then, after washing with PBST four times for 30 minutes each, secondary antibody in PBST was added for 24 hours at 4°C. For staining with TRITC-phalloidin, only the primary antibody staining procedure was used. After antibody staining, nuclei were stained with DAPI for 30 minutes. Samples were then washed with PBS twice for 5 minutes and imaged with confocal microscopy.

This protocol was effective at staining small spheroids within the 150μm limit established by Weiswald *et al*, however, significant signal loss was still observed (**Figure 2-10**). A custom MATLAB script was written to adjust signal values at different layers in spheroids, and used whenever 3D images of spheroids, or images of spheroid sections are displayed.

2.10 Histology

Histology is the study of tissues and their structure. Histological techniques for bulk tissues generally involve chemically fixing samples (*e.g.,* with formaldehyde), before embedding into paraffin wax or flash freezing. Then, samples are sectioned into thin layers ~5-50μm thick for staining and mounting onto microscopy slides for visualisation. In the case of bioprinted tumour spheroids, histological preparation enables staining and visualisation of the interior of large spheroids (>150μm) which would otherwise be very challenging to image *via* microscopy (**Figure 2-10**).

Common chemical stains used in histology include haematoxylin and eosin (H&E), Sirius red, safranin-O and others. These stains target different residues in biological tissues, for instance, eosin stains cell membranes and cytoplasm pink, targeting amino acid residues such as lysine.

However, these stains may also interact with components of bioinks and cause staining of the bulk gel alongside cells within (**Figure 2-11 A,** black arrow). Critically, H&E, the most common histological stain, stains alginate permanently[181], making cell-laden alginate-bioinks unsuited to direct histological staining. Additionally, gels can tear or be otherwise damaged, during the

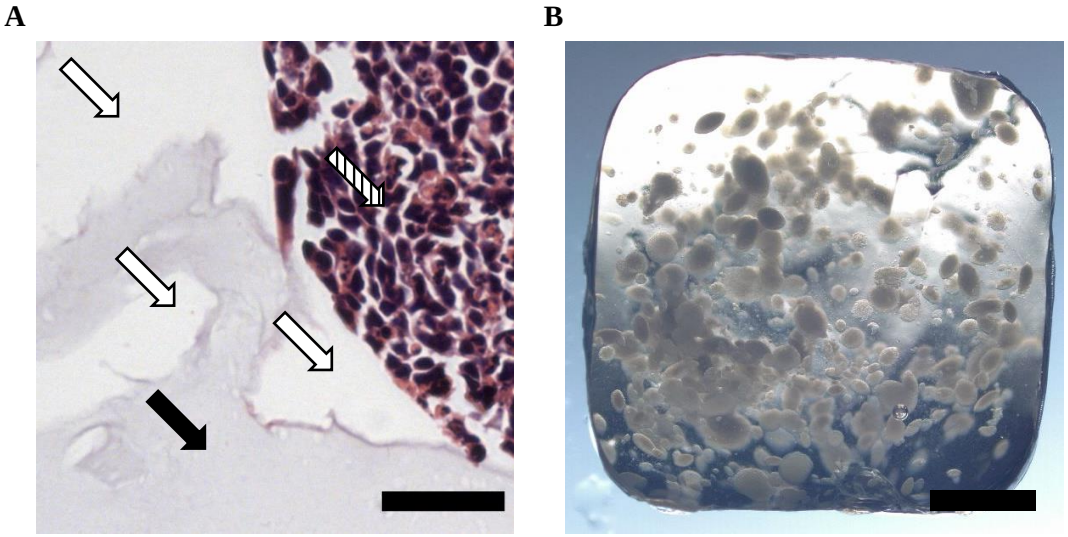

Figure 2-11 *Practical observations and techniques for histological staining of spheroid-laden alginate hydrogels.* ***A*** *Alginate hydrogels are stained by H&E staining, and tear when sectioning. Black arrow = alginate gel, white arrows = teared zone, dashed arrow = stained cells in a SW620 spheroid. scale bar = 50μm.* ***B*** *SW620 spheroids after harvesting from the bioink and embedding a 2% agarose gel. Spheroids were prepared in this way as standard for histological staining. scale bar = 2mm.*

paraffin embedding, dewaxing or microtome sectioning process (**Figure 2-11 A,** white arrows). Such damage to the hydrogel also causes damage to and losses of spheroids from the gel which are therefore not stained.

A protocol was developed to reduce background staining and enhance spheroid retention, using agarose. Agarose gels are simple to make and inexpensive, moreover, they are robust and typically do not uptake histological stains. Accordingly, agarose-embedded tissues have been used in the literature with success[31,182,183]. In this protocol, 2%(w/v) agarose gels were prepared by microwaving agarose powder and sterile, deionized water until dissolved. Spheroids were harvested from the bioink as described in section **2.5.2**, and fixed in 4% PFA overnight. Then, fixed spheroids were washed with PBS, pipetted into warm agarose gels, and cast into 8mm square plastic histology moulds and left to cool at 4°C (**Figure 2-11 B**). 2% agarose gel will gelate around 34-38°C, and tissue damage from heating can occur around 40°C[184] if samples are left above this temperature for long durations. As such, it is critical that the agarose gel is not

overly warm and is rapidly cooled after mixing with spheroid samples. After spheroid-agarose gels cooled, they were immersed in 70% ethanol overnight.

Samples were embedded in paraffin wax with a Thermo Excelsior tissue processor. The program used slowly increased the ethanol concentration in samples from 70% to 100%, then gradually substituted ethanol for xylene. Finally, warm lamb wax was infiltrated into the sample. Sectioning was performed with a Leica Jung Biocut 2035 microtome. Samples were sectioned into 10μm-thick layers, then mounted onto superfrost plus microscope slides (Thermo Fisher Scientific, UK) and left to dry overnight at 37°C.

2.10.1 Haematoxylin and Eosin (H&E) staining

Slides were dewaxed with HistoClear (National Diagnostics, Scientific Laboratory Supplies) for 30minutes, then rehydrated gradually with 100% Industrial Methylated Spirits (IMS), 90% IMS, 70% IMS, and tap water. Slides were stained with Haematoxylin (Alfa Aesar, UK) for 9 minutes, differentiated in acid alcohol (1% HCl in 70% Ethanol), then washed with Scott's Tap Water Substitute (STWS; Sigma Aldrich, UK). At this point the sample should have blue nuclei and a colourless background, confirmed with microscopy; If not, washing with acid alcohol and STWS is repeated. Slides were then stained with 1% Eosin solution for 10 seconds, rinsed with tap water, dehydrated with 70%, 90% and 100% IMS and washed with xylene for 5 minutes. DPX anti-fading mounting medium (Sigma Aldrich, UK) was used to preserve slides for imaging; Slides were stored at room-temperature, shielded from light.

2.10.2 Safranin-O staining

Slides were dewaxed and rehydrated identically to section **2.10.1**. Slides were stained with 0.1% Safranin-O solution at pH 2.35 for 5 minutes, then dehydrated with 70%,90% and 100% IMS, and washed with xylene for 5 minutes. DPX was used as the mounting medium; Slides were stored at room-temperature, shielded from light.

2.10.3 Sirius Red staining

Slides were dewaxed and rehydrated identically to section **2.10.1**. 1.3% Sirius Red solution (Sigma Aldrich, UK) was used to stain slides for one hour, then slides were washed twice with 0.5% acetic acid solution (Sigma Aldrich, UK), and rinsed with tap water. Slides were dehydrated with 70%,90% and 100% IMS, and washed with xylene for 5 minutes. DPX was used as the mounting medium; Slides were stored at room-temperature, shielded from light.

2.10.4 Masson's Trichrome staining

Weigerts iron haematoxylin, Masson's Red and Masson's Blue are the three components of the trichrome stain used, staining nuclei (purple), cytoplasm (red), and connective tissue (blue), respectively.

Slides were dewaxed and rehydrated identically to section **2.10.1**, then soaked overnight in Bouin's solution (Sigma Aldrich, UK) – a compound fixative containing formaldehyde, picric acid, and acetic acid. Then, slides were washed and stained with Weigerts iron haematoxylin for 1 minute. After washing with tap water and differentiating with acid alcohol, slides were washed with STWS for 18 seconds. The next stain, Masson's Red, was applied by first washing with distilled water for 5 minutes, dipping slides into Masson's Red solution for 10 seconds and washing thoroughly with distilled water. Phosphomolybdic acid washes were used for differentiation. The final stain, Masson's Blue, was applied by first rinsing with distilled water, then staining with Masson's Blue for 20 minutes. After the three stains were applied, slides were washed 4 times with distilled water, left to dry overnight, and washed with xylene for 5 minutes. DPX was used as the mounting medium; Slides were stored at room-temperature, shielded from light.

2.10.5 Hypoxia staining (HypoxyProbe)

For more accurate staining of hypoxic regions within spheroids HypoxyProbe was used in conjunction with spheroid sections. Unlike Image-iT, which fluoresces in live cells when ambient oxygen is lower than 5%, HypoxyProbe contains pimonidazole hydrochloride, which forms

adducts with cellular macromolecules (proteins, peptides, and amino acids) in hypoxic cells[185]. Specifically, activation has been shown to occur at cellular oxygen levels below 1.3%[185].

Spheroids were cultured for 11 days as described in section **2.5**, then incubated with 300μM HypoxyProbe for 3 hours at 37°C, 5% CO_2. Spheroids were then harvested from the bioink, fixed with PFA, and embedded in paraffin as described in sections **2.5.2** and **2.10**. Spheroid

sections were stained according to the manufacturer's protocol: Slides were dewaxed and rehydrated identically to section **2.10.1** and endogenous peroxidase quenched by washing with 3% hydrogen peroxidase buffer for 5 minutes. Fixation of samples can obstruct antigen sites and prevent binding in immunohistochemistry. As such, slides were processed with a heat-induced epitope retrieval protocol: 10mM Sodium citrate buffer (Sigma Aldrich, UK) was heated to 90°C and slides were submerged for 20 minutes, then left to cool to room temperature. Then, slides were washed with PBS and blocked with 3% BSA solution for 10 minutes at room temperature. A FITC-conjugated pimonidazole-binding antibody was supplied with HypoxyProbe and used to stain slides for one hour with a 1:200μL dilution. Finally, slides were washed with PBS, and mounted with VectaShield anti-fading mounting medium, with DAPI (Vectorlabs, UK).

2.11 Plate-Reader Assays

2.11.1 Measuring glucose

Because cellular metabolism is affected by pH and oxygen availability[186], glycolysis is known to be upregulated in tumours *in vivo*[187]. Glucose uptake was compared between cell monolayers and tumour at different timepoints, by measuring glucose concentration in the surrounding media. A standard glucose colorimetric assay was used (Stratech, eLabscience, UK), which used the glucose oxidase-peroxidase (GOP-POD) method to measure glucose. The assay contains glucose oxidase which interacts with glucose to produce hydrogen peroxide, which in turn reacts with a peroxidase in the presence of phenol, resulting in the formation of a coloured product.

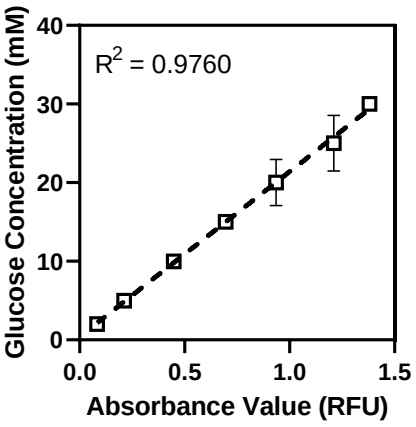

Figure 2-12 *Standard curve generated for glucose assays. Data shown are serial dilutions of a provided 30mM glucose solution. Line of best fit was used to determine glucose concentrations in other solutions.*

SW620 tumour spheroids were grown as described in section **2.5** for 11 days, then their media exchanged for high-glucose DMEM. Glucose concentration in high-glucose DMEM is 4.5g/L, or 24.98mM, which is within the detection range of the assay. SW620 cells were also seeded into 24 well plates with a seeding density $5x10^5$ cells/well and cultured in high-glucose DMEM for 24 hours. Then, media was aspirated exchanged with fresh media. In both conditions, 48 hours after fresh high-Glucose DMEM was added, aliquots of the media were taken from each well and used in the glucose assay. 3µL of media was added to 300µL of enzyme working solution in each well of a 96 well plate and incubated at 37°C for 15minutes before measurement. Furthermore, cells from both conditions were harvested and counted, to determine glucose consumption per million cells.

For controls, high-glucose DMEM, PBS, and high-glucose DMEM left in culture with cell-free bioink were used in addition to the glucose solution provided in the kit. A Cytation 5 platereader (BioTek, USA) measured absorbance at 505nm. A standard curve from known dilutions of the provided glucose solution was calculated from the plate reader measurements (**Figure 2-12**). All other glucose concentrations were determined through comparing absorbance values to the standard curve.

2.11.2 Measuring hypoxia

In addition to microscopy, Image-iT stain brightness was also measured quantitatively with a plate reader. $9x10^3$ SW620 cells/well were seeded into a 96 well plates and cultured for 24 hours. Spheroids were cultured in bioink for 11 days then harvested as stated in section **2.5.2**, and moved to 96 well plates. Each well was stained with Image-iT according to the manufacturer's recommendation: A 1μL/mL solution of Image-iT was added to each sample and incubated for 1 hour at 37°C, 5% CO_2. Samples were then washed three times with PBS and fluorescence measured with a Cytation 5 platereader with an 395nm/509nm excitation/emission. Unstained cell monolayers, unstained spheroids, PBS and media were used as controls.

2.12 Flow Cytometry

Flow cytometry (FACS) is a method for measuring staining of single-cell suspensions. Individual cells are rapidly passed by a series of excitation-lasers, measuring scattering of visible light as well as fluorescence. In this way, stained populations of cells can be analysed with high granularity, and subpopulations identified from differences in staining intensity. User-defined controls are used to "gate" populations of interest; trivially, live cells (*e.g.*, DAPI-negative cells), and single cells (determined by visible-light scatter) can be gated such that only those cells (*i.e.*, single, viable cells) are included in the analysis (**Figure 2-13**).

In this work, both cell monolayers and tumour spheroids were stained with for the cancer stem cell markers CD133 and CD44 and measured with FACS. Controls included dead cells only for gating live cell populations, untreated single cell suspensions for gating single cells only and fluorescence minus one (FMO) staining for background staining compensation. A BD Influx Cell Sorter (BD Biosciences, USA) was used in all cases, with the stains listed in **Table 2-5**.

2.12.1 Flow cytometry of SW620 cells from cell monolayers

SW620 cells were cultured in T25 flasks as harvested with trypsin/EDTA described in section **2.2**. Cells were centrifuged to form a pellet and counted with a countess II automated cell counter.

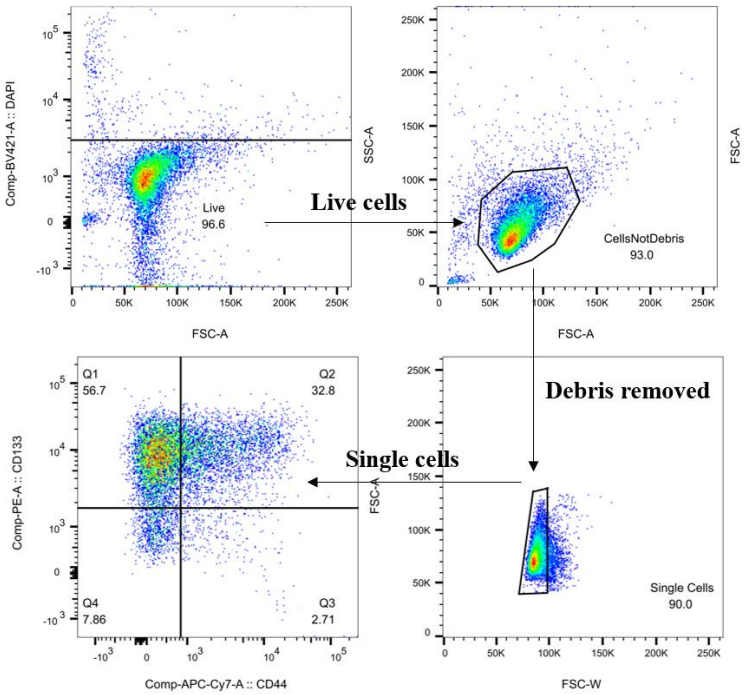

Figure 2-13 *Example of CD133 and CD44 gating from SW620 cells. Only live, single cells are included in the final quadrants; Debris, dead cells, and multiple cells are excluded.*

$2x10^5$ cells in 100µL were stained with for 30 minutes in glass FACS tubes (Fisher Scientific, UK) with the stains listed in **Table 2-5**. Initially, a range of concentrations were used for each stain, to determine optimal staining concentrations with low background and high signal: 10µL/100µL, 5µL/100µL, 2.5µL/100µL, 1.5µL/100µL, 1µL/100µL and 0.5µL/100µL stain/cell suspension were used. Optimal concentrations used are listed in **Table 2-5**. For each experiment with spheroids, cell monolayers were also used as controls to establish gating for single cells and fluorescence intensity.

2.12.2 Flow cytometry of SW620 cells from spheroids

SW620 spheroids were cultured for 11 days before being harvested according to section **2.5**. Some spheroids were treated with fluorouracil (5FU) or oxaliplatin (OX) using GI_{50} values calculated in section **2.13.2**. After harvesting, a single suspension was formed and counted with a Countess II automated cell counter. Identically to cell monolayers, $2x10^5$ cells in 100µL were

stained with the optimal staining concentration of each stain. Cell-free gels were dissolved and stained for use as controls to detect non-specific binding of the dyes to debris/undissolved gel products.

Table 2-5 *Stains used in flow cytometry*

Fluorescent Stain	***Staining Target***	***Optimal Concentration***
CD133-PE	CD133	0.5µL/100µL
CD44	CD44	1µL/100µL
Aqua Dead Stain	Dead cells	0.5µL/100µL
DAPI	Live cells	0.2µg/mL

2.13 Chemotherapy-Response Assays

Dose-response of cell monolayers and spheroids to the common chemotherapy agents 5FU and OX were compared through comparison of GI_{50} calculations. GI_{50} values represent 50% inhibition of growth and were calculated differently for cell monolayers and tumour spheroids. Cell lines used for chemotherapy-response calculations were SW620, SW480, LS174T and CACO2. Stock solutions of 5FU (Sigma Aldrich, UK) and OX (Sigma Aldrich, UK) were prepared from powder stock: 5FU powder was dissolved in 100µM NaOH to form a 100mM solution, and OX powder was dissolved in deionized water to form a 10mM solution. For use in culture with live cells, stock solutions were first diluted to 2mM, then diluted serially by 1/3rd with media to form a range of 8 concentrations. 30µL of each dose was added to 170µL media in 96 well plates, diluting chemotherapies to their final range of concentrations, starting at 300µM and decreasing by 1/3rd. Vehicle controls (VCs) were used as a reference for evaluating drug effect; Vehicle control conditions for oxaliplatin and were 2.7% deionized water in spheroid media and 2.7µM NaOH in spheroid media, respectively.

2.13.1 Chemotherapy-response of cell monolayers

$9x10^3$ cells of each cell line were seeded into each well of 96 well plates and cultured for 24 hours in high-glucose DMEM, after which media was aspirated and replaced with 200µL drug-

containing media. Samples were incubated with drug-containing for a further 72 hours, then, media was aspirated, and samples washed three times with PBS before fixing with 4% PFA for 15 minutes at room temperature. PFA was removed and samples washed three times with PBS, then stained with 0.5%(w/v) crystal violet solution (Sigma Aldrich, UK) for 10 minutes. Unbound crystal violet was removed by washing with PBS. Bound crystal violet was extracted with 10%(v/v) acetic acid (Sigma Aldrich, UK) and measured via absorbance at 540nm with a Cytation 5 platereader. Absorbance values were compared to vehicle control values to represent viability as a percentage of the control group. Wells containing PBS were used to calculate background signal.

Dose-response curves were calculated in GraphPad Prism ver. 8 (GraphPad Software, USA) and GI_{50} values calculated as the concentration corresponding with 50% relative viability.

2.13.2 Chemotherapy response of tumour spheroids

Cancer spheroids were bioprinted into 96 well plates and cultured as described in sections **2.4** and **2.5**. 4 days after printing, media was exchanged with 200µL drug-containing media for 72hours, then media was exchanged with fresh spheroid media for a further 4 days. Spheroid sizes were imaged with automated brightfield microscopy as described in section **2.8.1**, then measured with a custom MATLAB script, outlined in section **2.15**. Dose-response curves were calculated in GraphPad Prism ver. 8 (GraphPad Software, USA) by plotting average spheroid sizes as percentages of vehicle controls. GI_{50} values were calculated as concentrations corresponding with 50% relative viability.

2.14 Radiotherapy and Chemoradiotherapy

Radiotherapy with and without 5FU was performed with both cell monolayers and spheroids. The radiation source was Caesium-137 ($^{137}55Cs$), which has a half-life of approximately 30.2 years. $^{137}55Cs$ decays primarily through beta decay to barium-137m (^{137m}Ba), an unstable isotope with a half-life of 153 seconds. ^{137m}Ba decays to a stable form of barium, barium-137, emitting gamma

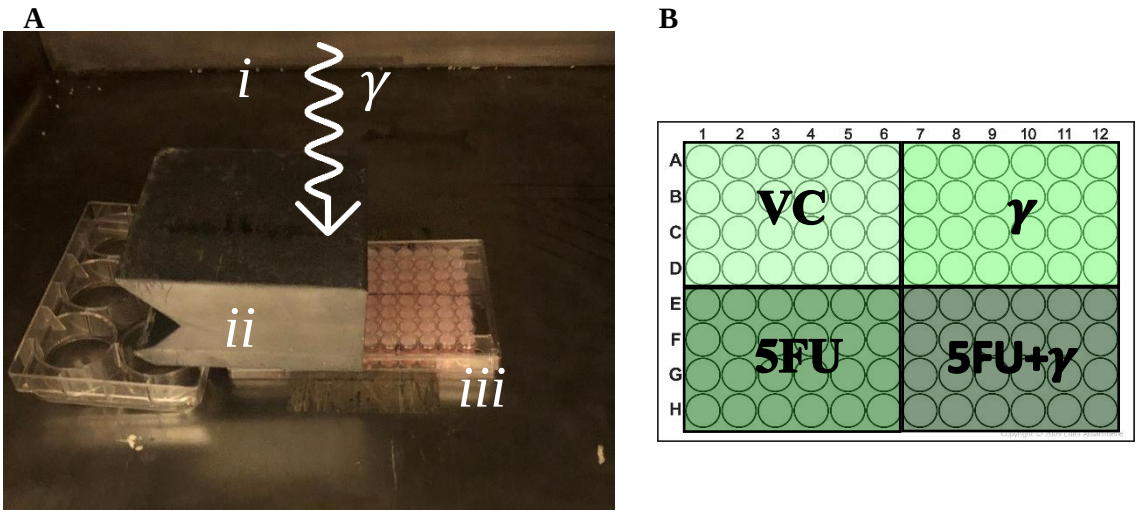

Figure 2-14 *Experimental setup for chemoradiotherapy assays.* ***A*** *Spheroids in a 96 well plate, placed in a lead-lined chamber prior to irradiation.* ***i*** *Plates were centred 60cm below the* ^{137}*55Cs radiation-source which is exposed for a defined time.* ***ii*** *Lead block is covers regions of the plate to inhibit radiation exposure.* ***iii*** *half-exposed 96 well plate.* ***B*** *Plates were divided into quadrants. The left-hand quadrants were concealed by the lead block and therefore not irradiated. 5FU was added to the bottom-most quadrants such that the effects of radiation, chemotherapy and chemoradiation were all measured in each plate.*

rays in the process; Gamma radiation from decaying ^{137m}Ba is the only source of gamma rays from ^{137}55Cs, and therefore the principal source of radiation for *in vitro* tissue samples.

Radiation doses of 2.5Gr and 5Gr were used. These doses were calculated using the known dose-rate of the caesium source in 1997 when the machine was last tested, and an assumed half-life of 30.2 years. Moreover, absorbed radiation theoretically decreases by inverse-square with distance between the sample and source, so final dose calculations took into consideration the radioactivity of the source, the distance between the sample and the source, and the time for which the samples were exposed to the source. Specifically, dose-rate in 1997 was measured to be approximately 11.09 Gymin^{-1} 10cm from the source, corresponding to 6.54 Gymin^{-1} in 2019 using the half-life equation. 6.54 Gymin^{-1} 10cm from the source decreases to 3.03 mGys^{-1} (assumed inverse square behaviour with distance) 60cm from the source, the distance at which samples were placed. Exposure times for 2.5Gr and 5Gr were therefore calculated to be 826s and 1652s (13min 46s, 26min 32s, respectively) for plates placed 60cm from the source.

Table 2-6 *Step-by-step overview of the spheroid image analysis code.*

Step	***Description***	***Associated Files***
1. Loading Images to Memory	Uses bioformats plugin to load .lif files into memory.	Bioformats plugin
2. Creating Projections	Creates 2D maximum projections from z-stacks and subtracts background.	maxstack.m
3. Adaptive thresholding	Threshold projections to binary. Thresholding is local, defined by user input. Ellipses can be fit to object boundaries	adaptivethreshold.m fitellipse.m plotellipse.m closeBoundary.m
4. Size Exclusion	Exclude thresholded objects which are outside size boundaries (user-defined). Watershedding separates touching objects.	
5. Shape Exclusion	Exclude objects exceeding limits on eccentricity or surface roughness.	smoothTest.m
6. Exporting Data	Detected & measured objects are exported in a .csv file. Centre of geometry, area, semi-axis lengths, aspect ratio and orientation are measured. A separate Excel macro aggregates the data.	AnalysisMacro.xlsm

For chemotherapy experiments, spheroids were bioprinted and cultured in 96 well plates as described sections **2.4** and **2.5**. 4 days after bioprinting, spheroids were exposed to either 2.5Gr or 5Gr radiation, with some samples dosed immediately before with GI_{50} concentrations of 5FU to observe for radio-sensitizing effects (**Figure 2-14**). Cell monolayers were also treated. $1x10^4$ cells were seeded in each well of a 6 well plate and exposed to radiation 24 hours after plating. Radiation response was measured with crystal violet staining as described in section **2.13.1**.

2.15 High-Throughput Image Analysis of Spheroids

To maximise the utility of the high throughput "droplet printing" setting on the BioX bioprinter, and the automation of the microscope, an image analysis program was written in MATLAB to measure spheroid sizes directly from microscope image files. In this way, bioprinted spheroid assays were made scalable by automating the entire pipeline: printing, imaging, and analysis. The script written in MATLAB consists of the steps outlined in **Table 2-6**.

2.15.1 Step 1: Loading images into memory

Microscope images can come in a variety of forms, however, Leica microscopes uniquely output Leica Image Files (.lif files). These files can contain many images of different types from a single microscope session, *e.g.*, 8-bit z-stack images and single-plane RGB images can be contained in a single .lif file. Moreover, microscopy conditions are stored as metadata in .lif files, such as X,Y,Z resolution, optical filters used, and objective lenses used. As such, .lif files are convenient ways of packaging microscope data and useful for analysis because they retain critical information from the imaging session.

.lif files cannot be opened directly in either ImageJ or MATLAB. However, the Open Microscopy Environment (OME) organisation produces free-to-use plugins to access and edit .lif files. For instance, the ImageJ package, FIJI, contains the Bio-Formats plugin developed by OME by default which enables working with .lif files. Similarly, the MATLAB script used for analysis in this research uses the Bio-Formats plugin, which has already been optimised to load .lif files into memory in MATLAB. The MATLAB *profiler* tool was used generally to optimise function efficiency within the code, and it was found that the Bio-Formats *bfopen.m* and *bfGetPlane.m* functions are the most time-consuming processes. Collectively, Bio-Formats commands are on average ~4 times more time consuming than *maxstack.m*, the next longest-running function. As such, further optimisation of the code would not yield large returns overall, as the Bio-Formats commands cannot be reasonably optimised further.

2.15.2 Step 2: Creating image projections

The MATLAB script is intended for use with single channel, z-stack .lif files of stained tumour spheroids. However, computationally, spheroid parameters are not measured with 3D reconstructions, but rather from 2D projections, sometimes referred to as focus-stacking. The function *maxstack.m* generates projections by taking maximum pixel values across all the z-planes of the z-stack image, forming a maximum projection. The maximum projection will contain increased background, *i.e.*, regions not containing spheroids will become brighter. The illumination profile across the image also may not be uniform. Consequently, simple background

subtraction and normalization is included in *maxstack.m*: A background image is created by repeated averaging with a disk-shaped frame, then subtracted from the projection (**Figure 2-16 A-C**).

2.15.3 Step 3: Thresholding

Thresholding is the process of segmenting an image by comparing pixel intensities to a threshold, *T*. For grayscale images (such as single channel, 8bit microscopy images), such segmentation results in a binary image (*i.e.,* black-and-white. Black pixels are background and white are foreground). *T* may be a single value ("global thresholding"), or it may vary across the pixel space ("adaptive thresholding"). For this program, an adaptive thresholding algorithm was used, *adaptivethreshold.m*, made publicly available by Guanglei Xiong, Tsinghua University, Beijing, China. In this algorithm, a local averaging filter of a certain size is declared by the user (*e.g.,* 100x100 pixels) which is convolved with the original image. An offset value, *C*, is subtracted from the local average and effectively defines the local threshold, T_{LOCAL}, when compared to the original image.

2.15.4 Step 4: Size exclusion

After thresholding, the image is binary and objects can be measured simply by the number and distribution of connected, white pixels. However, thresholding can cause adjacent objects in the original image to become merged in the binary image, where they are not clearly separate objects. Watershedding is an image transformation which can be understood as treating an image as a topographical map, with lines drawn along the "ridges"; For object detection, merged objects can be split apart along the lines in the watershedding map. A variety of different watershedding algorithms exist, but in MATLAB the *watershed* function uses the Fernand Meyer algorithm in conjunction with the distance-transform of the thresholded image. In this case, the binary image is used, obtained from *adaptivethreshold.m*, and the distance-transform calculated. Here, the value of each foreground pixel (*i.e.,* each white pixel) is now the distance to the nearest background pixel, consequently, the distance transform is a gray-scale image. The Fernand Meyer algorithm acts upon the gray-scale distance-transform to produce a

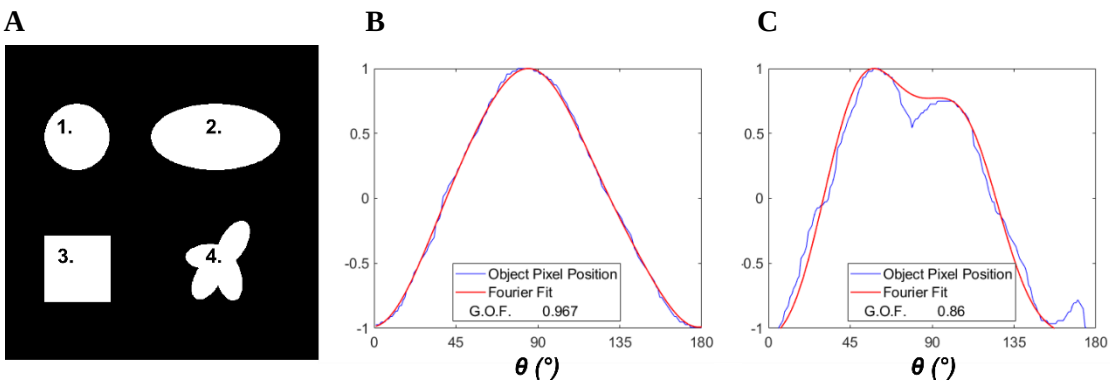

Figure 2-15 *Exclusion by object smoothness.* ***A*** *Four objects of different shapes, increasing in roughness.* ***B,C*** *Shapes 1 (circle) and 4 from* ***A****, with the x-value of the boundary pixels plotted (blue line) and compared with a third-order Fourier fit (red line). G.O.F. is the goodness of fit between the Fourier solution and pixel positions. Objects can be arbitrarily thresholded by G.O.F. to exclude rougher objects*

binary image with lines separating regions of high pixel intensity, resulting in a map where boundaries intersect connected objects which are not entirely merged.

After the watershed map is applied to the thresholded image (**Figure 2-16 D,E**), objects can be detected and measured automatically in MATLAB. The *bwboundaries* function returns the boundary pixels of each object and stores their (x,y) position, and the *regionprops* function calculates object areas, which can be used to exclude objects which are too large or small.

2.15.5 Step 5: Shape exclusion

Object measurement in image analysis can be simplified if certain facts about the objects are known. In this instance, it is known from experimental observation that tumour spheroids are smooth and rounded in shape. As such, after thresholding and size exclusion, the "smoothness" of each object is measured and used as another form of exclusion. Objects which are "rough" are likely spheroids which have merged, either by physically growing into one another, or as an artefact of the image projection. The measure of smoothness is arbitrary, but defined here as the goodness-of-fit of the object boundary to a third order Fourier series (**Equation 4**):

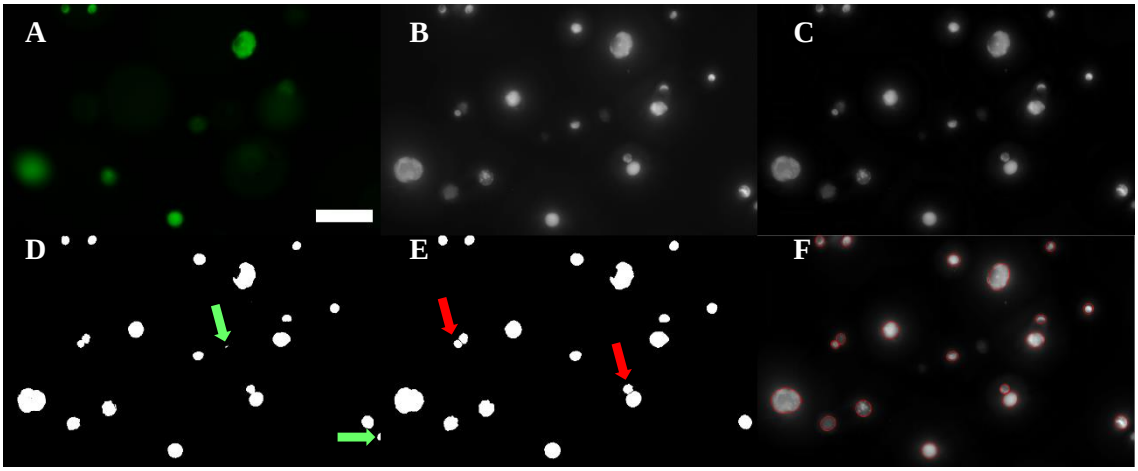

Figure 2-16 *Step-by-step example of spheroid measurement in MATLAB.* ***A*** *Random plane from a z-stack image of tumour spheroids, stained with calceinAM green.* ***B*** *Maximum projection of* ***A****.* ***C*** *Background subtraction from* ***B****.* ***D*** *Binary, thresholded image from* ***C****.* ***E*** *Watershedding and object exclusion from* ***D****. Watershedding shown with red arrows. Excluded objects shown with green arrows.* ***F*** *Ellipses fit to the boundary pixels of objects in* ***E****, overlayed in red lines over the maximum projection. Scale bar = 200μm*

Equation 4 *The Fourier series*

$$f(x) = a_0 + \sum_{n=1}^{3}\left(a_n \cos\frac{n\pi x}{L} + b_n \sin\frac{n\pi x}{L}\right)$$

$$where:\ \ a_0 = \frac{1}{L}\int_{2L} f(x)dx\,, \qquad a_n = \frac{1}{L}\int_{2L} f(x)\cos\frac{n\pi x}{L}dx, \qquad b_n = \frac{1}{L}\int_{2L} f(x)\sin\frac{n\pi x}{L}dx$$

For a circle or oval, a plot of pixel number vs pixel coordinate will show a smooth curve closely approximated by a third-order Fourier series. However, the same plot of an object with a rough surface yields a curve only well-approximated by Fourier series containing higher-order terms. Hence, the goodness-of-fit between the computed Fourier series and actual image boundaries is calculated in *smoothTest.m* and used to discriminate against "rough objects" which were not segmented by watershedding (**Figure 2-15**).

After rough objects have been removed, the remainder can be adjusted to more accurately fit spheroids contained in the original image. Specifically, as spheroids grow into rounded structures, thresholded objects are assumed to be similarly rounded. An ellipse is fitted to each object boundary from the thresholded image, which was previously not excluded (**Figure 2-16 F**). The fitting algorithm was adapted from publicly available code written by Richard Brown (mathworks.com), but is based upon the solution of Gander *et al*[188]. In this case, an ellipse is fitted

to a collection of known points by using the linear "least-squares" solution: The distance from each known point to the centre of the ellipse is squared and summed. The solution is the ellipse for which this sum is closest to zero. *fitellipse.m* and *plotellipse.m* calculate and plot ellipse solutions. *closeBoundary.m* checks that continuous ellipse solutions (*i.e.,* ellipse equations) are fully enclosed when they are moved to discrete pixel space.

2.15.6 Step 6: Exporting data

After steps 1-5, a set of objects has been detected and measured for a given image-projection. The measured quantities for each object are: Centre of geometry, semi-axes, aspect ratio, area and orientation (rotation). These measurements are exported as an Excel workbook, where each worksheet contains measurements for each image-projection. A custom Excel macro was written to aggregate this data usefully. For instance, for chemotherapy-response, each column of the 96 plate is a separate treatment condition. As such, the macro outputs an excel file where treatment groups are collected as specified by the user. Finally, data was moved to GraphPad prism for analysis.

2.16 Statistical Analysis

All statistical analysis was performed in GraphPad Prism version 8 (GraphPad, USA). Statistical tests used are described in the relevant figures or tables. Generally, T-tests were used to compare the difference in two means, whereas one-way ANOVA with Tukey's multiple comparison post-hoc test was used to compare the differences in 3 or more means. In all cases "*n.s.*" refers to non-significant differences ($p>0.05$) and significant p-values follow the *,**,*** etc. nomenclature where: * = $p<0.05$. ** = $p<0.01$, *** = $p<0.001$, **** = $p<0.0001$.

Chapter 3 : Design of a Biocompatible Bioink for Bioprinting Colorectal Tumour Spheroids

3.1 Introduction

In this chapter, the formulation of a biocompatible, bioprintable hydrogel is described for use in tumour spheroid assays. A range of hydrogel compositions were tested and evaluated by their ability to facilitate spontaneous tumour spheroid formation of the metastatic colorectal adenocarcinoma line, SW620. The mechanical properties and internal structures of these bioinks are explored and their influence on cellular growth dynamics is discussed.

3.1.1 Alginate-F127 Bioinks

Prior to this work, Armstrong *et al.* developed a hybrid alginate/Pluronic F127 bioink for use in extrusion bioprinting of cartilage and bone models. As mentioned in section **1.10**, Pluronic F127 is a tri-block copolymer used in bioprinting as a structural, sacrificial component which can be removed after printing. The innovation in this work was in creating alginate/F127 blends which improved the poor mechanical properties of low wt.% alginate gels.

These gels exhibited interesting chemistries. Cold F127 solutions are liquid and can easily be blended into low viscosity alginate solutions. Upon heating, the critical micelle concentration of F127 lowers, and F127 molecules form micelles to shield their hydrophobic cores. As heating approaches physiological temperatures, the micelle volume fraction increases and crystallizes in a sol-gel transition[189]. The temperature-dependence of this process means that cold immersion rapidly washes away F127 structures. In the blended alginate/F127 bioinks, Armstrong *et al.* discovered a formulation in which the evacuation of the F127 phase was synchronous with the crosslinking of the alginate, *via* room temperature $CaCl_2$ immersion. The evacuation of the F127 phase resulted in the formation of macropores which improved the mechanical strength of the gel. Primary human mesenchymal stem cells were highly viable when cultured in this bioink and differentiated down the osteogenic linage over a 21-day culture window. The development of this bioink underpins much of the work in this chapter, and the final, 6 wt.% alginate/ 13 wt.% F127 bioink outlined by Armstrong *et al.* was used for initial 3D culture of colorectal cancer cells.

3.1.2 SW620 as a model cell line

SW620 was selected as a model cell line for evaluating bioink performance for several reasons. First, SW620 is a metastatic CRC line and therefore of interest clinically, as metastasis in cancer is linked to recurrence and poor patient prognosis[190,191]. Moreover, SW480, another CRC line, is related to SW620, SW480 being the non-metastatic parent population. As such, SW620 is an apt choice of model cell line as it can be later compared to SW480 to unpack differences in the behaviour of metastatic and non-metastatic cells in 3D. Second, SW620 is a common cell line in the literature, which is useful for reference; for instance, the GI_{50} values of various common chemotherapy treatments has been reported for this cancer line[192]. Additionally, SW620 spheroids have been grown and characterized through traditional cell-aggregation approaches[193–196]; enabling comparison between spheroids generated in this work and other studies. Finally, SW620 is a robust cell line which proliferates rapidly in 2D and is resistant to chemotherapy[192] and radiotherapy[197]. As the 3D microenvironment challenges cell lines which are adapted to 2D cell culture conditions, the initial selection of a robust cell line is useful in refining the 3D culture approach.

3.2 Aims

In this chapter, the primary aim is the optimisation of a bioink formulation which is bioprintable and supportive of tumour spheroid formation in SW620 cell line. More specifically, the optimum bioink formulation and method of fabrication must be readily applied to a high throughput bioprinting approach with a variety of colorectal cancer cell (CRC) lines. Finally, a secondary aim is to understand the factors (*e.g.* gel stiffness, cell line, crosslinking method, culture conditions *etc.*) which influence tumour spheroid formation in 3D generally, to further the design of cancer-spheroid-supportive bioinks in the future.

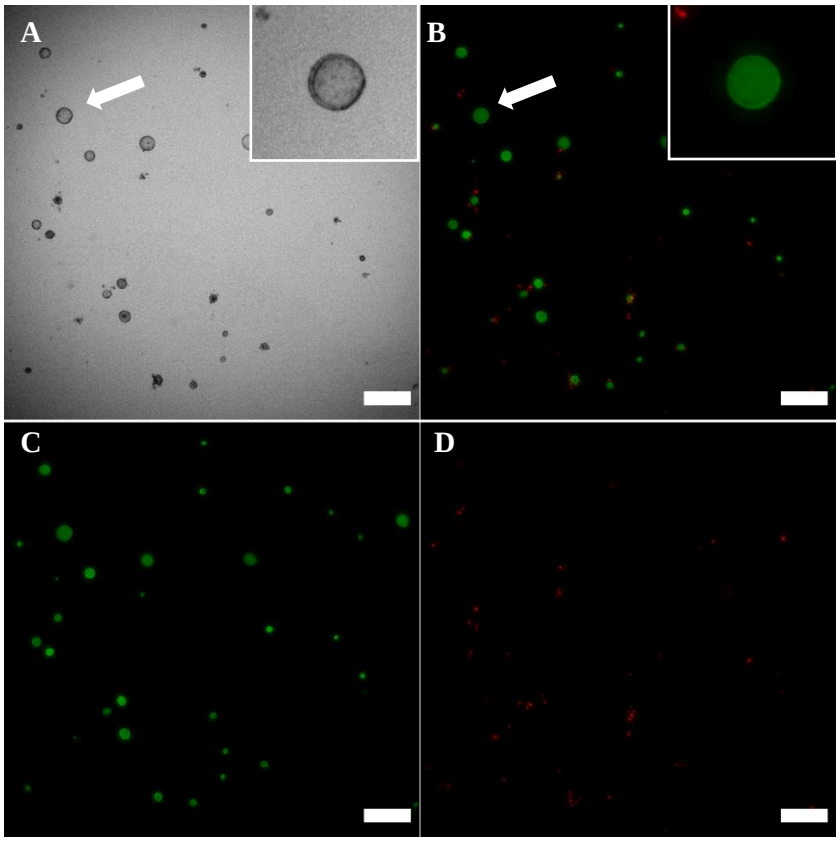

Figure 3-1 *Widefield microscopy of SW620 spheroids growing in Matrigel after 9 days of culture.* ***A*** *Brightfield image, inset is enlarged image of a single spheroid (white arrow).* ***B*** *Composite image of live-stained cells (**C**) with calceinAM and dead-stained cells (**D**) with ethidium homodimer III. Scale bar = 300μm*

3.3 Results and Discussion

3.3.1 Matrigel culture

Matrigel, a biocompatible hydrogel comprised of basement-membrane matrix derived from Engelbreth–Holm–Swarm mouse sarcoma cells, is considered the "gold-standard" for culturing cells in 3D[198–200]. However, Matrigel has a number of drawbacks, including high cost, significant batch-to-batch variability[201], and exceedingly poor printability[122,133]. Consequently, in bioprinting applications Matrigel is avoided, or else blended into other bioinks[133].

Here, Matrigel was used as a positive control to validate the spheroid-forming capacity of SW620 cells in 3D. Although SW620 cells have been reported to grow into spheroids in Matrigel in the literature[202,203], variation between cell lines due to passaging or other culture conditions can cause differences in experimental results, even where immortalized cell lines are used. The culture

conditions used were derived from the work of Sato *et al.*[89,90] who pioneered protocols for the expansion of colorectal organoids in Matrigel from (Leucine Rich Repeat Containing G Protein-Coupled Receptor 5) Lgr5+ intestinal stem cells. Importantly, media used for the expansion for spheroids in 3D ("spheroid media") was adapted from this work and described in section **2.5.1**.

For 3D culture with Matrigel, $1x10^4$ cells/mL were dispersed into Matrigel by pipetting, then cultured in spheroid media over a period of 9 days and imaged with widefield microscopy (**Figure 3-1**). Individual cells grew over this time into viable spheroids of different sizes which were clearly visible in both brightfield and stained images, exhibiting circular morphologies with few dead cells in the surrounding gel. These initial observations demonstrated that the SW620 cells used throughout this work have spheroid-forming capacity in 3D cultures, and were the basis for the use of SW620 cells in further investigations.

3.3.2 Alginate-F127 bioinks

Having validated the spheroid forming capacity of SW620 cells in Matrigel, alternative bio-printable hydrogels were used as a substitute. The first bioink used was described by Armstrong *et al.*[134] and is an optimised blend of alginate and Pluronic F127. As described in section **3.1.1**, the F127 component is added as a viscous liquid into the gel and forms micro domains when mixed, which in turn undergo a sol-gel transition around 37°C. When crosslinking the alginate component with $CaCl_2$, the gelled F127 dissolves into solution, resulting in a porous gel architecture, with pore size corresponding to the size of the F127 domains. This bioink was shown to support the culture of bioprinted human mesenchymal stem cells (hMSCs) over 21 days and was therefore used as a starting point for SW620 culture in 3D.

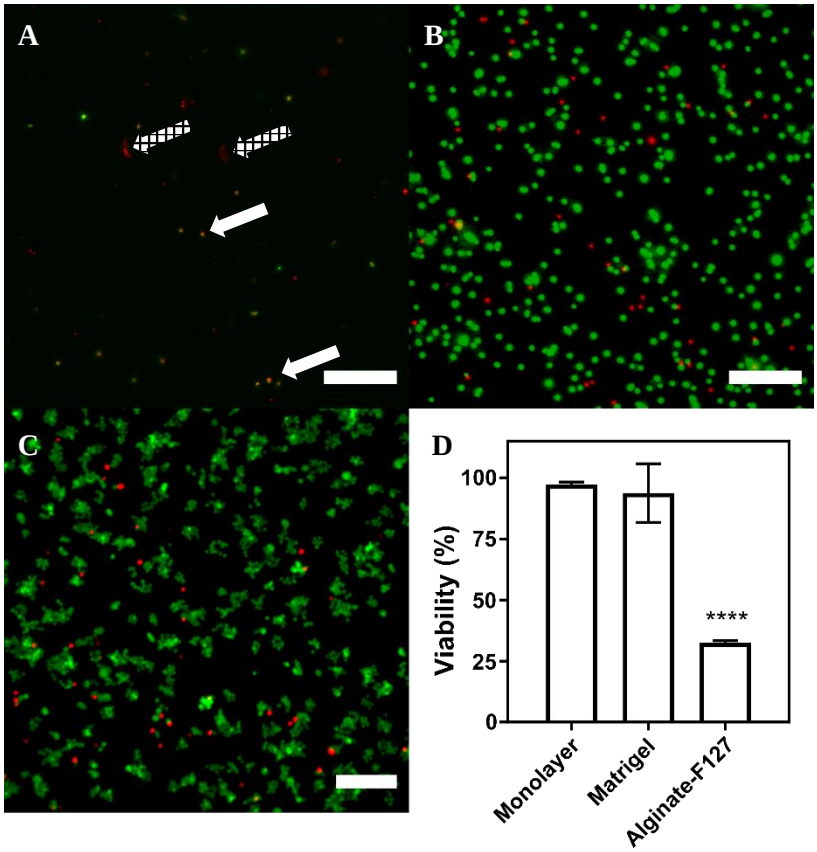

Figure 3-2 *Widefield microscopy of Live/Dead staining of SW620 cells 24 hours after bioprinting.* ***A*** *SW620 cells in the alginate-F127 bioink, seeded at 10^5 cells/mL. White arrows show cells positive for both stains. Checked arrow shows background staining of the dead stain from the alginate gel.* ***B*** *SW620 cells in Matrigel, seeded at 10^4 cells/mL.* ***C*** *SW620 cells seeded into a 96-well plate, seeded at 10^4 cells/mL.* ***D*** *Viability analysis from the ratio of live cells:total cells, measured in CellProfiler, compared to the cell monolayer control. All scale bars = 200μm. ****p<0.0001by one-way ANOVA with Tukey's post-hoc test*

3.3.2.1 SW620 culture in the unmodified Alginate-F127 bioink

As cancer cells have never been bioprinted in this bioink before, experimental work initially set out to determine cell viability in the bioink after printing and crosslinking. $1x10^5$ cells/mL were blended into bioink and their viability measured 24 hours after bioprinting by live/dead staining with calceinAM and ethidium homodimer III. Viability was determined using a custom *CellProfiler* pipeline described in section **2.8.2** to threshold live and dead images and count the number of cells in each.

Initial viability of SW620 cells was low in the alginate bioink (32%), with many cells staining positive for both live and dead stain simultaneously (**Figure 3-2**, **A**, white arrows), indicating that these retained some active metabolism, although their membrane integrity was compromised.

Additionally, some background staining of the bioink was evident (**Figure 3-2**, **A**, checked arrows), however, the large area and elongated shape of such stained regions meant these could be filtered-out during image analysis. In contrast, cell viability was high in both Matrigel (94%) and cell monolayer controls (97%).

The observation of low early viability in the alginate-F127 bioink when compared to Matrigel could have a range of causes. Firstly, mixing forces from the dual asymmetric centrifuge (DAC) when blending cells into the bioink, could be significant and is absent in Matrigel cultures, where cells are mixed into the gel bulk by hand-pipetting. Secondly, shear forces from the printing process could stress cells and are similarly missing in Matrigel cultures, which were not bioprinted. Thirdly, cell seeding density could be significant, with anoikis being induced due to cells not being too distant to form cell-cell contacts. Finally, the structure of the alginate 3D environment could be the cause of cell death, as it differs compositionally from Matrigel, lacking extracellular matrix (ECM) components, growth factors and other biomaterials present in Matrigel[126]. As such, DAC settings, cell seeding density and bioprinting extrusion protocols were further investigated to establish their impact on cell viability and to optimise printing parameters for this gel.

3.3.2.2 Impact of the DAC on dispersion and viability

The preparation of alginate-F127 bioinks was altered from the original protocol to incorporate the DAC as a substitute for mixing alginate and F127 pre-gels by hand, improving reproducibility and eliminating the introduction of air bubbles into the bulk gel. Although the primary use for the DAC was to ensure thorough blending of gel components, live cells were also blended into the gel with the DAC. The dispersion of cells was measured by staining cell nuclei with Hoechst after crosslinking, then imaging with z-stack imaging with a widefield microscope. The X,Y,Z coordinates of each cell were determined using *TrackMate*, an ImageJ plugin (**Figure 3-3**). A Jarque Bera test was performed in Excel which confirmed that the distributions of X,Y and Z coordinates were all uniform. These data show that the 1500RPM, 30 second spin setting on the DAC is suitable for uniformly distributing cells in 3D.

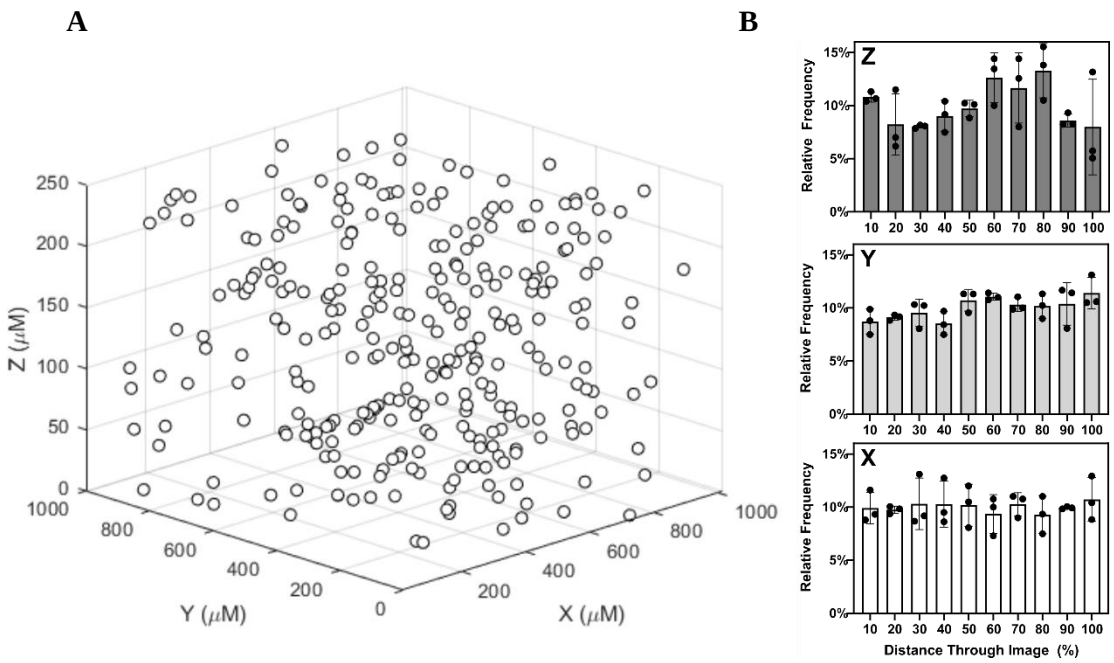

Figure 3-3 *Distribution of cells in 3D bioprints.* ***A*** *Example pointcloud of cells in focal volume measuring 1000x1000x250μm.* ***B*** *X,Y,Z coordinates of cells from three experiments and plotted as histograms. Bins represent proportion of cells in image regions. Data is mean ± s.d. where points show n=3 experimental results.*

As initial viability of SW620 cells was low, different DAC conditions were tested to determine if DAC spin speed or spin time decreased cell viability. The highest (3500rpm) spin speed possible was used between the shortest (10 seconds) and longest (5 minutes) spin times which could be set on the instrument. When tested, the DAC was found to have no statistically significant impact on cell viability (**Figure 3-4**, **A**).

3.3.2.3 Impact of seeding density on viability

The apoptotic process, anoikis, is a form of cell death which can occur due to loss of cell-cell contact between cells. Unlike other bioprinting applications, such as for regenerative medicine, very high seeding densities (>10^6 cells/mL) cannot be used as cancer spheroids grow exponentially over time and therefore require large spaces into which they can grow. As such, when cells are loosely dispersed through the 3D environment, cell-cell contacts are only formed after cell division. Consequently, the effects of anoikis would be most prominent at early timepoints. Cell density was varied between 1x10^4-2x10^5 cells/mL, and viability measured 24

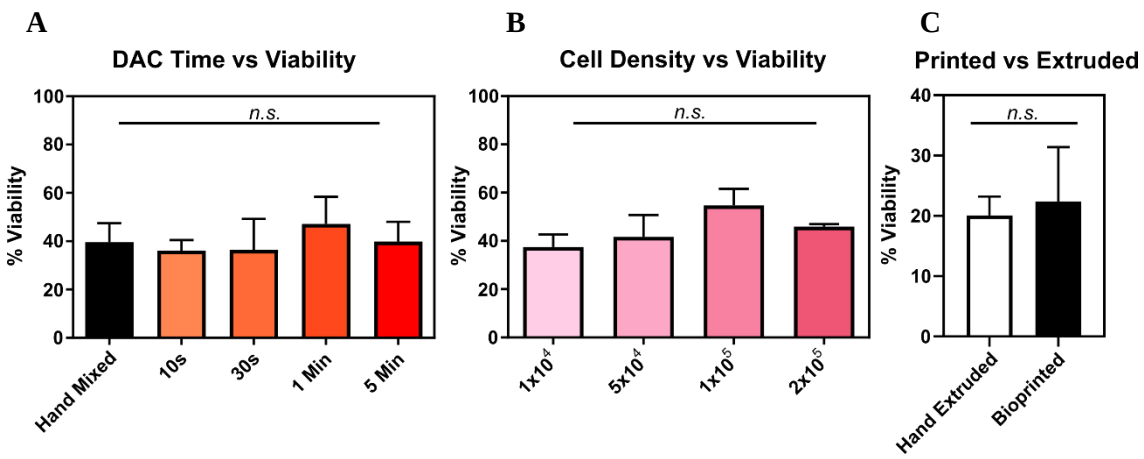

Figure 3-4 *Screening experimental conditions for optimisation of cell viability of SW620 cells.* ***A*** *Viability of cells mixed with differing DAC spin times at 3500RPM compared to mixing by hand.* ***B*** *Viability of SW620 cells at different seeding densities.* ***C*** *Viability of SW620 cells after printing and extruding. n.s. = not significant*

hours after bioprinting. These seeding densities were selected to allow room for spheroids to grow over time in culture. Observationally, higher seeding densities resulted in spheroids merging into one another at later timepoints. Viability appeared to increase with cell density, up to $1x10^5$ cells/mL, before decreasing at the highest concentration: $2x10^5$ cells/mL, however, this difference was not significant (**Figure 3-4**, **B**).

Resistance to anoikis for the SW620 cell line is expected, as a hallmark of metastatic cancers is their ability to evade apoptotic pathways[204]. Metastatic cells such as SW620 have a mesenchymal phenotype, having undergone epithelial-mesenchymal transition (EMT), a process which down-regulates proteins involved in cell-cell and cell-matrix interactions, such as E-cadherin[205]. Moreover, SW620 cells grown in Matrigel are seeded at low densities (10^4 cells/mL) and are nonetheless highly viable. The decrease in cell viability beyond $1x10^5$ cells/mL could be explained by media diffusion and competition, whereby higher cell densities increase competition for nutrients and thereby starve cells further away from gel periphery. Although the results were not significant, $1x10^5$ cells/mL was carried forward as the standard seeding density unless otherwise stated.

3.3.2.4 Impact of bioprinting on viability

During bioprinting, forces act on the bioink passing through the nozzle and are transmitted to the cells within. Mechanotransduction of the local force by cells can result in cytoskeletal rearrangement, followed by cell death[206]. In Matrigel, only weak extrusion forces exist as it is not bioprinted, and therefore this could be a cause of high viability in this gel. Bioprinted constructs were compared to gels which were "printed" by hand extrusion with a positive displacement pipette. Here, no difference in viability was found, suggesting that printing forces used have negligible impact on SW620 cell viability (**Figure 3-4**, **C**). The effect of printing forces on cell viability of cells has not been studied extensively, however, Ning *et al* have provided a mathematical model and experimental data of printing damage to RSC96 and L8 cells (rat neuronal and skeletal muscle cells, respectively). In their study, printing forces between 50kPa and 400kPa were applied to these cells suspended in 2%(w/v) alginate gels and printed through needles of various gauges. Reduction in viability up to 5% was observed at 50kPa, and 20% at 400kPa, the highest printing force[160]. Rough estimates of the printing force applied in this work varies but is at most 30kPa, varying with printing protocol, and therefore these data conform with the results of Ning *et al.* Interestingly, Ning *et al* conclude that damage to cells during printing is primarily caused by elongation of the cell in the flow field as it enters the printing needle. Consequently, printing damage can be mitigated using tapered nozzles rather than needles, which was adopted here for all further bioprints.

3.3.2.5 Viability of other cell lines

To rule out the possibility that the SW620 line was not representative of how other colorectal cancer lines would grow in the bioink, 5 other cell lines were screened: HCT116, LOVO, SW1463, LS174T and SW480. Day 1 viability was measured and compared to the results with SW620 cells. Here, it was found that viability was not only low with SW620 cells, but for all cell lines tested; in all cases, viability was below ~50% (**Figure 3-5**). Collectively, viability data establishes a clear trend that regardless of cell line, mixing and printing forces or cell seeding

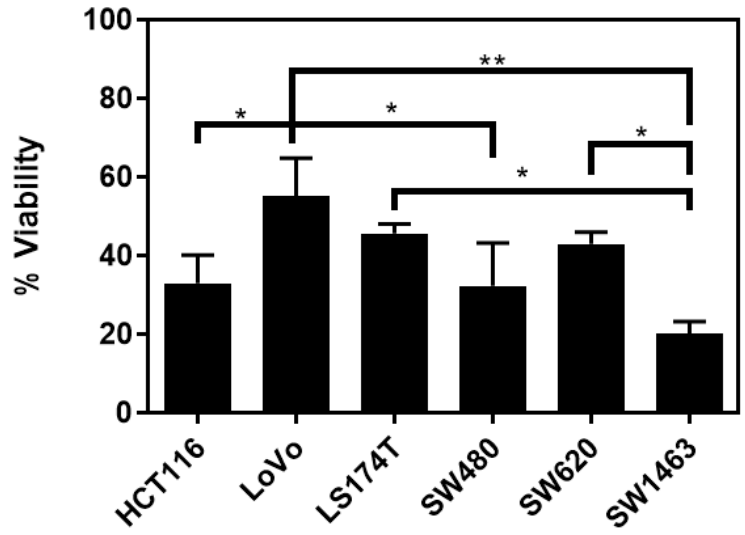

Figure 3-5 *Day 1 viability of various CRC cell lines in the Alginate-F127 bioink. *p<0.05, **p<0.01 for one-way ANOVA with Tukey's multiple comparison post-hoc test*

density, viability remains low in the alginate-F127 bioink. As such, although well-suited to hMSCs, the composition of the alginate-F127 bioink is not conducive to CRC spheroid culture.

3.3.2.6 Morphology of cell colonies in the alginate-F127 bioink

Despite low viability of CRC cells in this bioink, viable cells did form colonies over time in the bioink for some cell lines. SW1463 did not form viable colonies, whereas HCT116, LOVO, LS174T, SW480 and SW620 did grow over time in the bioink (**Figure 3-6**). However, low initial viability typically meant few colonies formed. Interestingly, the morphology of all cell colonies was distinctly non-spheroidal, unlike experimental data and reports in the literature using Matrigel for these lines. As such, the non-spheroidal growth of these colonies is likely due to microenvironment of this bioink, which lacks ECM components present in Matrigel. To test whether the addition of ECM components would change the viability and morphology of CRC cells and spheroids, the alginate-F127 bioink was altered to include either gelatin or Matrigel.

3.3.2.7 Addition of gelatin

Gelatin, an irreversibly hydrolysed form of collagen, includes the tripeptide RGD (Arg-Gly-Asp) cellular binding motif present in ECM[207]. Gelatin was added to the alginate-F127 bioink by

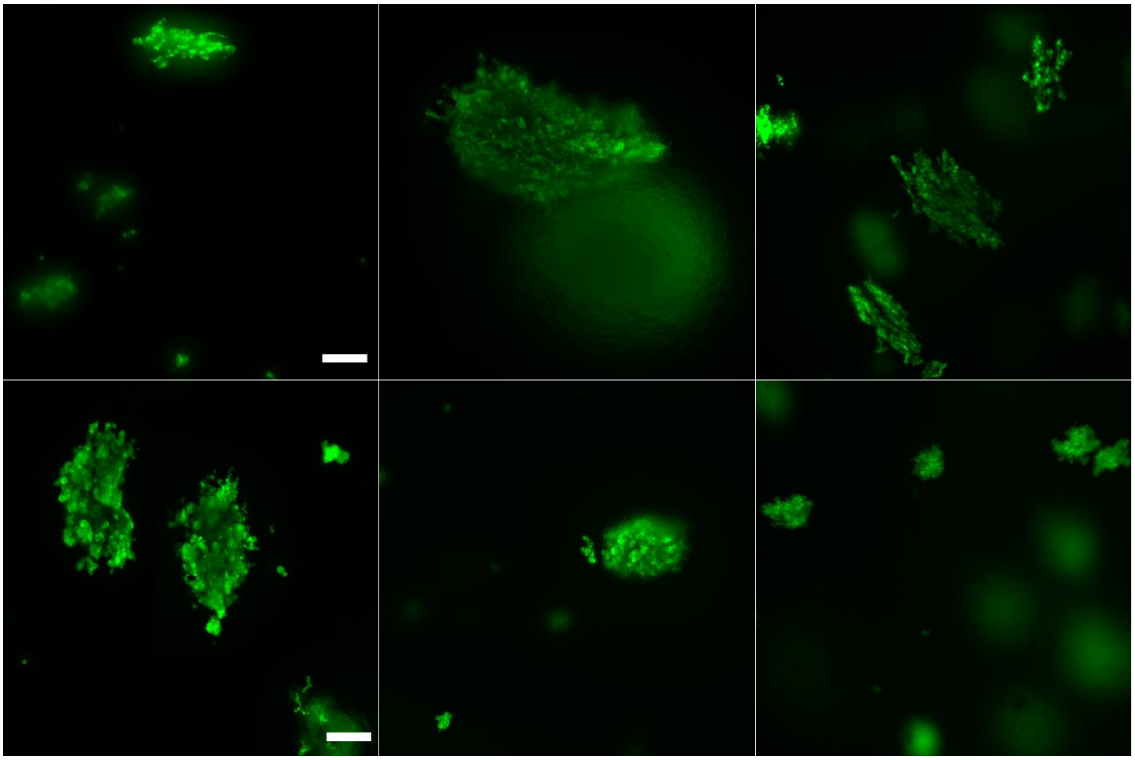

Figure 3-6 *Morphology of CRC spheroids from different cell lines 12 days after bioprinting, stained with calceinAM live stain.* ***A*** *LS174T,* ***B*** *LOVO,* ***C*** *SW620,* ***D*** *SW480,* ***E*** *HCT116,* ***F*** *SW1463 scale bar = 200μm*

dissolving alginate powder into warmed gelatin solution using the DAC, then mixing the F127 component and CRC cells as before. A range of gelatin concentrations from 0.5%(w/v) – 5%(w/v) was added to the bioink and the viability was measured. Here, it was found that the day 1 viability of SW620 cells remained unchanged with the addition of gelatin to bioink (**Figure 3-7**, **A**). Because a small, increase in viability was recorded for the 3%(w/v) gelatin addition, 3% gelatin was added to the bioink and SW620 cells were cultured over 14 days. Interestingly, when left in culture, more colonies were observed in the 3% gelatin gel than the unaltered bioink (**Figure 3-7**, **C,D**). The average size of these colonies was the same as colonies grown in the unaltered bioink. As such, the addition of gelatin did have an impact on 3D cultures of SW620 cells, which was observed in longer cultures. This result suggests that viability in the unaltered bioink may be decreasing beyond 24 hrs relative to the gelatin-bioink, resulting in more colonies forming in the gelatin-bioink over time.

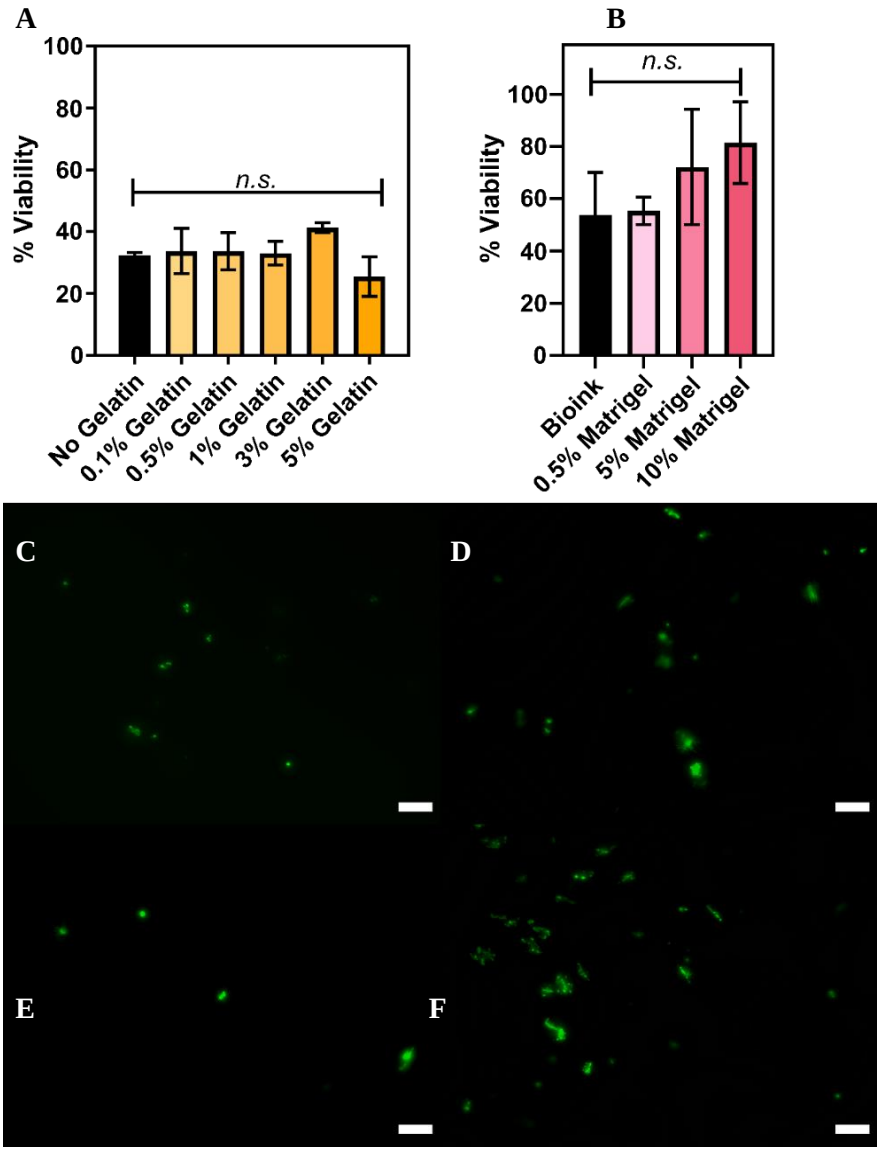

Figure 3-7 *Viability and colony count with different Matrigel/gelatin conditions.* ***A, B*** *SW620 cell viability in the Alginate-F127 bioink supplemented with gelatin (**A**) or Matrigel (**B**).* ***C,D*** *SW620 colonies 5 days after printing in either the unaltered Alginate-F127 bioink (**C**) or with 3%(w/v) gelatin (**D**).* ***E,F*** *SW620 colonies 5 days after printing in either the unaltered Alginate-F127 bioink (**E**) or with 10%(v/v) Matrigel (**F**). Scale bar = 200μm*

3.3.2.8 Addition of Matrigel

Matrigel was added to the alginate-F127 bioink to test whether the viability and morphology of SW620 cells in Matrigel could be mimicked by simply supplementing the bioink with small volumes of Matrigel (0.5%(v/v) – 10%(v/v)). Viability appeared to increase with the addition of Matrigel; however, it was not statistically significant (**Figure 3-7**, **B**). Here, the large variability

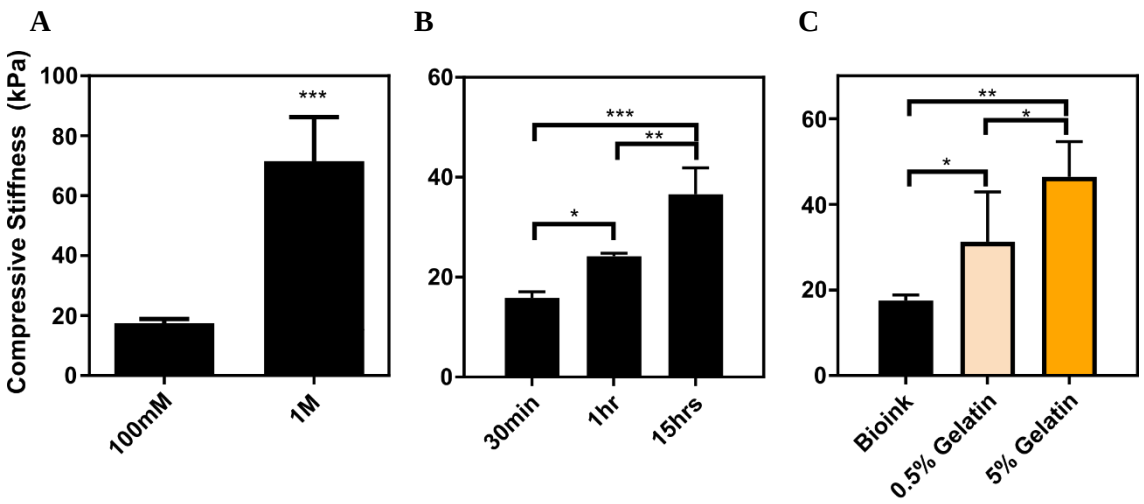

Figure 3-8 *Compressive stiffnesses of different bioinks, measured by unconfined compression testing.* ***A*** *Stiffness of the alginate-F127 bioink, measured after crosslinking in 100mM and 1M $CaCl_2$ for 30 minutes. ***p<0.001 using a student's t-test.* ***B*** *Stiffness of the alginate-F127 bioink, measured after crosslinking with 100mM $CaCl_2$ for 30 minutes, 1 hour and 15 hours.* ***C*** *Stiffnesses measured after crosslinking with 100mM $CaCl_2$ for 30 minutes in the alginate-F127 bioink supplemented with 0.5%(w/v) and 5%(w/v) gelatin. *p<0.05,**p<0.01 for one-way ANOVA with Tukey's multiple comparison post hoc test (**B-C**)*

in viability is likely due to poor mixing of the Matrigel into the alginate-F127 bioink. Matrigel is only liquid at temperatures of 0-4°C, above which it gelates thermally. Mixing Matrigel into the bioink with the DAC is a process which produces excess heat, gelling the Matrigel before it is mixed thoroughly, and forming regions of Matrigel within the final bioink structure causing varied cell viability. 10% Matrigel addition resulted in the highest viability of SW620 cells in 3D and was therefore used for longer cultures. Similar to gelatin addition, more colonies were visible where Matrigel was added (**Figure 3-7**, **E,F**). Together with the gelatin results, these data suggest that initial cell viability, long-term colony formation and morphology are indeed separate parameters which can be altered independently of one another. Specifically, the addition of ECM components to the alginate-F127 bioink did not produce significant increases in early viability, however, did result in more colonies forming over time.

3.3.2.9 Compression testing

To further unpack the differences in cellular viability and growth between Matrigel and the alginate-F127 bioink variants, mechanical properties were experimentally determined and compared. Tissue stiffnesses in the body vary by origin and disease pathology, for instance, the stiffness of bone has been reported to be between 15-20GPa[208,209], whereas the stiffness of healthy

and inflamed intestinal tissue has been reported as 2.6kPa and 16.7kPa, repectively[210]. More specifically to CRC, colorectal tumours also have higher reported stiffnesses than surrounding healthy tissue[71,211], which is thought to arise due to higher ECM concentrations in the tumour structure[212].

Matrigel, which gels thermally, can be stiffness-tuned only via alterations in protein density[213] and therefore has a standard stiffness of 450Pa, as measured by atomic force microscopy[132]. Alginate gels, however, can be stiffness-tuned through changing alginate concentration, crosslinker formulation, crosslinker concentration or crosslinking time[123,158]. The compressive stiffness of the alginate-F127 gel was measured under standard crosslinking conditions and with increased crosslinker concentration. As hydrogels have a complex stress-strain curve, stiffness values were reported simply as slope of the linear fit to the first 10% of the curve.

Compressive stiffness of the alginate-F127 bioink was 17.6kPa and 71.5kPa for normal (100mM) crosslinking and increased (1M) crosslinking concentrations (**Figure 3-8**, **A**). Stiffness also increased with increasing crosslinking time, demonstrating the variability of gel stiffness with different crosslinking conditions(**Figure 3-8**, **B**). Importantly, the stiffness of the standard alginate-F127 bioink used was more than 6-fold higher than the stiffness of healthy intestinal tissue. Moreover, addition of gelatin further increased stiffness, with stiffness rising at higher gelatin concentrations (**Figure 3-8, C**).

Collectively, these data make it clear that stiffnesses of bioinks used were far higher than relevant stiffnesses *in vivo*. As such, high matrix stiffness could be responsible for reducing cell viability and influencing CRC colony growth and morphology.

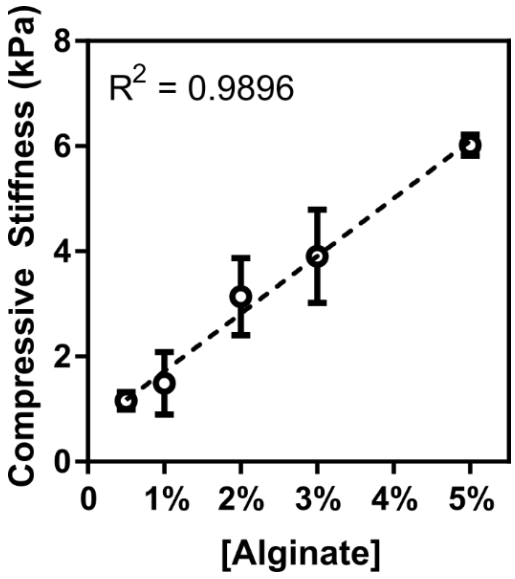

Figure 3-9 *Compressive stiffness of gelatin-alginate hydrogels. The concentration (w/v) of alginate was varied and the concentration of gelatin was kept constant at 10% (w/v). Crosslinking was performed as standard by immersion with 100mM $CaCl_2$ for 15 minutes. Stiffness was measured in each condition with unconfined compression testing, and linear regression performed in GraphPad Prism.*

3.3.3 Alginate-Gelatin Bioinks

3.3.3.1 Gel preparation and varying alginate concentration

As experimental data revealed the high stiffnesses of the bioinks used in the preceeding sections, and the positive impact of gelatin on colony formation, a new bioink formulation of gelatin and alginate was tested. Here, the bulk of the hydrogel was comprised of gelatin, and with a small amount of alginate. A 10%(w/v) gelatin solution was kept constant as the gel base, into which alginate powder was mixed using the DAC, where the alginate concentration was systematically varied from 0.5%(w/v)-5%(w/v). Due to the thermal properties of this hydrogel, a new mixing and printing protocol was designed around the BioX bioprinter, which is fully temperature controlled. For this gel, alginate powder was mixed with prewarmed gelatin solution, then a cell suspension was optionally added. The bioink was cooled in the fridge for 3-5minutes, then printed in a cool room onto a chilled print bed (10°C), controlled by the BioX printer (see section **2.4.3**).

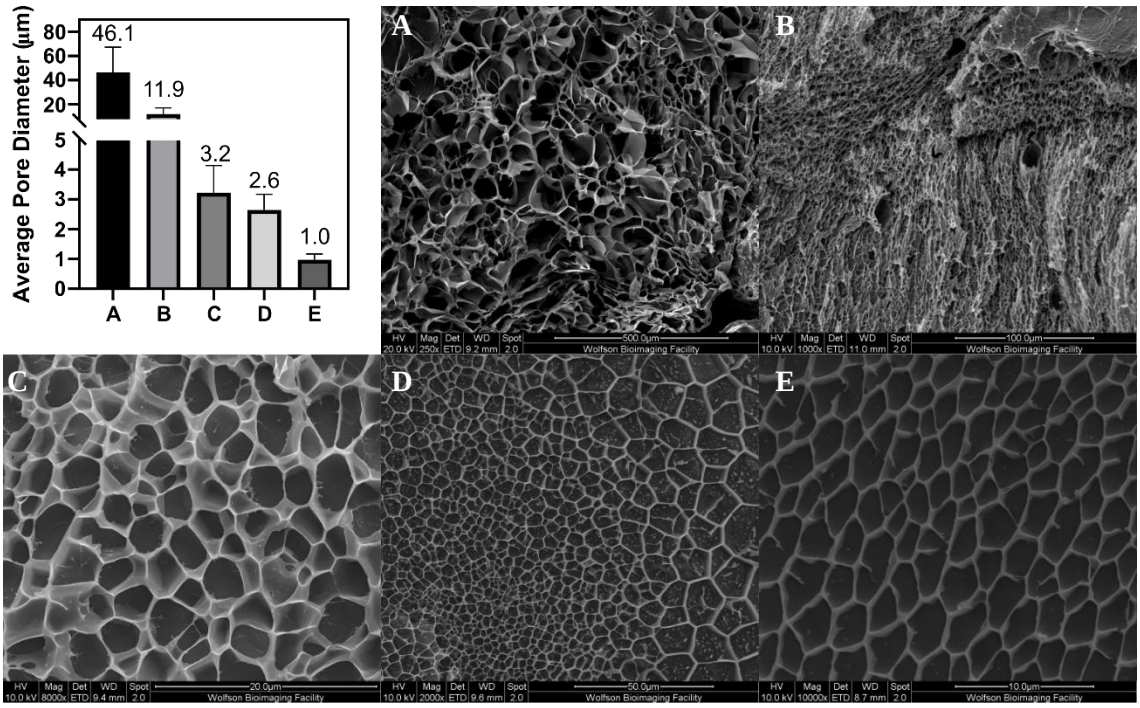

Figure 3-10 *Electron micrographs of 10% gelatin 1% alginate gels under different conditions.* ***A*** *Freeze-dried gels were sputter coated then imaged with SEM.* ***B*** *Liquid nitrogen plunging immediately prior to freeze-drying, prepared and imaged identically to* ***A****.* ***C*** *CryoSEM using liquid nitrogen as the cryogen and a 3-minute sublimation time.* ***D****, CryoSEM imaging identically to* ***C****, with a 1-hour sublimation time.* ***E*** *CryoSEM imaging identically to* ***C****, with liquid ethane used as the cryogen.*

3.3.3.2 Compression testing of different alginate/gelatin blends

The compressive stiffness of alginate-gelatin bioinks was found to be significantly lower than the alginate-F127 bioink, ranging from 1.1-6.0kPa, and therefore more similar to *in vivo* stiffnesses of intestinal tissue (**Figure 3-9**). A linear trend was observed between alginate concentration and compressive stiffness, with each 1%(w/v) alginate addition resulting in a stiffness increase of ~1.1kPa. Consequently, this bioink formulation has a highly predictive and therefore easily tuned compressive stiffness.

When compared to the alginate-F127 bioink, compressive stiffness is predicted to be lower, even at identical alginate concentrations (6.5% w/v), suggesting that final gel structures of these two gel types is significantly different, despite compositional similarities. To investigate such structures, and electron microscopy protocol for imaging hydrogel structures was developed.

3.3.3.3 Electron Microscopy of hydrogels

To evaluate how internal gel structure was changing between bioink formulations, samples were prepared and imaged with electron microscopy (EM). Here, the challenge in revealing gel structures is in successfully dehydrating samples such that the "true" gel structure is not significantly altered. As such, before proceeding with a given EM protocol, different EM techniques were evaluated by comparing the structure of a 1% alginate, 10% gelatin gel (**1A10G**) for each EM protocol.

Freeze-drying is a method where samples are rapidly frozen and exposed to vacuum conditions, resulting in a steady sublimation of vitrified water, and therefore uncovering a dehydrated gel structure which can be heavy metal coated. In the literature, freeze drying is used extensively to show hydrogel structures, with samples simply being exposed to both vacuum and low temperature simultaneously[214–216], before fracturing the sample then sputter coating fracture plane and imaging with scanning electron microscopy (SEM). 1A10G gel was freeze dried and sputter coated with gold-palladium before imaging with SEM. It was observed that exposing samples to vacuum rapidly caused large and immediate shrinkage of the gel samples, which would likely lead to changes in the imaged structures. As such, vacuum exposure was performed as gently as possible, and the freeze-drying performed over 5 days. The imaged structures closely resembled those in the literature of other alginate and alginate-gelatin hydrogels, with large pores (46.1μm±21.1μm) present in the gel (**Figure 3-10**, **A**). Notably, the imaged pore size was on average ~4 times smaller (11.9μm±5.0μm) in samples which were plunged into liquid nitrogen immediately before freeze-drying (**Figure 3-10**, **B**). This suggests that the final pore-size is dependant on the freezing rate of the sample, which is relatively slow and difficult to control with conventional freeze drying.

The observation that cooling rate influences the structure of alginate hydrogels has been explored in depth by Aston *et al*[177] who remark that many published works report inaccurate hydrogel structures because the cooling rate was not rigorously controlled. Specifically, slow cooling results in the formation of large ice crystals which alter gel structure, known as eutectic artefacts.

To minimise the impact of such artefacts, cooling rate should therefore be as fast as possible to reduce ice crystal size to below the expected size of structural features, such as pore networks.

CryoSEM was used as the EM imaging technique for finer control over cooling rate and sublimation conditions. In this approach, samples are vitrified, sublimed, fractured and sputter coated *in situ* under controlled conditions, unlike the freeze-drying approach where samples must be fractured then moved to the sputter coater in atmospheric conditions, causing some re-hydration of the sample. Moreover, cooling rate can be altered by varying cryogen, and sublimation times can also be varied.

1A10G gels were imaged with cryoSEM, using liquid nitrogen and liquid ethane as the cryogen, and 3 minutes and 1 hour as the sublimation time(**Figure 3-10**). Here, a regular pore structure was revealed with smaller measured pore sizes than freeze-dried gels, varying between 1.0-3.2μm. Moreover, pore size was the smallest when liquid ethane was used as the cryogen over liquid nitrogen slurry (LNS), although this comparison was not statistically significant. This suggests that the cooling rate of LNS may be insufficient for hydrogels and the perceived pore structure of these gels could arise entirely from eutectic artefacts. Increasing sublimation time led to a small decrease in pore size (3.2μm±0.9μm vs 2.6μm±0.5μm), which was also not statistically significant (**Figure 3-10**, **A**).

To determine the impact of eutectic artefacts, and to better understand the impact of the gelatin gel component, an alginate-only gel was compared to the alginate-gelatin gels. The simpler gel structure of alginate should not contain large pores as there is no porous component to gel akin to the F127 sacrificial element in the alginate-F127 gel. Moreover, the pore size of alginate hydrogels has been reported as far less than 1μm but varies by gel composition and crosslinking method[176,177]. Without the addition of gelatin, alginate gels were observed to have very fine microstructures with pore size being in the order of hundreds of nm across (**Figure 3-11**, **A**). This data is therefore consistent with literature values, although these gels are typically not produced in the same way. For instance, Aston *et al* use dehydrated alginate films in their imaging

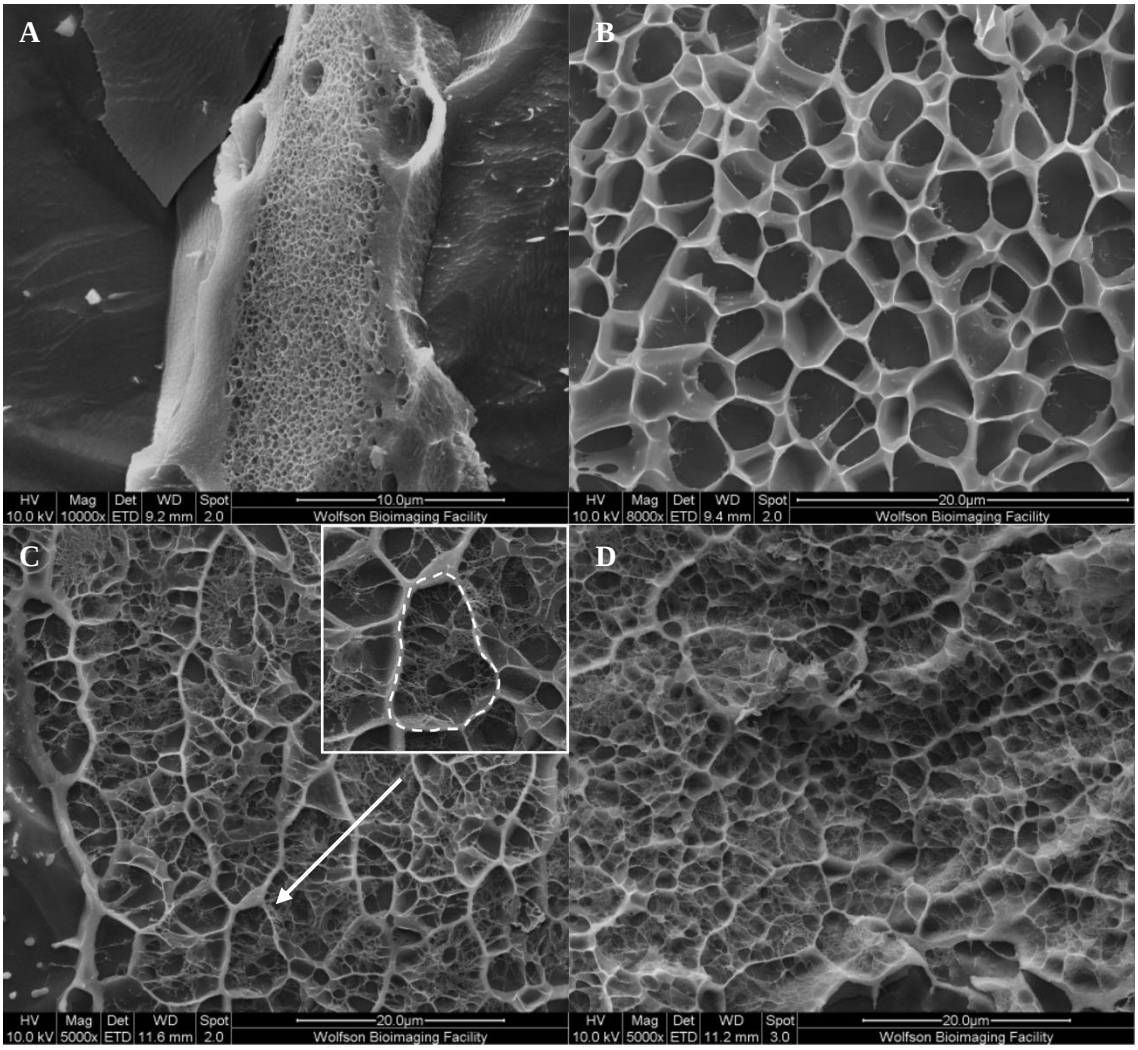

Figure 3-11 *CryoSEM of different hydrogels, using liquid nitrogen slurry as the cryogen and using a 3-minute sublimation time.* ***A*** *1%(W/v) alginate gel.* ***B*** *1% Alginate, 10% Gelatin gel.* ***C*** *3% Alginate, 10% Gelatin gel.* ***D*** *5% Alginate, 10% Gelatin gel.*

protocols[177]. As such, although cooling rate may impact pore size to some extent, it is likely that the porous nature of the 1A10G gel is genuine.

Increasing the alginate content in the alginate-gelatin gels yielded interesting results. The clear pore-structure of the 1A10G gel (**Figure 3-11**, **B**) deteriorated with increasing alginate content and gave rise instead to porous meshes (**Figure 3-11**, **C**, **D**). Here, there is some evidence of large macro-pores which are infilled with a fine mesh in the 3A10G condition (**Figure 3-11**, **C**, Inset), which become smaller and less apparent in the 5A10G condition.

The gelatin gel component is independently a liquid at 37°C, the temperature at which these gels were maintained before imaging. To test if the gelatin component also liquified in the 1A10G gel,

A 1A10G gel was prepared with fluorescent, FITC-conjugated gelatin and imaged for 12 hours, in which time it was observed that the gelatin slowly dissolved into solution (Appendix **A**). Collectively, these data suggest that the gelatin component of the bioink takes the role of a fugitive bioink component, supporting the crosslinking of the alginate, then dissolving into solution and leaving behind a porous alginate architecture. The porosity of this matrix decreases with increasing alginate concentration, with alginate infilling the inter-pore spaces. This in turn increases the mechanical strength, with the inter-pore alginate structurally supporting the larger porous mesh and resulting in higher compressive stiffnesses.

3.3.3.4 SW620 viability and growth

Having characterized the compressive stiffness and internal structure of the gelatin-alginate bioink, the viability and colony formation of SW620 cells was tested as with the alginate-F127 bioink. 10^5 cells were blended into different alginate-gelatin bioinks and the viability measured 24 hours after bioprinting. The same three alginate-gelatin gels were used as examined by EM: 1A10G, 3A10G and 5A10G. Here, the 10% gelatin 1% alginate gel (10G1A) produced the highest initial viability, with viability decreasing in the 10G3A and 10G5A gels (**Figure 3-12**, **A,C**). More importantly, the long-term culture of SW620 cells gave rise to dramatically fewer colonies in the 3A10G and 5A10G conditions 5 days after printing (**Figure 3-12**, **B,C**). As such, it appears that increasing alginate content in alginate-gelatin gels results in reduced porosity and higher mechanical stiffness which in turn reduces cell viability. Here, it is possible that denser, stiffer gel structures impede cell division and thus result in poor viability at the initial stages of culture, and poorer growth in the longer term. In response to these results, the 1A10G condition was generally used for all future bioprinting. An in-depth characterisation of tumour spheroids grown in this condition is the subject of Chapter 4.

Alongside the mechanical analysis and structural imaging of these gels, these data suggest that matching gel stiffness to *in vivo* stiffness of intestinal tissue is the most significant factor in the viability and growth of SW620 cells. Specifically, the 1A10G gel had the highest cell viability (85%) whilst also being closest in stiffness to the reported stiffness of intestinal tissue (1.5kPa vs

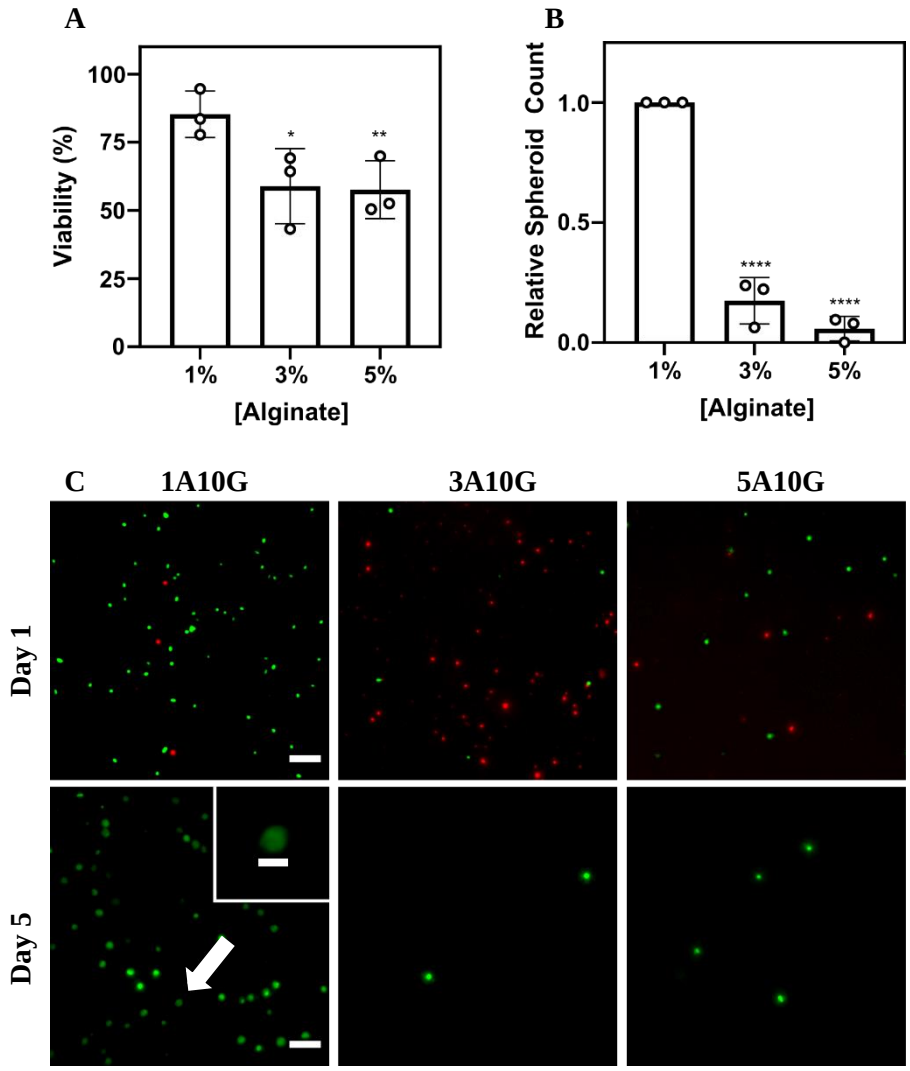

Figure 3-12 *Viability and growth of SW620 cells in different alginate-gelatin bioinks.* ***A*** *Viability as measured by live/dead (calceinAM/Ethidium Homodimer III) staining 24 hours after bioprinting.* ***B*** *Relative tumour spheroid count 5 days after bioprinting, with average spheroid number compared to the 1% alginate, 10% gelatin condition.* ***C*** *Representative live/dead images of SW620 cells 1 and 5 days after bioprinting. Inset shows an enlarged view a SW620 spheroid. Scale bar is 200μm, inset scale bar is 50μm.. $^{*}p<0.05$, $^{**}p<0.01$, $^{***}p<0.001$, $^{****}p<0.0001$ for one-way ANOVA with Tukey's multiple comparison post-hoc test, comparing between differences between groups and the 1A10G control*

2.6kPa). Moreover, the measured stiffness of alginate-F127 gels were on average 17.6kPa or more, ~6.8-fold higher than *in vivo* conditions, and here the viability of SW620 cells was very low (32%, **Figure 3-2**, **D**). Interestingly, viability in Matrigel was high (94% **Figure 3-2**, **D**) despite being ~5.8-fold less stiff than *in vivo* conditions. This suggests that increasing stiffness beyond *in vivo* conditions is more detrimental to cell viability than lower stiffnesses. However, there is some uncertainty around the true stiffness of intestinal tissue, and it may be lower than

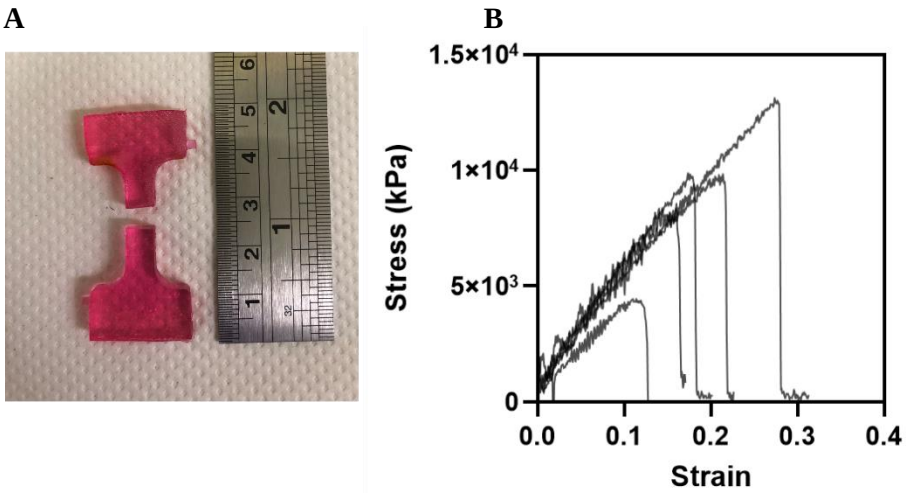

Figure 3-13 *Tensile testing of 1% alginate, 10% gelatin bioink.* ***A*** *Example specimen removed from the testing rig after failure.* ***B*** *Example stress-strain curves from the samples shown in* ***A***

Parameter	***Mean Value ± Standard Deviation***
Elastic Modulus, E (kPa)	46.7 ± 5.5
Failure Strain, ε_F (%)	19.6 ± 5.9
Failure Stress, σ_F (kPa)	9.3 ± 3.2

Table 3-1 *Calculated parameters from the linear regions of the stress-strain curves shown in* ***Figure 3-13****. Data shown is mean ± s.d.*

the 2.6kPa value reported by Johnson *et al*[210]. For instance, Stewart *et al.*[217] report the stiffness of human ileum, the terminal region of the small intestine, as 0.64±0.34kPa. The differences between these values may result from approach used: Johnson *et al.* use conventional unconfined compression testing, whereas Stewart *et al* use nanoindentation.

The 2.6kPa value from Johnson *et al* has been listed here most frequently because the method used is the same as in this work. In the case of Matrigel, the true stiffness is also unclear, with the 0.45kPa value being reported from Soofi *et al.*[132], who used atomic force microscopy (AFM) for this calculation, which is different in approach to both unconfined compression testing and nanoindentation. Consequently, it is difficult to say how similar the stiffness of Matrigel is intestinal tissue.

3.3.3.5 Tensile testing of the 1A10G bioink

Having selected the 1A10G bioink for further use with bioprinted tumour spheroid assays, additional mechanical testing was undertaken. First, tensile testing of the 1A10G gel was performed using bioink specimens cast into porous 3D printed moulds, similarly to compression testing. The mould design and experimental setup is described in section **2.7.2** and an example specimen shown after failure in **Figure 3-13**, **A**.

Linear force-extension and stress-strain behaviour was observed for all samples, with a small plastic region before failure (**Figure 3-13**, **B**). The modulus of elasticity was calculated from the linear regions and averaged 46.7kPa (**Table 3-1**). Most samples failed around 20% strain, under a mean failure stress of 9.3kPa. These results can be compared to the compression behaviour of this gel sample, which was calculated earlier (**3.3.2.9**Compression testing), revealing that the modulus of elasticity is roughly 30-fold higher than the compressive stiffness (46.7kPa vs 1.5kPa).

Physiologically, the tensile behaviour of whole bowel sections has been characterized. Ergorov *et al*[218] measured mechanical properties of human cadaveric sections of oesophagus, stomach, small and large intestine. The failure strain, ε_F , of human bowel sections ranged from 138.9%-205.5% and the failure stresses, σ_F, ranged from 0.533MPa-0.920MPa. Ergorov *et al* do not report values for the elastic modulus, E, however, it can be estimated to be roughly ~2.5MPa from the data provided. This data is supported by the work of Christensen *et al*[219] who calculated ε_F to be from 62.8%-113.2%, σ_F to be from 0.58MPa-0.87MPa and E to be from 1.83MPa-5.18MPa. The variance in ε_F between these two works arises from differences in how the point of failure is determined: Ergorov *et al* use the point at which $\sigma = 0$ whereas Christensen *et al* use the point at which $\sigma = max$.

Comparing these literature values to the experimental data for 1A10G gels shows significant differences in ε_F, σ_F and E. These differences are due to specimen selection. Both Christensen *et al* and Ergorov *et al* use whole-gut specimens which are hybrid materials, containing layers of

different cell types and ECM components. In particular, the muscularis of the gut is thought to provide much of the mechanical strength, whereas the submucosa is thought to provide much of the elasticity[220]. This hybrid material property is evident in the bimodal form of the stress- strain curve of whole-gut specimens, whereby the muscular layer fails first, typically at σ_{MAX}, followed by a period of considerable elongation before a second peak and subsequent failure.

In this work, the bioinks used are primarily designed to replicate the mucosa, or inner-most layer of the gut, as this is the region where CRC tumours grow. As such, it is not appropriate to compare whole-gut specimens to the bioinks outlined in this work. Unfortunately, there exists an absence of data in the literature of the elastic properties of the mucosa region specifically. This is possibly due to difficulty in precisely sectioning the mucosa and testing it independently. Alternatively, as the mucosa is known to have poor mechanical properties[219], it is likely challenging to test through conventional tensile testing, where samples must support their own self-weight under gravity.

Although the results of tensile testing cannot be directly compared to literature values using whole-gut specimens, some observations can be made. First, whole gut specimens are stiffer in tension than compression, with a higher elastic modulus and a lower compressive stiffness. This trend is mimicked by the 1A10G bioink, for which the elastic modulus is some 30-fold higher. Second, the failure strain of the 1A10G bioink, 19.6%, may be sufficient for common axial strains experienced in the gut, which have been proposed to be in the region of 20%[221,222], although further mechanical testing would be required as strain in the bowel is 3-dimensional, with some regions in tension and the others in compression.

3.3.3.6 Bioprinting

Accurate bioprinting requires the bioink to be shear-thinning, such that upon extrusion the bioink flows evenly and deposited accurately. The alginate-F127 bioink has already been characterized with rheology by Armstrong *et al* and is known to be shear thinning. The 1A10G bioink, which gave the best results with SW620 cell culture, was characterized by rheometry to determine if it was shear thinning. Here, the 1A10G bioink was found to have shear thinning behaviour, with viscosity decreasing exponentially with applied shear (**Figure 3-14**, **A**). The flow index was

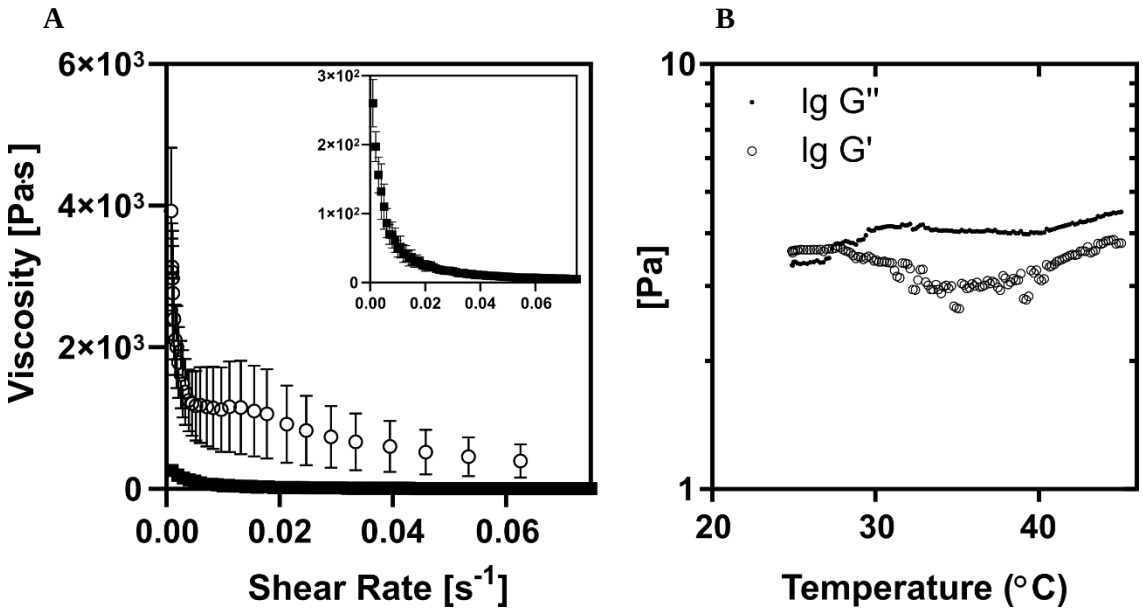

Figure 3-14 *Rheology of alginate-f127 and alginate-gelatin bioinks.* ***A*** *Viscosity-response to applied shear. Open circles = alginate-f127 bioink, closed squares = 1% alginate, 10% gelatin bioink (1A10G). Inset shows an enlarged region of the graph at lower viscosities.* ***B*** *Temperature sweep of the 1A10G bioink, showing the storage (G') and loss (G'') moduli behaviour at different temperatures. The crossover point of G' and G'' is used to determine the melting temperature,* T_m.

calculated from this curve using the Ostwald–de Waele relationship (Section **2.7.3**) and determined to be 0.078±0.022, with the uncertainty representing the standard error of the linear regression. This value is far below 1 and therefore exhibited shear-thinning behaviour.

The shear thinning behaviour of this hydrogel was expected, as alginate gels[158], gelatin gels[223] and alginate-gelatin[224] gels have been used in the literature and reported to have shear-thinning behaviour. Indeed, the initial selection of alginate-gelatin gels for screening was informed by these reports.

As the 1A10G gel contains a gelatin component, it is a temperature sensitive gel. The melting point, T_m , was calculated by rheology. The storage and loss modulus, G' and G'', respectively, were plotted as a function of temperature (**Figure 3-14**, **B**) and the crossover point, where viscous behaviour starts to dominate elastic behaviour, used to calculate T_m. The value of T_m was determined to be between 27.3°C-27.5°C, indicating that this gel is suitable for use at room temperature, providing it is not heated further. However, the bioprinter itself emits heat as it

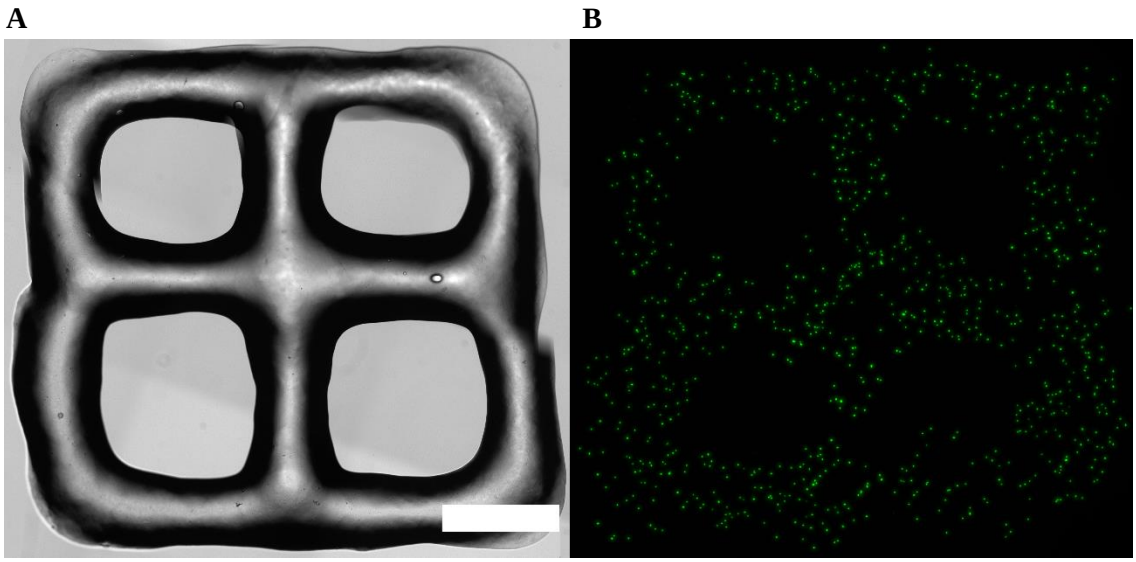

Figure 3-15 *Bioprinted shapes with the 1% alginate, 10% gelatin bioink.* ***A*** *Brightfield image of an acellular bioprint.* ***B*** *Live stain (calceinAM) of SW620 cells inside a cell-laden bioprint. Scale bar =2mm.*

operates, and therefore the room was cooled and the print bed chilled to prevent bioprinted samples from melting.

Due to the shear-thinning behaviour of this bioink, and by controlling printing temperatures, the printing properties of this bioink were acceptable, with small feature sizes (~1mm) being printed successfully (**Figure 3-15 A,B**). Critically, the rapid, "droplet printing" function of the BioX was compatible with this bioink. Here, a set volume is rapidly extruded into each well of a 96 well plate, with all 96 wells being printed in around 3 minutes. Consequently, the bioink physical properties were robust, with limited trailing, dripping or blockages during printing.

3.3.3.7 Optical properties

As many 3D assays require the use of imaging to elucidate the structure of 3D colonies, or to otherwise measure response in 3D, optical properties of bioinks are important. One advantage of the 1A10G bioink over the original alginate-F127 bioink is the increase in transparency. Spheroids were clearly visible under both brightfield and fluorescent staining conditions, with lower signal-to-noise ratios of fluorescent stains (**Figure 3-16**). The favourable optical properties

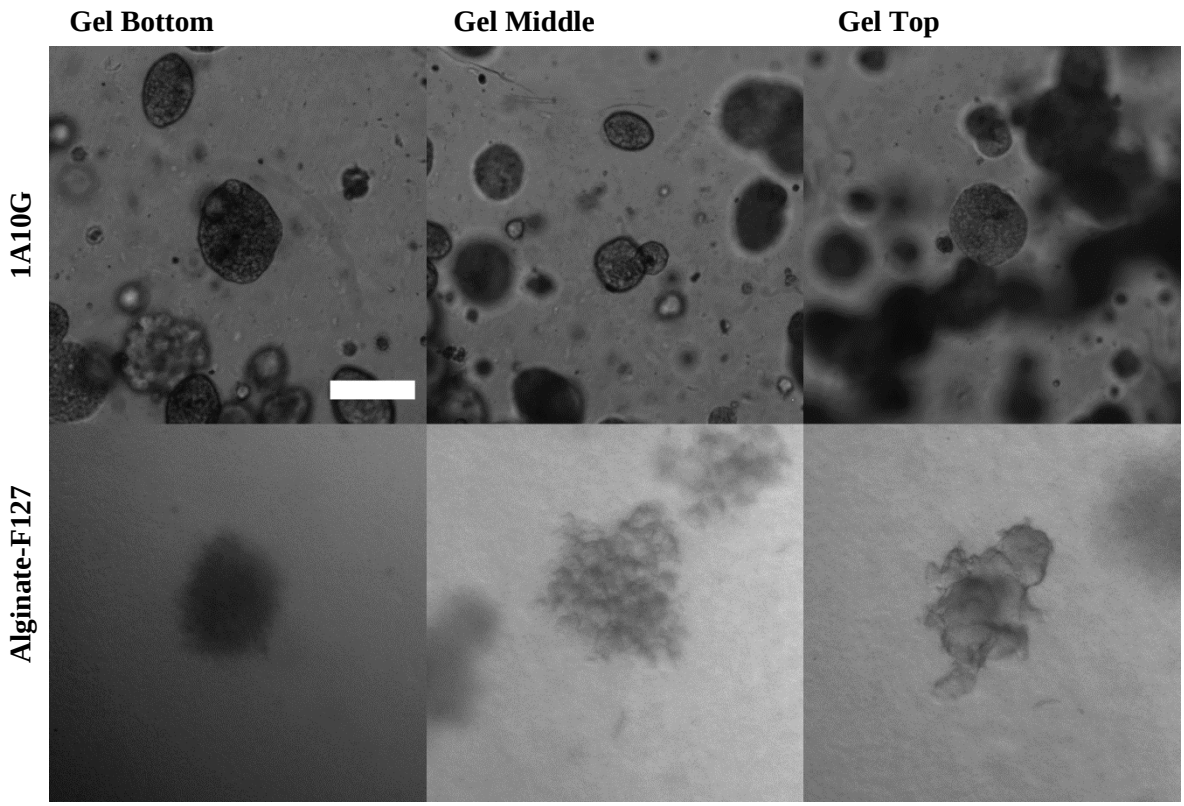

Figure 3-16 *Brightfield images of SW620 colonies grown in the 1% alginate 10% gelatin bioink, compared with colonies grown in the alginate-F127 bioink. Spheroids were selected from different z-planes in the bioinks, from either the top, middle or bottom of the bioprinted gel. Scale bar =200μm.*

of the 1A10G gel enabled the rapid bioprinting protocol ("droplet printing") to be later combined with high throughput imaging to perform analysis on spheroid populations.

3.4 Conclusions and Discussion

The basis of this work was the study by Armstrong *et al* who developed and characterized the alginate-F127 bioink and used it successfully to culture and differentiate hMSCs as a model for cartilage repair. However, applying this approach to human colorectal cancer cells was challenging, as it was found that cell viability was low in all cancer lines tested. A systematic review of the culture conditions was performed, and various factors were considered, using SW620 as a model cell line. At first, the low viability of SW620 cells was thought to be due to aspects of the bioink preparation or printing process. Here, the centrifugation step with the DAC

and printing forces applied by the extrusion printing method were ruled out as negatively affecting cell viability. Then, other cell lines were tested and performed similarly, reaffirming that low cell viability was present with all cell lines and was not unique to SW620 cells.

From this, the composition of the alginate-F127 bioink was altered to include ECM components. Both gelatin and Matrigel, in which cell viability is high, were added to the bioink. Here, cell viability did not increase significantly, but colony-formation of SW620 cells in the long-term was improved. As mechanical properties, as well as chemical or biochemical properties of hydrogels can change cell viability, mechanical testing on the alginate-F127 gels was performed. The compressive stiffness of all gels was compared to literature values for human intestinal tissue and found to be significantly higher. Moreover, any supplementation of the gel with gelatin only drove the stiffness higher. As such, it was determined that the biocompatibility of the alginate-F127 was unlikely to improve through simple supplementation with other factors. Another gel formulation was required with lower compressive stiffnesses, closer to *in vivo* conditions, but was also bio-printable and biocompatible.

The positive impact of gelatin on colony-formation led to the use of gelatin as the base of the new bioink formulations. The use of gelatin or alginate-gelatin bioinks is widely reported[122,124,163,225], although none have been reported for tumour-spheroid formation of these cell lines. As such, the new bioink formulations were generated by varying alginate concentration in a 10%(w/v) gelatin gel. Critically, mechanical testing revealed these gels to have predictable compressive stiffnesses simply by varying alginate concentration, and to have similar mechanical properties to *in vivo* intestinal tissue. Three different alginate-gelatin blends were selected and tested by measuring the response of resident SW620 cells.

Interestingly, a sharp decline in viability and colony formation was observed at higher stiffness alginate-gelatin gels, corresponding to increased alginate concentration. These data support the hypothesis that cell viability in the original, alginate-F127 gel was low due to high stiffnesses. To understand this phenomenon further, a protocol was systematically developed for imaging the internal structure of these bioinks with electron microscopy. Here, two separate approaches were

used: Freeze-drying, both with and without liquid nitrogen (LN) plunging, was compared to cryoSEM procedures in which sublimation time and cryogen were varied. The resulting structures clearly indicate that "true" structures of hydrogels are very challenging to image, as removal of water from the sample can result in artefacts. Freeze-drying was difficult to control and produced varied structures, especially when first vitrified with LN. As such, freeze-drying protocols were excluded and cryoSEM protocols investigated further. Some variation in pore-size was observed when cryogen was varied, however, practical limitations of working with liquid ethane were discovered, whereby clean sample fractures were difficult.

A final cryoSEM protocol was selected, and an alginate-only gel used as a control, revealing a very fine mesh, consistent with alginate structures from other rigorous studies in the literature, and was therefore a robust protocol for imaging the structure of the bioinks. Significant variations in structure between different alginate-gelatin gels was observed, with the large, regular porous network of the 1A10G gel becoming denser mesh-networks with increasing alginate concentrations. The degradation of the ordered pore network with increasing alginate corresponded with stiffer gels and reduced cell viability and colony count. This result indicates that cancer cell lines prefer a deformable environment which is pliable for spheroid formation, whereby the gel structure readily yields to forces applied from growing spheroids. This conclusion is echoed by both Cheng *et al.*[226] and Helmlinger *et al.*[227], who observed higher stiffness agarose gels impeded the growth of colorectal spheroids.

From the experimental data, the 1A10G bioink was selected and tested further. This bioink was found to be shear-thinning and stiffer in tension than compression, a known property of the human intestine. A printing protocol was designed for this bioink which used the temperature-controlled print bed of the BioX to maintain the gel structure and print small features. SW620 cells in this gel had the highest viability and formed the most spheroids compared to other gels. Consequently, the 1A10G bioink developed here was carried forward and used for all later experiments detailed in Chapter 4 and Chapter 5.

3.5 Acknowledgement of Collaboration

Work in this chapter was completed by the author unless otherwise mentioned here. The author would like to thank Prof. Ann Williams for generously providing all colorectal cancer cell lines used and Dr. Bethany Hickton for performing rheometry. The author would also like to thank Dr. Judith Mantel, who performed all the EM imaging, with samples prepared by the author.

Chapter 4： Characteristic Features of Grown Tumour Spheroids

4.1 Introduction

To develop physiologically relevant *in vitro* tumour models, characteristic features of the *in vivo* tumour microenvironment (TME) should be recapitulated. These features include cell-cell interactions between different cell types, cell-ECM interactions *via* cell adhesion molecules, cell-matrix interactions *via* mechanotransduction and gradients of pH, nutrients and oxygen.

Of the different facets of the TME, reduced oxygen availability is of particular importance due its known inhibition of both chemotherapy and radiotherapy. Malignant tumours *in vivo* often develop regions of hypoxia, a lower, non-physiological level of oxygen tension. For healthy bowels, ordinary oxygenation, "physoxia", is difficult to define precisely, as an oxygen gradient exists between the apical mucosa closest to the lumen and the more vascularized submucosa. Tissue oxygen levels in the mucosa are often below 1%[228,229], not only due to poor vascularization but also due to butyrate-producing microbiota, which is oxidized by resident colonocytes of the bowel into carbon dioxide[230,231]. However, oxygen concentration rises sharply away from the apical surface increasing to roughly 6% in the submucosa and 7-10% in the muscularis[232].

Oxygen concentration in colorectal tumours *in vivo* varies with vascularisation of the tumour. Mattern *et al*[233] report the mean oxygen concentration in rectal tumours as 3.38%, dropping to 2.24% in vascular endothelial growth factor (VEGF) negative tumours. Furthermore, there exists an oxygen gradient within tumours themselves, often zoned as normoxic, hypoxic and anoxic regions[234], which in turn correlate with cellular proliferation, quiescence, and necrosis.

Visualizing and measuring hypoxia can be performed with different imaging probes, one of the most widely used being pimonidazole. Pimonidazole is a 2-nitroimidazole-based agent which accumulates in hypoxic cells, binding to macromolecules[235]. The proposed mechanism of this interaction is intracellular enzyme-mediated reduction, terminating with the amino derivative, amino-pimonidazole, which is known to bind to -thiol groups in cytoplasmic proteins[236]. Here, the initial reduction of pimonidazole is reversible with oxygen, as it has a higher electron affinity than the nitro group. Consequently, rate of oxidation and therefore accumulation is dependent on intracellular oxygen concentrations; Specifically, pimonidazole accumulation is reported to begin

around 1.3% oxygen concentration in tumour spheroids[237]. For visualisation of accumulated pimonidazole in tissues, fluorophore-conjugated anti-pimonidazole antibodies were used in conjunction with standard antibody staining protocols.

4.2 Aims

Having developed a robust bioink for tumour spheroid formation in the SW620 CRC cell line, detailed in the previous chapter, the aims of this section is to develop methods to interrogate tumour spheroids, and use them to uncover features of the tumour spheroids grown *in vitro*. Specifically, cell-cell, cell-matrix and nutrient and oxygen gradients will be examined, as these phenomenon are able to be recapitulated in the bioprinted spheroid model. Thorough examination and analysis of these features will enable comparison to known features of *in vivo* tumours, to discuss the physiological relevance of this model.

4.3 Results

4.3.1 Viability, growth, and morphology of colorectal cancer spheroids

The alginate-gelatin bioinks described in Chapter 3 are used here for long-term culture of tumour spheroids for 4 colorectal cell lines (SW620, SW480, CACO2 and LS174T), selected for their availability and reported differences in drug-response[192]. Then, the morphology, growth and structure of grown tumour spheroids were characterized.

4.3.1.1 Stiffness-response of other colorectal cancer lines

Having successfully grown the SW620 cell line, other CRC cell lines were grown in the bioink to determine whether this bioink is more widely applicable to other lines and whether the stiffness-response of SW620 is unique. The gel stiffness assay in section **3.3.3.1** was repeated with 3 other CRC cell lines: LS174T, SW480 and CACO2. These lines were selected because amongst available cell lines, these represent a range of chemotherapy responses to two common

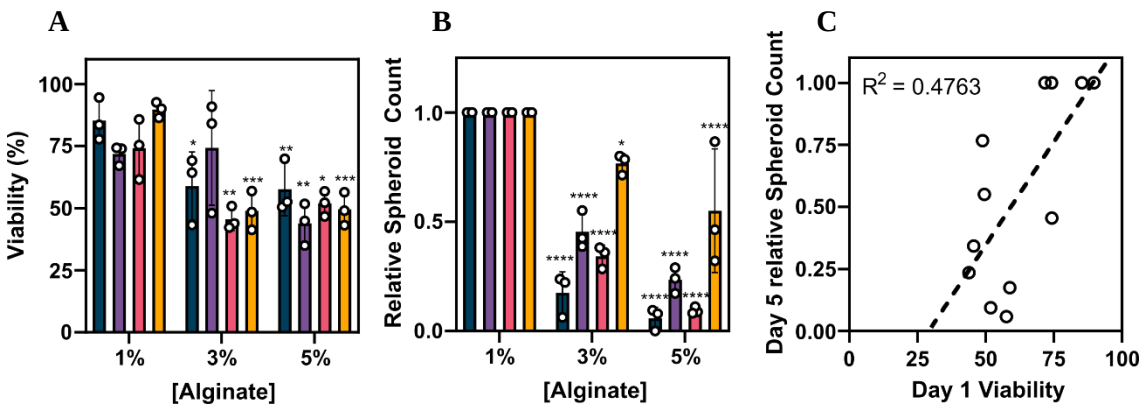

Figure 4-1 *Viability and growth of different colorectal cancer lines in different alginate-gelatin gels.* ***A*** *Viability 24hours after seeding in 1A10G, 3A10G and 5A10G gels.* ***B*** *Spheroid count 5 days after seeding. Spheroid counts are listed as a proportion of the number of spheroids in the 1A10G gel.* ***C*** *Correlation between viability at day 1 and spheroid count at day 5. Different coloured bars represent different cell lines: SW620 (blue), SW480 (purple), LS174T (pink), CACO2 (orange). Statistical analysis was performed with one-way ANOVA and Tukey's multiple comparisons post-hoc test, measuring statistical differences between groups and the 1A10G control.* $^{*}p<0.05$, $^{**}p<0.01$, $^{***}p<0.001$, $^{****}p<0.0001$

anticancer drugs: 5-fluorouracil and Oxaliplatin. The chemotherapy response of these spheroids is described in Chapter 5.

Repeating the gel stiffness assay in section **3.3.3.1** with 3 other colorectal lines showed that the deleterious response to increased stiffness shown in the SW620 cell line was mimicked in these other lines. Both viability and spheroid number decreased in gels of higher stiffnesses (3%Alginate/10%Gelatin {3A10G} and 5%Alginate/10%Ggelatin {5A10G})(**Figure 4-1**, **A,B**). Here, the link between day 1 viability and spheroid number at day 5 is not clear. For example, LS174T and CACO2 in the 3A10G gel have similar viabilities at day 1 (45.6% and 48.9%), but significantly different relative spheroid counts at day 5 (0.34 and 0.77). Mathematically, the correlation between viability and spheroid number is poor ($R^2 = 0.48$, **Figure 4-1**, **C**), indicating that whilst day 1 viability is useful as a rough indicator of colony formation, it is not entirely predictive, with large variation between cell lines. This is significant, as many authors in the literature compare bioink performance using the day 1 viability metric and do not go on to perform longer cultures, whereas these results indicate prolonged culture is necessary to determine bioink suitability[238]. However, in the case of tumour spheroids, reliably facilitating spheroid formation is the primary goal of the 3D culture and appears to be a separate factor to early viability.

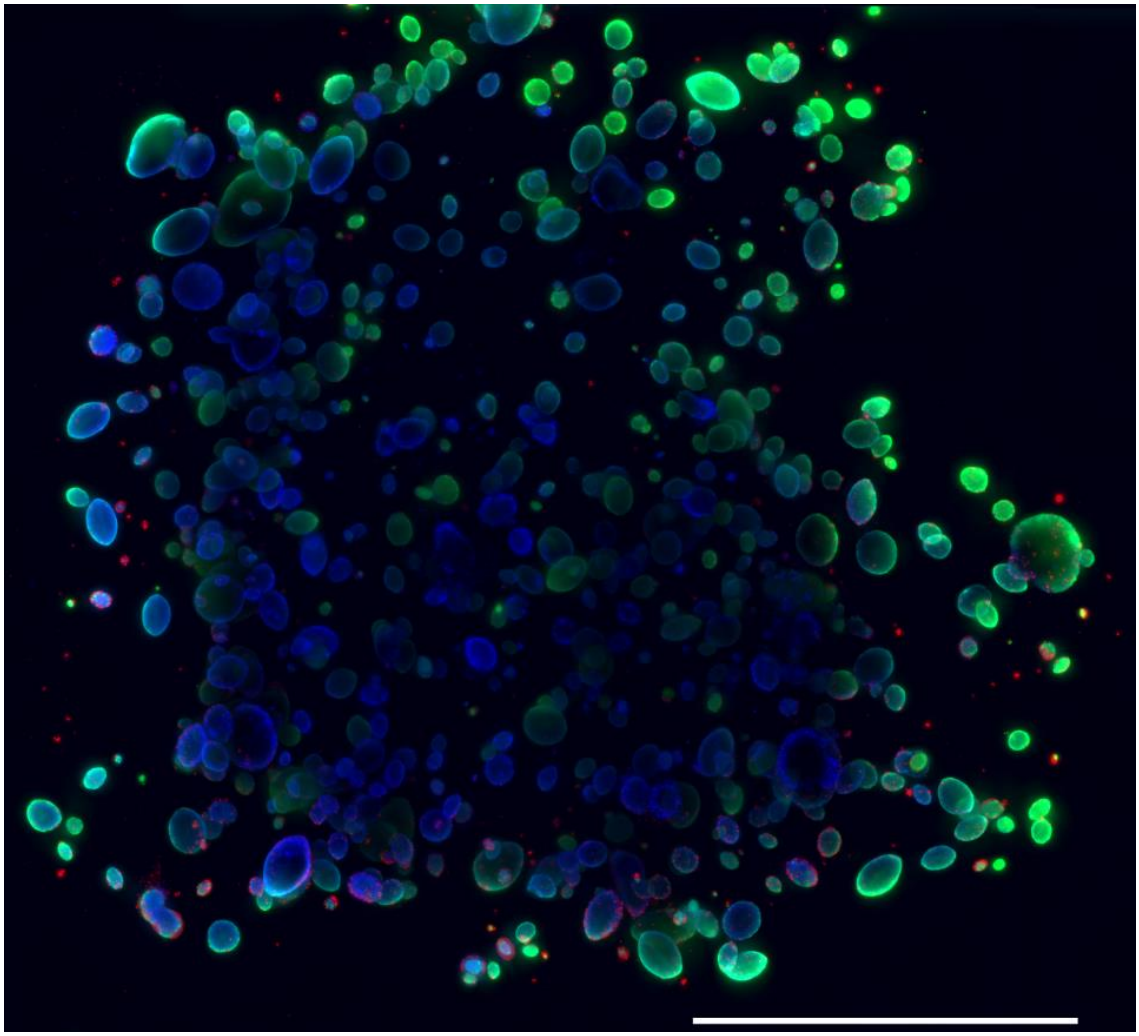

Figure 4-2 *SW620 spheroids 11 days after bioprinting in the 1A10G hydrogel. Blue = nuclear (DAPI), green = live (calceinAM), red = dead (ethidium homodimer III). Scale bar = 2mm.*

As the best performance for all 4 lines was the 1A10G bioink, the 1A10G bioink was carried forward for use with all other cell lines.

4.3.1.2 Morphology of SW620 spheroids

As noted in chapter 3 and shown in **Figure 3-16** and **Figure 3-12**, the 1A10G bioink robustly facilitated dense SW620 spheroid growth with a rounded morphology which was visible 4 days into culture and was maintained throughout the assay until the final timepoint 11 days after bioprinting (**Figure 4-2**). This morphology was compared to the morphology of SW620 colonies in the alginate-F127 bioink at identical timepoints (**Figure 4-3 A-F**). Here, the rounded features of SW620 spheroids in the 1A10G gel are more apparent and visible at all timepoints with high

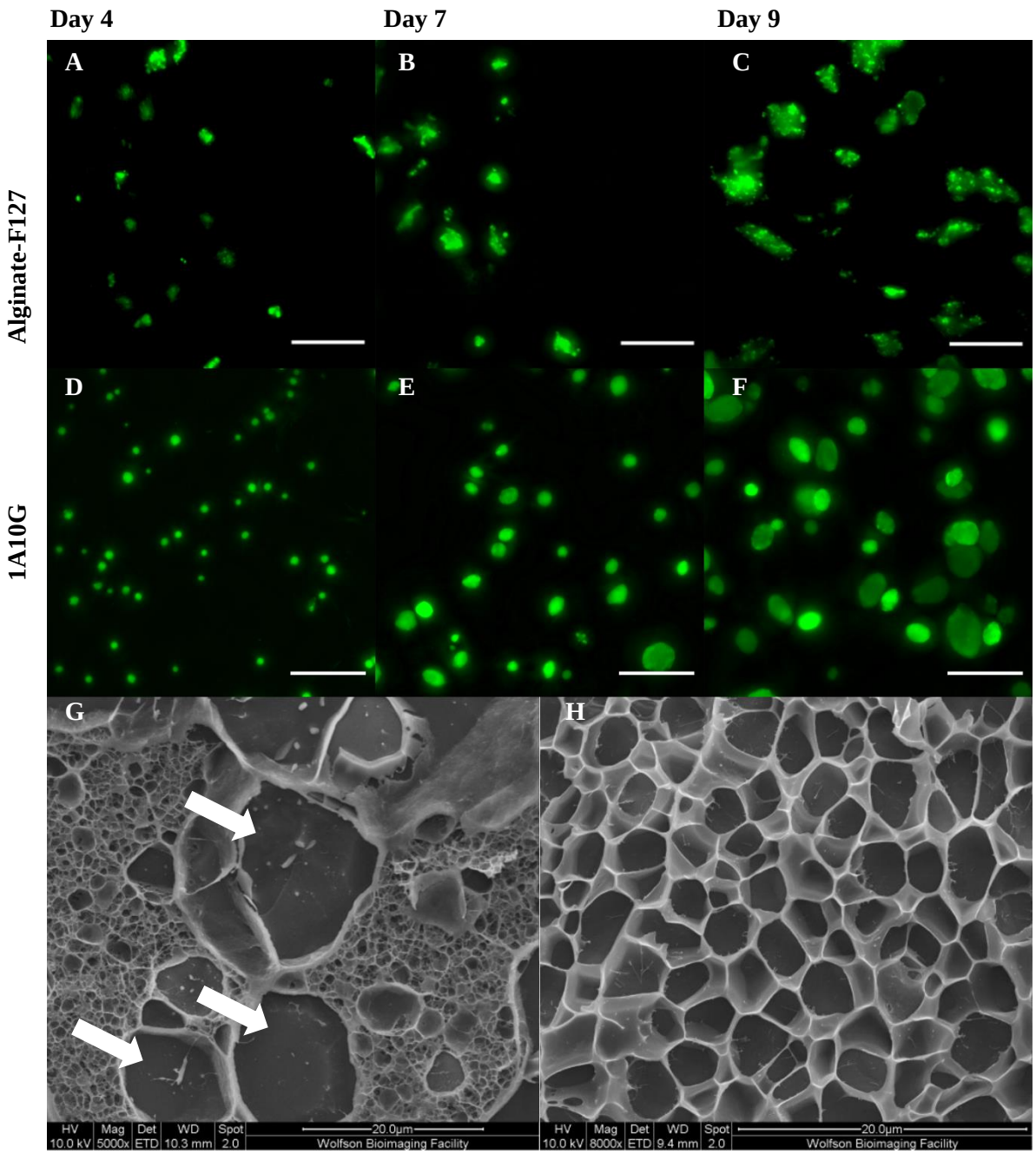

Figure 4-3 *Comparison between SW620 spheroids grown in the alginate-F127 bioink and the 1A10G bioink.* ***A-C*** *CalceinAM-stained spheroids 4,7 and 9 days after bioprinting, in the alginate-F127 bioink.* ***D-F*** *CalceinAM-stained spheroids 4,7 and 9 days after bioprinting, in the 1A10G bioink. Scale bars = 300µm.* ***G***,***H*** *Electron micrograph of the alginate-f127 (****G****) and 1A10G (****H****) hydrogel.*

uniformity, whereas SW620 spheroids in the alginate/F127 gel exhibit a wide range of morphologies with no discernible conservated features. Spheroids in the alginate/F127 bioink exhibited rough surfaces with random regions of high staining intensity, indicating structures protruding out of the image plane in the Z direction, whereas staining intensity was more uniform

in spheroids in the 1A10G gel. Moreover, high shape uniformity is apparent for SW620 spheroids in the 1A10G

An obvious factor in this morphological difference is the bioink structure itself. Ideed, scanning electron microscopy of the alginate-F127 bioink revealed a dense alginate network interspersed with large micro-pores(**Figure 4-3 G**, white arrows). Conversely, the pores within the 1A10G bioink were smaller and more ordered, existing in a less disperse range of sizes, with no indication of large micropores similarly to alginate-F127 electron micrographs (**Figure 3-10 B**, **Figure 3-11 C**, **Figure 4-3 H**). Mechanically, the alginate-F127 bioink structure was shown to result in a much stiffer material than the 1A10G bioink, with a ~10-fold decrease in stiffness measured (sections **3.3.2.9** & **3.3.3.2**, **Figure 3-8 A**, **Error! Reference source not found.**).

The differences in spheroid growth can be reconciled with the differences in the hydrogel stiffness and structure. As spheroids grow, cell division exerts forces on the surrounding matrix. If the surrounding matrix is soft, these forces may be sufficient to deform or displace the matrix, permitting unstressed growth of the tumour spheroid. Moreover, if the matrix is deformable by cells, and the matrix properties are isotropic, one would expect the growth of a spherical body as no directional preference would exist for growth. However, if the matrix is not deformable, or the deformability is anisotropic or orthotropic, growth could follow the "path of least resistance", resulting in the growth of non-spherical bodies. As such, the growth of non-spheroidal colonies in the high-stiffness alginate-F127 gel suggests that cells are unable to deform or displace the surrounding matrix effectively as they grow, instead growing along the internal porous structure, which arises from the removal of the F127 porogen. Conversely, the rounded growth of the same cells in the low-stiffness alginate-gelatin gel suggests this matrix is isotropically deformable, readily yielding in response to stresses from dividing cells. Furthermore, as the gelatin component was observed to dissolve into the surrounding media within ~12 hours, and alginate contains no binding domains for cell adhesion molecules, it is likely that matrix deformation in these bioinks is independent of cell-ECM interactions. This conclusion is also consistent with the spherical growth of SW620 cells in Matrigel (**Figure 4-4**, **A**), the microstructure of which is known to be

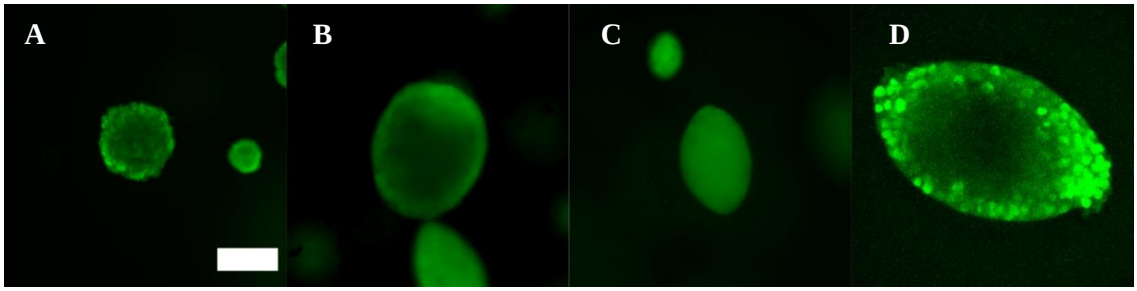

Figure 4-4 *Morphologies of SW620 spheroids.* ***A*** *Round SW620 spheroid at day 11 of culture in Matrigel.* ***B,C*** *Round (**B**) and oblate (**C**) spheroid at day 11 of culture in the 1A10G bioink.* ***D*** *Image adapted from Cheng et al. showing a 67NR (murine mammary carcinoma) oblate spheroid grown in an agarose gel. Scale bar = 200μm.*

loosely-bundled fibres, predominantly collagen IV, which cells can displace and migrate through, and is less stiff than both the alginate-F127 and 1A10G gel.

Although SW620 spheroids in the 1A10G gel are generally circular, upon closer examination, two distinct subpopulations are apparent: "Circular" spheroids, which are close to perfect spheres (**Figure 4-4**, **B**), and "Oblate" spheroids, which are elliptical (**Figure 4-4**, **C**), and taper along a semi-axis. The growth of oblate spheroids has been reported by Cheng *et al.*[226], who grew spheroids of oblate morphologies in 0.5%(w/v) agarose gels (**Figure 4-4**, **D**). To better understand this phenomenon, the stiffness of 0.5%(w/v) agarose gel was measured experimentally through unconfined compression testing. The compressive stiffness of this gel was determined to be 19.6±3.6kPa, ~13-fold stiffer than the 1A10G bioink, and similar in stiffness to the alginate-F127 bioink (17.6kPa). However, in the alginate-F127 bioink, oblate spheroids do not form, suggesting that matrix stiffness alone cannot completely describe spheroid morphology. Cheng *et al.* note that forces experienced in the agarose gel bulk from growing spheroids sometimes cause microcracks which are visible by microscopy, and that oblate spheroids only grow around such cracks. These microcracks represent local mechanical failure as the gel deforms to accommodate larger spheroids, which grow preferentially away from cracks, causing oblate spheroid morphology.

Microcracks were not observed near spheroids in the 1A10G gel, indicating that the 1A10G bioink does not fail mechanically like agarose gels. Here, alginate gels may instead deform plastically, "slumping" in response to stress, rather than fracturing, but nonetheless providing

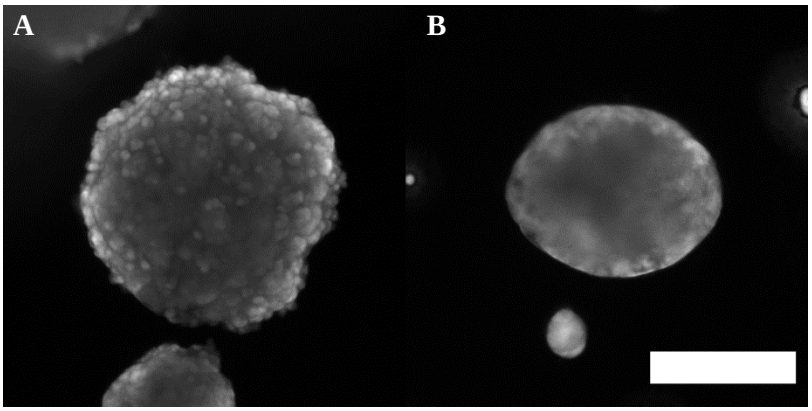

***Figure 4-5** Morphology of SW620 spheroids in Matrigel and the 1A10G bioink. **A**, **B** SW620 spheroids at day 11 in culture in Matrigel (**A**) and the 1A10G bioink (**B**). Scale bar = 200μm*

local regions of reduced resistance for spheroids to grow into. In Matrigel, the absence of oblate spheroids is likely a result of it yielding at very low applied stresses, as Matrigel is known to be easily deformable by single cells[239]. As such, the gel matrix of Matrigel does not apply significant resistance to growing spheroids, and therefore spheroids have no directional preference when growing.

The characteristic plasticity of Matrigel may explain the difference in morphology between large spheroids grown in Matrigel and the 1A10G bioink. Here, the ability of individual cells to restructure the surrounding matrix enables a rougher spheroid surface where individual cells can be seen to protrude (**Figure 4-5 A**)[239]. In the 1A10G bioink however, the greater resistance of the matrix forces a smoother surface, as individual cells cannot locally deform the gel (**Figure 4-5 B**).

4.3.1.3 Growth of other colorectal cancer lines

Following the successful growth of rounded SW620 spheroids, a range of CRC cell lines were cultured in the 1A10G bioink. SW480, LS174T, LOVO, CACO2, HCT116, SW837 and HT29 cells cultured using the same seeding density and growth conditions as SW620 cells. In all lines tested, the 1A10G bioink supported spheroid formation (**Figure 4-6**). This result represents the most extensive screen of the spheroid-forming capacity of colorectal cancer in any bioink to-date.

Variance in colony count and spheroid size was noted, indicating that each cell line contains subpopulations which grow at different rates in the bioink. This is an expected outcome of the spheroid-assay, as spheroids grow from single cells dispersed through the bioink, therefore selecting for subpopulations which are suited to growth in 3D.

4.3.1.4 Growth of the breast cancer lines MDA-MB-231 and MCF-7

MDA-MB-231 is a triple-negative breast carcinoma line of interest as a model of resistant breast cancer. Swaminathan *et al.*[122] attempted to grow spheroids of this cell line in bioprintable collagen-alginate and gelatin-alginate bioinks. Interestingly, the gelatin-alginate bioink used was identical to the 1A10G bioink in composition. Swaminathan *et al.* report that the cell lines MDA-MB-231, MCF-7 and MCF10A do not spontaneously grow into spheroid from single cells in a 1% alginate 10% gelatin bioink but transferred spheroids from Matrigel culture do continue growing for ~72hours in these bioinks, after which spheroids lose integrity, with cells migrating outward from the spheroid into the surrounding gel . Swaminathan *et al.* go on to conclude that these lines and other cancer cells must first be cultured into spheroids in Matrigel, then harvested and moved into bioinks for bioprinting applications.

In order to test the wide-spread applicability of the bioinkm MDA-MB-231 and MCF-7 cells were generously provided by Dr. Claire Perks, and bioprinted and cultured in the same way as SW620 cells. Here, it was found that under the bioprinting and culture conditions developed for SW620 spheroids, both cell lines formed spheroids over time in the 1A10G bioink, contrary to the findings of Swaminathan *et al.* (Appendix **D**), suggesting that bioink formulation alone is not sufficient for successful spheroid culture. In the experiments performed by Swaminathan *et al.*, a 3%(w/v) $CaCl_2$ solution (~270mM) was used for crosslinking, whereas in this work a 100mM $CaCl_2$ solution was used. Given the relationship between gel stiffness and crosslinking concentration, and the negative impact of high stiffness gels on cell viability and spheroid growth reported in this work, it seems

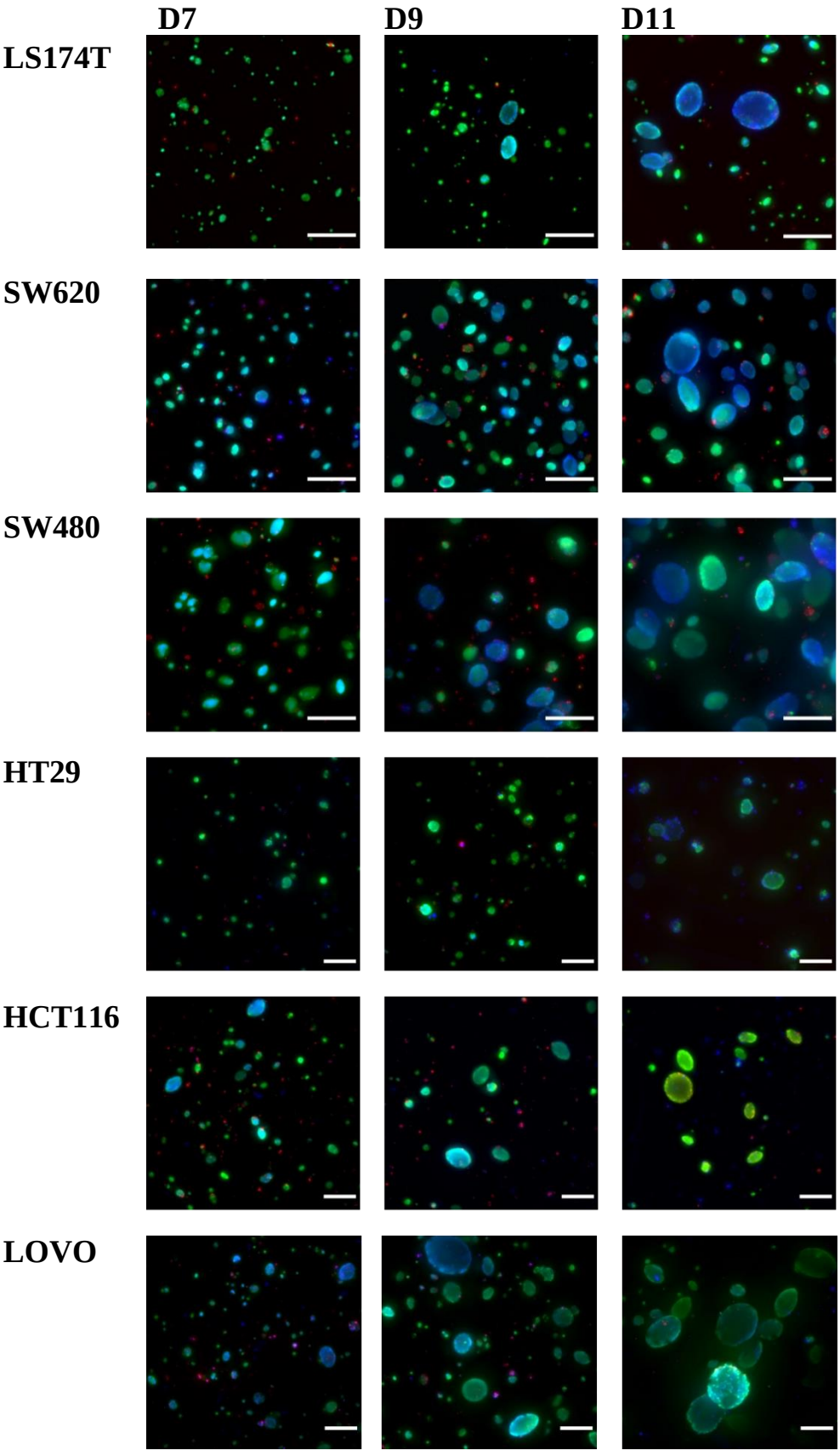

Figure 4-6 *Growth and morphology of different colorectal lines, 7,9 and 11 days after bioprinting. Scale bar = 200µm. Green = live (calceinAM), red = dead (Ethidium Homodimer III), blue = nuclear (Hoechst)*

likely that Swaminathan *et al.* over-crosslinked their gels, driving up the compressive stiffness well above *in vivo* conditions and preventing cells from surviving and proliferating in the gel.

Collectively, these data demonstrate that the culture conditions and experimental setup of the bioprinted 1A10G tumour-spheroid assay outlined in this work is a robust way of bioprinting tumour spheroids from a range of cancer lines. Although all cancer lines used were of breast or colorectal origin, the success of this approach with the 10 cancer cell lines used suggests a broad applicability to other cancers, and potentially to primary cancer cells.

4.3.2 Structure of SW620 spheroids grown in the 1A10G bioink

To better understand the structure of SW620 spheroids, a protocol was developed for harvesting them from the 1A10G bioink for use with other experimental techniques. The ability to harvest spheroids from the bioink is a critical step which is necessary for confocal microscopy, histology, flow cytometry and other assays. The method outlined in section **2.5.2** proved successful in harvesting spheroids with high viability. Briefly, a 200mM ethylenediaminetetraacetic acid (EDTA) solution chelated Ca^{2+} ions used to crosslink the alginate in the gel, causing the alginate gel to dissolve into solution. Then, spheroids were washed and concentrated by gentle centrifugation, which did not cause significant structural damage to the spheroids.

4.3.2.1 Confocal microscopy of SW620 spheroids

Harvesting spheroids from the bioink was an important step for confocal microscopy. High magnification lenses, especially oil or glycerol immersion lenses, typically have short working distances (<0.5mm), and therefore are unsuited to imaging through gel structures. Moreover, staining deep into tissues is challenging, thus staining spheroids in solution results in more complete staining than staining spheroids through a gel. A method for staining spheroids in solution was developed by Weiswald *et al.*[179] which was adapted for use with spheroids grown in the 1A10G bioink (section **2.9.2**). This protocol was successful in staining spheroids 150μm or less in diameter, and a custom MATLAB script was written to compensate for loss of signal through spheroids (**Figure 2-10**). SW620 spheroids were harvested one week after seeding, fixed

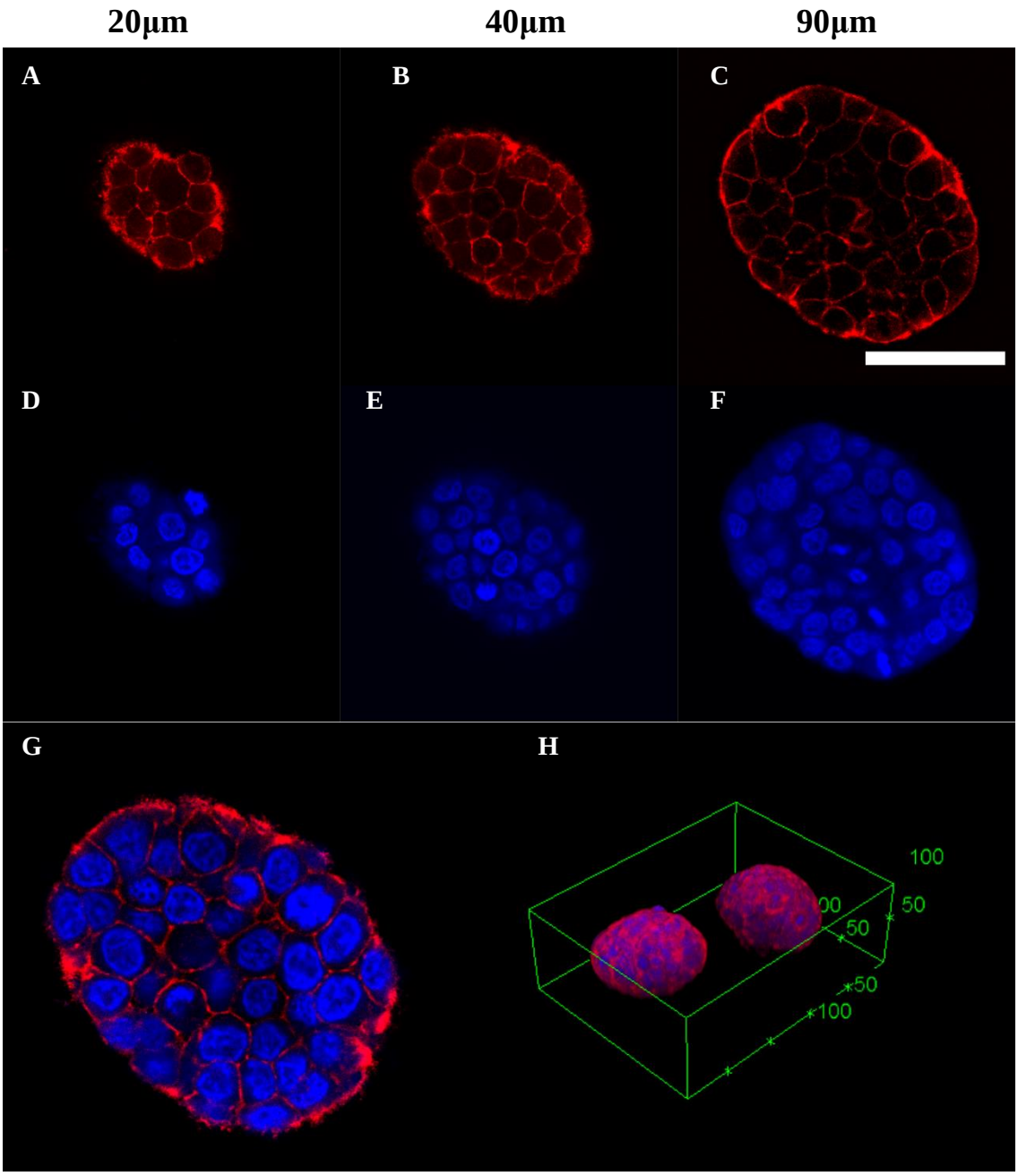

Figure 4-7 *Confocal microscopy with SW620 spheroids.* ***A-F*** *Actin (A-C) and nuclear (D-F) staining of SW620 spheroids at 20µm ,40µm and 90µm into the spheroid structure.* ***G*** *Merged image of the maximum cross-section of the spheroid.* ***H*** *3D rendering of two SW620 spheroids from confocal z-stack imaging. Red = Actin (TRITC-phalloidin), blue = nuclear (DAPI). Scale bar = 50µm. Units in* ***H*** *are µm.*

in paraformaldehyde (PFA), stained, and imaged with confocal microscopy. Spheroids were not harvested from later time points because their size would exceed 150*µm* and preclude high-quality imaging.

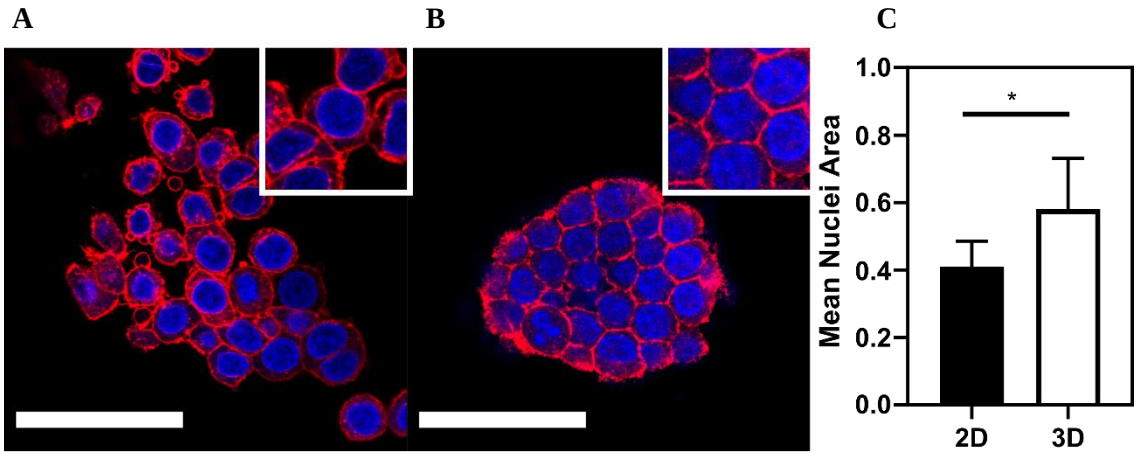

Figure 4-8 *Comparison of SW620 cell monolayers and tumour spheroids.* ***A*** *SW620 cell monolayer.* ***B*** *SW620 spheroid.* ***C*** *Nuclear space, enumerating the area of cell nuclei as a fraction of total cell area. Insets highlight the denser packing of cells in spheroids when compared to cells growing as a monolayer. Scale bars = 50μm.*

Here, confocal microscopy of SW620 spheroids revealed a densely packed structure throughout, with no signs of necrosis in the spheroid core (**Figure 4-7 A-G**). This packing is apparent by the high nuclear-cytoplasm ratio of cells within the spheroid structure, with cell nuclei (blue) physically occupying most of the cell (**Figure 4-7 G**). Spheroids were clearly rounded in 3D, a fact difficult to determine with widefield imaging, where significant signal diffusion in the Z-direction impedes 3D reconstruction of images taken in this way (**Figure 4-7 H**).

As the cellular packing within spheroids seemed higher than normal, SW620 cell monolayers were similarly stained and visualized with confocal microscopy (**Figure 4-8**, **A**,**B**). The space occupied by cell nuclei was determined by image analysis, by comparing the area of cell nuclei to the actin-visualized cell boundary (**Figure 4-8**, **C**). The proportion of cellular space occupied by the nucleus was significantly higher in spheroids than cell monolayers, increasing by ~40% (41% to 58%). This increase was driven primarily by a decrease in cell area, with differences in nucleus size being non-significant. Collectively these data indicate that SW620 cells growing in 3D are more densely packed in the 1A10G bioink with smaller cytoplasmic spaces, increasing the proportion of the cell occupied by the nucleus. The cause of higher packing density in SW620 spheroids is unclear. It could be the case that SW620 cells always form denser colonies when

grown in 3D, with spheroids produced in other works appearing to be similarly tightly packed[202]. Alternatively, cell spreading on tissue culture surfaces is a known phenomenon, and therefore the packing density in spheroids could be more representative of *in vivo* tumours. Indeed, the packing density of cells in tumours is reported to be higher than healthy tissue and a significant impediment to drug treatment[240], with studies suggesting that pre-treatment of tumours with apoptotic compounds to reduce cell density increases the efficacy of conventional chemotherapies[240].

However, it is also known that stiffer matrices also cause denser spheroids, and can limit the maximum size reached by a tumour spheroid[227]. As such, it could be the case that SW620 cells exhibit smaller cytoplasm's in response to mechanical stress from the 1A10G environment, thereby causing increased density of the spheroid. The hexagonal packing structure (**Figure 4-8**, **B** inset) of regions within the spheroid supports this hypothesis, as such structures are optimal arrangements of spheres which self-organise in response to external forces[241]. For instance, Alcinesio *et al.*[140] show that droplet packing in 3D can be patterned into different close-packing arrangements by controlling surface tension between lipid-coated droplets. However, further examination of spheroids grown in gels of different stiffnesses would be required to validate this hypothesis.

4.3.2.2 Electron microscopy of SW620 spheroids

SW620 spheroids were prepared for electron microscopy after 11 days of culture. Spheroids were either harvested from the gel or left embedded in the gel. Protocols for both approaches were developed (sections **2.6.2** and **2.6.3**), with liberated spheroids being critical point dried, sputter coated then imaged *via* SEM and embedded spheroids being freeze-dried *in situ* then fractured, sputter coated and imaged *via* SEM. Alternatively, liberated spheroids were embedded in BSA gels, sectioned and imaged *via* TEM.

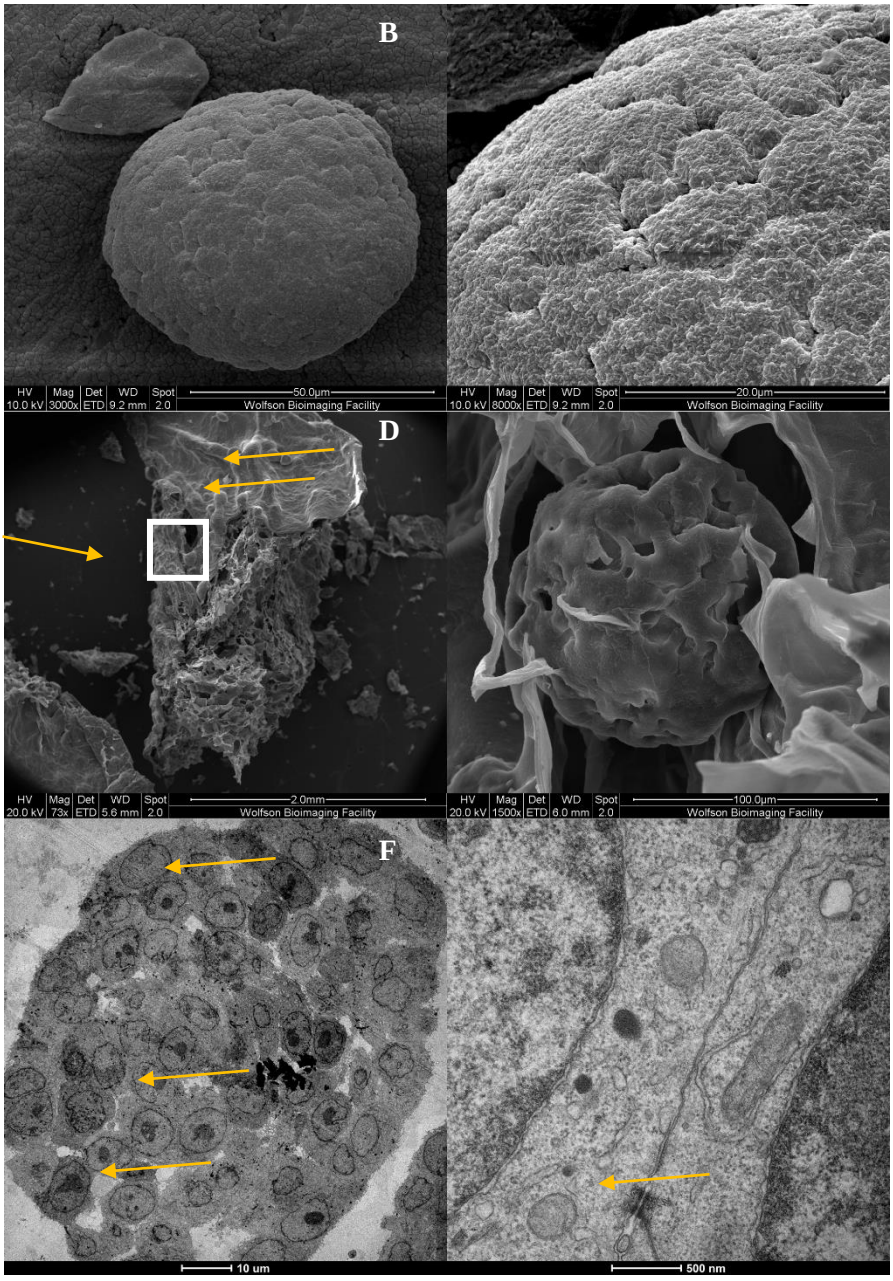

Figure 4-9 *Electron micrographs of SW620 tumour spheroids.* ***A*** *SW620 spheroid imaged after harvesting from the 1A10G bioink after 11 days in culture, with an enlarged image of the spheroid surface (**B**).* ***C*** *Image of the fracture surface of a freeze-dried spheroid-laden 1A10G gel. Yellow arrows show where shrinkage of the gel front during the freeze-drying process has caused spheroids to protrude from the gel surface. White box shows the region imaged in greater detail in **D**.* ***E*** *Low-power TEM of a spheroid section, yellow arrows show small regions of ECM inside the spheroid.* ***F*** *High-power TEM of two adjacent cells in a tumour spheroid, cell-cell junctions, namely desmosomes can be seen (yellow arrow)*

Here, SEM reveals structures which are fully rounded in 3D, similar to confocal micrographs (**Figure 4-9**). When removed from the gel and imaged, dense cell boundaries along the spheroid edge can be observed (**Figure 4-9**, **A**,**B**), but appear smaller due to spheroid shrinkage resulting

from critical point drying and glutaraldehyde fixation[242]. Spheroid surfaces were rough due to microvilli on cell surfaces, which were visible in TEM images (**Figure 4-9**, **E**). Spheroids were tightly packed, consistent with confocal micrographs, however, small regions of ECM were visible between some cells (**Figure 4-9**, **E**). Cells within spheroids were observed to form cell-cell contacts, indicating that grown spheroids are not independent collections of cells, but rather organized communities(**Figure 4-9**, **F**).

Freeze-drying spheroid-laden samples was shown to be effective at revealing spheroids *in situ* without apparent damage. Interestingly, PFA-fixed samples were observed to shrink more during the freeze-drying process than glutaraldehyde-fixed samples, leading to the use of glutaraldehyde as the fixative. However, some gel shrinkage was apparent in all cases (**Figure 2-6**). SEM images of the spheroids indicate that the gel front recedes during freeze-drying (**Figure 4-9**, **C**), whereas fixed spheroids remain in place causing them to protrude from the gel (**Figure 4-9**, **C**, yellow arrows), which was not observed in culture prior to freeze-drying. Spheroids imaged *in situ* appear to be connected to gel matrix in some way (**Figure 4-9**, **D**), although this is unclear as several mechanisms exist to explain these images. First, spheroid-matrix interactions could be artefacts of the freeze-drying process, which alters the gel structure. Second, spheroids could be binding to either deposited ECM or gelatin remaining in the gel. Third, cells could be growing through the porous gel structure, causing a physical entanglement with the gel, with no biochemical binding taking place. An emerging electron microscopy technique, serial block-face scanning electron microscopy, could provide more insight into spheroid-matrix interactions, by providing high resolution layer-by-layer, 3D EM images of spheroid-laden hydrogels.

4.3.2.3 Histology and immunohistochemistry

A major challenge with spheroid assays is effectively probing the core of the spheroid structure. Large spheroids (>150μm in diameter) are very challenging to image with confocal or widefield microscopy due to limited diffusion of molecular probes into the spheroid structure and low optical transparency through large structures. However, histological approaches allow for sectioning of spheroids, in turn enabling visualization of the spheroid core through extracting

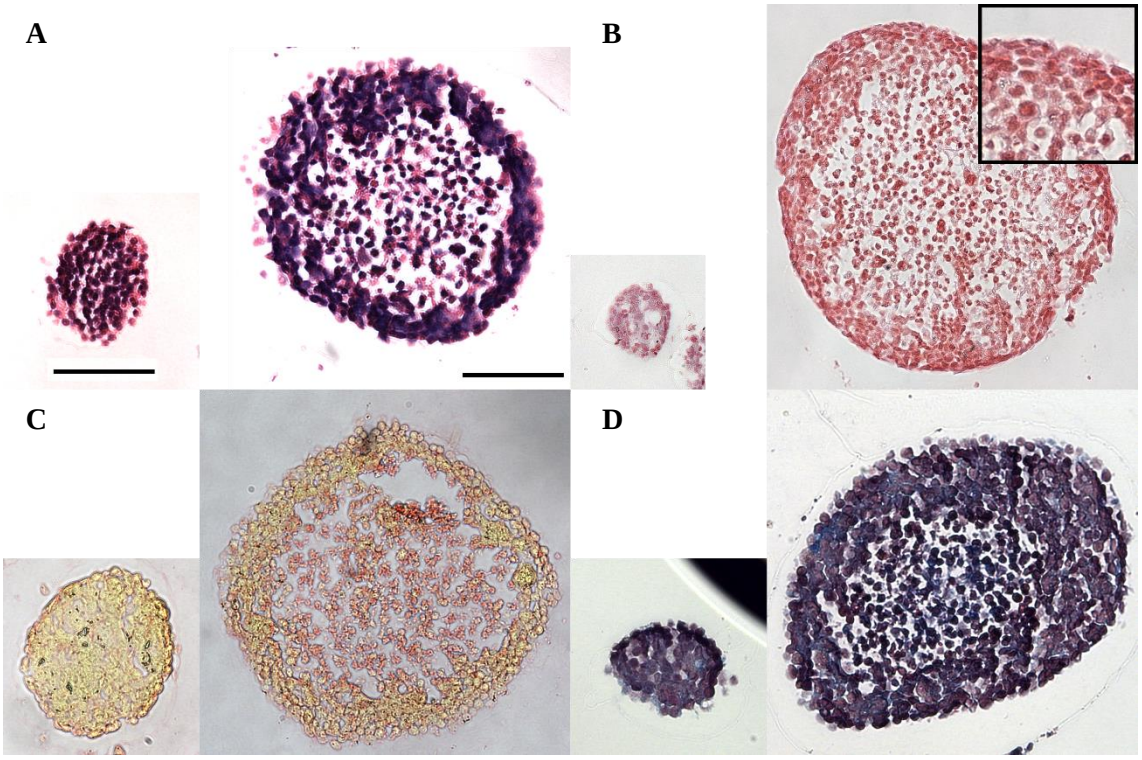

Figure 4-10 *Histological staining of spheroid sections.* ***A*** *Haematoxylin and Eosin.* ***B*** *Safranin-O.* ***C*** *Sirius Red.* ***D*** *Masson's Trichrome. Scale bars = 100μm.*

sections through the widest part of the spheroid. Unfortunately, many common bioink components are unsuited to direct sectioning and staining with commonly used histological stains. For instance, alginate permanently uptakes haematoxylin and eosin (H&E) stains, leading to large background signals[181]. Many ECM proteins, such as collagen, are targeted by common stains such as Sirius red and Safranin-O, making hydrogels containing these components challenging to stain as differentiating between cell-derived ECM and components of the hydrogel is difficult. Consequently, direct staining of spheroids in a 1A10G gel was unsatisfactory. Moreover, tearing of the gel when sectioning, and background staining of the gel components were notable issues (**Figure 2-11**, **A**).

In response, histology protocols were adjusted to resuspend spheroids in an agarose gel for more robust sectioning. The spheroid harvesting procedure outlined in section **2.5.2** was used to harvest spheroids from the 1A10G bioink then embed them in a 2%(w/v) agarose gel (**Figure 2-11**, **B**). Here, spheroids were embedded successfully without damage; Sectioning was improved, with less gel tearing, and background staining eliminated.

Spheroid sections were stained with several different stains: Hematoxylin and eosin (H&E), for staining cell nuclei and ECM, Sirius red for staining collagen, Safranin-O for staining proteoglycans, and Masson's trichrome for differentiating between cell cytoplasm and ECM components (**Figure 4-10**). Larger (>100μm) spheroids were visibly less dense toward the spheroid core, whereas smaller spheroids were densely packed in general. A MATLAB script was written to measure the depth at which cell density decreased and mean solidity in H&E-stained spheroids (Appendix **C**). Solidity was estimated by thresholding images of H&E-stained spheroid sections using QuPath, then comparing this area to the total area of the spheroid. Cell density was calculated to decrease 48μm±13μm from the spheroid edge into H&E-stained spheroids, which is in agreement confocal microscopy images of densely-packed spheroids approximately 100μm in diameter. Solidity of larger spheroids was estimated to be 76%±8%.

Safranin-O staining gave the best insight into spheroid structure near the spheroid edge, showing densely packed nuclei similar to confocal imaging (**Figure 4-10**, **B** inset). Safranin-O also stains for type II collagen, but as the staining was not bright away from cell nuclei through the spheroid structure. Accordingly, it can be concluded that type II collagen was likely not being deposited by SW620 cells, although this is not unusual as SW620 cells are not reported to produce ECM, with ECM deposition in tumours *in vivo* caused by recruited fibroblasts. Sirius red staining is yellow for cell nuclei and cytoplasm, and red for collagen I & III fibres. Small spheroids were yellow throughout with some red appearing towards the core of larger spheroids (**Figure 4-10**, **C**). This could indicate that SW620 cells are able to deposit ECM in the spheroid core, although the staining is not distinctive enough to demonstrate this alone. Masson's trichrome is a three-part stain which stains collagen blue, nuclei purple and cytoplasm red. As with Sirius red staining, small spheroids clearly stained cell nuclei, with some evidence of collagen staining in the core of larger spheroids (**Figure 4-10**, **D**).

Collectively, these stains demonstrate that SW620 spheroids grown in the 1A10G bioink grow into densely packed structures only at small sizes, with cell density decreasing as spheroids grow. Staining for ECM proteins was largely negative, with weak evidence of collagen fibres from

Sirius red and Masson's trichrome staining. A fluorescent collagen I antibody stain was also used but did not detect collagen I in spheroid sections.

To examine further the structure of SW620 spheroids, two separate hypoxia stains were used to establish whether spheroid cores were hypoxic, which could explain why spheroid cores have low cell densities. Hypoxia is a characteristic feature of tumours *in vivo*, arising due to poor blood supply into the tumour structure and driving changes in metabolism, protein, and gene expression[75,186]. A sensitive hypoxia stain, *Image-iT*^{TM}, was first used with spheroids growing in ordinary 3D culture. This proprietary stain is stated as activating inside cells when oxygen drops below 5%, resulting in fluorescence. Staining of spheroids revealed uniform activation of this dye for spheroids of all sizes tested, with no staining apparent in cell monolayers (**Figure 4-11**, **A**). Harvesting spheroids from the gel allowed for quantification of this stain with a plate reader, which had 4.7-times greater fluorescence intensity than cell monolayers (**Figure 4-11**, **B**).

Image-iT^{TM} staining indicated that spheroids were hypoxic but was too sensitive to precisely characterise the hypoxic gradient. Consequently, a more sensitive hypoxia stain was used in conjunction with immunohistochemistry. *HypoxyProbe*, comprised of pimonidazole hydrochloride, uses the well-understood oxidation of pimonidazole as a hypoxic marker. Spheroids were cultured with *HypoxyProbe* before paraffin embedding, sectioning, and staining with an anti-pimonidazole fluorescent secondary antibody. Being less sensitive than *Image-iT*^{TM}, pimonidazole is activated intracellularly below 1.3% oxygen concentration[185]. Here, for small spheroids, pimonidazole staining was not uniform along spheroid cross sections, but rather localised at spheroid cores (**Figure 4-11**, **C-F**).

For larger spheroids, hypoxia staining appeared in a band near the spheroid periphery, diminishing toward the spheroid core. This could be due to poor diffusion of pimonidazole hydrochloride into the spheroid core, or alternatively, as pimonidazole hydrochloride is dependent on cell metabolism, lack of staining could indicate a necrotic core. A MATLAB script

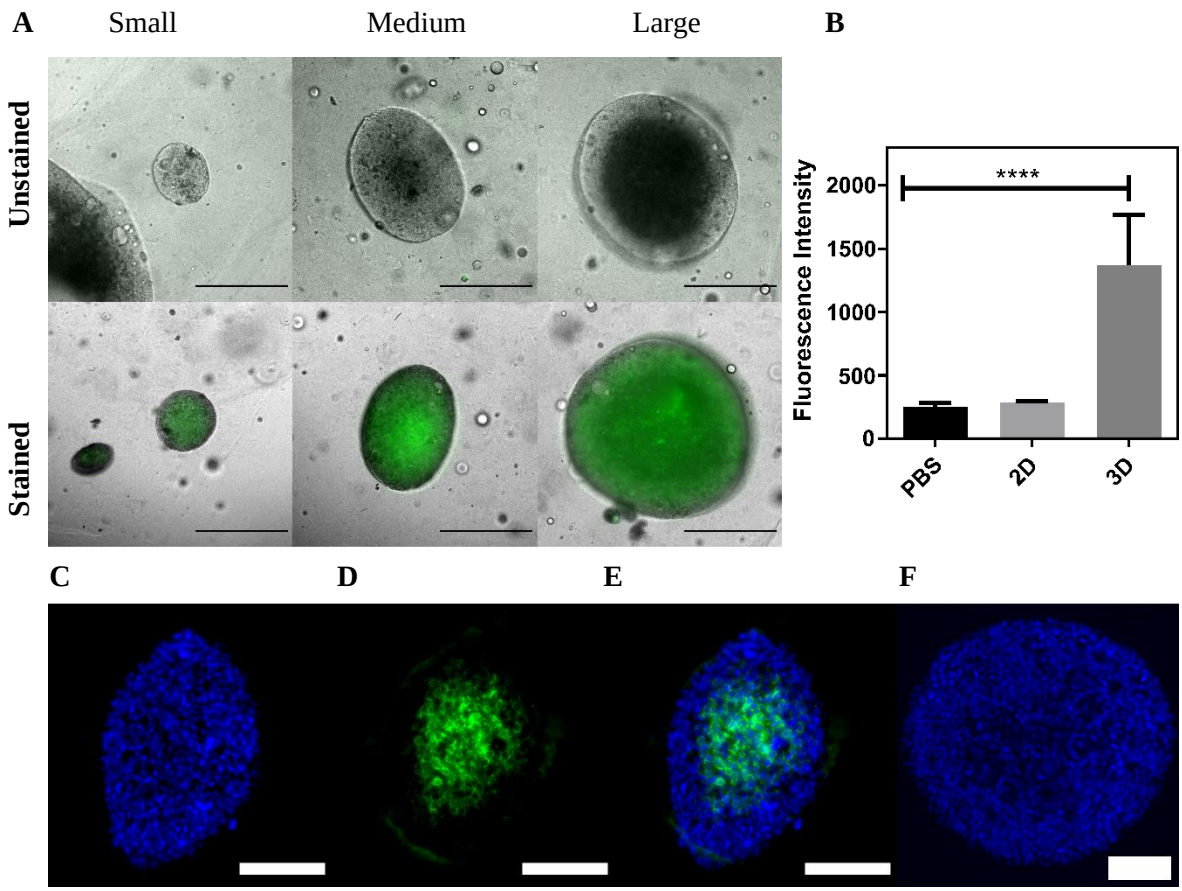

Figure 4-11 *Hypoxia staining of SW620 spheroids.* ***A*** *Image-iT^{TM} staining of SW620 spheroids, with fluorescence being compared to unstained spheroids. Green = Image-iT^{TM}, scale bars = 500μm* ***B*** *Fluorescence intensity of stained spheroids compared to stained monolayers, measured with a plate reader.* ***C-E*** *HypoxyProbe staining of paraffin-embedded SW620 spheroid sections. Blue = DAPI, green = HypoxyProbe, scale bars = 100μm.* ***F*** *Control sample, incubated with HypoxyProbe but not stained with the fluorescent secondary. Scale bars = 100μm.*

was written to measure sizes of hypoxic regions in relation to the overall size of the spheroid through thresholding and segmentation of nuclear and hypoxic staining (**Figure 4-12**, **A-C**). These regions represent spheroid areas with no hypoxia staining (**Figure 4-12**, **A**), dense hypoxia staining (**Figure 4-12**, **B** green line) and sparse hypoxia staining (**Figure 4-12**, **B** yellow line).

The staining in these regions was compared to an oxygen diffusion model written in MATLAB, adapted from the published work of Grimes and Currell, who produced a model for oxygen diffusion in liberated, immersed spheroids[243]. Critically, this model does not assume tumour spheroids are perfectly spherical, accounting for eccentricity of oblate spheroids grown in the

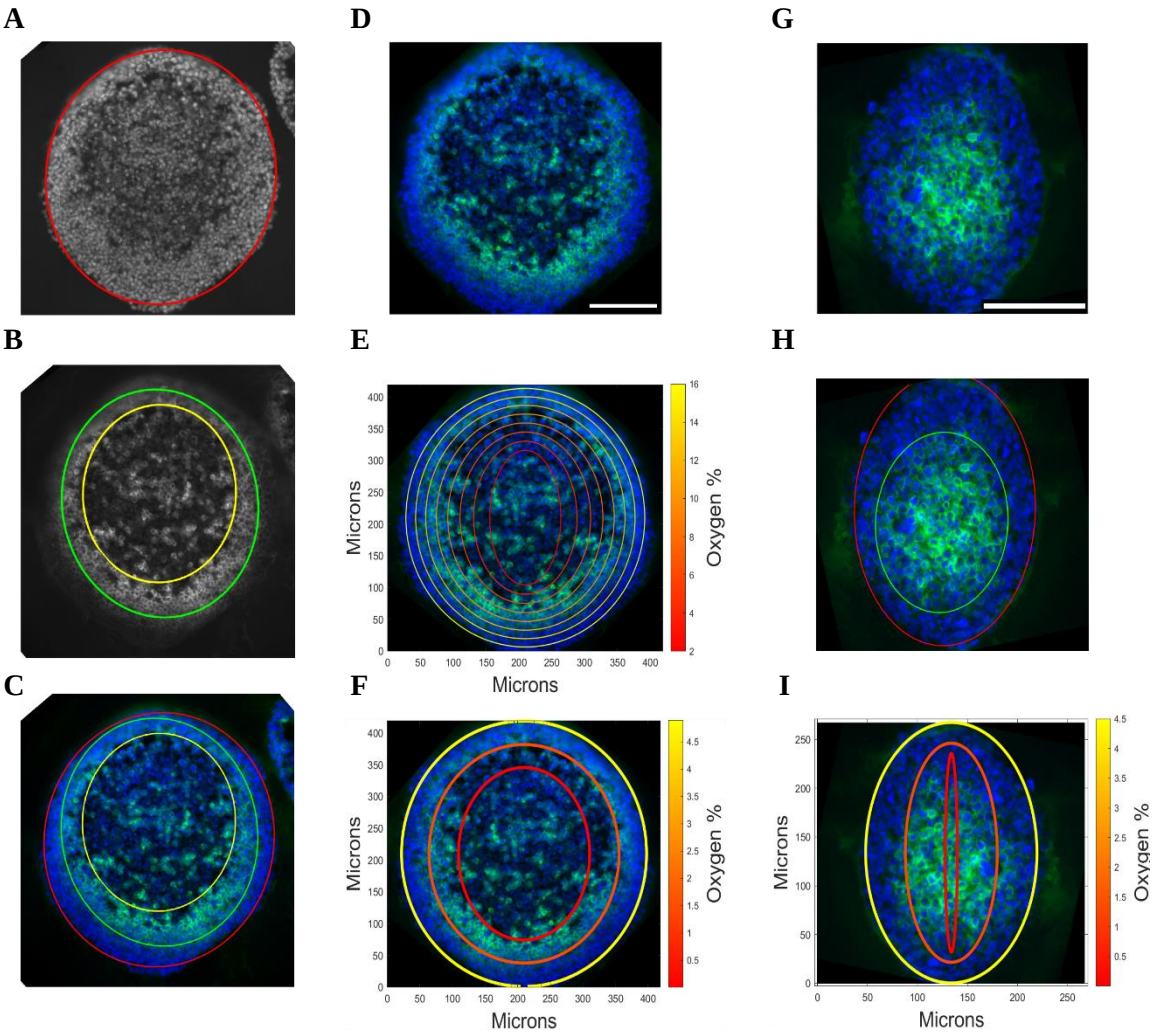

Figure 4-12 *Mathematical modelling of oxygen concentrations in tumour spheroids.* ***A-C*** *Determination of spheroid area (**A**), dense hypoxic zone (**B** – green ellipse) and dispersed hypoxic zone (**B** – yellow ellipse) using image analysis of nuclear and hypoxia stains.* ***D-F*** *Results of the mathematical model for a large tumour spheroid (**D**), where the external oxygen concentration was input as 17% (**E**) or 5% (**F**). Lines in **F** represent 5%, 1.3% and 0% oxygen contours.* ***G-I*** *Mathematical model applied to a small spheroid (G), with the hypoxic zone determined by image analysis (**H**) and modelled using a 5% external oxygen concentration. Lines in **I** represent 5% and 1.3% oxygen contours. All scale bars = 100μm.*

1A10G bioink. As pimonidazole hydrochloride is known to accumulate in cells at oxygen concentrations below 1.3%, regions of bright *HypoxyProbe* staining must correspond to similar levels of oxygen. However, when inputting the ambient oxygen conditions as 17% oxygen, the typical oxygen concentration in laboratory incubators, the model is a poor predictor of *HypoxyProbe* staining, with most of the stained regions existing between 8%-14% oxygen (**Figure 4-12**, **E**).

Because it was noted that spheroids fluoresced uniformly when stained with *ImageIt*^{TM}, which activates when oxygen is below 5% (**Figure 4-11**, **A**), an ambient oxygen concentration of 5%

was used in the mathematical model. Predictions from the model corresponded better with the experimental data, with the contours between 1.3%-0% oxygen (**Figure 4-11**, **F,I** orange-to-red region) more precisely matching the stained regions identified through image analysis (**Figure 4-11 C**, **H**). Interestingly, this model predicted that for larger spheroids, central regions of low *HypoxyProbe* staining correlate with large anoxic zone, whereas for smaller spheroids, anoxic zones, where they existed, were very small.

Collectively, these data indicate that oxygen concentration inside spheroids is reduced. As the stained sections were taken from deep within bioink samples, it is also likely that oxygen concentrations within 1A10G bioink is also lower than incubated conditions, with an estimate of 5% or lower in standard culture conditions. This is likely due to the local effect of collective oxygen consumption of many tumour spheroids growing together, and the diffusivity of oxygen through the gel itself. As such, spheroids grown in the 1A10G bioink express proportionally larger hypoxic regions than single spheroid-aggregates growing in low adherent microwells, which was the experimental basis of the mathematical model put forward by Grimes and Currell[243]. It is therefore likely that regions of low cell-density in histological staining, such as H&E, are a result of severely hypoxic, or anoxic zones within grown tumour spheroids.

4.3.3 Tumour spheroid metabolism

Studies both *in vivo* and *in vitro* have described changes in tumour metabolism in response to hypoxic conditions[186]. Notably, increased anaerobic glycolysis (the "Warburg Effect") leads to faster glucose consumption in tumours *in vivo*[186]. To determine whether this effect was observable for bioprinted SW620 spheroids, spheroid media was exchanged for high-glucose DMEM after 11 days of culture, and glucose concentration measured 24hrs later. A calibration curve of known glucose concentrations was used to calibrate the glucose oxidase-based plate reader assay.

When compared to cell monolayers, glucose concentration in spheroid culture was lower after 24 hours (**Figure 4-13**, **A**). However, differences in cell number between samples require this data be adjusted. Accordingly, cells were harvested and counted in 2D and 3D, then glucose consumption stated as glucose consumed per million cells (specific glucose consumption). Here,

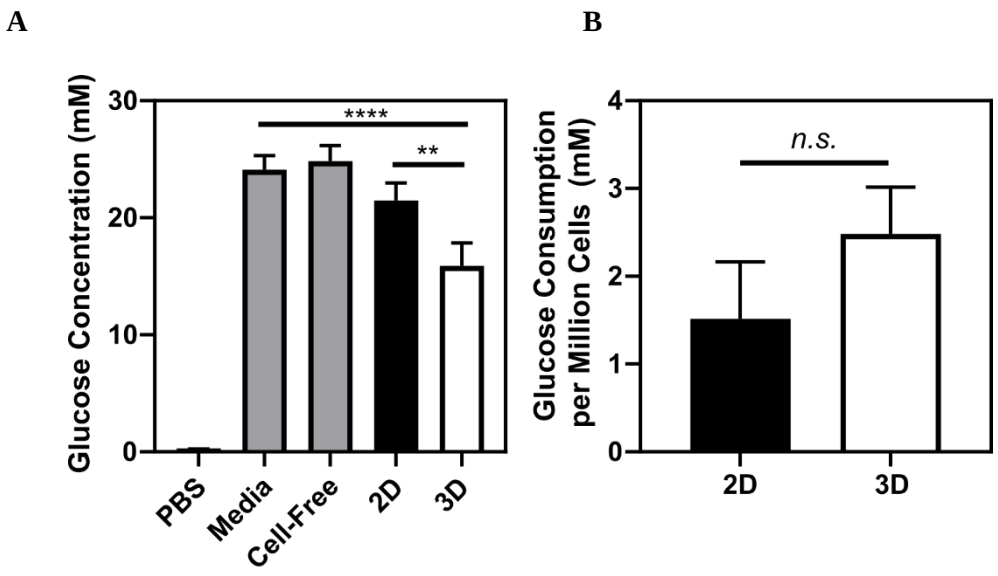

Figure 4-13 *Glucose consumption by SW620 cell monolayers and tumour spheroids.* ***A*** *Glucose concentration in culture media 24 hours after media exchange. Media = high glucose DMEM. Cell Free = acellular 1A10G gel.* ***B*** *Specific glucose consumption of SW620 monolayers and spheroids.*

specific glucose consumption in spheroid culture appeared higher but was not significantly increased (**Figure 4-13**, **B**).

These data suggest that the transition to 3D culture does not impact glucose consumption of SW620 cells. However, the cell counts required for stating specific glucose consumption could have included dead cells from spheroid cores, which would systematically deflate specific glucose consumption values. To improve the reliability of this experiment, cell counts should be performed with flow cytometry, with robust gating to count live cells in all samples. Then, specific glucose consumption should be stated as glucose consumption per million live cells.

4.4 Conclusions and Discussion

In this chapter, spheroids were grown and characterized in the optimised bioink formulation and spheroid-assay protocol described in chapter 3. When compared to the initial, alginate-F127 bioink, spheroids in the 1A10G bioink formed more regular, circular structures in culture. Here, differences in spheroid morphology are likely due to differences in mechanical properties and internal structures of the two bioinks, as both the F127 and gelatin components of these gels

dissolve gradually into solution over time and thus both gels become crosslinked alginate structures in culture. As such, it seems that the stiffer alginate-F127 gel cannot be displaced by dividing cells, whereas the less stiff, 1A10G gel can be displaced, resulting in rounded spheroid formation in the 1A10G gel, and more random colony formation in the alginate-F127 gel.

When applied to other cancer cell lines, the 1A10G bioink was found to be a robust platform for the growth of tumour spheroids for all colorectal cancer cell lines tested. Thus, this culture system provides an optimal 3D environment for the proliferation and organisation of CRC spheroids. Furthermore, the bioink was readily applicable to two breast cancer lines, both of which grew formed tumour spheroids using the optimised CRC protocol without adaptation. As such, there is good evidence that this bioink could be applied to other types of cancer line, and possibly to primary cells.

To better study bioprinted spheroids, a reliable spheroid-harvesting protocol was developed to allow spheroids to be interrogated by other assays. Confocal microscopy of harvested spheroids grown in the 1A10 bioink revealed dense and tightly packed structures at small sizes ($<100\mu m$), with significantly increased Nuclear:cytoplasm ratios in SW620 spheroids compared to SW620 monolayers, an observation which was supported by TEM images. This denser packing of cells could be a the norm for growth of cells in 3D, as cells have a tendency to spread over tissue-culture-treated surfaces , or a result of matrix stiffness, which is known to increase the packing of cancer spheroids in agarose gels. Dense packing of cells, "cellularity", is thought to be indicative of tumour aggressiveness, with studies indicating that denser colorectal tumours are more likely to metastasise[244]. Accordingly, the high cellularity of SW620 spheroids, which is itself a metastatic line, is consistent with these clinical observations.

For larger spheroids, beyond ~$100\mu m$ in size, histological sectioning of agarose-embedded spheroids revealed that tight cellular packing visualized with confocal microscopy and TEM becomes sparser toward the spheroid core. In the literature, such regions are often quiescent, with an absence of proliferating cells, and correlating with increased hypoxia. To determine if such a correlation with hypoxia exists in the bioprinted culture system, two hypoxia stains of differing

sensitivities were employed. First, a sensitive stain, activating in cells when oxygen concentration drops below 5%, was used. Here, bright staining in spheroids of all sizes was noted, indicating that ambient oxygen concentration in the bioink is around 5% or lower. Next, a less sensitive stain, pimonidazole hydrochloride, activating in cells below 1.3% oxygen concentration, was used. This stain revealed that not only are spheroids in culture hypoxic generally, but a hypoxia gradient exists across spheroid structure. For small spheroids, hypoxia staining was localised in a central region, whereas for larger spheroids, hypoxia staining existed in a bright band near the spheroid surface, becoming darker toward the spheroid core. Critically, this dark region within the hypoxic band correlates with the regions of low cell-density in histological staining.

Collectively, these results indicate that spheroids in this culture system become more centrally hypoxic as they grow. Beyond approximately 100-150μm in diameter, cells in spheroid cores become quiescent or necrotic, and cease to metabolically oxidise the pimonidazole stain. Mathematically, models for oxygen gradients in tumour spheroids exist which predict the formation of physoxic, hypoxic and anoxic zones. A model of oxygen diffusion in oblate spheroids from Grimes and Currell was adapted and was in good agreement with our experimental data, predicting that at normal incubated oxygenated conditions little-to-no pimonidazole staining should be present, but around 5% ambient O_2, pimonidazole staining should appear. Moreover, this model predicted sizeable anoxic regions in larger tumour spheroids, which would be consistent with the hypothesis that quiescent or necrotic cells populate the low-density regions observed in histological staining of spheroid sections.

4.5 Acknowledgement of Collaboration

Work in this chapter was completed by the author unless otherwise mentioned here. The author would like to thank Dr. Judith Mantel, who performed SEM imaging on tumour spheroids, and Dr. Chris Neal, who performed TEM imaging on spheroids, with samples prepared by the author.

Chapter 5: Development of a High Throughput Tumour Spheroid Chemotherapy and Radiotherapy-Response Assay

5.1 Introduction

Drug-response of cell monolayers is the most commonly reported method of assessing the effectiveness of different therapeutic compounds. The advantages of this approach are practical, as cell monolayers are easy to establish, scale and measure. Here, metabolism or cell number can be used as a metric for viability, and therefore drug-response, measured using metabolic assays such as MTT-assays[245], or colorimetric stains, such as crystal violet[246]. In cell monolayer culture, drug accessibility is high, as diffusion effects are absent contributing to the systematic issue whereby cell monolayers over-predict the efficacy of treatment[247].

Drug-response of tumour aggregates and tumour spheroids is more challenging to measure. The best approaches to measuring drug-response in tumour aggregates use scalable microplate setups with an individual tumour aggregate in each well, providing a uniform and highly controlled environment for drug treatment. Because of the 3D structure of the tumour aggregate model, aggregate size can be used in some cases as a proxy for viability and hence drug effect. However, cell aggregates do not always exhibit a clear dose-size relationship and may not decrease in size unless treated with extremely high drug concentrations, which are not physiologically relevant[91,248]. As such, metabolic assays are frequently used alongside staining for necrosis.

In the tumour spheroid model, drug penetration is limited by diffusion through the aggregate structure and also the ECM-analogue. As such, drug effect can take time to accumulate, indeed other studies involving tumour spheroids use early and prolonged treatment to permit drug effect to accumulate[31]. In other works, changes in spheroid size do appear to emerge over time in 3D culture[31,249], although this relationship does not appear to have been studied.

Clinically, tumour size is an important factor as it influences operability and surgical invasiveness, with chemotherapy often applied to shrink tumours preoperatively[250]. Moreover, tumour shrinkage in response to therapy is a measure of therapeutic success. Consequently, a model in which spheroid size and drug effect can be linked would exhibit increased clinical relevance whilst being non-invasive.

5.2 Aims

In this chapter, the 1A10G bioink and bioprinted spheroid-forming assay described in chapters 3 and 4 was incorporated into a high throughput platform for rapid screening of cancer therapies. Here, the primary aim was on the successful establishment of a high throughput, automated pipeline where bioink formulation, bioprinting, spheroid formation, treatment, imaging, and analysis are controlled and reliable. Then, the secondary aim was to use this system to analyse the performance of different therapies on tumour spheroids, including chemotherapy and radiotherapy, and compare these results internally and to cell monolayers.

5.3 Developing a high-throughput treatment-response assay

Having established a robust bioink formulation in chapter 3 and used it successfully to induce tumour spheroid self-growth in chapter 4, a reliable, high-throughput spheroid assay was designed around automating spheroid printing, measurement, and analysis procedures (**Figure 5-1**). Here, each step of the spheroid assay was examined to maximise throughput via automation. Preparation of the bioink and bioprinting were already automated and optimised, as gels were prepared under identical conditions using the DAC and could be stored at 4°C for several days before use. For bioprinting, the BioX bioprinter "droplet print" setting was customised for 96 well plate printing with the 1A10G bioink, providing standardised and highly reproducible 96 well plate prints, with print times below 5 minutes a plate.

For measurement and analysis, custom MATLAB code (Appendix **F**) was written to semi-automate microscopy and image analysis. A standard Leica widefield microscope was used for microscopy, with the MATLAB code automating the Z-stack imaging of 96 well plates using the known centre-to-centre distance between wells in conjunction with precise sample positioning from the bioprinting protocol (section **2.8.1**). In principle, this code can be applied to any Leica widefield microscope. Microscopy time was approximately 15 minutes per 96 well plate, permitting for measurement of multiple plates in a single imaging session, and driving down associated imaging costs. Designing this assay around widefield microscopy rather than confocal microscopy increases the utility of this approach, as confocal microscopes are more expensive,

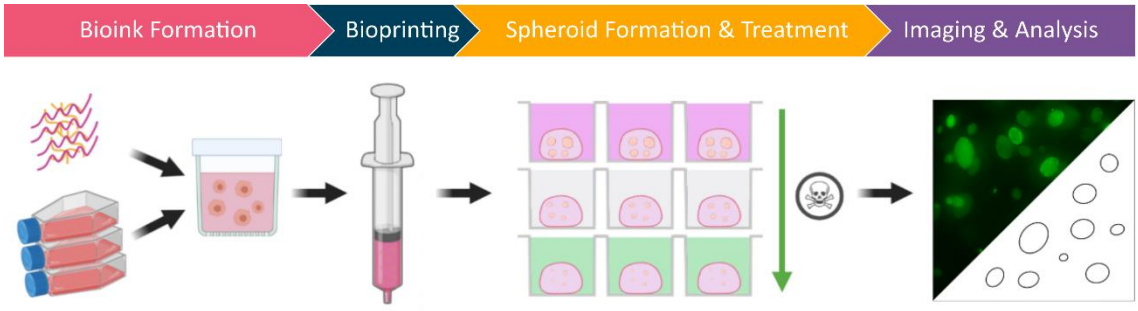

Figure 5-1 *Overview of the semi-automated, high-throughput tumour spheroid assay. Gel components and cell monolayers are mixed in the DAC to form cell-laden bioinks, with uniform dispersion of cells throughout. Then, a custom BioX bioprinting setting is used to rapidly dispense a small volume of cell-laden bioink into each well of a 96 well plate. The resultant spheroids growing in each well are exposed to different treatment conditions, causing a range of spheroid sizes to emerge, measured by an automated microscopy program, and analysed with custom code in MATLAB.*

more challenging to use, and harder to configure for high-content microscopy. Analysis of z-stack images of spheroids was also performed in MATLAB with bespoke code, designed specifically for the detection and measurement of spheroids directly from microscope image files. The functioning of this code is described in detail in section **2.15** and provided in (Appendix **F**). However, briefly, this code first generates 2D image projections from z-stack images then detects spheroids and measures geometric properties. Different parameters are required to be input by the user before running the code (*e.g.* minimum and maximum expected spheroid size). The output of the analysis program is a series of measurements for each spheroid, including centre of geometry, area, smoothness, and eccentricity.

Ultimately, this approach provides highly granular data suitable for mapping *in vitro* spheroid populations, as repeated imaging at different timepoints unpacks how spheroid populations evolve over time when challenged with chemo/radiotherapy, compared to normal expansion conditions.

5.4 High throughput measurements of SW620 spheroid growth-curves

To validate the high-throughput pipeline, the growth of untreated SW620 spheroids was measured. 1A10G bioink containing SW620 cells was bioprinted into 96 well plates and cultured before imaging and analysis 4 (**Figure 5-2**, **A**),7,9 and 11(**Figure 5-2**, **B**) days after bioprinting.

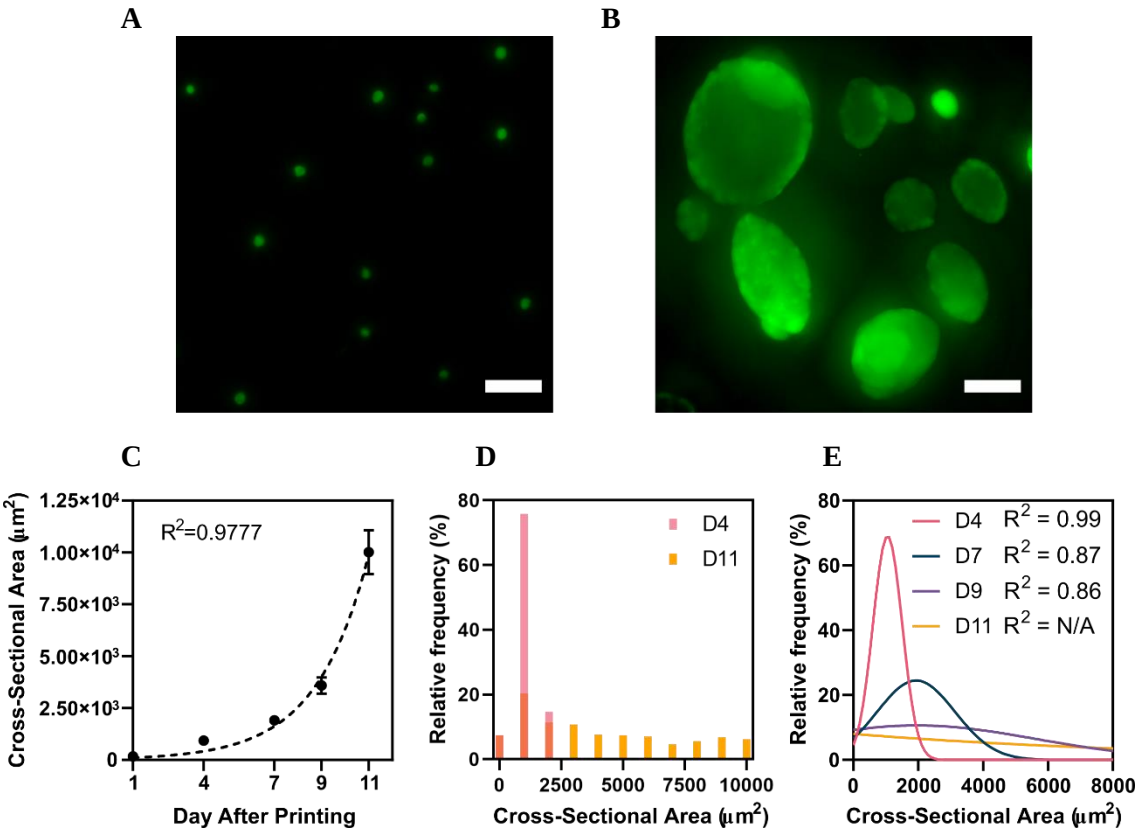

Figure 5-2 *Size distribution of bioprinted tumour spheroids in the 1A10G bioink. Live stain (calceinAM) microscopy images of SW620 spheroids 4 (**A**) and 11 (**B**) days after printing, scale bars = 100µm. **C** Mean spheroid cross-sectional area from n=3 experiments totalling 14,631 spheroids. **D** Histogram of spheroid sizes 4 and 11 in culture. **E** Gaussian-fits to spheroid size histograms at days 4,7,9 and 11.*

The automated imaging script described in section **2.8.1** and the image analysis program described in section **2.15** were used to rapidly image each plate and calculate the cross sectional area of spheroids. Here, an average of 4877 spheroids were measured per 96 well plate, totalling 14,631 spheroids for the experimental triplicate, or ~51 spheroids per well, although the number of measured spheroids is lower than the real number of spheroids, as the analysis code discriminates against objects which are difficult to measure (*e.g.* very dark objects, merged objects, and objects which contact the image boundary).

When plotting the average spheroid size at each timepoint, a clear exponential trend exists, with the experimental data fitting an exponential function with an R^2 of 0.978 (**Figure 5-2**, **C**). This growth relationship is expected of tumour spheroid growth, which is known to be exponential in spheroids of small-to-medium size[251], only plateauing *in vitro* when spheroids outgrow their nutrient supply due to lack of vasculature. More specific mathematical models exist for describing

tumour spheroid growth, namely the Gompertz model[251], whereby growth initiates in an exponential state, but decays over time, forming an S-shaped curve which accounts for the tendency of tumour spheroids to reach a limiting size ("asymptotic volume"). However, reaching such a limit requires very long cultures, sometimes exceeding 1 month[252]. As such, a Gompertzian curve could not be fit to the experimental data as the asymptotic volume of tumour spheroids was never reached. Therefore, despite hypoxic cores, SW620 spheroid growth curves indicate that tumour spheroids are provided with adequate nutrients for unperturbed in this 11-day assay, where media changes occur alongside imaging at days 4,7,9 and 11, with all experimental timepoints existing within the spheroid exponential growth phase.

An advantage of using imaging to monitor spheroid growth is that individual spheroid measurements can be collated to understand population dynamics. As spheroids in the 1A10G bioink grow from single cells through division, variance in spheroid size is expected, which arises from cellular heterogeneity where certain subpopulations, and therefore certain spheroids, may proliferate more rapidly in 3D. Experimentally, it was observed that spheroids at early timepoints were tightly distributed in size (**Figure 5-2**, **A**), and spheroids at later timepoints exhibited wider size distributions (**Figure 5-2**, **B**), made apparent when overlaying histograms of early and late timepoints (**Figure 5-2**, **D**).

Fitting Gaussians to such histograms shows how size distributions evolve over time (**Figure 5-2**, **E**). Here, a peak initially exists around ~30-40μm in diameter (~1000-2000μm^2 area) at day 4 where spheroid size is tightly distributed (σ = 441μm^2), closely fitting a normal distribution (R^2>0.99). This peak shifts downward and to the right at later timepoints, showing a broadening in spheroid size distributions, with the standard deviation increasing to σ_{D7} = 1201μm^2 and σ_{D9} = 3689μm^2, resulting in larger error bars at later timepoints in spheroid growth curves. The quality of the Gaussian fit decreased at later timepoints (R_{D4}^2>0.99, R_{D7}^2=0.87 and R_{D9}^2=0.86), with the D11 timepoint not fitting a Gaussian distribution. Other distributions, such as the Lorentzian, or the sum of two Lorentzians or Gaussians, did not produce improved R^2 values. As such, it is unlikely that spheroid sizes at later timepoints are multi-modal.

Collectively, these data suggest that cellular heterogeneity within the SW620 cell line results in a range of spheroid growth rates in the 1A10G bioink. At longer timepoints the cumulative effect of differing growth rates results in a highly disperse set of spheroid sizes, furthermore, as spheroids growing in culture compete with one another for nutrients and oxygen, it is likely that differences in growth rate widen due to competition increasing scarcity. For instance, hypoxia staining and glucose measurements described in chapter 4 showed significant decreases in both oxygen and glucose in 3D culture. Consequently, differences in growth rates may be further compounded by access to higher concentrations of oxygen and glucose.

5.5 High throughput measurements of CRC spheroid growth-curves

Having developed a high throughput bioprinting approach for tumour spheroid culture and tested it by characterising the growth behaviour of untreated SW620 spheroids, three other CRC lines were also analysed: LS174T, SW480 and CACO2. These lines were selected to establish a panel of four CRC lines for later spheroid chemotherapy screening.

LS174T , SW480 and CACO2 cells were bioprinted using the 1A10G bioink into 96 well plates, and their size monitored over 11 days *via* microscopy, similarly to SW620 cells (**Figure 5-3**, **A**). Here, the growth of all lines were exponential, as with SW620, with R^2 values of $0.88<R^2<0.99$. However, by day 11, LS174T spheroids were significantly smaller on average than the other three CRC lines, with differences in size between the other lines being non-significant. Examination of the spheroid distribution showed similar trends to SW620 data, with spheroid sizes at day 4 being tightly distributed but becoming more disperse toward day 11, resulting in growth histograms becoming right-shifted, flatter, and wider at later timepoints (**Figure 5-3**, **B-D**). Interestingly, for LS174T spheroids, the best fit was generated with a bimodal distribution, with R^2 increasing from $R^2=0.84$ to $R^2=0.93$ with the bimodal fit (**Figure 5-3**, **D**). This observation aligns with imaging data in which LS174T spheroid cultures appear to contain a small population of spheroids much larger in size than the average, becoming more apparent at later timepoints (**Figure 5-3**, **E-F**, white arrows). Moreover, whilst some LS174T spheroids grew noticeably larger than the mean spheroid size, other spheroids remained the same size even at later timepoints (**Figure 5-3**, **E-F**,

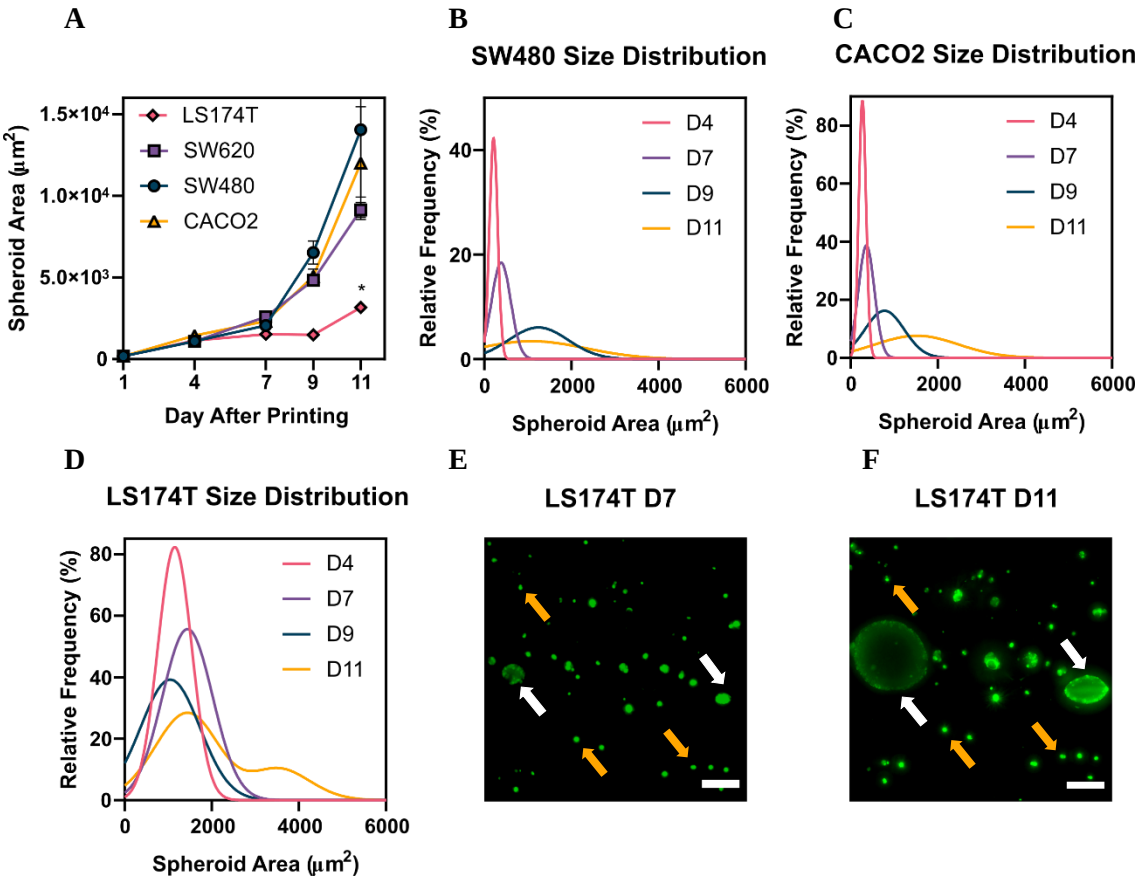

Figure 5-3 *Growth data for SW480, CACO2 and LS174T spheroids.* ***A*** *Average spheroid cross-sectional area measured 4,7,9 and 11 days after bioprinting for n=3 experiments. *p<0.05 for one-way ANOVA with Tukey's post hoc test.* ***B-D*** *Size distribution of SW480 (**B**), CACO2 (**C**) and LS174T (**D**) spheroids at different timepoints. Curves represent Gaussian distribution lines of best-fit to size histograms. In all cases R^2>0.9.* ***E-F*** *Repeated imaging of the same LS174T spheroids 7 (**E**) and 11 (**F**) days after bioprinting. Green = live cells. Scale bar = 200µm. White arrows show spheroids which have grown substantially between D7 and D11 timepoints, yellow arrows show spheroids which have remained approximately the same size.*

yellow arrows). These spheroids stained positively for the metabolic live stain, calceinAM, and therefore possessed active metabolisms at all timepoints. As such, the size and staining of these spheroids suggest a subpopulation of LS174T cells grow into small spheroids, then enter a quiescent state, whereas another subpopulation grow rapidly in culture. As these observations were for untreated conditions, this quiescence is presumably responsive to the 3D culture environment. Furthermore, as this did not occur for SW620, SW480 and CACO2 spheroids, this effect is unique to the LS174T cell line.

However, LS174T spheroids were found to grow readily in Matrigel, with no such quiescence observed or reported in the literature[253,254]. As such, the unique response of LS174T cells appears

to be linked to the gel environment, suggesting that either matrix stiffness or ECM composition could play a role in driving proliferation of LS174T spheroids. Further experiments with this line in different 3D environments would be required to elucidate the effect of matrix-parameters on spheroid proliferation.

5.6 Chemotherapy dose-response

Having demonstrated an ability to monitor the size of SW620, SW480, LS174T and CACO2 spheroids over time, these CRC lines were then challenged with chemotherapy. These four cell lines were selected due to their availability and ability to grow readily in the 1A10G bioink. Moreover, these lines are reported to exhibit varying chemoresistance to the common chemotherapies: fluorouracil (5FU) and oxaliplatin (OX), in 2D culture[192].

5.6.1 Chemotherapy treatment of cell monolayers

Before treatment of tumour spheroids, cells from the four lines selected were first cultured in 2D conditions and treated with both 5FU and oxaliplatin, as a reference for later 3D chemotherapy-response. Cells were seeded at a density of $9x10^3$ cells/well of a 96 well-plate and cultured in ordinary expansion media for 24 hours before media was exchanged with drug-containing media. Then, cells were incubated with chemotherapies for 72 hours; A range of 8 drug concentrations was established by $1/3^{rd}$ serial dilution of a prepared 300μM chemotherapy solution. Drug effect was measured by crystal violet colourimetric staining of cell monolayers, with brighter staining indicating more cells in culture and therefore a smaller drug effect. Live/Dead staining was also performed to validate the cytotoxic effect of both drugs (**Figure 5-4**, **A**). Comparison of staining intensities to the vehicle control condition was performed to calculate relative viability, where 100% relative viability indicates no difference in cell number between a given treatment condition and the untreated, vehicle control group.

Plotting relative viability against log(Drug Concentration) for each cell line produced sigmoidal curves for both drugs (**Figure 5-4**, **B-E**), which are characteristic curves for dose-response data

of cells challenged with cytotoxic drugs[255]. Dose-response curves were fit to experimental data in GraphPad prism, with R^2 values between $0.91<R^2<0.99$. Here, 5FU dose-response data produced curves with extended upper asymptotic regions relative to OX, with relative viability dropping at higher drug concentrations than OX. Oxaliplatin is known to be a more toxic drug at equal concentrations to 5FU and thus the difference in response is expected and consistent with literature studies involving both drugs on CRC monolayers[256,257]. Clinically, patients undergoing chemotherapy regimens involving both drugs (*e.g.* FOLFOX: Folinic acid, 5FU and Oxaliplatin), receive higher doses of 5FU than oxaliplatin, in the region of 10-30 fold. Moreover, 5FU treatment in combined therapies is often repeated several times, whereas oxaliplatin treatment is most commonly administered once at the beginning of treatment[258–260].

GI_{50} (50% Inhibition of Growth) values were calculated from the dose-response curves, which state the concentration of the drug corresponding to a 50% reduction in cell growth compared to the vehicle control. This metric is sometimes erroneously referred to as the IC_{50} (50% Inhibitory Concentration), which is functionally identical, but has a broader definition encompassing general agonist-antagonist activity and is not specific to cell viability. The GI_{50} metric is preferred in the literature for comparing the toxicity of drugs on living cells, as it provides an indication of the expected cytotoxic effects[192]. However, analysis and comparison of GI_{50} values is unintuitive. Best-fit approaches using sigmoidal models generate estimates for log(GI_{50}), log(Standard Error) and confidence intervals, which do not translate well from logarithmic space to arithmetic space, as the logarithmic axis results in asymmetric confidence intervals in arithmetic space, *i.e.* the GI_{50} value is not the geometric mean of the standard error in arithmetic space. Consequently, simply taking the antilog of log(standard error) then adding and subtracting it to the GI_{50} is inappropriate and can result in the prediction of negative GI_{50} values. Many studies do not state uncertainty in GI_{50}, IC_{50} or EC_{50} values at all[192,261,262], whereas others will report the mean GI_{50}, calculated by taking the antilog of the mean log(GI_{50}) from three or more separate dose-response curves[263]. In this work the latter approach is used to show a measure of the spread of GI_{50} values calculated, with error stated as the standard deviation of the independent GI_{50} values (**Figure 5-4**, **F,G**).

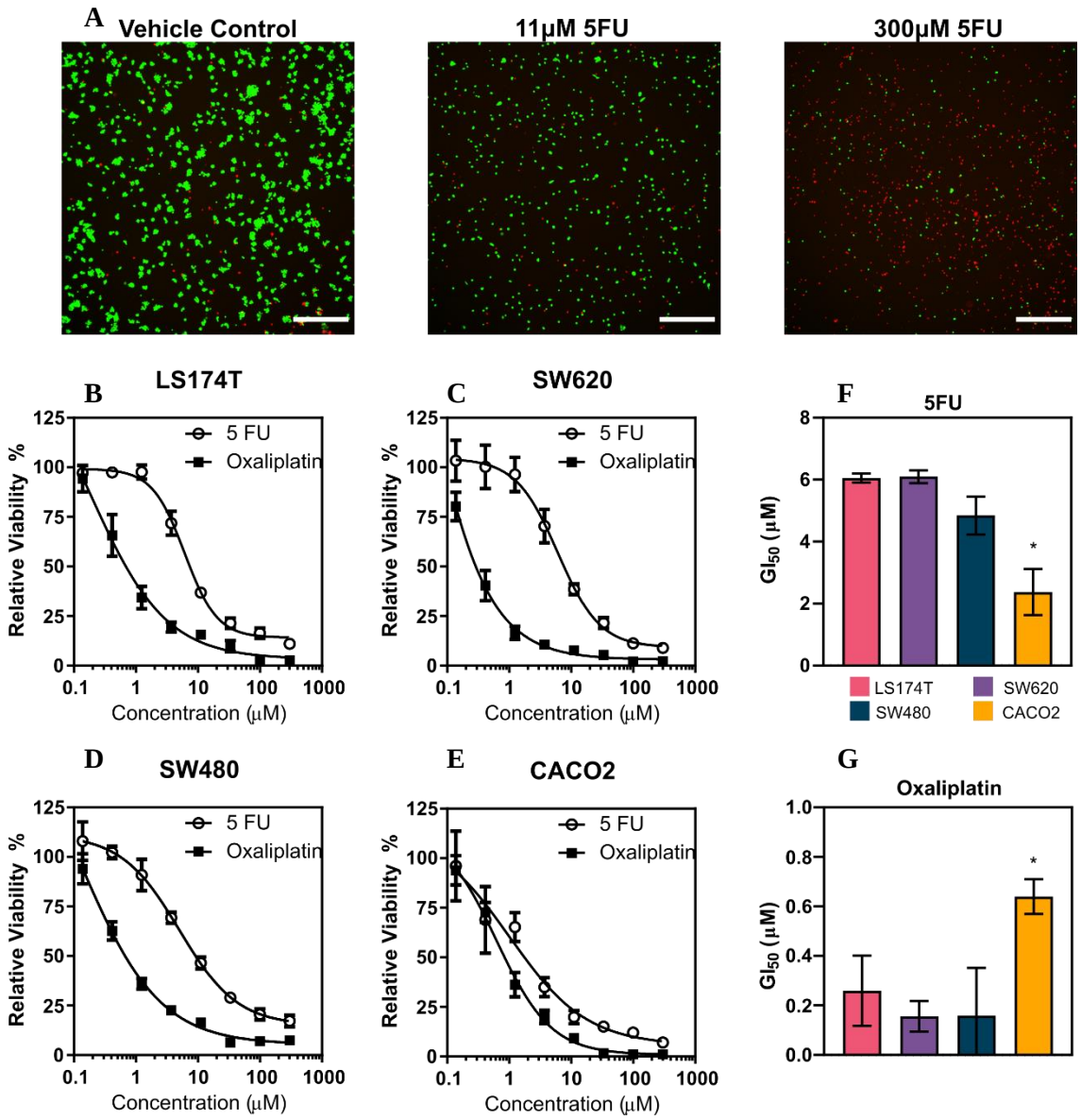

Figure 5-4 *Dose-response curves for cell monolayers cultured with chemotherapies.* ***A*** *Live (green) / Dead (red) (CalceinAM/Ethidium HomodimerIII) staining of SW620 cell monolayers of after 5FU treatment. Scale bar = 500μM.* ***B-E*** *Dose-response of four CRC cell lines in response to the common chemotherapy drugs, 5FU and Oxaliplatin.* ***F-G*** *GI_{50} values for 5FU (**F**) and Oxaliplatin (**G**) for each cell line. Data is from n=4 experiments, showing the antilog of the mean log(GI_{50}) ± S.D. of GI_{50} values.*

To compare GI_{50} values, mean dose-response curves collated from all the independent experiments were compared using an extra-sum-of-squares F test, which compares the goodness-of-fit of nested models. The null hypothesis is the simpler model that both datasets fit a sigmoid with shared a log(GI_{50}), and thus the alternative hypothesis that both sigmoids have different log(GI_{50}) values.

5FU GI_{50} values for LS174T, SW620 and SW480 were found to be similar (**Figure 5-4**, **F**), with no statistically significant differences between these lines (6.1, 6.1 and 4.8μM, respectively). CACO2 had the lowest 5FU GI_{50} at 2.4μM, which was significantly lower than all three other lines. Bracht et al.[192] conducted an extensive panel of 5FU treatments on 77 different CRC lines, following a similar protocol using a 72 hour treatment window and categorising chemoresistance as "sensitive", "intermediate" and "resistant". Here, Bracht et al. classified LS174T, SW620 and SW480 as "resistant" lines, and CACO2 as a "intermediate" line, with GI_{50} values decreasing in this order (17.9, 17.2, 6.4 and 2.5μM, respectively). No "sensitive" cell lines were readily available for this work, so CACO2 was selected as the most chemosensitive line available. Broadly, trends in the experimental data agreed with this work, with LS174T and SW620 having the highest and very similar GI_{50} values and CACO2 having the lowest GI_{50} value. SW480 5FU chemoresistance was higher than expected and was not significantly different from SW620. A number of studies in the literature report that SW620 is more resistant to 5FU than SW480[192,264,265], however, GI_{50} values were often not compared statistically. For instance, Slater *et al* report increased 5FU resistance in SW620 relative to SW480, but was not statistically significant[256].

Oxaliplatin was found to be substantially more cytotoxic than 5FU, with dose-response curves lacking an upper asymptotic region and showing decreased viability even at the lowest concentrations tested (0.137μM and 0.046μM). Although the dose-response curves had reasonable R^2 values, large uncertainties in GI_{50} values arose due to insufficient data points at very low concentrations. Similarly to the 5FU data, the only significant difference was between CACO2 and the other lines (**Figure 5-4**, **G**). Similarly to this work, Dahan *et al.* report that CACO2 is more resistant to oxaliplatin than SW620 and SW480, and that no difference in resistance exists between SW620 and SW480[266]. Unfortunately, no study could be found which compared oxaliplatin resistance for the four lines collectively.

5.6.2 High throughput tumour spheroid chemotherapy-response assay

Having tested and optimised a high-throughput bioprinting approach for tumour spheroid culture and characterised the dose-response behaviour of various CRC cell lines in 2D, Spheroid-dose response was measured. The timeline of this assay is critical as the timing of treatments must permit for adequate growth of tumour spheroids and therefore for the effect of treatment to measurably emerge. Previously, spheroid data listed in this work has detailed spheroid growth 4,7,9 and 11 days after bioprinting (**Figure 4-3**, **Figure 4-6**, **Figure 5-2**, **Figure 5-3**). This timeline was intentional as the initial D1-D4 culture period is sufficient for the formation of small spheroids, and the 72-hour D4-D7 period allows for spheroid treatment with the same protocol as cell monolayers. Indeed, other works involving treatment of tumour spheroids similarly apply treatments 3-5 days after the start of culture[31]. 11 days after bioprinting, cultures were stopped as spheroids grew too large to be imaged accurately.

LS174T, SW620, SW480 and CACO2 spheroids were bioprinted and cultured for 4 days before incubation with either 5FU or Oxaliplatin. Identically to cell monolayer experiments, the maximum treatment concentration was 300μM, decreasing by 1/3rd for a total of 8 doses, alongside a vehicle control condition. From imaging, the effect of treatment on spheroid growth was clear, with high doses of 5FU or oxaliplatin decreasing spheroid growth rate and causing the formation of smaller spheroids at later timepoints (**Figure 5-5**, **A**). Using the high-throughput imaging approach, spheroid sizes were calculated for each line at each timepoint and treatment condition (**Figure 5-5**, **B**). Here, differences in growth rate under different treatment conditions become apparent, with higher doses (darker lines) generally resulting in flatter curves in all cases, whereas very low doses (lighter lines) generally closely followed the control condition (yellow lines).

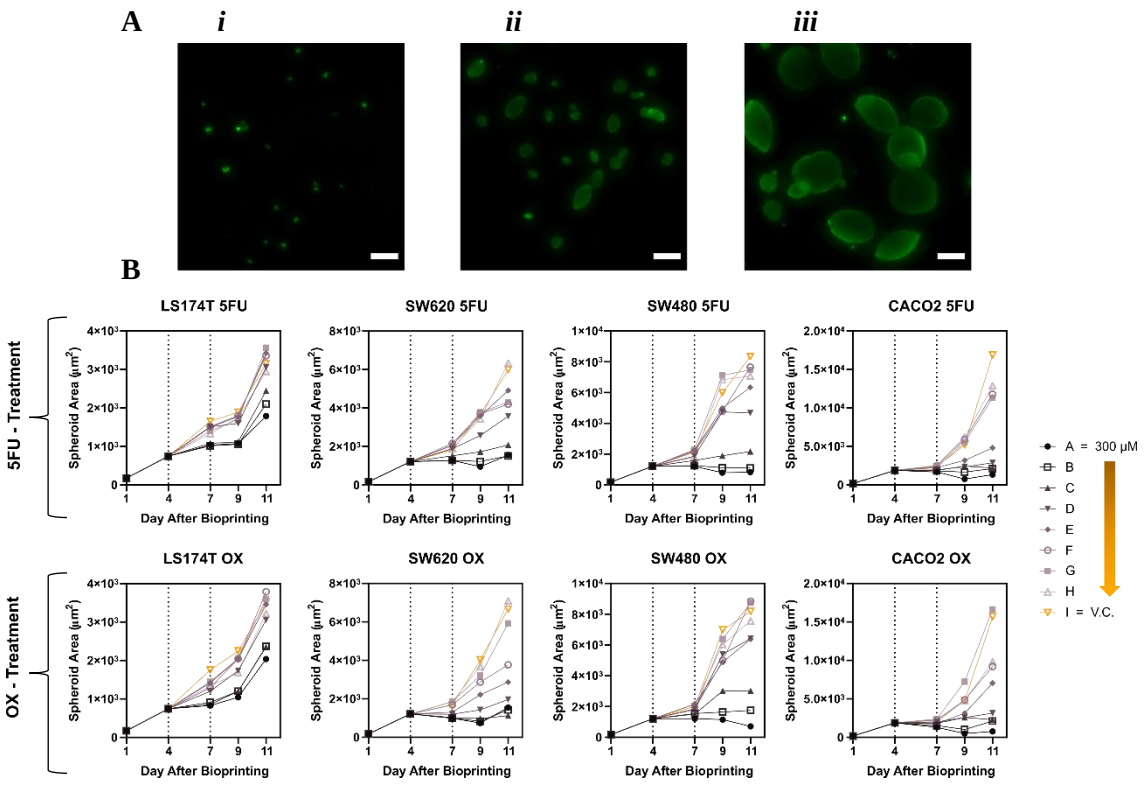

Figure 5-5 *Tumour spheroids treated with either fluorouracil (5FU) or oxaliplatin (OX).* ***A*** *SW620 spheroids 11 days after bioprinting treated with a high* ***(i)****, medium* ***(ii)*** *or low* ***(iii)*** *dose of 5FU.* ***B*** *Growth curves of 5FU and OX-treated tumour spheroids. Different coloured lines represent different treatment conditions, with darker lines indicating stronger chemotherapy doses. Dashed lines at D4 and D7 show the treatment window within which spheroids were incubated with chemotherapy. Data is for n=3 experiments, with points showing mean values; error bars removed for clarity.*

For SW620, SW480 and CACO2, high doses of both 5FU and oxaliplatin appeared to have a cytostatic effect, whereby tumour size often remained constant after treatment. Indeed, spheroids of these lines cultured under the 100µM treatment condition for both drugs were not significantly different at day 11 to the pre-treatment size. For LS174T, the mean spheroid size increased in all treatment conditions, although spheroid size at day 11 still negatively correlated with treatment concentration. Spheroid quiescence was observed in all LS174T cultures, as described in **Figure 5-3**, with this common quiescence resulting in a smaller divergence between treatment groups when compared to other cell lines. However, both treatments affected the population of rapidly proliferating LS174T spheroids, with the proportion of 'large' spheroids (at least 5-fold larger than the mean size for that treatment condition) significantly dropping from 2.2%±0.9% in the vehicle control condition to 0.1%±0.1% in the maximum, 300µM treatment ($p \approx 0.017$).

Broadly, the effective dose of both drugs can be seen by the grouping of treatment conditions in the spheroid growth curves. For instance, CACO2 spheroids treated with 5FU clearly formed two distinct treatment groups, with the four-lowest and the five-highest treatment conditions aggregating (**Figure 5-5**, **B**). Growth curves within these two groups were similar, with spheroids growing to similar sizes at day 11, with a large divide between groups. R^2 values for exponential fits were generally highest for VC and low-treatment conditions, worsening at stronger treatments and sometimes becoming negative, indicating that horizontal lines are often better models for the data than exponential functions at the highest treatment conditions. For example, in the case of CACO2-5FU, R^2 values for exponential fits decreased from 0.98 in the VC condition, to 0.09 for the maximum treatment of 5FU.

To better analyse the impact of chemotherapy on spheroid growth, spheroid size was plotted against log(drug concentration), and relative spheroid size was used to present spheroid growth as a percentage of the vehicle control (untreated) condition, similar to cell monolayer dose-response. SW620 spheroid dose-response curves were generated at day 7, 9 and 11 for both drugs to test the power of the imaging approach. Here, it was found that dose-response behaviour was measurable using spheroid area as a proxy for viability (**Figure 5-6**). Some values were above 100% relative viability for low-treatment conditions, as mean spheroid size in these samples were on average larger than the vehicle control. Such observations have been reported in the literature[267], and is likely due to the vehicle control conditions in which a small amount of the chemotherapy solvent (*e.g. DMSO*) is added without the chemotherapy compound. The solvent concentration used is the same as for the maximum drug concentration, which is serially diluted alongside the chemotherapy itself to produce the range of conditions. As such, solvent concentrations are higher in the vehicle control than for the low treatment conditions and would explain why spheroids grow larger in these cases.

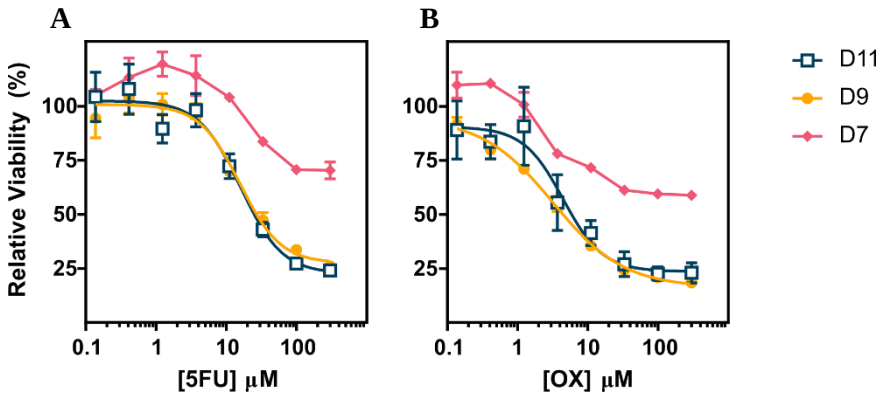

Figure 5-6 *Dose-response curves of treated SW620 spheroids at day 7,9 and 11, for both fluorouracil (5FU) (**A**) and oxaliplatin (OX) (**B**). D11 and D9 data shows size measurements and best-fit sigmoidal curves, whereas D7 data shows connected measurements as a sigmoidal curve could not be fit to the data. Data is mean values ± S.D. from n=3 experiments .*

Measuring spheroids at different timepoints produced different dose response curves (**Figure 5-6**). Here, it was found that measuring spheroids immediately after treatment (*i.e.* at day 7) was not sufficient to reliably fit dose-response curves to spheroid growth data. Moreover, as the maximum drop in relative viability was sometimes less than 41%, an absolute GI_{50} value could not always be calculated for this timepoint as the line $y = 50\%$ does not necessarily intersect D7 dose-response curves. Dose-response curves for D9 and D11 were very similar, suggesting that the dose-response behaviour in this assay may trend toward a steady-state. In this work, the D11 timepoint was used throughout for generating dose-response curves and for GI_{50} calculation, however, this data suggests that this assay could be terminated at the D9 timepoint and still produce robust data.

Having demonstrated that the high-throughput image-based approach is appropriate for evaluating drug-response of bioprinted tumour spheroids, chemoresistance of tumour spheroids of all four lines to both 5FU and OX was measured. Dose-response curves at the D11 timepoint were generated and GI_{50} values calculated as described earlier and compared to cell-monolayer performance. All CRC spheroids fitted dose response curves (**Figure 5-7**, **A**, yellow curves), although R^2 values were lower than for cell monolayers, with $0.73<R^2<0.87$ for spheroid curves and $0.91<R^2<0.99$ for cell monolayers. The poorer fits were due to larger uncertainty in spheroid

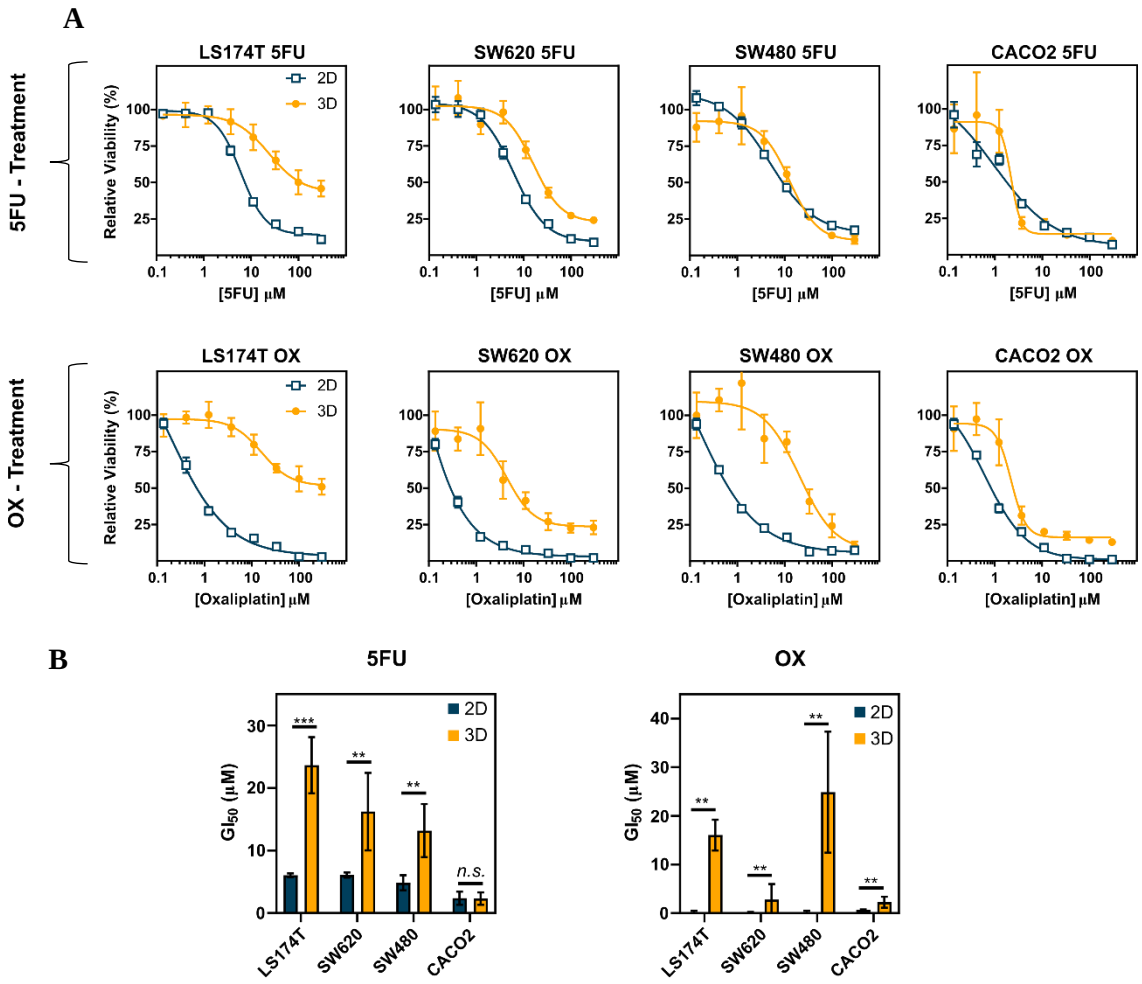

Figure 5-7 *Chemotherapy response of bioprinted tumour spheroids, compared to cell monolayers.* ***A*** *Dose-response curves for cancer spheroids and cancer monolayers treated with either fluorouracil (5FU) or oxaliplatin (OX). Data is mean±s.d. for n=3 (3D) or n=4 (2D) experiments.* ***B*** *GI_{50} values for 5FU and OX treatment for tumour spheroids (yellow bars) and cell monolayers (blue bars). Data is the antilog of the mean log(GI_{50}) ± s.d. $^{*}p<0.05$, $^{**}p<0.01$, $^{***}p<0.001$, for extra-sum-of-squares F test comparing the log(GI_{50}) of 2D and 3D dose-response curves.*

measurements relative to 2D data, as shown by the larger error bars in spheroid data. This highlights the challenge of working with 3D assays generally, where performing accurate measurements is inherently more challenging than for the established cell monolayer model, about which most assays have been optimised. However, collectively these data demonstrate that this approach produces reasonable dose-response curves for multiple CRC lines and is therefore likely extendable to all bioprinted tumour spheroid models.

Relative to 2D data, 3D dose-response curves are generally right-shifted, with an extended upper asymptote, increasing the GI_{50} concentration and indicating enhanced chemoresistance.

Cell Line	*Treatment*	*2D GI_{50} (μM)*	*3D GI_{50} (μM)*	*Fold Increase*
LS174T	5FU	6.05±0.29	23.64±4.50	3.91
SW620	5FU	6.09±0.41	16.22±6.19	2.66
SW480	5FU	4.84±1.22	13.17±4.24	2.72
CACO2	5FU	2.37±1.06	2.31±0.99	0.97
LS174T	OX	0.26±0.25	16.06±3.17	62.04
SW620	OX	0.16±0.09	2.79±3.21	17.71
SW480	OX	0.16±0.34	24.87±4.24	156.77
CACO2	OX	0.64±0.14	2.26±1.15	3.53

Table 5-1 *GI_{50} values for cell monolayers and tumour spheroids.*

Moreover, this effect was more pronounced in oxaliplatin treatment than 5FU treatment, whereby 3D dose-response curves exhibited an extended upper asymptotic region relative to 2D.

GI_{50} values were calculated from spheroid dose-response curves in the same way as for cell monolayers. Here, the right-shifting of spheroid dose-response curves relative to cell monolayers was commensurate with significant increases in GI_{50} for both drugs (**Figure 5-7**, **B**). In all cases, with the singular exception of CACO2-5FU, chemoresistance increased in 3D as shown by significantly higher GI_{50} values. In the case of 5FU treatment, GI_{50} values for spheroids followed the same trend as for cell monolayers, with LS174T having the highest GI_{50}, followed by SW620, SW480 then CACO2. However, in OX treatment, spheroid GI_{50} values did not follow the same trend as cell monolayers: CACO2 was the most resistant to oxaliplatin in 2D and was the least resistant to oxaliplatin in 3D.

GI_{50} increases were more prominent for OX-treated spheroids than for 5FU-treated spheroids, with the mean significant GI_{50} fold-increase between spheroids and cell monolayers being 3.1-fold for 5FU and 60.1-fold for oxaliplatin. The highest increase in GI_{50} was recorded for SW480-OX, increasing from 0.16μM to 24.87μM. GI_{50} values and fold-increases for other cell lines are listed in **Table 5-1**.

Collectively, dose-response data for bioprinted tumour spheroids suggests that spheroids in the bioprinted environment are more resistant to chemotherapy than cell monolayers. Differences in chemoresistance in these two models can be attributed to a variety of factors. First, diffusivity

limitations of the two chemotherapy drugs through the 1A10G bioink may impede effective treatment of all the spheroids in culture. Secondly and likewise, the physical structure of spheroids themselves may cause a chemotherapy gradient to exist within the spheroid, preventing adequate treatment of cells in the spheroid core. Third and finally, the 3D environment may be selecting for a more chemoresistant population of CRC cells, over time leading to the formation of chemoresistant spheroids independent of the chemotherapy treatment.

Unpacking these potential factors is challenging as cancer chemoresistance is multifaceted. The staining procedures used in this work have demonstrated that high molecular weight stains (phalloidin-TRITC, 1200g/mol), low molecular weight stains (DAPI, 277g/mol) and oxygen exist in gradients in the spheroid structure, even for permeabilised spheroids. However, the diffusion and uptake of pharmacological compounds is more complex. 5FU, when administered clinically, is largely catabolically metabolised hepatically into inactive degradation products, or excreted unchanged in urine; In sum, greater than 90% of administered 5FU is ultimately excreted in urine either unchanged or as the terminally catabolised inactive product, α-fluoro-β-alanine (FBAL)[268]. As a uracil analogue, 5-FU is actively transported into cells using uracil transport pathways[269], where 1-3% is anabolised into active cytotoxic agents, principally FdUMP (fluorodeoxyuridine monophosphate)[268], which forms a complex with thymidine synthase, inhibiting DNA synthesis[270]. The complexity of this interaction is not well recapitulated in *in vitro* models, as the catabolism of 5FU is driven by the hepatic enzyme dihydropyrimidine dehydrogenase (DPD), which is not present in CRC cells.

Oxaliplatin is more readily absorbed than 5FU, which, after intravenous injections, readily forms many different compounds that bind to blood or cell proteins, such as albumin, haemoglobin, and cysteine[271]. After infusion, oxaliplatin blood concentration decreases rapidly due to its high reactivity and the half-life of intact oxaliplatin as measured by blood concentration from patients post-infusion has been measured as 14.1 minutes[272]. This half-life is similar to that of 5FU, which is estimated to be between 8-20 minutes[273], however, the short half-life of 5FU is a result of its degradation into inactive products in the liver, whereas the short half-life of oxaliplatin is a result

of its high reactivity with organic macromolecules. Oxaliplatin enters cells through a combination of passive diffusion and active transport. The exact set of transport proteins is not known, but is thought to include copper transporters[274] and organic cation transporters[275]. Within cells, oxaliplatin and other platinum-based chemotherapies are thought to act primarily through the formation of platinum-DNA adducts, known as DNA lesions, in which platinum acts as a DNA crosslinker[276].

For both drugs, active transport and passive diffusion play a role in drug uptake. Passive diffusion is known to be related to the lipophilicity of the compound[277], as cell membranes are composed of a lipid bilayer. Lipophilicity of a molecule can be measured by the partition coefficient, P, which states the relative affinity of a molecule to hydrophilic and lipophilic phases, typically 1-octanol and water. Here, 5FU is reported to have the greater P value of 0.14 (logP = -0.85), whereas oxaliplatin has a reported P value of 0.04 (logP = -1.39)[263].

As diffusion plays a greater role in the bioprinted spheroid model than the cell monolayer model, the difference in the partition coefficient of these drugs could explain why oxaliplatin resistance increased in 3D more than 5FU resistance. Here, the greater lipophilicity of 5FU increases the diffusivity of 5FU into spheroids, permitting higher effective doses of 5FU than oxaliplatin, leading to a greater relative increase in GI_{50} for oxaliplatin.

Active transport of chemotherapies is also significant. As 5FU and oxaliplatin have distinct and separate mechanisms of action, genetic or epigenetic changes due to the spheroid microenvironment could impact chemoresistance of one drug more than another and therefore contribute toward increased GI_{50} in 3D. Ideally, a large qPCR panel would be used to investigate treated and untreated tumour spheroids and cell monolayers, incorporating genes associated with chemoresistance to both 5FU and oxaliplatin. Such a qPCR assay was planned but not carried out. A challenge with performing qPCR with 3D assays is providing high-purity DNA as dissolved gel components can contaminate lysates and result in poor amplification. A qPCR assay was designed and successfully tested using the TBP housekeeping gene, which was successfully amplified from spheroid-lysate (Appendix **D**), but disruption due to COVID-19 prevented testing

this further. Consequently, it is unknown whether drug-associated active transport (both for influx and efflux) proteins are up- or down-regulated in spheroids relative to cell monolayers, and therefore the extent to which active transport contributes to chemoresistance in 3D is unclear.

5.7 SW620 spheroid chemoradiotherapy-response assay

Having demonstrated the applicability of high throughput tumour spheroid bioprinting to chemotherapy-response assays, a chemoradiotherapy assay was designed to test whether the bioprinted model could be broadly extended to more complex, multimodal therapies. Two radiation doses, 2.5 and 5 Gray (Gy) were used in conjunction with the GI_{50} value for 5FU calculated in section **5.6.2**. These doses represent clinically relevant values, with 5Gy being a common maximal radiation dose which is generally not exceeded in a single radiotherapy session[278]. For spheroids, radiation exposure was broadly synchronous with chemotherapy application, occurring roughly 1hr after chemotherapy treatment. Ojima *et al.* studied the timing of radiotherapy in combined chemoradiotherapy treatment of colorectal cancer cells and concluded that for most CRC cells, there was no difference between radiotherapy pre- or post-chemotherapy[197]. Radiation exposure times were calculated using the known half-life of Caesium-137 ($^{137}55Cs$), which was used as the radiation source, and are listed in section **2.14**. For cell monolayers, data was kindly provided by Ms. Tracey Collard, who previously performed radiation-exposure experiments with the same SW620 cells used in this work.

SW620 Spheroids were found to be responsive to radiotherapy, with the 5Gy treatment group being visibly smaller at D11 when compared to untreated spheroids (**Figure 5-8**, **A**). 2.5Gy was less effective, with differences in spheroid size not being readily apparent. Combination therapy of both radiation with chemotherapy was also effective, with a clear reduction in spheroid size relative to untreated spheroids.

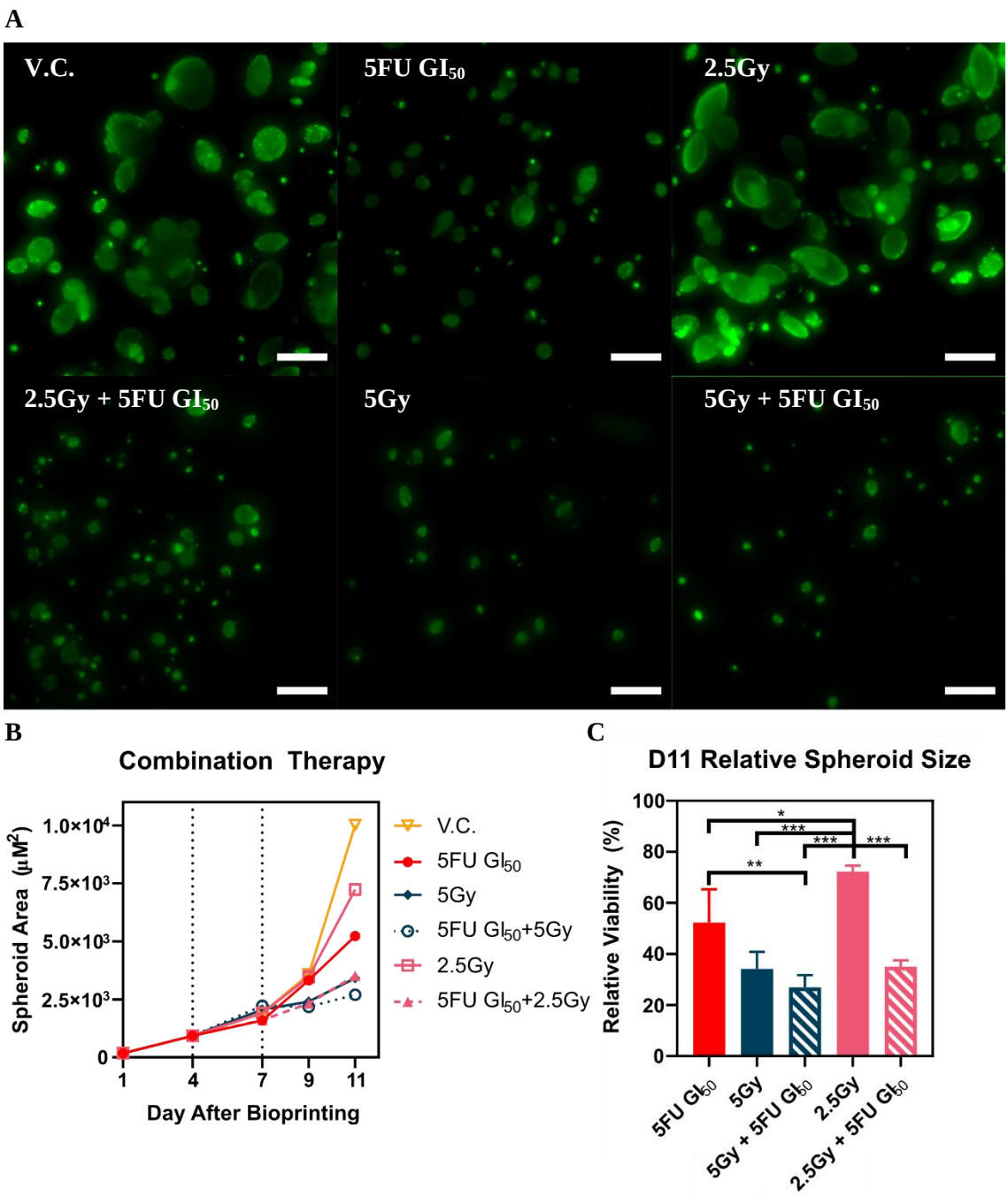

Figure 5-8 *Dose-response of SW620 spheroids to radiation, chemotherapy, and combination therapy.* ***A*** *Widefield microscopy of live-stained (calceinAM) SW620 spheroids in different treatment groups. V.C. = vehicle control, 5FU = fluorouracil. Gy = Gray. GI_{50} = 50% inhibition of growth. Scale bar = 300μM.* ***B*** *Growth curves of spheroids treated with radiation, chemotherapy and chemoradiotherapy for n=3 experiments. Error bars removed for clarity.* ***C*** *Relative viability in the different treatment groups, representing the mean spheroid size as a proportion of the mean spheroid size in the control group. *p<0.05, **p<0.01, ***p<0.001 for one way ANOVA with Tukey's multiple comparisons post-hoc test.*

Growth curves and relative viabilities were calculated for SW620 spheroids using the same imaging approach as applied in section **5.6.2**. Similarly to spheroid chemotherapy growth curves, spheroid radiotherapy and chemoradiotherapy growth curves diverged from the vehicle control

(untreated) condition over time (**Figure 5-8**, **B**). Radiotherapy is known to be a treatment which, for *in vitro* assays with cancer cell lines, requires early treatment and long culture times to produce a measurable effect, with some studies using a 21-day timeline for radiotherapy studies with cell monolayers[279]. This work supports this trend, with no significant differences in spheroid size for radio- and chemoradiotherapy treated spheroids 72 hours after treatment, and the impact of radiotherapy emerging over time.

Spheroid sizes at D11 were compared to the vehicle control to calculate relative viabilities (**Figure 5-8**, **C**). Here, the GI_{50} value for 5FU calculated earlier was appropriate, *i.e.* spheroids treated with the GI_{50} concentration were on average 52.3%±13.1% of the size of untreated spheroids. All the treatment conditions produced spheroids statistically significantly smaller than the untreated condition, however, there was significant variation between the different treatment groups. Here, the least effective treatment was the 2.5Gy radiotherapy, causing only a small reduction in spheroid size (72.3%±2.3% of the V.C.). 5Gy, the highest radiation dose, produced a much larger reduction in spheroid size (34.6%±6.8% of the V.C.), which interestingly appeared to be proportionate, as doubling the radiation dose resulted in twice the decrease in spheroid growth.

Relative to cell monolayers, spheroids were significantly more resistant to irradiation (**Figure 5-9**, **A**). SW620 spheroids and cell monolayers were irradiated with 2.5Gy and the surviving fraction of cell monolayer compared to the relative viability of irradiated spheroids; relative viabilities were 54.0%±9.5% and 72.3%±2.3% for cell monolayers and spheroids, respectively. As the effects of ionising radiation can sometimes be seen in electron micrographs, *via* abnormal mitochondrial morphology, irradiated and untreated spheroids were harvested 11 days after bioprinting (7 days after treatment), fixed and embedded in a BSA gel for sectioning, staining, and imaging *via* TEM. Mitochondria are known to shrink and express fewer cristae after irradiation[280], however, electron micrographs of untreated and irradiated (5Gy) spheroids showed no such distortion of spheroid mitochondria (**Figure 5-9**, **B-C**). Ionising radiation causes the formation of reactive oxygen species (ROS) which are harmful to cells. However, lower oxygen

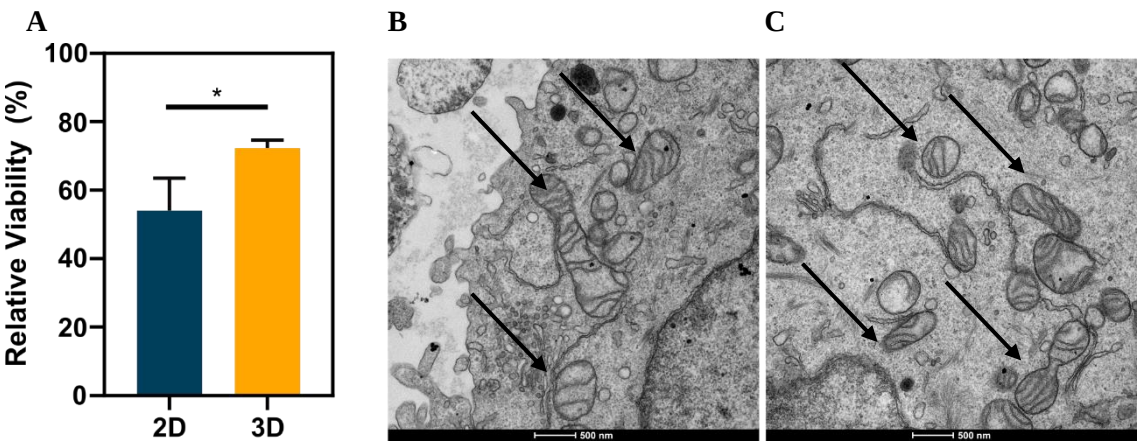

Figure 5-9 *Effect of radiation on cell monolayers and tumour spheroids.* ***A*** *Relative viability for SW620 cell monolayers and spheroids irradiated with 2.5Gy. *, p<0.05, determined by Student's T test.* ***B-C*** *Electron micrographs (TEM) of mitochondria (arrows) of an untreated (**B**) and irradiated (**C**) spheroids (5Gy).*

concentrations can inhibit ROS formation and therefore reduce the effect of radiotherapy. Indeed, lower oxygen concentrations within tumours *in vivo* is a significant factor in the clinical application of radiotherapy[281]. As spheroids in the 1A10G bioink have exhibited oxygen gradients and hypoxic regions, this may be the cause of the observed increased in radioresistance of SW620 spheroids.

Clinically, 5FU and radiotherapy can be combined as multimodal therapy for CRC. For this therapy, 5FU acts as a "radiosensitiser", supporting radiotherapy which is typically the primary treatment. Here, the combined 5FU/radiotherapy spheroid assay was designed to test whether similar radiosensitisation could be measured in tumour spheroids using the high throughput bioprinting approach. Results of combined therapy did show increased efficacy when 5FU and radiation were combined, with both 5Gy+5FU and 2.5Gy+5FU being statistically significantly more effective that 5FU alone, as determined by one-way ANOVA. However, it is unclear if a synergistic effect was taking place between 5FU and radiation in these treatments. The most prominent theory behind the radiosensitisation effect of 5FU is that TS inhibition caused by 5FU impairs DNA repair and therefore enhances radiation-induced DNA damage[282]. Consequently, the timing and dosage of 5FU treatment becomes significant, with both long-term, low concentration 5FU treatment prior to irradiation[283] and short-term, high concentration 5FU prior to irradiation being effective[279]. Specifically, Valdes *et al.* report that a 1mM 5FU treatment, one

hour before irradiation, is sufficient to cause a radiosensitisation effect in radioresistant cancer lines[279].

In this work, 5FU treatment occurred 4 days after bioprinting, approximately one hour before irradiation, and continuing after irradiation for ~72hours. Irradiation was applied on day 4, after 5FU treatment, to both allow for a 5FU radiosensitisation effect, and also to provide as much time as possible for radiation damage to accrue and produce measurable changes in spheroid size. However, it could be the case that irradiating later would be more effective, as it would provide more time for 5FU-induced TS inhibition to occur and thus increase any radiosensitising effect, although this would be at the cost of decreased culture time post-irradiation, which is necessary for the measurable emergence of radiation cytotoxicity. Additional experiments altering the timing of chemotherapy would be required to optimise a radiosensitising protocol for tumour spheroids.

5.8 Flow cytometry of SW620 spheroids

Chemotherapy of bioprinted tumour spheroids revealed increased chemoresistance in the 3D setting. In the cancer stem cell (CSC) model, chemoresistance in tumours is attributed to a population of resistant and proliferative cells which survive chemotherapy and continue to proliferate. Such populations would explain the prominence of recurrent cancer, as the CSC population would effectively be untreated. Identifying CSCs in CRC is an ongoing pursuit, as CSC biomarkers appear to vary between cancer types. A number of putative biomarkers exist for CSCs in CRC, with the most common being CD133 and CD44, discovered due to their prognostic power, being linked with poorer patient outcomes[49]. SW620 is an appropriate cell line for the quantification of these markers, as it is known to express both CD133 and CD44[171,284].

A flow cytometry assay was developed for tumour spheroids to measure the population of $CD133^+$ and $CD44^+$ cells and compare these to cell monolayers. Grown SW620 spheroids were harvested from the bioink 11 days after bioprinting, dissociated to form single cell suspensions,

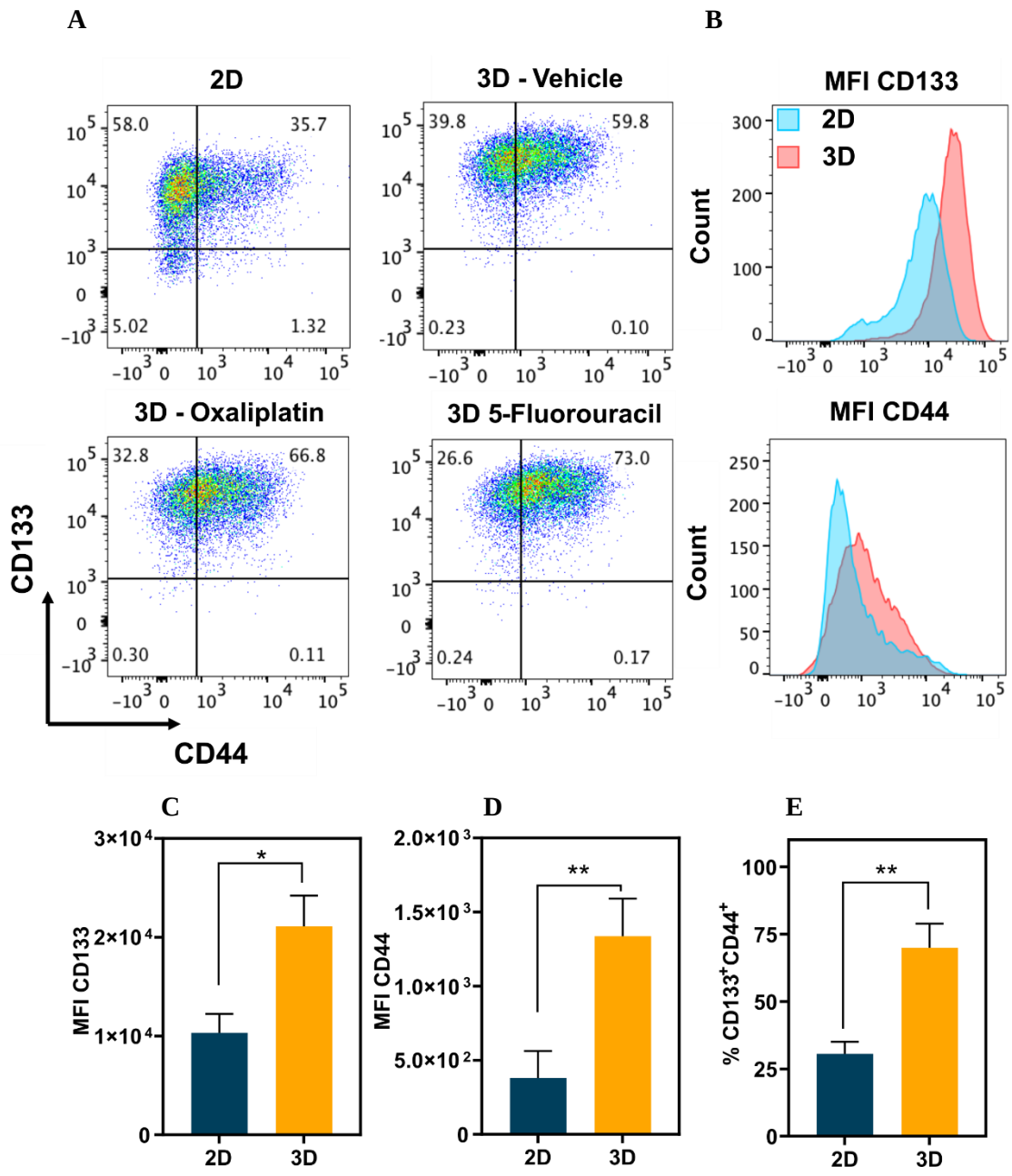

Figure 5-10 *Flow cytometry of tumour spheroids and cell monolayers.* ***A*** *Representative CD44/CD133 plots showing the distribution of subpopulations in 2D culture and 3D culture, with and without treatment with fluorouracil (5FU) and oxaliplatin (OX).* ***B*** *Mean fluorescent intensity (MFI) of CD133 (upper) and CD44 (lower) staining in 2D and 3D culture. 3D data is grouped from all three treatment conditions.* ***C-D*** *Comparison of MFI values from the plots in* ***B****, between 2D and 3D culture for n=3 experiments. *; 0.05<p, **; 0.01<p from Welch's unpaired t-test.* ***E*** *Comparison of the double $CD133^{+}CD44^{+}$ population in 2D and 3D for n=3 experiments. *; 0.05<p, **; 0.01<p from Welch's unpaired t-test.*

stained with anti-CD133 and anti-CD44, then measured with flow cytometry. These spheroids were in three treatment groups: V.C. (untreated), 5FU GI_{50}-treated, and Ox GI_{50}-treated, using the GI_{50} values calculated in section **5.6.2**. Initially, this assay resulted in low cell counts and poor viability of harvested cells, however, improvements were made which increased viability and cell

count to satisfactory levels. The final mean viability of harvested spheroid-derived cells was 86.9%±3.3%, compared with 94.2%±2.1% for cell monolayers; The optimised protocol is listed in section **2.12**. Positive and negative populations were quantified using gating, whereby the final quadrants were established from 2D data.

Flow cytometry data revealed a marked difference between the distribution of both CD133 and CD44 in 2D and 3D. SW620 monolayers exhibited distinct subpopulations in the 3 of the 4 quadrants, with an extremely small $CD44^+/CD133^-$ population (**Figure 5-10**, **A**). Relative to cell monolayers, distribution of CD133 and CD44 from tumour spheroids exhibited subpopulations in just two quadrants: $CD44^+/CD133^+$ and $CD44^-/CD133^+$. Notably, $CD133^-$ populations were absent in spheroid culture, with the mean $CD133^-$ population being 0.33%±0.11%. Interestingly, there were no statistically significant differences in quadrant distribution between the 3D treatment conditions; However, differences between 2D and 3D culture were significant.

Fluorescence intensity for both CD133 and CD44 were higher for spheroid-derived cells than cell monolayers (**Figure 5-10**, **B**), with statistically significant increases in MFI for both stains (**Figure 5-10**, **C-D**). $CD133^+$ populations increased from 89.8%±3.8% to 99.7%±0.10% in 3D, and $CD44^+$ populations increased from 32.7%±9.0% to 72.5%±5.8%. Consequently, the double positive population, $CD44^+/CD133^+$, saw the largest significant change, increasing from 30.6%±4.5% to 72.3%±5.8% in 3D (**Figure 5-10**, **E**).

Collectively, these data demonstrate that $CD133^+$, $CD44^+$ and $CD44^+/CD133^+$ populations are increased in the bioprinted spheroid culture relative to 2D. As treatment with both 5FU and OX did not significantly change the distribution of these populations relative to the untreated population, the 3D culture conditions and spheroid microenvironment must be responsible for the change in expression of these CSC markers. Here, it is possible that the 3D culture conditions select for $CD133^+$, $CD44^+$ and $CD44^+/CD133^+$ cells, whereby these cells preferentially grow into spheroids in the 1A10G bioink. To test this hypothesis, the $CD44^-/CD133^-$ population could be sorted via flow cytometry and used in spheroid culture to determine if spheroid formation is impeded. Alternatively, expression of CD133 and CD44 could change over time in response to

the 3D environment. For instance, CD44 is a known ECM-binding receptor[64], which could be upregulated here in response to the lack of ECM in the surrounding bioink. CD133 is known to be upregulated in hypoxic conditions by HIF1A[59], which could explain its enrichment in hypoxic spheroids.

CD133 expression in particular is associated with higher 5FU resistance in CRC cancer lines[285] and increased tumorigenicity, with $CD133^+$ CRC cells growing into larger tumours when implanted into SCID mice[286]. CD133 expression in CRC and oxaliplatin resistance is less studied *in vitro,* however, Asadzadeh *et al.* increased the sensitivity of HT-29 cells to oxaliplatin *via* siRNA-induced CD133 silencing, suggesting a link between CD133 and OX resistance[287]. CD44 expression is also associated with increased drug resistance, with Dallas *et al*. producing 5FU- and OX-resistant HT-29 cells, which exhibited a 2-fold enrichment of $CD44^+$ cells[288]. Here, Dallas *et al*. also found that CD133 enrichment occurred at a higher rate than CD44, with the 2-fold increase in CD44 expression commensurate with a 16-30-fold enrichment in $CD133^+$ cells. Similar observations have been reported in 3D by Cho *et al.* who found that Lgr5, CD44, CD133 and CD166 were enriched in 5FU-resistant murine organoids, with a 4-fold increase in CD133 expression and a 50% increase in CD44 expression[289]. In this work, SW620 cells highly expressed CD133 in standard monolayer culture, precluding the possibility of measuring large fold-increases in CD133 *via* flow cytometry. To determine if CD133 expression increased more in spheroid culture than CD44 expression, mRNA for these proteins would have to be quantified and compared.

In summary, SW620 spheroids were CD133 and CD44 enriched as a result of 3D culture conditions. Enrichment of these proteins is strongly linked to increase chemoresistance both clinically and in *in vitro* studies with CRC cell lines, consequently, these results suggest that increased expression of CSC markers in 3D could be an important factor in the increased resistance of tumour spheroids to 5FU and oxaliplatin relative to cell monolayers. However, further experiments measuring the dose-response of $CD44^-$ and $CD133^-$ spheroids to these drugs would be required to elucidate this resistance mechanism.

5.9 Conclusion and Discussion

In this chapter, the 1A10G bioink developed in chapter 3 was successfully used in a novel high-throughput bioprinting assay to measure chemotherapy, radiotherapy and chemoradiotherapy response of tumour spheroids. Here, the utility and power of the high-throughput system was demonstrated by the accurate measurement of chemotherapy dose-response of bioprinted spheroids from 4 different CRC lines. This approach overcomes many challenges with 3D assays, such as reliance on expensive, variable, and impractical gels like Matrigel and the lack of cell-matrix interactions found in spheroid-aggregate assays. As such, this solution represents a "best-of-both-worlds", with the high-throughput characteristics of low-attachment multi-well plates commonly used in spheroid assays preserved *via* the bioprinting approach, and the systematic complexity of *in vivo* conditions simulated through the recapitulation of cell-matrix interactions and other matrix effects.

With this procedure outlined in this work, a standard assay was developed for growing and treating bioprinted spheroids with chemotherapy. Thousands of tumour spheroids were repeatedly measured over long-term cultures to produce growth curves, dose-response curves, and thereby measure chemoresistance. Spheroids grown in this assay formed a wide range of sizes due to differences in proliferation propensity arising from cellular heterogeneity. However, the mean spheroid cross-sectional area was found to be a robust metric for measuring response to chemotherapy, radiotherapy and chemoradiotherapy, outputting relevant factors such as GI_{50} values.

Bioprinted tumour spheroids exhibited enhanced resistance to the common chemotherapy compounds fluorouracil (5FU) and oxaliplatin (OX), relative to cell monolayers. The effect of chemotherapy was not immediate, rather, the growth rate of tumour spheroids was progressively inhibited by increasing doses of chemotherapy, for both 5FU and OX; At higher doses, mean spheroid size remained static until the end of the assay, 7 days after treatment. A similar effect was observed in radiotherapy, with SW620 spheroids being more resistant to radiotherapy than cell monolayers, and ionizing radiation causing reduced growth-rate in spheroid culture.

Combined radiation and chemotherapy was more effective than either treatment alone, although the extent to which 5FU acted as a radiosensitizer in these instances is unclear. Collectively, these results appear to better mimic typical clinical responses to chemotherapy and radiotherapy, which rarely result in histological complete response, *i.e.* no cancer is detectable after treatment in biopsies, but do often result in tumour shrinkage[290].

The underperformance or non-response to both novel or established therapeutics is a pressing concern in colorectal cancer, which suffers from patient non-response to neoadjuvant chemotherapy[291], high recurrence rates[292] and metastasis[191]. The popular cancer stem cell (CSC) model proposes that a population within tumours is largely responsible for chemoresistance and recurrence[293]. These CSCs are thought to proliferate at a slower rate relative to the tumour bulk but exhibit increased chemoresistance linked to the expression of CSC markers. Two putative CSC markers for CRC, CD133 and CD44 were significantly upregulated in spheroid culture, with nearly 100% of cells in spheroids expressing CD133. The enrichment of these markers was found to be entirely responsive to the 3D environment itself, as treatment with either 5FU or OX did not impact expression. Here, the spheroid model appears to better mimic *in vivo* chemotherapy response, with spheroids positive for CSC markers being difficult to eradicate in culture, instead persisting in a quiescent state or proliferating slowly.

5.10 Acknowledgement of Collaboration

Work in this chapter was completed by the author unless otherwise mentioned here. The author would like to thank Ms. Tracey Collard for providing data on the irradiation of cell monolayers, and Dr. Adam Chambers for his assistance in performing radiotherapy.

Chapter 6 : Conclusions and Future Work

6.1 Conclusions

The aim of this work was to present a robust high throughput 3D colorectal cancer (CRC) spheroid model as a possible solution to the lack of scalable, complex cancer models in the literature. The clinical utility of such a system is clear, as several landmark studies have demonstrated the efficacy of low-throughput 3D CRC models in predicting patient response to chemotherapy, addressing the pressing concern in CRC of non-responsive patients who are administered chemotherapy with no therapeutic benefits; There is no method presently existing for the identification of non-responsive CRC patients. More broadly, as a stepwise improvement over existing approaches, such a high throughput system would have a variety of uses in basic biology or pharmaceutical research, such as cancer-immune cell interactions, gut microbiome interactions with CRC, and drug discovery.

The design specifications of this system were that it should be high throughput, bioprinter-based and convenient to analyse. For bioprinting, a printable bioink was required which supported the spontaneous self-assembly of tumour spheroids from single CRC cells. Initially, the alginate/F127 bioink developed by Armstrong *et al.* was used in 3D cancer culture. As this bioink supported the long term culture of hMSCs, it was initially thought it may be suitable for cancer cells. However, cell viability of all cultured CRC lines was low in the alginate/F127 bioink. Moreover, spheroid morphology was abnormal and non-circular. Consequently, an alginate/gelatin bioink was formulated for this purpose, which was found to support spontaneous spheroid self-assembly. Electron microscopy techniques were developed for imaging the internal structure of this gel, which was found to be porous with a mean pore diameter of 3.2μm. Mechanically, this gel exhibited low stiffness values relative to the alginate/F127 bioink and were comparable to the reported stiffness of healthy intestinal tissue. As such, these results suggest that cell viability and spheroid formation is stiffness-mediated on some level. Specifically for spheroid culture, this author proposes that in stiff biorthogonal matrices, cells conform to the internal structure, in this case a porous hydrogel, resulting in abnormal morphologies. In soft matrices, forces exerted from proliferating cells can deform the matrix to permit more rounded growth. As

such, the bioink used in this work generated robust spheroid cultures in a more physiologically representative environment.

The optimised alginate/gelatin bioink was used to culture cancer spheroids in 9 CRC cell lines and two breast cancer lines, demonstrating a broad applicability of this bioink to different cancers, and therefore possibly to primary cancer cells. Protocols were developed for harvesting viable spheroids for use in other assays, an important practical feature of the bioprinted culture model. SEM, TEM and confocal microscopy revealed that bioprinted spheroids were tightly packed at small sizes, with resident cells forming intracellular junctions and displaying high nuclear:cytoplasm ratios. However, histology of larger spheroids, beyond the limiting size for confocal imaging, revealed sparsely packed spheroid cores, with little ECM deposition. Immunohistochemistry of spheroid sections demonstrated that large hypoxic regions existed in spheroid cores, correlating with the observed lower cell density. These results mimic a common feature of tumours *in vivo*, which is the formation of senescent and necrotic regions due to poor nutrient and oxygen diffusion. Collectively, these data demonstrates that spheroids grow into ordered structures in the bioprinted system, becoming hypoxic and necrotic at larger sizes due to cellular oxygen consumption, similarly to their *in vivo* counterparts.

A high throughput system was developed to extrusion bioprint spheroid cultures, measure spheroid dose-response to chemotherapy and analyse the results in a robust and automated fashion. First, gel preparation was automated *via* a custom centrifuge for complete and reproducible mixing of the bioink. Then, a custom bioprinting setting was used for 96 well plate printing, with a print time of approximately 3 minutes per plate. High content microscopy was used as the measurement system, being non-invasive and widely accessible through the use of widefield microscopes. Custom code governed the microscopy imaging procedure, taking 15minutes/plate to image all 96 samples. Finally, analysis code was written in MATLAB to measure spheroid geometries generated from the microscope data. Overall, this pipeline enabled high performance analysis of thousands of tumour spheroids, measuring individual spheroid sizes over time.

To demonstrate the utility of the high throughput approach, for the first time, bioprinted CRC spheroids were challenged with the chemotherapy drugs, fluorouracil (5FU) and oxaliplatin (OX). Here, spheroid size was found to be an appropriate measurement of spheroid response to therapy, as spheroid growth rates were reduced with increasing chemotherapy doses, causing differences in spheroid size between treatment groups at later timepoints. Using spheroid size as a proxy for drug response, dose response curves and GI_{50} (drug concentrations corresponding to 50% inhibition of growth) values were calculated. Spheroids displayed enhanced resistance to both 5FU and OX relative to cell monolayers, however, fold-increase in resistance was significantly higher for OX, than 5FU. Here, diffusivity may be decreasing drug-effect, as 5FU more readily diffuses into cell membranes than OX. However, cancer stem cell (CSC) markers associated with drug resistance may also be a factor. The putative CSC markers CD133 and CD44 are associated clinically with poorer patient outcome in CRC and increased drug resistance in *in vitro* experiments. SW620 spheroids in the alginate/gelatin bioink exhibited increased populations of both markers, independent of treatment. As such, the spheroid microenvironment and 3D culture conditions are likely selective of CSCs in this model.

Finally, multimodal chemoradiotherapies were explored using the same protocol. Here, bioprinted SW620 spheroids were found to respond to radiation via changes in size, and thus able to be measured through the same high content microscopy approach. SW620 spheroids exhibited increased resistance to radiation relative to cell monolayers and benefitted from combined treatment with 5FU. 5FU is a known radiosensitizer, which under certain timings and doses, improves the performance of radiation by inhibiting the DNA repair process and thus allowing radiation-induced DNA damage to accumulate. Radiation with 5FU was more effective than either 5FU or radiation alone, although more work is required to understand the radiosensitising effect in 3D.

This work sought to overcome the myriad of practical challenges that hamper the ultilisation of sophisticated 3D cell cultures in research and clinically. Here, a novel combination of accessible and affordable techniques and methods, including extrusion bioprinting, low-cost bioink

components, and convenient imaging platforms were amalgamated into a high throughput, automated system. This system was validated through the dose-response measurement of chemotherapies on thousands of CRC spheroid cultures. In doing so, it further demonstrated the potential of spheroid cultures as viable and highly representative platforms for CRC research and makes progress towards the long-term goal of personalized medicine in cancer care.

6.2 Future work

The potential applications of tumour spheroid bioprinting are numerous, and consequently the utility of the high throughput platform described here is high and germane to various emergent areas of basic biology and tissue engineering. The potential application and improvement of this work system is discussed here.

Cancer spheroids grown in the alginate/gelatin bioink developed in Chapter 3 were observed to form oblate structures intermittently over time. This author speculated that these morphologies arise due to heterogeneity in hydrogel stiffness, resulting in growth being directed towards the "path of least resistance" and leading to non-spherical tumour spheroid formation. This hypothesis is in line with other research on spheroid formation in hydrogels of differing stiffnesses, but further experiments should be conducted to confirm this. To test this hypothesis, future work would aim to control anisotropy within the bioink such that oblate spheroid formation could be reliably directed. This could be done through a crosslinking gradient leading to regions of different stiffness within a bioprinted construct.

In Chapters 4 and 5, grown tumour spheroid were shown to exhibited a number of features more representative of *in vivo* conditions, such as hypoxic cores and enhanced chemoresistance. The progression of CRC *in vivo* is linked with a number of genetic and epigenetic changes resulting in upregulation of oncogenes and CSC markers, and the down regulation of tumour suppressors. Although two putative CSC markers for CRC, CD133 and CD44, were measured in this work, a broad and extensive study was not undertaken. Here, a custom qPCR panel involving genes

associated with metastasis, metabolism, drug resistance, CSCs and CRC pathology would be powerful. For example, genes involved in oxaliplatin influx and efflux could be measured to determine if the observed oxaliplatin resistance in tumour spheroids had a clear genetic basis. Such a qPCR panel was intended but interrupted due to the impact of sars-cov-2, but initial experiments were successful in extracting and amplifying DNA from spheroid lysates (Appendix **F**).

The prevalence of CSCs in spheroid growth and drug resistance was interesting, with nearly 100% of SW620 cells in spheroids expressing CD133. To further understand the role of CSCs in spheroid culture in alginate/gelatin bioinks, $CD133^-$ populations could be sorted from parent monolayers and used for spheroid culture. The results of this experiment could elucidate whether expression of CSC markers are necessary for spheroid growth, or whether CSC marker expression is altered in response to growth in the 3D environment. Clinically, there is significant relevance in selecting for CSCs as the emerging CSC model predicts that treatment ought to be tailored to these cells.

Obvious applications of this work are to patient-derived cells. Here, the systems described in this work would simply replace cancer cell lines with cancer cells from patient biopsy. One advantage of this work is the low initial seeding density relative to tumour aggregate technologies, which typically use between 1,000-5,000 cells per spheroid. In this work, many thousands of spheroids were grown from the initial seeding density of 50,000 cells/mL of bioink. For example, in **Figure 5-2**, 14,631 measurable spheroids were grown from approximately 2mL of bioink, which represents a cell:spheroid ratio of 6.8:1 or less. Using patient cells from patient cells with known chemotherapy resistances would be the most useful initial work, as these could be used as controls to validate this approach. Then, patient cells could be acquired in a co-clinical setting, and the results compared to patient outcomes.

One advantage of bioprinting is that patterning may be performed with cell-laden cells. In this work, only cancer cells were embedded within the bioink, however, more complex models could be produced which involve spheroid interactions with relevant cell types and thus better recapitulate the tumour microenvironment. For instance, stromal cells such as cancer-associated fibroblasts, immune cells, or gut flora could be added to the bioprinted model in a co-culture system, using different bioinks to optimise culture conditions for each cell type. A number of interesting interactions involve these cells, for instance, 5FU resistance can be acquired due to the metabolic inactivation by resident gut bacteria[294], an interaction for which no 3D model exists at present. Immune cell-tumour interaction is of obvious clinical interest, with T-cell therapies existing for the treatment of leukemia but are currently ineffective against solid tumours[295]. Indeed, this work is currently being progressed by other researchers as a model of T-cell/Tumour spheroid interactions in breast cancer, for the screening of T-cell modifications which are effective against solid tumours. Early results have shown that both the triple negative breast carcinoma line, MDA-MB-231, and primary human T cells (Appendix **E**), grow in the alginate/gelatin bioink, and therefore the high throughput bioprinting system could become the basis for comprehensive cell therapies in the future.

BIBLIOGRAPHY

1. Mármol, I., Sánchez-de-Diego, C., Dieste, A. P., Cerrada, E. & Yoldi, M. J. R. Colorectal carcinoma: A general overview and future perspectives in colorectal cancer. *International Journal of Molecular Sciences* (2017) doi:10.3390/ijms18010197.

2. *Cancer Research UK* www.cancerresearchuk.org. Date Accessed:23/6/2021

3. Siegel, R. L., Jemal, A. & Ward, E. M. Increase in incidence of colorectal cancer among young men and women in the United States. *Cancer Epidemiol. Biomarkers Prev.* (2009) doi:10.1158/1055-9965.EPI-09-0186.

4. Yiu, H. Y., Whittemore, A. S. & Shibata, A. Increasing colorectal cancer incidence rates in Japan. *Int. J. Cancer* (2004) doi:10.1002/ijc.20030.

5. Bogaert, J. & Prenen, H. Molecular genetics of colorectal cancer. *Annals of Gastroenterology* (2014) doi:10.1142/9789812795205_0027.

6. Stigliano, V., Sanchez-Mete, L., Martayan, A. & Anti, M. Early-onset colorectal cancer: A sporadic or inherited disease? *World Journal of Gastroenterology* (2014) doi:10.3748/wjg.v20.i35.12420.

7. Jasperson, K. W., Tuohy, T. M., Neklason, D. W. & Burt, R. W. Hereditary and Familial Colon Cancer. *Gastroenterology* (2010) doi:10.1053/j.gastro.2010.01.054.

8. Bishehsari, F., Mahdavinia, M., Vacca, M., Malekzadeh, R. & Mariani-Costantini, R. Epidemiological transition of colorectal cancer in developing countries: Environmental factors, molecular pathways, and opportunities for prevention. *World J. Gastroenterol.* (2014) doi:10.3748/wjg.v20.i20.6055.

9. Bradbury, K. E., Murphy, N. & Key, T. J. Diet and colorectal cancer in UK Biobank: A prospective study. *Int. J. Epidemiol.* (2020) doi:10.1093/ije/dyz064.

10. Wynder, E. L., Kajitani, T., Ishikawa, S., Dodo, H. & Takano, A. Environmental factors of cancer of the colon and rectum II. Japanese epidemiological data. *Cancer* (1969) doi:10.1002/1097-0142(196905)23:5<1210::AID-CNCR2820230530>3.0.CO;2-M.

11. Pelucchi, C., Tramacere, I., Boffetta, P., Negri, E. & Vecchia, C. La. Alcohol consumption and cancer risk. *Nutrition and Cancer* (2011) doi:10.1080/01635581.2011.596642.

12. Homann, N., Tillonen, J. & Salaspuro, M. Microbially produced acetaldehyde from ethanol may increase the risk of colon cancer via folate deficiency. *Int. J. Cancer* (2000) doi:10.1002/(SICI)1097-0215(20000415)86:2<169::AID-IJC4>3.0.CO;2-3.

13. Botteri, E. *et al.* Smoking and colorectal cancer: A meta-analysis. *JAMA - Journal of the American Medical Association* (2008) doi:10.1001/jama.2008.839.

14. Stintzing, S. Management of colorectal cancer. *F1000Prime Rep.* **6**, (2014).

15. Fleischer, D. E. *et al.* Detection and Surveillance of Colorectal Cancer. *JAMA J. Am. Med. Assoc.* (1989) doi:10.1001/jama.1989.03420040118031.

16. Montminy, E. M., Jang, A., Conner, M. & Karlitz, J. J. Screening for Colorectal Cancer. *Medical Clinics of North America* (2020) doi:10.1016/j.mcna.2020.08.004.

17. American Cancer Society. *Cacner Treatment & Survivorship. Facts & Figures 2019-2021*.

18. Heidelberger, C. *et al.* Fluorinated pyrimidines, a new class of tumour-inhibitory compounds. *Nature* (1957) doi:10.1038/179663a0.

19. Poon, M. A. *et al.* Biochemical modulation of fluorouracil: Evidence of significant improvement of survival and quality of life in patients with advanced colorectal carcinoma. *Journal of Clinical Oncology* (1989) doi:10.1200/JCO.1989.7.10.1407.

20. Longley, D. B., Harkin, D. P. & Johnston, P. G. 5-Fluorouracil: Mechanisms of action and clinical strategies. *Nature Reviews Cancer* (2003) doi:10.1038/nrc1074.

21. Ullman, B., Lee, M., Martin, D. W. & Santi, D. V. Cytotoxicity of 5 fluoro 2' deoxyuridine: Requirement for reduced folate cofactors and antagonism by methotrexate. *Proc. Natl. Acad. Sci. U. S. A.* (1978) doi:10.1073/pnas.75.2.980.

22. Goldberg, R. M. *et al.* A randomized controlled trial of fluorouracil plus leucovorin, irinotecan, and oxaliplatin combinations in patients with previously untreated metastatic colorectal cancer. *J. Clin. Oncol.* (2004) doi:10.1200/JCO.2004.09.046.

23. Colucci, G. *et al.* Phase III randomized trial of FOLFIRI versus FOLFOX4 in the treatment of advanced colorectal cancer: A Multicenter Study of the Gruppo Oncologico Dell'Italia Meridionale. *J. Clin. Oncol.* (2005) doi:10.1200/JCO.2005.07.113.

24. Tournigand, C. *et al.* FOLFIRI followed by FOLFOX6 or the reverse sequence in advanced colorectal cancer: A randomized GERCOR study. *J. Clin. Oncol.* (2004) doi:10.1200/JCO.2004.05.113.

25. Laurie, J. A. *et al.* Surgical adjuvant therapy of large-bowel carcinoma: an evaluation of levamisole and the combination of levamisole and fluorouracil. The North Central Cancer Treatment Group and the Mayo Clinic. *J. Clin. Oncol.* (1989) doi:10.1200/jco.1989.7.10.1447.

26. Moertel, C. G. *et al.* Levamisole and Fluorouracil for Adjuvant Therapy of Resected Colon Carcinoma. *N. Engl. J. Med.* (1990) doi:10.1056/nejm199002083220602.

27. Cassidy, J. Adjuvant 5-fluorouracil plus levamisole in colon cancer: The plot thickens? *Br. J. Cancer* (1994) doi:10.1038/bjc.1994.193.

28. Prigerson, H. G. *et al.* Chemotherapy use, performance status, and quality of life at the end of life. *JAMA Oncol.* (2015) doi:10.1001/jamaoncol.2015.2378.

29. Seymour, M. T. *et al.* Different strategies of sequential and combination chemotherapy for patients with poor prognosis advanced colorectal cancer (MRC FOCUS): a randomised controlled trial. *Lancet* (2007) doi:10.1016/S0140-6736(07)61087-3.

30. Ooft, S. N. *et al.* Patient-derived organoids can predict response to chemotherapy in metastatic colorectal cancer patients. *Sci. Transl. Med.* (2019) doi:10.1126/scitranslmed.aay2574.

31. Vlachogiannis, G. *et al.* Patient-derived organoids model treatment response of metastatic gastrointestinal cancers. *Science (80-.).* **926**, 920–926 (2018).

32. Khalek *et al.*, Colon cancer stem cells. *Gastrointest Cancer Res (Suppl 1)*, S16-S23 (2010).

33. Winawer, S. J. *et al.* Colorectal cancer screening: Clinical guidelines and rationale. *Gastroenterology* (1997) doi:10.1053/gast.1997.v112.agast970594.

34. Van Der Vlugt, M. *et al.* Adherence to colorectal cancer screening: Four rounds of faecal immunochemical test-based screening. *Br. J. Cancer* (2017) doi:10.1038/bjc.2016.399.

35. Dmello, R. S., To, S. Q. & Chand, A. L. Therapeutic targeting of the tumour microenvironment in metastatic colorectal cancer. *International Journal of Molecular Sciences* (2021) doi:10.3390/ijms22042067.

36. Nowell, P. C. The clonal evolution of tumor cell populations. *Science (80-.).* (1976) doi:10.1126/science.959840.

37. Davis, A., Gao, R. & Navin, N. Tumor evolution: Linear, branching, neutral or punctuated? *Biochim. Biophys. Acta - Rev. Cancer* (2017) doi:10.1016/j.bbcan.2017.01.003.

38. Walters, K. Colonic stem cell data are consistent with the immortal model of stem cell division under non-random strand segregation. *Cell Prolif.* (2009) doi:10.1111/j.1365-2184.2009.00600.x.

39. Singh, S. K. *et al.* Identification of a cancer stem cell in human brain tumors. *Cancer Res.* (2003).

40. Collins, A. T., Berry, P. A., Hyde, C., Stower, M. J. & Maitland, N. J. Prospective identification of tumorigenic prostate cancer stem cells. *Cancer Res.* (2005) doi:10.1158/0008-5472.CAN-05-2018.

41. Vermeulen, L. *et al.* Single-cell cloning of colon cancer stem cells reveals a multi-lineage differentiation capacity. *Proc. Natl. Acad. Sci. U. S. A.* (2008) doi:10.1073/pnas.0805706105.

42. Ke, J. *et al.* A subpopulation of CD24+ cells in colon cancer cell lines possess stem cell characteristics. *Neoplasma* (2012) doi:10.4149/neo_2012_036.

43. Dalerba, P. *et al.* Phenotypic characterization of human colorectal cancer stem cells. *Proc. Natl. Acad. Sci. U. S. A.* (2007) doi:10.1073/pnas.0703478104.

44. Takahashi, H. *et al.* Significance of Lgr5+ve cancer stem cells in the colon and rectum. *Ann. Surg. Oncol.* (2011) doi:10.1245/s10434-010-1373-9.

45. Horst, D., Kriegl, L., Engel, J., Kirchner, T. & Jung, A. CD133 expression is an independent prognostic marker for low survival in colorectal cancer. *Br. J. Cancer* (2008) doi:10.1038/sj.bjc.6604664.

46. Chen, S. *et al.* CD133 Expression and the Prognosis of Colorectal Cancer: A Systematic Review and Meta-Analysis. *PLoS One* (2013) doi:10.1371/journal.pone.0056380.

47. Du, L. *et al.* CD44 is of functional importance for colorectal cancer stem cells. *Clin. Cancer Res.* (2008) doi:10.1158/1078-0432.CCR-08-1034.

48. Jing, F. *et al.* Colon cancer stem cell markers CD44 and CD133 in patients with colorectal cancer and synchronous hepatic metastases. *Int. J. Oncol.* (2015) doi:10.3892/ijo.2015.2844.

49. Galizia, G. *et al.* Combined CD133/CD44 expression as a prognostic indicator of disease-free survival in patients with colorectal cancer. *Arch. Surg.* (2012) doi:10.1001/archsurg.2011.795.

50. Cimato, T. R. *et al.* CD133 Expression in Circulating hematopoietic Progenitor Cells. *Cytometry B Clin Cytom.* **96**, 39–45 (2019). doi:10.1002/cyto.b.21732

51. Peh, G. S. L., Lang, R. J., Pera, M. F. & Hawes, S. M. CD133 expression by neural progenitors derived from human embryonic stem cells and its use for their prospective isolation. *Stem Cells Dev.* (2009) doi:10.1089/scd.2008.0124.

52. Vander Griend, D. J. *et al.* The role of CD133 in normal human prostate stem cells and malignant cancer-initiating cells. *Cancer Res.* (2008) doi:10.1158/0008-5472.CAN-08-3084.

53. LaBarge, M. A. & Bissell, M. J. Is CD133 a marker of metastatic colon cancer stem cells?

Journal of Clinical Investigation (2008) doi:10.1172/JCI36046.

54. Immervoll, H., Hoem, D., Steffensen, O. J., Miletic, H. & Molven, A. Visualization of CD44 and CD133 in normal pancreas and pancreatic ductal adenocarcinomas: Non-overlapping membrane expression in cell populations positive for both markers. *J. Histochem. Cytochem.* (2011) doi:10.1369/0022155411398275.

55. TAN, Y., CHEN, B., XU, W., ZHAO, W. & WU, J. Clinicopathological significance of CD133 in lung cancer: A meta-analysis. *Mol. Clin. Oncol.* (2014) doi:10.3892/mco.2013.195.

56. Glumac, P. M. & LeBeau, A. M. The role of CD133 in cancer: a concise review. *Clin. Transl. Med.* (2018) doi:10.1186/s40169-018-0198-1.

57. Su, Y. J. *et al.* Polarized cell migration induces cancer type-specific CD133/integrin/Src/Akt/GSK3β/β-catenin signaling required for maintenance of cancer stem cell properties. *Oncotarget* (2015) doi:10.18632/oncotarget.5703.

58. Rappa, G. *et al.* Wnt interaction and extracellular release of prominin-1/CD133 in human malignant melanoma cells. *Exp. Cell Res.* (2013) doi:10.1016/j.yexcr.2013.01.003.

59. Iida, H., Suzuki, M., Goitsuka, R. & Ueno, H. Hypoxia induces CD133 expression in human lung cancer cells by up-regulation of OCT3/4 and SOX2. *Int. J. Oncol.* (2012) doi:10.3892/ijo.2011.1207.

60. Sohn, H. M. *et al.* Effect of CD133 overexpression on bone metastasis in prostate cancer cell line LNCaP. *Oncol. Lett.* (2019) doi:10.3892/ol.2019.10443.

61. Wang, R. *et al.* INOS promotes CD24+CD133+ liver cancer stem cell phenotype through a TACE/ADAM17-dependent Notch signaling pathway. *Proc. Natl. Acad. Sci. U. S. A.* (2018) doi:10.1073/pnas.1722100115.

62. Zhang, S. shan *et al.* CD133+CXCR4+colon cancer cells exhibit metastatic potential and predict poor prognosis of patients. *BMC Med.* (2012) doi:10.1186/1741-7015-10-85.

63. Domev, H., Amit, M., Laevsky, I., Dar, A. & Itskovitz-Eldor, J. Efficient engineering of vascularized ectopic bone from human embryonic stem cell-derived mesenchymal stem cells. *Tissue Eng. - Part A* (2012) doi:10.1089/ten.tea.2011.0371.

64. Senbanjo, L. T. & Chellaiah, M. A. CD44: A multifunctional cell surface adhesion receptor is a regulator of progression and metastasis of cancer cells. *Frontiers in Cell and Developmental Biology* (2017) doi:10.3389/fcell.2017.00018.

65. Lv, L. *et al.* Upregulation of CD44v6 contributes to acquired chemoresistance via the modulation of autophagy in colon cancer SW480 cells. *Tumor Biol.* (2016) doi:10.1007/s13277-015-4755-6.

66. Louderbough, J. M. V. & Schroeder, J. A. Understanding the dual nature of CD44 in breast cancer progression. *Molecular Cancer Research* (2011) doi:10.1158/1541-7786.MCR-11-0156.

67. Sun, B. S., Li, Y., Zhang, Z. F., You, J. & Wang, C. L. Osteopontin combined with CD44v6, a novel prognostic biomarker in non-small cell lung cancer undergoing curative resection. *Ann. Thorac. Surg.* (2013) doi:10.1016/j.athoracsur.2013.07.089.

68. Ma, L., Dong, L. & Chang, P. CD44v6 engages in colorectal cancer progression. *Cell Death and Disease* (2019) doi:10.1038/s41419-018-1265-7.

69. Zhou, J. Y. *et al.* Role of CD44high/CD133high HCT-116 cells in the tumorigenesis of colon cancer. *Oncotarget* (2016) doi:10.18632/oncotarget.7084.

70. Tsunekuni, K. *et al.* CD44/CD133-Positive Colorectal Cancer Stem Cells are Sensitive to Trifluridine Exposure. *Sci. Rep.* (2019) doi:10.1038/s41598-019-50968-6.

71. Bauer, J. *et al.* Increased stiffness of the tumor microenvironment in colon cancer stimulates cancer associated fibroblast-mediated prometastatic activin A signaling. *Sci. Rep.* (2020) doi:10.1038/s41598-019-55687-6.

72. Jing, X. *et al.* Role of hypoxia in cancer therapy by regulating the tumor microenvironment. *Molecular Cancer* (2019) doi:10.1186/s12943-019-1089-9.

73. Hillen, F. & Griffioen, A. W. Tumour vascularization: Sprouting angiogenesis and beyond. *Cancer and Metastasis Reviews* (2007) doi:10.1007/s10555-007-9094-7.

74. Persi, E. *et al.* Systems analysis of intracellular pH vulnerabilities for cancer therapy. *Nat. Commun.* (2018) doi:10.1038/s41467-018-05261-x.

75. Greijer, A. E. & Van Der Wall, E. The role of hypoxia inducible factor 1 (HIF-1) in hypoxia induced apoptosis. *Journal of Clinical Pathology* (2004) doi:10.1136/jcp.2003.015032.

76. Zunino, F. *et al.* Role of apoptotic response in cellular resistance to cytotoxic agents. *Pharmacology and Therapeutics* (1997) doi:10.1016/S0163-7258(97)00086-7.

77. Chen, J. *et al.* HIF-1α inhibition reverses multidrug resistance in colon cancer cells via downregulation of MDR1/P-Glycoprotein. *PLoS One* (2014) doi:10.1371/journal.pone.0098882.

78. Xu, K. *et al.* Hypoxia Induces Drug Resistance in Colorectal Cancer through the HIF-1α/miR-338-5p/IL-6 Feedback Loop. *Mol. Ther.* (2019) doi:10.1016/j.ymthe.2019.05.017.

79. Collado, M. & Serrano, M. Senescence in tumours: Evidence from mice and humans. *Nature Reviews Cancer* (2010) doi:10.1038/nrc2772.

80. Wei, S. C. *et al.* Matrix stiffness drives epithelial-mesenchymal transition and tumour metastasis through a TWIST1-G3BP2 mechanotransduction pathway. *Nat. Cell Biol.* (2015) doi:10.1038/ncb3157.

81. Medina, S. H. *et al.* Identification of a mechanogenetic link between substrate stiffness and chemotherapeutic response in breast cancer. *Biomaterials* (2019) doi:10.1016/j.biomaterials.2019.02.018.

82. Li, Y. *et al.* Matrix Stiffness-Regulated Growth of Breast Tumor Spheroids and Their Response to Chemotherapy. *Biomacromolecules* (2020) doi:10.1021/acs.biomac.0c01287.

83. Datta, P., Dey, M., Ataie, Z., Unutmaz, D. & Ozbolat, I. T. 3D bioprinting for reconstituting the cancer microenvironment. *npj Precis. Oncol.* (2020) doi:10.1038/s41698-020-0121-2.

84. Knowlton, S., Onal, S., Yu, C. H., Zhao, J. J. & Tasoglu, S. Bioprinting for cancer research. *Trends Biotechnol.* **33**, 504–513 (2015).

85. Charbe, N., McCarron, P. A. & Tambuwala, M. M. Three-dimensional bio-printing: A new frontier in oncology research. *World J. Clin. Oncol.* **8**, 21–36 (2017).

86. Ware, M. J. *et al.* Generation of homogenous three-dimensional pancreatic cancer cell spheroids using an improved hanging drop technique. *Tissue Eng. - Part C Methods* (2016) doi:10.1089/ten.tec.2015.0280.

87. Massai, D. *et al.* A versatile bioreactor for dynamic suspension cell culture. Application

to the culture of cancer cell spheroids. *PLoS One* (2016) doi:10.1371/journal.pone.0154610.

88. Sant, S. & Johnston, P. A. The production of 3D tumor spheroids for cancer drug discovery. *Drug Discovery Today: Technologies* (2017) doi:10.1016/j.ddtec.2017.03.002.

89. Sato, T. *et al.* Single Lgr5 stem cells build crypt-villus structures in vitro without a mesenchymal niche. *Nature* **459**, 262–265 (2009).

90. Sato, T. *et al.* Long-term expansion of epithelial organoids from human colon, adenoma, adenocarcinoma, and Barrett's epithelium. *Gastroenterology* **141**, 1762–1772 (2011).

91. Popova, A. A. *et al.* Facile One Step Formation and Screening of Tumor Spheroids Using Droplet-Microarray Platform. *Small* **15**, 1–9 (2019).

92. Chun, I. & Reneker, D. H. Nanometre diameter fibres of polymer, produced by electrospinning. *Nanotechnology* (1999).

93. Autissier, A., Le Visage, C., Pouzet, C., Chaubet, F. & Letourneur, D. Fabrication of porous polysaccharide-based scaffolds using a combined freeze-drying/cross-linking process. *Acta Biomater.* (2010) doi:10.1016/j.actbio.2010.03.004.

94. Agrawal, C. M. & Ray, R. B. Biodegradable polymeric scaffolds for musculoskeletal tissue engineering. *J. Biomed. Mater. Res.* (2001) doi:10.1002/1097-4636(200105)55:2<141::AID-JBM1000>3.0.CO;2-J.

95. Bolland, B. J. R. F. *et al.* The application of human bone marrow stromal cells and poly(dl-lactic acid) as a biological bone graft extender in impaction bone grafting. *Biomaterials* (2008) doi:10.1016/j.biomaterials.2008.04.017.

96. Ritcharoen, W. *et al.* Electrospun dextran fibrous membranes. *Cellulose* (2008) doi:10.1007/s10570-008-9199-3.

97. Valence, S. De *et al.* Plasma treatment for improving cell biocompatibility of a biodegradable polymer scaffold for vascular graft applications. *Eur. J. Pharm. Biopharm.* (2013) doi:10.1016/j.ejpb.2013.06.012.

98. Lee, S. J. *et al.* Surface modification of 3D-printed porous scaffolds via mussel-inspired polydopamine and effective immobilization of rhBMP-2 to promote osteogenic differentiation for bone tissue engineering. *Acta Biomater.* (2016) doi:10.1016/j.actbio.2016.02.006.

99. Bassi, G. *et al.* Scaffold-based 3D cellular models mimicking the heterogeneity of osteosarcoma stem cell niche. *Sci. Rep.* (2020) doi:10.1038/s41598-020-79448-y.

100. Kumar, A. & Han, S. S. PVA-based hydrogels for tissue engineering: A review. *International Journal of Polymeric Materials and Polymeric Biomaterials* (2017) doi:10.1080/00914037.2016.1190930.

101. Burdick, J. A. & Anseth, K. S. Photoencapsulation of osteoblasts in injectable RGD-modified PEG hydrogels for bone tissue engineering. *Biomaterials* (2002) doi:10.1016/S0142-9612(02)00176-X.

102. Peppas, N. A., Keys, K. B., Torres-Lugo, M. & Lowman, A. M. Poly(ethylene glycol)-containing hydrogels in drug delivery. *J. Control. Release* (1999) doi:10.1016/S0168-3659(99)00027-9.

103. Kraehenbuehl, T. P. *et al.* Three-dimensional extracellular matrix-directed cardioprogenitor differentiation: Systematic modulation of a synthetic cell-responsive PEG-hydrogel. *Biomaterials* (2008) doi:10.1016/j.biomaterials.2008.03.016.

104. Chuang, C. H., Lin, R. Z., Melero-Martin, J. M. & Chen, Y. C. Comparison of covalently and physically cross-linked collagen hydrogels on mediating vascular network formation for engineering adipose tissue. *Artif. Cells, Nanomedicine Biotechnol.* (2018) doi:10.1080/21691401.2018.1499660.

105. Kitahara, T. *et al.* Mesangial cells stimulate differentiation of endothelial cells to form capillary-like networks in a three-dimensional culture system. *Nephrol. Dial. Transplant.* (2005) doi:10.1093/ndt/gfh572.

106. Heck, T., Faccio, G., Richter, M. & Thöny-Meyer, L. Enzyme-catalyzed protein crosslinking. *Applied Microbiology and Biotechnology* (2013) doi:10.1007/s00253-012-4569-z.

107. Bae, M. S. *et al.* Photo-cured hyaluronic acid-based hydrogels containing growth and differentiation factor 5 (GDF-5) for bone tissue regeneration. *Bone* (2014) doi:10.1016/j.bone.2013.11.019.

108. Kilic Bektas, C. & Hasirci, V. Cell loaded 3D bioprinted GelMA hydrogels for corneal stroma engineering. *Biomater. Sci.* (2020) doi:10.1039/c9bm01236b.

109. Li, B. *et al.* Hydrosoluble, UV-crosslinkable and injectable chitosan for patterned cell-laden microgel and rapid transdermal curing hydrogel in vivo. *Acta Biomater.* (2015) doi:10.1016/j.actbio.2015.04.026.

110. Isaacson, A., Swioklo, S. & Connon, C. J. 3D bioprinting of a corneal stroma equivalent. *Exp. Eye Res.* (2018) doi:10.1016/j.exer.2018.05.010.

111. Hoeijmakers, J. H. J. DNA Damage, Aging, and Cancer. *N. Engl. J. Med.* (2009) doi:10.1056/nejmra0804615.

112. Shih, H. & Lin, C. C. Visible-light-mediated thiol-ene hydrogelation using eosin-Y as the only photoinitiator. *Macromol. Rapid Commun.* (2013) doi:10.1002/marc.201200605.

113. Lin, H. *et al.* Application of visible light-based projection stereolithography for live cell-scaffold fabrication with designed architecture. *Biomaterials* (2013) doi:10.1016/j.biomaterials.2012.09.048.

114. Fernandes-Cunha, G. M. *et al.* Immobilization of Growth Factors to Collagen Surfaces Using Pulsed Visible Light. *Biomacromolecules* (2017) doi:10.1021/acs.biomac.7b00838.

115. Kuo, C. K. & Ma, P. X. Ionically crosslinked alginate hydrogels as scaffolds for tissue engineering: Part 1. Structure, gelation rate and mechanical properties. *Biomaterials* (2001) doi:10.1016/S0142-9612(00)00201-5.

116. Lee, K. Y. & Mooney, D. J. Alginate: Properties and biomedical applications. *Progress in Polymer Science (Oxford)* (2012) doi:10.1016/j.progpolymsci.2011.06.003.

117. Idota, Y. *et al.* Relationship between physical parameters of various metal ions and binding affinity for alginate. *Biol. Pharm. Bull.* (2016) doi:10.1248/bpb.b16-00127.

118. Håti, A. G. *et al.* Versatile, cell and chip friendly method to gel alginate in microfluidic devices. *Lab Chip* (2016) doi:10.1039/c6lc00769d.

119. Workman, V. L., Dunnett, S. B., Kille, P. & Palmer, D. Microfluidic chip-based synthesis of alginate microspheres for encapsulation of immortalized human cells. *Biomicrofluidics* (2007) doi:10.1063/1.2431860.

120. Chandler, E. M. *et al.* Stiffness of photocrosslinked RGD-alginate gels regulates adipose progenitor cell behavior. *Biotechnol. Bioeng.* (2011) doi:10.1002/bit.23079.

121. Jiang, T. *et al.* Directing the Self-Assembly of Tumour Spheroids by Bioprinting Cellular Heterogeneous Models within Alginate/Gelatin Hydrogels. *Sci. Rep.* **7**, 1–9 (2017).

122. Swaminathan, S., Hamid, Q., Sun, W. & Clyne, A. M. Bioprinting of 3D breast epithelial spheroids for human cancer models. *Biofabrication* **11**, (2019).

123. Kadri, R. *et al.* Preparation and characterization of nanofunctionalized alginate/methacrylated gelatin hybrid hydrogels. *RSC Adv.* (2016) doi:10.1039/c6ra03699f.

124. Zhao, Y. *et al.* Three-dimensional printing of Hela cells for cervical tumor model in vitro. *Biofabrication* **6**, (2014).

125. Yellowley, C. E., Hancox, J. C. & Donahue, H. J. Effects of cell swelling on intracellular calcium and membrane currents in bovine articular chondrocytes. *J. Cell. Biochem.* (2002) doi:10.1002/jcb.10217.

126. Aisenbrey, E. A. & Murphy, W. L. Synthetic alternatives to Matrigel. *Nature Reviews Materials* (2020) doi:10.1038/s41578-020-0199-8.

127. Vukicevic, S. *et al.* Identification of multiple active growth factors in basement membrane matrigel suggests caution in interpretation of cellular activity related to extracellular matrix components. *Exp. Cell Res.* (1992) doi:10.1016/0014-4827(92)90397-Q.

128. Badea, M. A. *et al.* Influence of Matrigel on Single- and Multiple-Spheroid Cultures in Breast Cancer Research. *SLAS Discov.* **24**, 563–578 (2019).

129. Majo, S., Courtois, S., Souleyreau, W., Bikfalvi, A. & Auguste, P. Impact of Extracellular Matrix Components to Renal Cell Carcinoma Behavior. *Front. Oncol.* (2020) doi:10.3389/fonc.2020.00625.

130. Yeung, T. M., Gandhi, S. C., Wilding, J. L., Muschel, R. & Bodmer, W. F. Cancer stem cells from colorectal cancer-derived cell lines. *Proc. Natl. Acad. Sci. U. S. A.* (2010) doi:10.1073/pnas.0915135107.

131. Collard, T. J., Fallatah, H. M., Greenhough, A., Paraskeva, C. & Williams, A. C. BCL–3 promotes cyclooxygenase–2/prostaglandin E2 signalling in colorectal cancer. *Int. J. Oncol.* (2020) doi:10.3892/ijo.2020.5013.

132. Soofi, S. S., Last, J. A., Liliensiek, S. J., Nealey, P. F. & Murphy, C. J. The elastic modulus of Matrigel™ as determined by atomic force microscopy. *J. Struct. Biol.* (2009) doi:10.1016/j.jsb.2009.05.005.

133. Fan, R. *et al.* Bio-printing cell-laden Matrigel-agarose constructs. *J. Biomater. Appl.* (2016) doi:10.1177/0885328216669238.

134. Armstrong, J. P. K., Burke, M., Carter, B. M., Davis, S. A. & Perriman, A. W. 3D Bioprinting Using a Templated Porous Bioink. *Adv. Healthc. Mater.* **5**, 1724–1730 (2016).

135. Mironov, V. Printing technology to produce living tissue. *Expert Opinion on Biological Therapy* (2003) doi:10.1517/14712598.3.5.701.

136. Midha, S., Dalela, M., Sybil, D., Patra, P. & Mohanty, S. Advances in three-dimensional bioprinting of bone: Progress and challenges. *Journal of Tissue Engineering and Regenerative Medicine* (2019) doi:10.1002/term.2847.

137. Graham, A. D. *et al.* High-Resolution Patterned Cellular Constructs by Droplet-Based 3D Printing. *Sci. Rep.* **7**, 1–11 (2017).

138. Zhou, L. *et al.* Lipid-Bilayer-Supported 3D Printing of Human Cerebral Cortex Cells Reveals Developmental Interactions. *Adv. Mater.* (2020) doi:10.1002/adma.202002183.

139. Villar, G., Graham, A. D. & Bayley, H. A tissue-like printed material. *Science (80-.).* (2013) doi:10.1126/science.1229495.

140. Alcinesio, A. *et al.* Controlled packing and single-droplet resolution of 3D-printed functional synthetic tissues. *Nat. Commun.* (2020) doi:10.1038/s41467-020-15953-y.

141. Leigh Herran, C., Huang, Y. & Chai, W. Performance evaluation of bipolar and tripolar excitations during nozzle-jetting-based alginate microsphere fabrication. *J. Micromechanics Microengineering* (2012) doi:10.1088/0960-1317/22/8/085025.

142. Serra, P. & Piqué, A. Laser-Induced Forward Transfer: Fundamentals and Applications. *Advanced Materials Technologies* (2019) doi:10.1002/admt.201800099.

143. Gudapati, H., Yan, J., Huang, Y. & Chrisey, D. B. Alginate gelation-induced cell death during laser-assisted cell printing. *Biofabrication* (2014) doi:10.1088/1758-5082/6/3/035022.

144. Murphy, S. V. & Atala, A. 3D bioprinting of tissues and organs. *Nature Biotechnology* (2014) doi:10.1038/nbt.2958.

145. Hopp, B. Femtosecond laser printing of living cells using absorbing film-assisted laser-induced forward transfer. *Opt. Eng.* (2012) doi:10.1117/1.oe.51.1.014302.

146. Wang, Z. *et al.* A simple and high-resolution stereolithography-based 3D bioprinting system using visible light crosslinkable bioinks. *Biofabrication* (2015) doi:10.1088/1758-5090/7/4/045009.

147. Shie, M. Y. *et al.* 3D printing of cytocompatible water-based light-cured polyurethane with hyaluronic acid for cartilage tissue engineering applications. *Materials (Basel).* (2017) doi:10.3390/ma10020136.

148. Jansen, J., Melchels, F. P. W., Grijpma, D. W. & Feijen, J. Fumaric acid monoethyl ester-functionalized poly(D,L-Lactide)/N-vinyl-2- pyrrolidone Resins for the preparation of tissue engineering scaffolds by stereolithography. *Biomacromolecules* (2009) doi:10.1021/bm801001r.

149. Tummala, G. K. *et al.* Light scattering in poly(vinyl alcohol) hydrogels reinforced with nanocellulose for ophthalmic use. *Opt. Mater. Express* (2017) doi:10.1364/ome.7.002824.

150. Skoog, S. A., Goering, P. L. & Narayan, R. J. Stereolithography in tissue engineering. *Journal of Materials Science: Materials in Medicine* (2014) doi:10.1007/s10856-013-5107-y.

151. Molitch-Hou, M. Overview of additive manufacturing process. in *Additive Manufacturing: Materials, Processes, Quantifications and Applications* (2018). doi:10.1016/B978-0-12-812155-9.00001-3.

152. Kim, Y. B. *et al.* Mechanically reinforced cell-laden scaffolds formed using alginate-based bioink printed onto the surface of a PCL/alginate mesh structure for regeneration of hard tissue. *J. Colloid Interface Sci.* (2016) doi:10.1016/j.jcis.2015.09.044.

153. Merceron, T. K. *et al.* A 3D bioprinted complex structure for engineering the muscle-tendon unit. *Biofabrication* (2015) doi:10.1088/1758-5090/7/3/035003.

154. Ahn, S. H. *et al.* A novel cell-printing method and its application to hepatogenic differentiation of human adipose stem cell-embedded mesh structures. *Sci. Rep.* (2015) doi:10.1038/srep13427.

155. Pati, F. *et al.* Biomimetic 3D tissue printing for soft tissue regeneration. *Biomaterials* (2015) doi:10.1016/j.biomaterials.2015.05.043.

156. Melchels, F. P. W., Dhert, W. J. A., Hutmacher, D. W. & Malda, J. Development and characterisation of a new bioink for additive tissue manufacturing. *J. Mater. Chem. B* (2014) doi:10.1039/c3tb21280g.

157. Markstedt, K. *et al.* 3D bioprinting human chondrocytes with nanocellulose-alginate bioink for cartilage tissue engineering applications. *Biomacromolecules* (2015) doi:10.1021/acs.biomac.5b00188.

158. Cuomo, F., Cofelice, M. & Lopez, F. Rheological characterization of hydrogels from alginate-based nanodispersion. *Polymers (Basel).* **11**, (2019).

159. Liu, W. *et al.* Extrusion Bioprinting of Shear-Thinning Gelatin Methacryloyl Bioinks. *Adv. Healthc. Mater.* (2017) doi:10.1002/adhm.201601451.

160. Ning, L., Betancourt, N., Schreyer, D. J. & Chen, X. Characterization of Cell Damage and Proliferative Ability during and after Bioprinting. *ACS Biomater. Sci. Eng.* **4**, 3906–3918 (2018).

161. Kang, H. W. *et al.* A 3D bioprinting system to produce human-scale tissue constructs with structural integrity. *Nat. Biotechnol.* (2016) doi:10.1038/nbt.3413.

162. Mancha Sánchez, E. *et al.* Hydrogels for Bioprinting: A Systematic Review of Hydrogels Synthesis, Bioprinting Parameters, and Bioprinted Structures Behavior. *Front. Bioeng. Biotechnol.* (2020) doi:10.3389/fbioe.2020.00776.

163. Jiang, T. *et al.* Engineering bioprintable alginate/gelatin composite hydrogels with tunable mechanical and cell adhesive properties to modulate tumor spheroid growth kinetics. *Biofabrication* **12**, (2020).

164. Pan, H. *et al.* Strength-tunable printing of xanthan gum hydrogel: Via enzymatic polymerization and amide bioconjugation. *Chem. Commun.* (2020) doi:10.1039/d0cc00326c.

165. Homan, K. A. *et al.* Bioprinting of 3D Convoluted Renal Proximal Tubules on Perfusable Chips. *Sci. Rep.* (2016) doi:10.1038/srep34845.

166. Chimene, D. *et al.* Nanoengineered Osteoinductive Bioink for 3D Bioprinting Bone Tissue. *ACS Appl. Mater. Interfaces* (2020) doi:10.1021/acsami.9b19037.

167. Derr, K. *et al.* Fully Three-Dimensional Bioprinted Skin Equivalent Constructs with Validated Morphology and Barrier Function. *Tissue Eng. - Part C Methods* (2019) doi:10.1089/ten.tec.2018.0318.

168. Yi, H. G. *et al.* A bioprinted human-glioblastoma-on-a-chip for the identification of patient-specific responses to chemoradiotherapy. *Nat. Biomed. Eng.* (2019) doi:10.1038/s41551-019-0363-x.

169. Al-Ramadan, A., Mortensen, A. C., Carlsson, J. & Nestor, M. V. Analysis of radiation effects in two irradiated tumor spheroid models. *Oncol. Lett.* **15**, 3008–3016 (2018).

170. Hoffmann, O. I. *et al.* Impact of the spheroid model complexity on drug response. *J. Biotechnol.* (2015) doi:10.1016/j.jbiotec.2015.02.029.

171. Yang, Z. L., Zheng, Q., Yan, J., Pan, Y. & Wang, Z. G. Upregulated CD133 expression in tumorigenesis of colon cancer cells. *World J. Gastroenterol.* **17**, 932–937 (2011).

172. Chen, H. *et al.* 3D printed in vitro tumor tissue model of colorectal cancer. *Theranostics* (2020) doi:10.7150/thno.52450.

173. Shakibaei, M. *et al.* Curcumin potentiates antitumor activity of 5-fluorouracil in a 3D alginate tumor microenvironment of colorectal cancer. *BMC Cancer* (2015)

doi:10.1186/s12885-015-1291-0.

174. Leo, W. J., Mcloughlin, A. J. & Malone, D. M. Effects of Sterilization Treatments on Some Properties of Alginate Solutions and Gels. *Biotechnol. Prog.* (1990) doi:10.1021/bp00001a008.

175. Borten, M. A., Bajikar, S. S., Sasaki, N., Clevers, H. & Janes, K. A. Automated brightfield morphometry of 3D organoid populations by OrganoSeg. *Sci. Rep.* **8**, 1–10 (2018).

176. Koch, M. & Włodarczyk-Biegun, M. K. Faithful scanning electron microscopic (SEM) visualization of 3D printed alginate-based scaffolds. *Bioprinting* (2020) doi:10.1016/j.bprint.2020.e00098.

177. Aston, R., Sewell, K., Klein, T., Lawrie, G. & Grøndahl, L. Evaluation of the impact of freezing preparation techniques on the characterisation of alginate hydrogels by cryo-SEM. *Eur. Polym. J.* **82**, 1–15 (2016).

178. Ott, S. R. Confocal microscopy in large insect brains: Zinc-formaldehyde fixation improves synapsin immunostaining and preservation of morphology in whole-mounts. *J. Neurosci. Methods* (2008) doi:10.1016/j.jneumeth.2008.04.031.

179. Weiswald, L. B. *et al.* In situ protein expression in tumour spheres: Development of an immunostaining protocol for confocal microscopy. *BMC Cancer* **10**, 1–11 (2010).

180. Dickie, R. *et al.* Three-dimensional visualization of microvessel architecture of whole-mount tissue by confocal microscopy. *Microvasc. Res.* (2006) doi:10.1016/j.mvr.2006.05.003.

181. Verma, Y. K., Tripathi, R. P. & Gangenahalli, G. U. Electrophoretic detection of alginate by Hematoxylin and Eosin fluorescence: Implications in cell encapsulation/tissue engineering. *React. Funct. Polym.* **102**, 130–136 (2016).

182. Varoni, E. *et al.* Agarose gel as biomaterial or scaffold for implantation surgery: Characterization, histological and histomorphometric study on soft tissue response. *Connect. Tissue Res.* (2012) doi:10.3109/03008207.2012.712583.

183. Tsao-Wu, G. S., Weber, C. H., Budgeon, L. R. & Cheng, K. C. Agarose-embedded tissue arrays for histologic and genetic analysis. *Biotechniques* (1998) doi:10.2144/98254st02.

184. Chernov, M. M., Chen, G. & Roe, A. W. Histological assessment of thermal damage in the brain following infrared neural stimulation. *Brain Stimul.* (2014) doi:10.1016/j.brs.2014.01.006.

185. Varia, M. A. *et al.* Pimonidazole: A novel hypoxia marker for complementary study of tumor hypoxia and cell proliferation in cervical carcinoma. *Gynecol. Oncol.* (1998) doi:10.1006/gyno.1998.5163.

186. Romero-Garcia, S., Lopez-Gonzalez, J. S., B´ez-Viveros, J. L., Aguilar-Cazares, D. & Prado-Garcia, H. Tumor cell metabolism. *Cancer Biol. Ther.* **12**, 939–948 (2011).

187. Warburg, O. On the origin of cancer cells. *Science (80-.).* (1956) doi:10.1126/science.123.3191.309.

188. Gander, W., Golub, G. H. & Strebel, R. Least-squares fitting of circles and ellipses. *Bit* **34**, 558–578 (1994).

189. Jeong, B., Kim, S. W. & Bae, Y. H. Thermosensitive sol-gel reversible hydrogels. *Advanced Drug Delivery Reviews* (2012) doi:10.1016/j.addr.2012.09.012.

190. Zacharakis, M. *et al.* Predictors of survival in stage IV metastatic colorectal cancer. *Anticancer Res.* (2010).

191. Wang, J. *et al.* Metastatic patterns and survival outcomes in patients with stage IV colon cancer: A population-based analysis. *Cancer Med.* (2020) doi:10.1002/cam4.2673.

192. Bracht, K., Nicholls, A. M., Liu, Y. & Bodmer, W. F. 5-Fluorouracil response in a large panel of colorectal cancer cell lines is associated with mismatch repair deficiency. *Br. J. Cancer* **103**, 340–346 (2010).

193. Zhang, Z. Y., Zheng, S. H., Yang, W. G., Yang, C. & Yuan, W. T. Targeting colon cancer stem cells with novel blood cholesterol drug pitavastatin. *Eur. Rev. Med. Pharmacol. Sci.* (2017).

194. Holzner, S. *et al.* Intravasation of SW620 colon cancer cell spheroids through the blood endothelial barrier is inhibited by clinical drugs and flavonoids in vitro. *Food Chem. Toxicol.* (2018) doi:10.1016/j.fct.2017.11.015.

195. Stadler, M. *et al.* Exclusion from spheroid formation identifies loss of essential cell-cell adhesion molecules in colon cancer cells. *Sci. Rep.* (2018) doi:10.1038/s41598-018-19384-0.

196. Ayinde, O., Wang, Z. & Griffin, M. Tissue transglutaminase induces Epithelial-Mesenchymal-Transition and the acquisition of stem cell like characteristics in colorectal cancer cells. *Oncotarget* (2017) doi:10.18632/oncotarget.15370.

197. Ojima, E. *et al.* The optimal schedule for 5-fluorouracil radiosensitization in colon cancer cell lines. *Oncol. Rep.* **16**, 1085–1091 (2006).

198. Ogura, M., Bridgeman, V. L. & Malanchi, I. Macrophages unlock progression of breast cancer cells experiencing matrigel-segregation in transplantation models. *Sci. Rep.* (2017) doi:10.1038/s41598-017-11403-w.

199. Azarin, S. M. & Palecek, S. P. Matrix revolutions: A trinity of defined substrates for long-term expansion of human ESCs. *Cell Stem Cell* (2010) doi:10.1016/j.stem.2010.06.008.

200. Chen, Z. *et al.* Study on Development of Composite Hydrogels With Tunable Structures and Properties for Tumor-on-a-Chip Research. *Front. Bioeng. Biotechnol.* (2020) doi:10.3389/fbioe.2020.611796.

201. Hughes, C. S., Postovit, L. M. & Lajoie, G. A. Matrigel: a complex protein mixture required for optimal growth of cell culture. *Proteomics* (2010) doi:10.1002/pmic.200900758.

202. Sargenti, A. *et al.* Physical Characterization of Colorectal Cancer Spheroids and Evaluation of NK Cell Infiltration Through a Flow-Based Analysis. *Front. Immunol.* **11**, 1–13 (2020).

203. Cattin, S., Ramont, L. & Rüegg, C. Characterization and In Vivo Validation of a Three-Dimensional Multi-Cellular Culture Model to Study Heterotypic Interactions in Colorectal Cancer Cell Growth, Invasion and Metastasis. *Front. Bioeng. Biotechnol.* **6**, 1–14 (2018).

204. Kim, Y. N., Koo, K. H., Sung, J. Y., Yun, U. J. & Kim, H. Anoikis resistance: An essential prerequisite for tumor metastasis. *Int. J. Cell Biol.* **2012**, (2012).

205. Dai, X., Ge, J., Wang, X., Qian, X. & Li, X. OCT4 regulates epithelial-mesenchymal transition and its knockdown inhibits colorectal cancer cell migration and invasion. *Oncol. Rep.* (2013) doi:10.3892/or.2012.2086.

206. Boularaoui, S., Al Hussein, G., Khan, K. A., Christoforou, N. & Stefanini, C. An overview of extrusion-based bioprinting with a focus on induced shear stress and its effect on cell viability. *Bioprinting* **20**, e00093 (2020).

207. Davidenko, N. *et al.* Evaluation of cell binding to collagen and gelatin: a study of the effect of 2D and 3D architecture and surface chemistry. *J. Mater. Sci. Mater. Med.* (2016) doi:10.1007/s10856-016-5763-9.

208. Dong, X. N., Acuna, R. L., Luo, Q. & Wang, X. Orientation dependence of progressive post-yield behavior of human cortical bone in compression. *J. Biomech.* (2012) doi:10.1016/j.jbiomech.2012.08.034.

209. Bayraktar, H. H. *et al.* Comparison of the elastic and yield properties of human femoral trabecular and cortical bone tissue. *J. Biomech.* (2004) doi:10.1016/S0021-9290(03)00257-4.

210. Johnson, L. A. *et al.* Matrix stiffness corresponding to strictured bowel induces a fibrogenic response in human colonic fibroblasts. *Inflamm. Bowel Dis.* **19**, 891–903 (2013).

211. Kawano, S. *et al.* Assessment of elasticity of colorectal cancer tissue, clinical utility, pathological and phenotypical relevance. *Cancer Sci.* (2015) doi:10.1111/cas.12720.

212. Sahai, E. *et al.* A framework for advancing our understanding of cancer-associated fibroblasts. *Nature Reviews Cancer* (2020) doi:10.1038/s41568-019-0238-1.

213. Slater, K., Partridge, J. & Nandivada, H. Tuning the Elastic Moduli of Corning ® Matrigel ® and Collagen I 3D Matrices by Varying the Protein Concentration Application Note. **1**, 1–8 (2018).

214. Yao, B. *et al.* Enzymatically degradable alginate/gelatin bioink promotes cellular behavior and degradation in vitro and in vivo. *Biofabrication* **11**, (2019).

215. Liu, Y. *et al.* Stiffness-mediated mesenchymal stem cell fate decision in 3D-bioprinted hydrogels. *Burn. Trauma* **8**, 1–13 (2020).

216. Wei, L. *et al.* An approach for mechanical property optimization of cell-laden alginate–gelatin composite bioink with bioactive glass nanoparticles. *J. Mater. Sci. Mater. Med.* **31**, (2020).

217. Stewart, D. C. *et al.* Quantitative assessment of intestinal stiffness and associations with fibrosis in human inflammatory bowel disease. *PLoS One* **13**, 1–16 (2018).

218. Egorov, V. I., Schastlivtsev, I. V., Prut, E. V., Baranov, A. O. & Turusov, R. A. Mechanical properties of the human gastrointestinal tract. *J. Biomech.* **35**, 1417–1425 (2002).

219. Christensen, M. B., Oberg, K. & Wolchok, J. C. Tensile properties of the rectal and sigmoid colon: a comparative analysis of human and porcine tissue. *Springerplus* **4**, (2015).

220. Egorov, V. I., Schastlivtsev, V., Turusov, R. A. & Baranov, A. O. Participation of the intestinal layers in supplying of the mechanical strength of the intact and sutured gut. *Eur. Surg. Res.* (2002) doi:10.1159/000065712.

221. Dou, Y., Zhao, J. & Gregersen, H. Morphology and stress-strain properties along the small intestine in the rat. *J. Biomech. Eng.* (2003) doi:10.1115/1.1560140.

222. Miftakhov, R. N. & Wingate, D. L. Biomechanics of small bowel motility. *Med. Eng. Phys.* (1994) doi:10.1016/1350-4533(90)90007-U.

223. Gharaie, S. S., Dabiri, S. M. H. & Akbari, M. Smart shear-thinning hydrogels as injectable drug delivery systems. *Polymers (Basel).* **10**, (2018).

224. Mondal, A. *et al.* Characterization and printability of Sodium alginate -Gelatin hydrogel

for bioprinting NSCLC co-culture. *Sci. Rep.* **9**, 1–12 (2019).

225. Bhise, N. S. *et al.* A liver-on-a-chip platform with bioprinted hepatic spheroids. *Biofabrication* **8**, (2016).

226. Cheng, G., Tse, J., Jain, R. K. & Munn, L. L. Micro-environmental mechanical stress controls tumor spheroid size and morphology by suppressing proliferation and inducing apoptosis in cancer cells. *PLoS One* **4**, (2009).

227. Helmlinger, G., Netti, P. A., Lichtenbeld, H. C., Melder, R. J. & Jain, R. K. Solid stress inhibits the growth of multicellular tumor spheroids. *Nature Biotechnology* **15**, (1997).

228. Kelly, C. J. *et al.* Crosstalk between Microbiota-Derived Short-Chain Fatty Acids and Intestinal Epithelial HIF Augments Tissue Barrier Function. *Cell Host Microbe* **17**, 662–671 (2016). doi:10.1016/j.chom.2015.03.005

229. Albenberg, L. *et al.* Correlation between intraluminal oxygen gradient and radial partitioning of intestinal microbiota. *Gastroenterology* (2014) doi:10.1053/j.gastro.2014.07.020.

230. Donohoe, D. R., Wali, A., Brylawski, B. P. & Bultman, S. J. Microbial Regulation of Glucose Metabolism and Cell-Cycle Progression in Mammalian Colonocytes. *PLoS One* (2012) doi:10.1371/journal.pone.0046589.

231. Rivera-Chávez, F. *et al.* Depletion of Butyrate-Producing Clostridia from the Gut Microbiota Drives an Aerobic Luminal Expansion of Salmonella. *Cell Host Microbe* (2016) doi:10.1016/j.chom.2016.03.004.

232. Schwerdtfeger, L. A., Nealon, N. J., Ryan, E. P. & Tobet, S. A. Human colon function ex vivo: Dependence on oxygen and sensitivity to antibiotic. *PLoS One* **14**, 1–17 (2019).

233. Mattern, J., Kallinowski, F., Herfarth, C. & Volm, M. Association of resistance-related protein expression with poor vascularization and low levels of oxygen in human rectal cancer. *Int. J. Cancer* (1996) doi:10.1002/(SICI)1097-0215(19960703)67:1<20::AID-IJC5>3.0.CO;2-1.

234. Dini, S. *et al.* Identifying the necrotic zone boundary in tumour spheroids with pair-correlation functions. *J. R. Soc. Interface* (2016) doi:10.1098/rsif.2016.0649.

235. Krohn, K. A., Link, J. M. & Mason, R. P. Molecular imaging of hypoxia. *Journal of Nuclear Medicine* (2008) doi:10.2967/jnumed.107.045914.

236. Raleigh, J. A. & Koch, C. J. Importance of thiols in the reductive binding of 2-nitroimidazoles to macromolecules. *Biochem. Pharmacol.* (1990) doi:10.1016/0006-2952(90)90086-Z.

237. Gross, M. W., Karbach, U., Groebe, K., Franko, A. J. & Mueller-Klieser, W. Calibration of misonidazole labeling by simultaneous measurement of oxygen tension and labeling density in multicellular spheroids. *Int. J. Cancer* (1995) doi:10.1002/ijc.2910610422.

238. Giuseppe, M. Di *et al.* Mechanical behaviour of alginate-gelatin hydrogels for 3D bioprinting. *J. Mech. Behav. Biomed. Mater.* **79**, 150–157 (2018).

239. Reed, J., Walczak, W. J., Petzold, O. N. & Gimzewski, J. K. In situ mechanical interferometry of matrigel films. *Langmuir* (2009) doi:10.1021/la8033098.

240. Jessie, L. S., Jang, S. H. & Wientjes, M. G. Clinical aspects of drug delivery to tumors. *J. Control. Release* (2002) doi:10.1016/S0168-3659(01)00488-6.

241. Hales, T. *et al.* A FORMAL PROOF of the KEPLER CONJECTURE. *Forum Math. Pi* (2017) doi:10.1017/fmp.2017.1.

242. Han, E. S. & goleman, daniel; boyatzis, Richard; Mckee, A. 済無No Title No Title. *J. Chem. Inf. Model.* **53**, 1689–1699 (2019).

243. Grimes, D. R. & Currell, F. J. Oxygen diffusion in ellipsoidal tumour spheroids. *bioRxiv* (2018) doi:10.1101/271890.

244. Tworek, J. A., Appelman, H. D., Singleton, T. & Greenson, J. K. Stromal tumors of the jejunum and ileum. *Mod. Pathol.* (1997) doi:10.1097/00125480-199711000-00034.

245. Larsson, P. *et al.* Optimization of cell viability assays to improve replicability and reproducibility of cancer drug sensitivity screens. *Sci. Rep.* (2020) doi:10.1038/s41598-020-62848-5.

246. Tsuchiya, T., Ikarashi, Y., Arai, T., Ohhashi, J. & Nakamura, A. Improved sensitivity and decreased sample size in a cytotoxicity test for biomaterials: A modified colony microassay using a microplate and crystal violet staining. *J. Appl. Biomater.* (1994) doi:10.1002/jab.770050412.

247. Langhans, S. A. Three-dimensional in vitro cell culture models in drug discovery and drug repositioning. *Frontiers in Pharmacology* (2018) doi:10.3389/fphar.2018.00006.

248. Mittler, F. *et al.* High-content monitoring of drug effects in a 3D spheroid model. *Front. Oncol.* (2017) doi:10.3389/fonc.2017.00293.

249. Schneider, M. *et al.* Characterization of colon cancer cells: A functional approach characterizing CD133 as a potential stem cell marker. *BMC Cancer* (2012) doi:10.1186/1471-2407-12-96.

250. Heinemann, V. *et al.* Early tumour shrinkage (ETS) and depth of response (DpR) in the treatment of patients with metastatic colorectal cancer (mCRC). *European Journal of Cancer* (2015) doi:10.1016/j.ejca.2015.06.116.

251. Olea, N. *et al.* Evaluation of the growth rate of MCF-7 breast cancer multicellular spheroids using three mathematical models. *Cell Prolif.* (1994) doi:10.1111/j.1365-2184.1994.tb01418.x.

252. Chignola, R. *et al.* Forecasting the growth of multicell tumour spheroids: Implications for the dynamic growth of solid tumours. *Cell Prolif.* (2000) doi:10.1046/j.1365-2184.2000.00174.x.

253. Kawai, S. *et al.* Three-dimensional culture models mimic colon cancer heterogeneity induced by different microenvironments. *Sci. Rep.* (2020) doi:10.1038/s41598-020-60145-9.

254. Yeung, T. M., Gandhi, S. C. & Bodmer, W. F. Hypoxia and lineage specification of cell line-derived colorectal cancer stem cells. *Proc. Natl. Acad. Sci. U. S. A.* (2011) doi:10.1073/pnas.1014519107.

255. Gardner, S. N. A mechanistic, predictive model of dose-response curves for cell cycle phase-specific and -nonspecific drugs. *Cancer Res.* (2000).

256. Slater, C., De La Mare, J. A. & Edkins, A. L. In vitro analysis of putative cancer stem cell populations and chemosensitivity in the SW480 and SW620 colon cancer metastasis model. *Oncol. Lett.* (2018) doi:10.3892/ol.2018.8431.

257. Kjellström, J., Kjellén, E. & Johnsson, A. In vitro radiosensitization by oxaliplatin and 5-fluorouracil in a human colon cancer cell line. *Acta Oncol. (Madr).* (2005) doi:10.1080/02841860500247552.

258. Bokemeyer, C. *et al.* Cetuximab plus 5-FU/FA/oxaliplatin (FOLFOX-4) versus

FOLFOX-4 in the first-line treatment of metastatic colorectal cancer (mCRC): OPUS, a randomized phase II study. *J. Clin. Oncol.* (2007) doi:10.1200/jco.2007.25.18_suppl.4035.

259. Cassidy, J. *et al.* XELOX vs FOLFOX-4 as first-line therapy for metastatic colorectal cancer: NO16966 updated results. *Br. J. Cancer* (2011) doi:10.1038/bjc.2011.201.

260. de Gramont, A. *et al.* Leucovorin and fluorouracil with or without oxaliplatin as first-line treatment in advanced colorectal cancer. *J. Clin. Oncol.* (2000) doi:10.1200/JCO.2000.18.16.2938.

261. Webb, N. E., Montefiori, D. C. & Lee, B. Dose-response curve slope helps predict therapeutic potency and breadth of HIV broadly neutralizing antibodies. *Nat. Commun.* (2015) doi:10.1038/ncomms9443.

262. Hazekawa, M., Nishinakagawa, T., Kawakubo-Yasukochi, T. & Nakashima, M. Evaluation of IC50 levels immediately after treatment with anticancer reagents using a real-time cell monitoring device. *Exp. Ther. Med.* (2019) doi:10.3892/etm.2019.7876.

263. Margiotta, N. *et al.* Revisiting [PtCl2(cis-1,4-DACH)]: An underestimated antitumor drug with potential application to the treatment of oxaliplatin-refractory colorectal cancer. *J. Med. Chem.* **55**, 7182–7192 (2012).

264. Chai, H., Liu, M., Tian, R., Li, X. & Tang, H. miR-20a targets BNIP2 and contributes chemotherapeutic resistance in colorectal adenocarcinoma SW480 and SW620 cell lines. *Acta Biochim. Biophys. Sin. (Shanghai).* (2011) doi:10.1093/abbs/gmq125.

265. Chen, H., Pei, L., Xie, P. & Guo, G. Circ-prkdc contributes to 5-fluorouracil resistance of colorectal cancer cells by regulating mir-375/foxm1 axis and wnt/β-catenin pathway. *Onco. Targets. Ther.* (2020) doi:10.2147/OTT.S253468.

266. Dahan, L., Sadok, A., Formento, J. L., Seitz, J. F. & Kovacic, H. Modulation of cellular redox state underlies antagonism between oxaliplatin and cetuximab in human colorectal cancer cell lines. *Br. J. Pharmacol.* (2009) doi:10.1111/j.1476-5381.2009.00341.x.

267. Berrouet, C., Dorilas, N., Rejniak, K. A. & Tuncer, N. Comparison of drug inhibitory effects (IC50) in monolayer and spheroid cultures. *bioRxiv* 1–18 (2020) doi:10.1101/2020.05.05.079285.

268. Miura, K. *et al.* 5-FU metabolism in cancer and orally-administrable 5-FU drugs. *Cancers (Basel).* **2**, 1717–1730 (2010).

269. Wohlhueter, R. M., McIvor, R. S. & Plagemann, P. G. W. Facilitated transport of uracil and 5-fluorouracil, and permeation of orotic acid into cultured mammalian cells. *J. Cell. Physiol.* (1980) doi:10.1002/jcp.1041040305.

270. Peters, G. J. *et al.* Induction of thymidylate synthase as a 5-fluorouracil resistance mechanism. *Biochimica et Biophysica Acta - Molecular Basis of Disease* (2002) doi:10.1016/S0925-4439(02)00082-0.

271. Luo, F. R., Wyrick, S. D. & Chaney, S. G. Biotransformations of oxaliplatin in rat blood in vitro. *J. Biochem. Mol. Toxicol.* (1999) doi:10.1002/(sici)1099-0461(1999)13:3/4<159::aid-jbt6>3.0.co;2-c.

272. Ehrsson, H., Wallin, I. & Yachnin, J. Pharmacokinetics of oxaliplatin in humans. *Med. Oncol.* **19**, 261–265 (2002).

273. Diasio, R. B. & Harris, B. E. Clinical Pharmacology of 5-Fluorouracil. *Clinical Pharmacokinetics* (1989) doi:10.2165/00003088-198916040-00002.

274. Howell, S. B., Safaei, R., Larson, C. A. & Sailor, M. J. Copper transporters and the cellular

pharmacology of the platinum-containing cancer drugs. *Molecular Pharmacology* (2010) doi:10.1124/mol.109.063172.

275. Ciarimboli, G. *et al.* Organic cation transporter 2 mediates cisplatin-induced oto- and nephrotoxicity and is a target for protective interventions. *Am. J. Pathol.* (2010) doi:10.2353/ajpath.2010.090610.

276. Spreckelmeyer, S., Orvig, C. & Casini, A. Cellular transport mechanisms of cytotoxic metallodrugs: An overview beyond cisplatin. *Molecules* **19**, 15584–15610 (2014).

277. Ghezzi, A. R., Aceto, M., Cassino, C., Gabano, E. & Osella, D. Uptake of antitumor platinum(II)-complexes by cancer cells, assayed by inductively coupled plasma mass spectrometry (ICP-MS). *J. Inorg. Biochem.* (2004) doi:10.1016/j.jinorgbio.2003.08.014.

278. Rovirosa, A. *et al.* Three or four fractions of 4-5 Gy per week in postoperative high-dose-rate brachytherapy for endometrial carcinoma. *Int. J. Radiat. Oncol. Biol. Phys.* (2011) doi:10.1016/j.ijrobp.2010.06.001.

279. Valdes, G. & Iwamoto, K. S. Re-evaluation of cellular radiosensitization by 5-fluorouracil: High-dose, pulsed administration is effective and preferable to conventional low-dose, chronic administration. *Int. J. Radiat. Biol.* **89**, 851–862 (2013).

280. Li, X., Zhuang, X. & Qiao, T. Role of ferroptosis in the process of acute radiation-induced lung injury in mice. *Biochem. Biophys. Res. Commun.* (2019) doi:10.1016/j.bbrc.2019.08.165.

281. Wang, H., Jiang, H., Van De Gucht, M. & De Ridder, M. Hypoxic radioresistance: Can ROS be the key to overcome it? *Cancers (Basel).* **11**, (2019).

282. Pu, A. T., Robertson, J. M. & Lawrence, T. S. Current status of radiation sensitization by fluoropyrimidines. *ONCOLOGY* (1995).

283. Hakala, M. T. Assessment of Growth-Limiting Events Caused by 5-Fluorouracil in Mouse Cells and in Human Cells. *Cancer Res.* (1980).

284. Wang, C. *et al.* Evaluation of CD44 and CD133 as cancer stem cell markers for colorectal cancer. *Oncol. Rep.* **28**, 1301–1308 (2012).

285. Paschall, A. V. *et al.* CD133+CD24lo defines a 5-Fluorouracil-resistant colon cancer stem cell-like phenotype. *Oncotarget* (2016) doi:10.18632/oncotarget.12168.

286. Kawamoto, H. *et al.* Characteristics of CD133+ human colon cancer SW620 cells. *Cell Transplant.* **19**, 857–864 (2010).

287. Asadzadeh, Z. *et al.* The combination effect of Prominin1 (CD133) suppression and Oxaliplatin treatment in colorectal cancer therapy. *Biomed. Pharmacother.* (2021) doi:10.1016/j.biopha.2021.111364.

288. Dallas, N. A. *et al.* Chemoresistant colorectal cancer cells, the cancer stem cell phenotype, and increased sensitivity to insulin-like growth factor-I receptor inhibition. *Cancer Res.* (2009) doi:10.1158/0008-5472.CAN-08-2023.

289. Cho, Y. H. *et al.* 5-FU promotes stemness of colorectal cancer via p53-mediated WNT/β-catenin pathway activation. *Nat. Commun.* (2020) doi:10.1038/s41467-020-19173-2.

290. Carethers, J. M. Review: Systemic treatment of advanced colorectal cancer: Tailoring therapy to the tumor. *Therapeutic Advances in Gastroenterology* (2008) doi:10.1177/1756283X08093607.

291. Chauvin, A. *et al.* The response to neoadjuvant chemoradiotherapy with 5-fluorouracil in locally advanced rectal cancer patients: A predictive proteomic signature. *Clin.*

Proteomics (2018) doi:10.1186/s12014-018-9192-2.

292. Duineveld, L. A. M. *et al.* Symptomatic and asymptomatic colon cancer recurrence: A multicenter cohort study. *Ann. Fam. Med.* **14**, 215–220 (2016).

293. Zhou, Y. *et al.* Cancer stem cells in progression of colorectal cancer. *Oncotarget* (2018) doi:10.18632/oncotarget.23607.

294. Spanogiannopoulos, P. *et al.* Drug resistant gut bacteria mimic a host mechanism for anticancer drug clearance. *bioRxiv* (2019) doi:10.1101/820084.

295. Marofi, F. *et al.* CAR T cells in solid tumors: challenges and opportunities. *Stem Cell Research and Therapy* (2021) doi:10.1186/s13287-020-02128-1.

Appendix A: Dissolution of Gelatin in Alginate/Gelatin Gels

T=0 T=12hrs

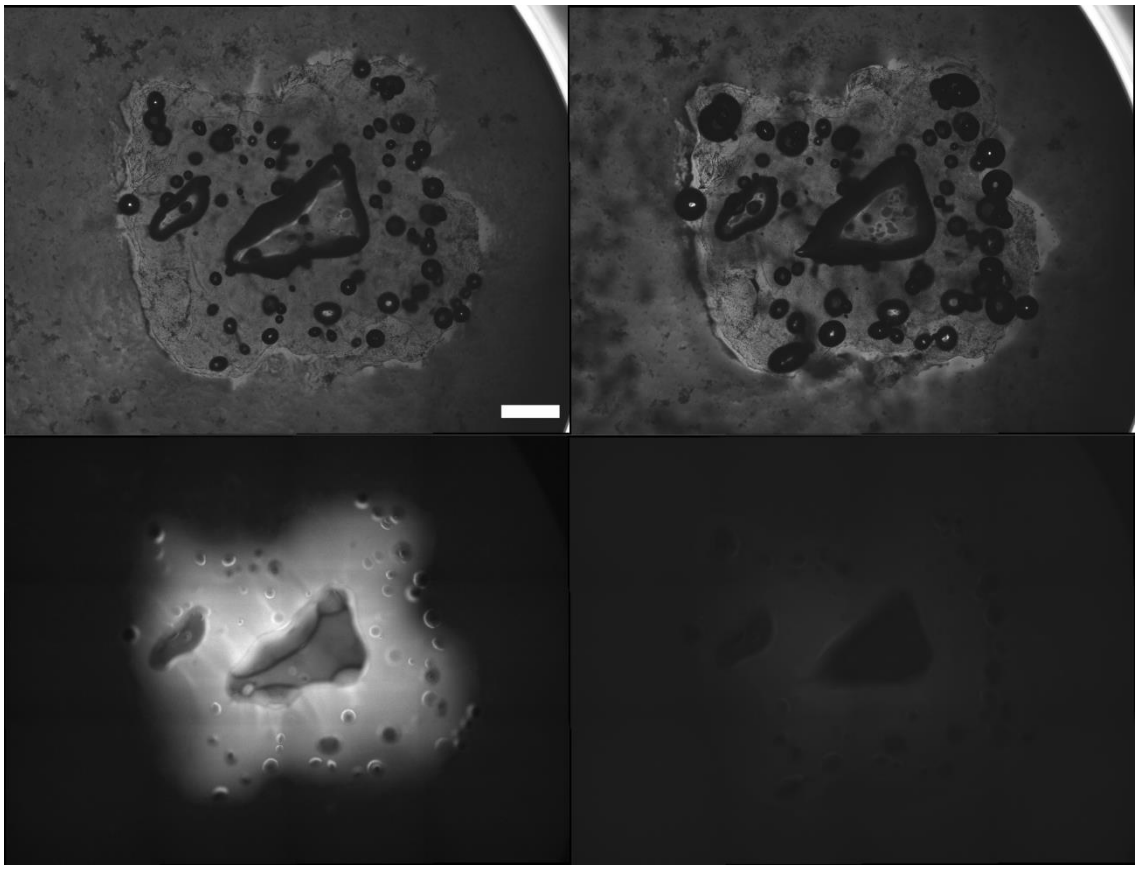

Microscopy data of a 1A10G bioink containing fluorescent gelatin. 1A10G_Flour bioink was immersed in standard culture conditions for 12 hours. Fluorescence of the gelatin component (bottom row) was less localised after 12 hours of immersion, diffusing into the surrounding media. scale bar = 1000μm.

Appendix B: Growth of Breast Cancer Lines

A

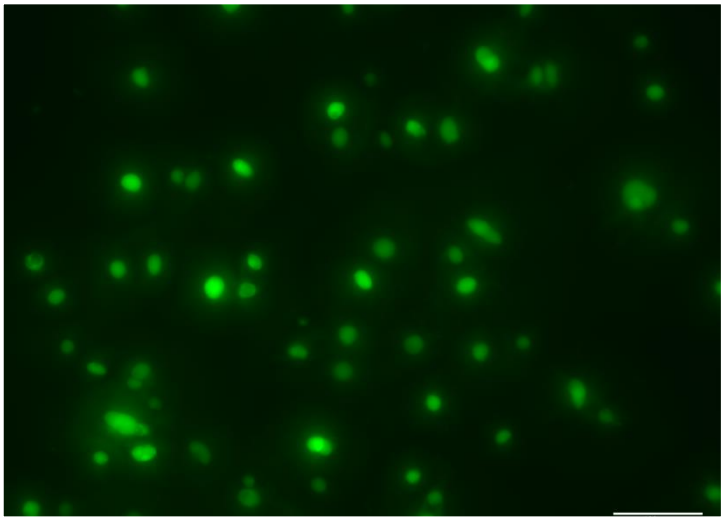

B

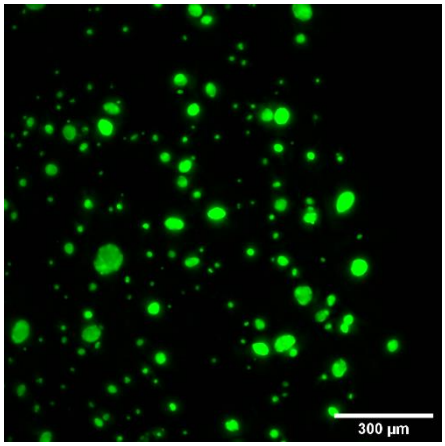

Live-stained (calceinAM) breast cancer spheroids in the 1A10G bioink . **A** MCF7, at day 7, scale bar = 200µm. **B** MDA-MD-231 at day 13, scale bar = 300µm.

Appendix C: Solidity profiling of H&E-stained Spheroids

A B C

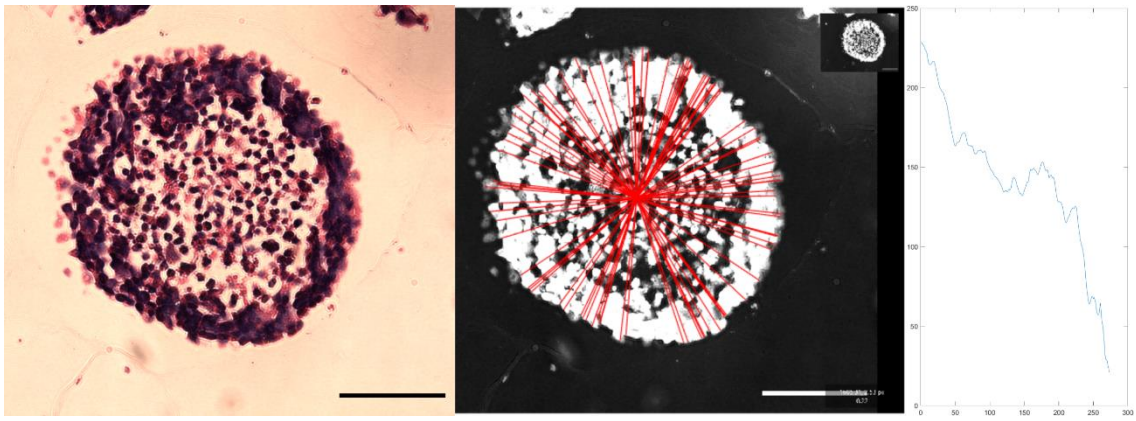

Determination of spheroid solidity using radial evaluation. **A** H&E-stained spheroid. **B** grayscale image produced with thresholding. **C** Mean intensity plot showing the average brightness for the 8 bit image (maximum brightness = 2^8 = 256), calculated by measuring brightness along lines from the spheroid edge to the spheroid core (red lines, **B**).

Appendix D: qPCR Data

A

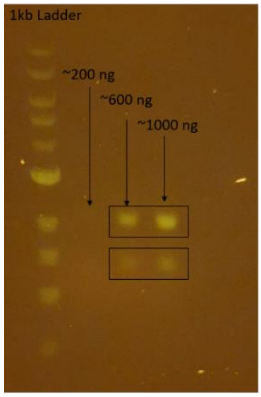

B

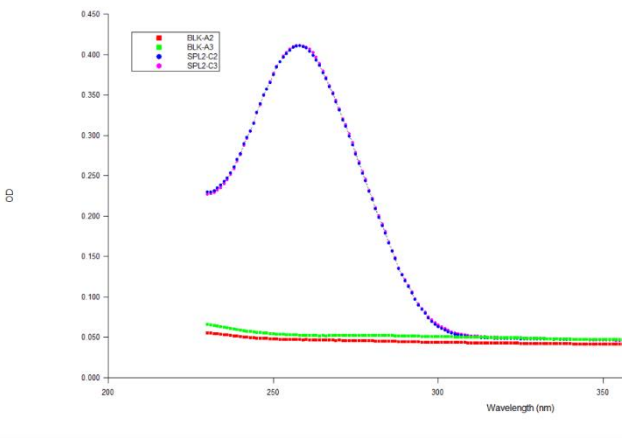

C

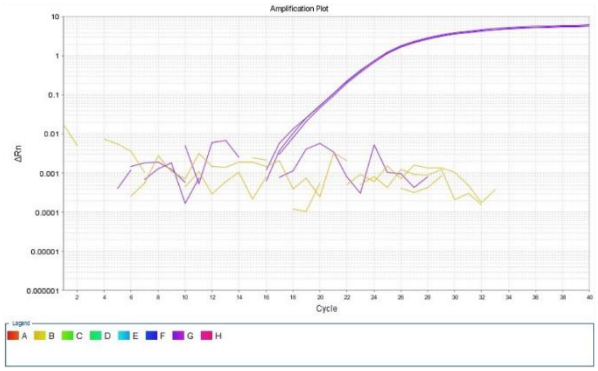

qPCR data from spheroid lysates, showing the presence of DNA (**A**,**B**) and the amplification of the TBP housekeeping gene (**C**).

Appendix E: Growth of Primary Human T Cells

24 hrs

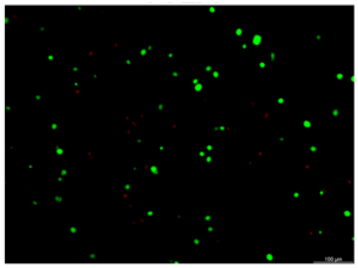

48 hrs

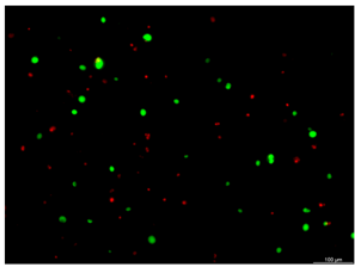

72 hrs

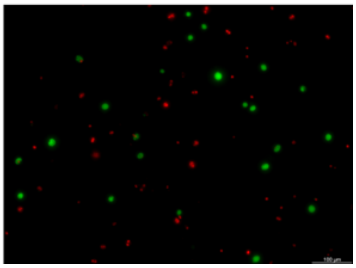

Live/Dead staining of primary human T cells in the alginate/gelatin bioink at different timepoints. Green = live (calceinAM), red = dead (ethidium homodimer III). Data kindly provided by Ms. Ximena Vasto Anzaldo.

Appendix F: Image Analysis Code

Main code file:

```
function SpheroidMeasure(~,~)
%% Choose .lif with UI - ONLY .lif file accepted
clc
clear all
%multiple conditions
multipleConditionsTF = 0;
[im_fname, im_pname, load_cnd] = uigetfile({'*.tif;*.tiff;*.jpg;*.jpeg;*.png;*.bmp;*.lif'}, 'Load
image');
if load_cnd == 0
    return
end
cd(im_pname)
%% Use bfmatlab commands to open .lif & take data/metadata
lif_name=strcat([im_pname, im_fname]);

% fileparts function gives the file loc, name and extension
[pathstr,lif_name,ext] = fileparts(lif_name);
pathstr = strcat(pathstr,'\');

if ext == '.lif'
    % open .lif with bfopen
    lif_name=strcat(lif_name,'.lif');
    data=bfopen(char(lif_name));

    % .lif metadata - get number of channels, scale
    omeMeta = data{1, 4};
    numberOfChannels=omeMeta.getChannelCount(0);

    % Scaling is px:um
    try
        scaling=double(omeMeta.getPixelsPhysicalSizeX(0).getValue());
    catch
        scaling=double(omeMeta.getPixelsPhysicalSizeX(0).value());
    end

    %% Make cell array of 2D images, 1 for each series (ch1 only)

    % Number of rows = number of series
    [rowCount,  ColCount] = size(data);
    ThreeDCh1Data = cell(rowCount,1);

    % take data from channel 1 if multichannel image
    if numberOfChannels == 1
        i = 1;
        for i = 1:rowCount
            ThreeDCh1Data{i,1} = data{i,1};
        end
    else
        % MultiChannel image
        loadMultichannelLif;
        i = 1;
        for i = 1:rowCount
            ThreeDCh1Data{i,1} = ch1Data{i,1};
        end
    end

    % Call maxstack function to Make maximum 2D projection
    % Make Array of 2D images "TwoDCh1Data"
    TwoDCh1Data = cell(rowCount,1);
    voxelSizeX = omeMeta.getPixelsPhysicalSizeX(0).value(ome.units.UNITS.MICROMETER);
    voxelSizeY = omeMeta.getPixelsPhysicalSizeY(0).value(ome.units.UNITS.MICROMETER);
    scaleVal = num2str(double(voxelSizeX(1,1)));

    i = 1;
    TwoDfilename = '1';
    for i = 1:rowCount
        TwoDfilename = num2str(i);
        im = ThreeDCh1Data{i,1};
        im = maxstack(im);
        %im = fstack(im); - old projection code
        TwoDCh1Data{i} = im;
    end
    %% .TIFF FILES - each slice should be a 2D image, not a z stack
elseif contains(ext,'.tif')
    % Find number of images in the tiff & add to cell
    fileInfo = imfinfo(strcat(lif_name,ext));
    numimgs = size(imfinfo(strcat(lif_name,ext)),1);
    scaleVal = [];
    TwoDCh1Data = cell(numimgs,1);
```

```
    data = cell(numimgs,1);
    for i = 1:numimgs
       I = imread(strcat(lif_name,ext),i);
       TwoDCh1Data{i} = I;
    end
    data = TwoDCh1Data;
else
    msg = '.lif and .tiff images only';
    error(msg)
end
%% SETUP GUI
%The main figure
ss = get(0,'ScreenSize');
h.h = figure('CloseRequestFcn', @closeWindowMode);

set(h.h,'Position',[ss(3)/2-(ss(4)/2)-50 50 ss(4)+100 ss(4)-150], 'Visible','off');

%Two panels, one folgr\f gr the image, the other for the controls
h.h_im_cont_p = uipanel('Position',[0.01 0.01 0.7 0.98],'FontSize',12);%Main fig
h.h_cont_tg = uitabgroup('Parent',h.h,'Position',[0.72 0.22 0.28 0.77]);%Main tabs
h.h_dis_p = uipanel('Position',[0.72 0.01 0.27 0.2],'FontSize',12); %bottom-right panel
h.h_det_t = uitab('Parent',h.h_cont_tg,'Title','<html><font size=4 color="black">Spheroid analysis
transmitted light','Tag','1');
h.h_im_cont_p_ax = axes('Parent',h.h_im_cont_p,'Position',[0 0 1 1],'Visible','on');

cont_top = 0.9;
bt_h = 0.055;
gap = bt_h + 0.0075; %space between buttons/objects
edit_offs = 0.01;

% Load defaults & Global variables
myMode = 1;
kernelSize=50;
EccenCutoff = 0.85;
smoothDefault = 0.7;
offset=-0.07;
size1=70;
size2=5000;
se = strel('disk',2);
scaling=1;
L=[];
B=[];
mask5=[];
properties=[];
focusedProcessed=[];

%Set up Random Colourmap for images
x=[0:255];
T=rand(256,3);
map=T;
map(1,:,:)=[0,0,0];

%Buttons and controls (Fluorescent,KernelSize,SizeFilters,Offset)
set(h.h,'Position',[ss(3)/2-(ss(4)/2)-50 50 ss(4)+100 ss(4)-150], 'Visible','on');
pos = -0.75;
pos=pos;
posMod = 1.0;
fluorescence_text =
uicontrol('Parent',h.h_det_t,'Style','text','String','Fluorescence','FontSize',12,'Units','normalize
d','HorizontalAlignment','left','Position',[0.1, cont_top-gap*pos, 0.54, bt_h-edit_offs]);
fluorescence=uicontrol('Parent',h.h_det_t,'Style','checkbox','FontSize',24,'Units','normalized','Hor
izontalAlignment','left','Enable','on','Value',1,'Position',[0.75, cont_top-gap*pos, 0.54, bt_h-
edit_offs]);
pos = pos + 0.75*posMod;
Smoothing_text = uicontrol('Parent',h.h_det_t,'Style','text','String','Fit
Ellipse','FontSize',12,'Units','normalized','HorizontalAlignment','left','Position',[0.1, cont_top-
gap*pos, 0.54, bt_h-edit_offs]);
Smoothingbox=uicontrol('Parent',h.h_det_t,'Style','checkbox','FontSize',24,'Units','normalized','Hor
izontalAlignment','left','Enable','on','Value',1,'Position',[0.75, cont_top-gap*pos, 0.54, bt_h-
edit_offs]);
pos = pos + posMod;
Smooth_text = uicontrol('Parent',h.h_det_t,'Style','text','String','Smoothness
Cutoff','FontSize',12,'Units','normalized','HorizontalAlignment','left','Position',[0.1, cont_top-
gap*pos, 0.54, bt_h-edit_offs]);
Smoothness =
uicontrol('Parent',h.h_det_t,'Style','edit','String',num2str(smoothDefault),'FontSize',12,'Units','n
ormalized','Position',[0.7, cont_top-gap*pos, 0.22, bt_h]);
pos = pos + posMod;
Eccentricity_text = uicontrol('Parent',h.h_det_t,'Style','text','String','Eccentricity
Cutoff','FontSize',12,'Units','normalized','HorizontalAlignment','left','Position',[0.1, cont_top-
gap*pos, 0.54, bt_h-edit_offs]);
Eccentricity =
uicontrol('Parent',h.h_det_t,'Style','edit','String',num2str(EccenCutoff),'FontSize',12,'Units','nor
malized','Position',[0.7, cont_top-gap*pos, 0.22, bt_h]);
pos = pos + posMod;
KS_text = uicontrol('Parent',h.h_det_t,'Style','text','String','Kernel
Size:','FontSize',12,'Units','normalized','HorizontalAlignment','left','Position',[0.1, cont_top-
gap*pos, 0.54, bt_h-edit_offs]);
```

```
KS_edit =
uicontrol('Parent',h.h_det_t,'Style','edit','String',num2str(kernelSize),'FontSize',12,'Units','norm
alized','Position',[0.7, cont_top-gap*pos, 0.22, bt_h]);
pos = pos + posMod;
offset_text =
uicontrol('Parent',h.h_det_t,'Style','text','String','Offset:','FontSize',12,'Units','normalized','H
orizontalAlignment','left','Position',[0.1, cont_top-gap*pos, 0.54, bt_h-edit_offs]);
offset_edit =
uicontrol('Parent',h.h_det_t,'Style','edit','String',num2str(offset),'FontSize',12,'Units','normaliz
ed','Position',[0.7, cont_top-gap*pos, 0.22, bt_h]);
pos = pos + posMod;
sizeFilter1_text = uicontrol('Parent',h.h_det_t,'Style','text','String','Min Size
(pix):','FontSize',12,'Units','normalized','HorizontalAlignment','left','Position',[0.1, cont_top-
gap*pos, 0.54, bt_h-edit_offs]);
sizeFilter1_edit =
uicontrol('Parent',h.h_det_t,'Style','edit','String',num2str(size1),'FontSize',12,'Units','normalize
d','Position',[0.7, cont_top-gap*pos, 0.22, bt_h]);
pos = pos + posMod;
sizeFilter2_text = uicontrol('Parent',h.h_det_t,'Style','text','String','Max Size
(pix):','FontSize',12,'Units','normalized','HorizontalAlignment','left','Position',[0.1, cont_top-
gap*pos, 0.54, bt_h-edit_offs]);
sizeFilter2_edit =
uicontrol('Parent',h.h_det_t,'Style','edit','String',num2str(size2),'FontSize',12,'Units','normalize
d','Position',[0.7, cont_top-gap*pos, 0.22, bt_h]);

%Change image slider and number
pos = pos + 1.5;
image_number =
uicontrol('Parent',h.h_det_t,'Style','slider','String','Image','Callback',@changeImage,'Min', 1,
'Max', size(data,1), 'Value', 1, 'SliderStep', [1/(size(data,1)-1),
1],'FontSize',12,'Units','normalized','Position',[0.1, cont_top-gap*pos, 0.8, bt_h]);
pos = pos + 1.5;
cont_image_text = uicontrol('Parent',h.h_det_t,'Style','text','String','Image
Number:','FontSize',12,'Units','normalized','HorizontalAlignment','left','Position',[0.1, cont_top-
gap*pos, 0.54, bt_h-edit_offs]);
cont_image_edit =
uicontrol('Parent',h.h_det_t,'Style','edit','String',num2str(get(image_number,'Value')),'Callback',@
changeImageNumber,'FontSize',12,'Units','normalized','Position',[0.7, cont_top-gap*pos, 0.22,
bt_h]);

%Detect, reset and run all, supress im out
pos = pos + posMod;
Detect_button =
uicontrol('Parent',h.h_det_t,'Style','pushbutton','String','Detect','FontSize',12,'Callback',@detect
,'Units','normalized','Position',[0.05, cont_top-gap*pos, 0.9, bt_h]);
pos = pos + posMod;
Crop_button = uicontrol('Parent',h.h_det_t,'Style','pushbutton','String','Delete
Region','FontSize',12,'Callback',@cropIm,'Units','normalized','Position',[0.5, cont_top-gap*pos,
0.45, bt_h]);
Reset_button = uicontrol('Parent',h.h_det_t,'Style','pushbutton','String','Clear
Outlines','FontSize',12,'Callback',@clearOutlines,'Units','normalized','Position',[0.05, cont_top-
gap*pos, 0.45, bt_h]);
pos = pos + posMod;
display_label_button = uicontrol('Parent',h.h_det_t,'Style','pushbutton','String','Display
Labels','FontSize',12,'Callback',@displayLabels,'Units','normalized','Enable','off','Position',[0.05
, cont_top-gap*pos, 0.9, bt_h]);
pos = pos + posMod;
Run_All_button = uicontrol('Parent',h.h_det_t,'Style','pushbutton','String','Run
All','FontSize',12,'Callback',@runAll,'Units','normalized','Position',[0.05, cont_top-gap*pos, 0.9,
bt_h]);
pos = pos + posMod;
imOut_text = uicontrol('Parent',h.h_det_t,'Style','text','String','Output Images with Run
All?','FontSize',12,'Units','normalized','HorizontalAlignment','left','Position',[0.05, cont_top-
gap*pos, 0.9, bt_h-edit_offs]);
imOut_edit =
uicontrol('Parent',h.h_det_t,'Style','checkbox','FontSize',24,'Units','normalized','HorizontalAlignm
ent','left','Enable','on','Value',0,'Position',[0.75, cont_top-gap*pos, 0.9, bt_h-edit_offs]);

%Save Images, Scale Bar
pos=3.5;
Scale_text =
uicontrol('Parent',h.h_dis_p,'Style','text','String','Scale(px:um)','FontSize',12,'Units','normalize
d','HorizontalAlignment','left','Position',[0.05, cont_top-gap*pos, 0.9, bt_h+0.1]);
ScaleBox_edit =
uicontrol('Parent',h.h_dis_p,'Style','edit','String',scaleVal,'FontSize',12,'Units','normalized','Po
sition',[0.375, cont_top-gap*pos, 0.2, bt_h+0.1]);
Scale_Bar_text = uicontrol('Parent',h.h_dis_p,'Style','text','String','Scale
Bar','FontSize',12,'Units','normalized','HorizontalAlignment','left','Position',[0.6, cont_top-
gap*pos, 0.9, bt_h+0.1]);
ScaleBar =
uicontrol('Parent',h.h_dis_p,'Style','checkbox','FontSize',24,'Units','normalized','HorizontalAlignm
ent','left','Enable','on','Position',[0.85, cont_top-gap*pos, 0.9, bt_h+0.1]);
pos=7;
disco_button = uicontrol('Parent',h.h_dis_p,'Style','pushbutton','String','Save Image With
Labels','FontSize',12,'Callback',@runDisco,'Units','normalized','enable','off','Position',[0.05,
cont_top-gap*pos, 0.9, bt_h+0.1]);
pos=pos+3.5;
```

```
save_preview_button = uicontrol('Parent',h.h_dis_p,'Style','pushbutton','String','Save Image without
Labels','FontSize',12,'Callback',@savePreview,'Units','normalized','Position',[0.05, cont_top-
gap*pos, 0.9, bt_h+0.1]);


curr_im = imshow(TwoDCh1Data{1},[],'Parent',h.h_im_cont_p_ax);
dcm = datacursormode(h.h);
set(dcm, 'UpdateFcn', @dcmCallback);
drawnow;
%% FUNCTIONS
    % maxstack,adaptivethreshold,ellipse-fitting functions,bfmatlab are separate .m files

    % For multi channel image take only z planes from ch1 for each series
    function loadMultichannelLif(~,~)
        % Always use channel 1 from a multichannel lif.
        channelAssignment = {'1'};
        % bfGetReader for less memory usage
        reader=bfGetReader(lif_name);
        omeMeta = reader.getMetadataStore();
        seriesNum = reader.getSeriesCount;

        % For each series take all ch 1 z planes - output as ch1Data
        ch1Data = cell(seriesNum,1);
        for series = 1:seriesNum
            reader.setSeries(series-1);
            iPlaneBeg = 1;
            iPlaneEnd = reader.getIndex(reader.getSizeZ-1,0,0)+1;
            sData{series} = data{series,1};
            sData2 = cell(iPlaneEnd,1);
            j=1;
            for j=1:iPlaneEnd
                sData2{j,1} = sData{1,series}{j,1};
                sData2{j,2} = sData{1,series}{j,2};
            end
            ch1Data{series} = sData2;
            clear sData2;
        end
    end

    % Go to next image
    function changeImage(~,~)
        set(h.h, 'pointer', 'watch')
        drawnow;
        set(cont_image_edit,'String',num2str(round(get(image_number,'Value'))));
        currentImageNumber = round(get(image_number,'Value'));
        curr_im = imshow(TwoDCh1Data{currentImageNumber},[],'Parent',h.h_im_cont_p_ax);
        set(display_label_button,'Enable','off');
        set(disco_button,'Enable','off');
        set(h.h, 'pointer', 'arrow');
    end

    % Go to image number
    function changeImageNumber(~,~)
        set(h.h, 'pointer', 'watch')
        drawnow;
        set(image_number,'Value',(str2double(get(cont_image_edit,'String'))));
        currentImageNumber = str2double(get(cont_image_edit,'String'));
        curr_im = imshow(TwoDCh1Data{currentImageNumber},[],'Parent',h.h_im_cont_p_ax);
        set(display_label_button,'Enable','off');
        set(disco_button,'Enable','off');
        set(h.h, 'pointer', 'arrow')
    end

    % Detect Spheroids
    function detect(~,~)
        myMode = 1;
        %myMode = 1 - detect spheroids in current image.
        runData(myMode);
    end

    % Measure all objects in all images and export as .csv
    function runAll(~,~)
        myMode = 2;
        runData(myMode);
    end

    % Clear outlines of detected objects
    function clearOutlines(~,~)
        set(h.h, 'pointer', 'watch')
        drawnow;
        set(image_number,'Value',(str2double(get(cont_image_edit,'String'))));
        currentImageNumber = str2double(get(cont_image_edit,'String'));
        curr_im = imshow(TwoDCh1Data{currentImageNumber},[],'Parent',h.h_im_cont_p_ax);
        set(display_label_button,'Enable','off');
        set(disco_button,'Enable','off');
        set(h.h, 'pointer', 'arrow')
    end
```

```
    % Delete a selected region from the current image
    function cropIm(~,~)
        set(h.h, 'pointer', 'watch')
        drawnow;
        %get current image
        currentImageNumber = round(get(image_number,'Value'));
        curr_im = imshow(TwoDCh1Data{currentImageNumber},[],'Parent',h.h_im_cont_p_ax);
        CropIm = TwoDCh1Data{currentImageNumber};
        %user define crop region
        [xi,yi] = getpts(gcf);
        freezeInterface
        if size(xi,1) < 50
            %define a polygon from the points & find coodrinates inside
            cBoundXmin = round(floor(min(xi())),0);
            cBoundXmax = round(ceil(max(xi())),0);
            cBoundYmin = round(floor(min(yi())),0);
            cBoundYmax = round(ceil(max(yi())),0);
            xq = linspace(cBoundXmin, cBoundXmax, (cBoundXmax-cBoundXmin+1));
            yq = linspace(cBoundYmin, cBoundYmax, (cBoundYmax-cBoundYmin+1));
            xq1s = (xq .* 0)+1;
            yq1s = (yq .* 0)+1;
            xfinal = yq1s'*xq;
            yfinal = yq'*xq1s;
            xfinal = xfinal(:);
            yfinal = yfinal(:);

            [in,on] = inpolygon(xfinal,yfinal,xi,yi);
            inon = in | on;
            idx = find(inon(:));
            idx = idx'; % Linear Indices Of 'inon' Points
            xCoordsCrop = xfinal(idx);    % X & y Coordinates Of 'inon' Points
            yCoordsCrop = yfinal(idx);

            %set cropped pixels value to 0
            for j = 1:size(xCoordsCrop)
               CropIm(yCoordsCrop(j),xCoordsCrop(j)) = 0;
            end

            TwoDCh1Data{currentImageNumber} = CropIm;
            curr_im = imshow(TwoDCh1Data{currentImageNumber},[],'Parent',h.h_im_cont_p_ax);
        else
            error('crop region has too many points (>50)');
        end
        unFreezeInterface
        set(h.h, 'pointer', 'arrow');
    end

    % Show object boundaries and enumerate
    function displayLabels(~,~)
        counter = 1;

        maxBright = max(im2double(focusedProcessed(:)));
        imshow(focusedProcessed*(1/(maxBright)));

        for k = 1:length(B)
            boundary_Master = B{k};
            line(boundary_Master(:,2), boundary_Master(:,1),...
            'color','r','LineWidth',1);
            text(mean(boundary_Master(:,2)), mean(boundary_Master(:,1)), sprintf('%d',
counter),'FontSize', 20, 'Color', 'white','FontWeight','Bold');
            counter = counter + 1;
        end
        set(disco_button,'Enable','on');
    end

    %Add 200um scale bar. Change "ScaleBarLengthInuM" to adjust
    function imWithScaleBar = addScaleBar(ImgForScaleBar,GreenOrGray)
        ScaleBarLengthInuM = 200;
        Im = ImgForScaleBar;
        greenMaporGrayScale = GreenOrGray;
        if isa(Im,'uint8')
            bitDepth = 8;
        elseif isa(Im,'uint16')
            bitDepth = 16;
        elseif isa(Im,'uint32')
            bitDepth = 32;
        elseif isa(Im,'uint64')
            bitDepth = 64;
        end
        %Green map for green live stains
        x2 = [0:(2^bitDepth-1)];
        Gmap = [zeros(2^bitDepth,1) x2' zeros(2^bitDepth,1)];
        Gmap = Gmap/(2^bitDepth-1);

        Scale = str2double(get(ScaleBox_edit,'String'));
        barLengthPx = ScaleBarLengthInuM/Scale;
        barHeightPx = round(size(Im,1)/50,0);
        %scale bar position is 5% of the image width from edge
```

```
        barOffsetFromEdge = round(size(Im,2)*0.05,0);
        scaleLengthPx = barLengthPx*Scale;
        initialPosX = size(Im,1)-barOffsetFromEdge;
        initialPosY = size(Im,2)-barOffsetFromEdge;

        if size(Im,3) == 1
           %grayscale img
           if strcmp(greenMaporGrayScale,'green') == 1
               rgbImage = ind2rgb(Im, Gmap);
           else
               rgbImage = Im;
           end
        else
           %rgb img
           if strcmp(greenMaporGrayScale,'green') == 1
               rgbImage = rgb2gray(Im);
               rgbImage = ind2rgb(rgbImage, Gmap);
           else
               rgbImage = Im;
           end
        end

        if size(rgbImage,3) == 3
            rgbImage(initialPosX-barHeightPx:initialPosX,initialPosY-barLengthPx:initialPosY,1) =
2^bitDepth;
            rgbImage(initialPosX-barHeightPx:initialPosX,initialPosY-barLengthPx:initialPosY,2) =
2^bitDepth;
            rgbImage(initialPosX-barHeightPx:initialPosX,initialPosY-barLengthPx:initialPosY,3) =
2^bitDepth;
        else
            rgbImage(initialPosX-barHeightPx:initialPosX,initialPosY-barLengthPx:initialPosY) =
2^bitDepth;
        end

        imWithScaleBar = rgbImage;
    end

    %Save images as png
    function savePreview(~,~)
        SingleImOrAllIms = questdlg('Save This Image or All Images?','SaveDialog','This Image
Only','All Images','Cancel');
        switch SingleImOrAllIms
            case 'This Image Only'
            mkdir(strcat(date,'_PreviewImages'));
            prompt = {'Input File Name (without extension):'};
            title = 'Save as...';
            dims = [1 35];
            definput = {'myFile'};
            fileName = inputdlg(prompt,title,dims,definput);
            fileName = strcat(char(fileName), '.png');
            fileName = strcat(date,'_PreviewImages/',fileName);
            currentImageNumber = round(get(image_number,'Value'));

            if get(ScaleBar,'Value')==1 && ~isempty(get(ScaleBox_edit,'String')) == 1
                %add scale
                imWithScaleBar = addScaleBar(TwoDCh1Data{currentImageNumber},'gray');
                outIm = imWithScaleBar;
            else
                outIm = TwoDCh1Data{currentImageNumber};
            end

            imwrite(outIm,fileName);

            case 'All Images'
                mkdir(strcat(date,'_PreviewImages'));
                for k = 1:size(TwoDCh1Data,1)
                    fileName = strcat('img_',num2str(k));
                    fileName = strcat(char(fileName), '.png');
                    fileName = strcat(date,'_PreviewImages/',fileName);
                if get(ScaleBar,'Value')==1 && ~isempty(get(ScaleBox_edit,'String')) == 1
                    %add scale
                    imWithScaleBar = addScaleBar(TwoDCh1Data{k},'green');
                    outIm = imWithScaleBar;
                else
                    outIm = TwoDCh1Data{k};
                end
                    imwrite(outIm,fileName);
                end
        end
    end

    %Save Current Image With Labels
    function runDisco(~,~)
                %figure ('Visible','off')
                displayLabels
                img=getframe(h.h_im_cont_p_ax);
                outImg = img.cdata;
```

```
            im = TwoDCh1Data{1};
            imgXResolution = size(im,2);
            imgYResolution = size(im,1);

            mkdir(strcat(date,'_PreviewImages'));
            prompt = {'Input File Name (without extension):'};
            title = 'Save as...';
            dims = [1 35];
            definput = {'myFile'};
            fileName = inputdlg(prompt,title,dims,definput);
            fileName = strcat(char(fileName), '.png');
            fileName = strcat(date,'_PreviewImages/',fileName);

            %Scale Bar
            if get(ScaleBar,'Value')==1 && ~isempty(get(ScaleBox_edit,'String')) == 1
                %add scale
                imWithScaleBar = addScaleBar(outImg,'gray');
                outIm = imWithScaleBar;
            end
            imwrite(outIm,fileName);

end

%Set buttons inactive
function freezeInterface(~,~)
    set(cont_image_edit,'Enable','off');
    set(Detect_button,'Enable','off');
    set(Reset_button,'Enable','off');
    set(Crop_button,'Enable','off');
    set(display_label_button,'Enable','off');
    set(Run_All_button,'Enable','off');
    set(save_preview_button,'Enable','off');
    set(disco_button,'Enable','off');
    %should this be here??
    unFreezeInterface;
end

%Set buttons active
function unFreezeInterface(~,~)
    set(cont_image_edit,'Enable','on');
    set(Detect_button,'Enable','on');
    set(Reset_button,'Enable','on');
    set(Crop_button,'Enable','on');
    set(display_label_button,'Enable','on');
    set(Run_All_button,'Enable','on');
    set(save_preview_button,'Enable','on');
    set(disco_button,'Enable','on');
end

%Run all images with current settings
function runData(~,~)
    allDataCounter = 0;
    conditionCounter = 0;
    mode = myMode;
    currentImageNumber = round(get(image_number,'Value'));
    im = TwoDCh1Data{currentImageNumber};
    imgXResolution = size(im,2);
    imgYResolution = size(im,1);
    xRes = imgXResolution;
    yRes = imgYResolution;
    %mode, 1 = detect, 2 = run all images
    if mode == 2
        progress = waitbar(0,'Running...');
        startImRun = 1;
        endImRun = size(data,1);
    else
        %detect
        set(h.h, 'pointer', 'watch')
        drawnow;
        currentImageNumber = str2double(get(cont_image_edit,'String'));
        curr_im = imshow(TwoDCh1Data{currentImageNumber},[],'Parent',h.h_im_cont_p_ax);
        startImRun = currentImageNumber;
        endImRun = currentImageNumber;
    end

    for allData=startImRun:endImRun
        allDataCounter = allDataCounter + 1;

        maxObjSize = round(str2double(get(sizeFilter2_edit,'String')));
        minObjSize = round(str2double(get(sizeFilter1_edit,'String')));
        kernelSizeVal = str2double(get(KS_edit,'String'));
        offsetVal = str2double(get(offset_edit,'String'));
        eccenLimit = str2double(get(Eccentricity,'String'));

        if(startImRun<endImRun)
            freezeInterface;
        end
        excelData=[];
```

```
            %im names are im_[im_number]
            name = strcat('im',num2str(allData));
            [filepath,myname,ext] = fileparts(char(name));
            name = myname;
            im=TwoDCh1Data{allData};
            focused=im;

            if get(fluorescence,'Value')==0
                focusedProcessed=imcomplement(focused);
            else
                focusedProcessed=focused;
            end

            %Image Thresholding with adaptivethreshold
            mask=adaptivethreshold(focusedProcessed,kernelSizeVal,offsetVal,0);
            mask=imdilate(mask,se);
            mask2=imfill(mask,'holes');
            mask3=bwareaopen(mask2,minObjSize);
            D = -bwdist(~mask3);
            Ld = watershed(D);
            bw2 = mask3;
            bw2(Ld == 0) = 0;
            extendMin = imextendedmin(D,2.5);
            D2 = imimposemin(D,extendMin);
            Ld2 = watershed(D2);
            bw3 = mask3;
            bw3(Ld2 == 0) = 0;
            bw4=bwareaopen(bw3,minObjSize);
            mask4=imclearborder(bw4);
            mask5=immultiply(focusedProcessed,mask4);

            [B,L,N,A] = bwboundaries(mask4);

properties=regionprops(L,focused,'Area','Centroid','MajorAxisLength','MinorAxisLength','Eccentricity
','Perimeter');
            propsExOld=struct2cell(properties);

            % Threshold for goodness-of-fit against a fourier series
            SmoothnessThreshold = str2double(get(Smoothness,'String'));

            %object rejection based on smoothness (fourier approach)
            Bcounter = 1;
            B2 = cell(size(B,1),size(B,2));
            removePoints = [];
            for i = 1:length(B)
                dataPoints = B{i,1}(:,:);
                xDataPoints = dataPoints(:,2);
                yDataPoints = dataPoints(:,2);
                fitVal = SmoothTest(xDataPoints,yDataPoints);
                if fitVal > SmoothnessThreshold
                    B2{Bcounter,1} = B{i,1};
                    Bcounter = Bcounter+1;
                else
                    removePoints = [removePoints i];
                end
            end
            B2 = B2(1:Bcounter-1);
            propsExOld(:,removePoints) = [];
            B = B2;
            FitMaskFourier = zeros(yRes,xRes);
            counter = 0;
            for i = 1:length(B)
                if ~isempty(B{i}) == 1
                    curArr = B{i};
                    for j = 1:size(B{i,1},1)
                        FitMaskFourier(curArr(j,1),curArr(j,2)) = 1;
                    end
                else
                    B(i-counter,:) = [];
                    counter = counter+1;
                end
            end

            % Fit elipse to object outlines
            if get(Smoothingbox,'Value')==1
                FitCell = cell(length(B),1);
                FitRes = zeros(length(B),7);
                FitMask = zeros(yRes,xRes);

                for i = 1:length(B)
                    noSol = 0;
                    FitMask = zeros(yRes,xRes);
                    curArr = B{i};
                    [zt, at, bt, alphat] = fitellipse(curArr, 'linear', 'constraint', 'trace');
                    if (zt+at+bt+alphat)>0
                        curArr = plotellipse2(zt, at, bt, alphat, 'k--');
                        curArr = curArr';
```

```
                        if (mean(curArr(:,1)) - curArr(1,1)) ~= 0 %if all elements in curArr are the
same, then the solution is single pixel.
                            curArr(curArr<1) = 1;
                            for j = 1:length(curArr)
                                FitMask(curArr(j,1),curArr(j,2)) = 1;
                            end

                            %chk that the fit elipse is completely enclosed
                            FitMask = imbinarize(FitMask);
                            holeChk = imfill(FitMask,'holes') - FitMask;
                            if sum(holeChk(:)) > 0 %elipse is solid
                                FitMask = imfill(FitMask,'holes');
                            else %elipse is just a boundary - close
                                cB = closeBoundary(FitMask);
                                if ~isempty(cB) == 1
                                    FitMask = zeros(yRes,xRes);
                                    for j = 1:length(cB)
                                        FitMask(cB(j,1),cB(j,2)) = 1;
                                    end
                                    FitMask = imfill(FitMask,'holes');
                                    if sum(FitMask(:)) > ((yRes*xRes)-1) %ignore very large
solutions
                                        noSol = 1;
                                    end
                                else
                                    noSol = 1; %no solution
                                end
                            end

                            %Ellipse parameters (centroid, semi axis, angle)
                            %Another check. img res should be consistent.
                            %should be all white pixels or not of type logical.
                            if size(FitMask,1)~=yRes || size(FitMask,2)~=xRes || mean(FitMask(:))>=
1
                                %Do nothing
                            else
                                if noSol == 0 && sum(FitMask(:))<maxObjSize
                                    FitRes(i,1) = zt(1,1);
                                    FitRes(i,2) = zt(2,1);
                                    FitRes(i,3) = at;
                                    FitRes(i,4) = bt;
                                    FitRes(i,5) = at / bt;
                                    FitRes(i,6) = pi*at*bt;
                                    FitRes(i,7) = alphat;
                                    FitCell{i} = FitMask;
                                else
                                    stophereplease = 1;
                                end
                            end
                        end
                    end
                end

                %Add together
                FitMask = zeros(yRes,xRes);
                counter = 0;
                for i = 1:length(FitCell)
                    if ~isempty(FitCell{i}) == 1
                        curArr = FitCell{i};
                        FitMask = FitMask + curArr;
                    else
                        FitRes(i-counter,:) = [];
                        counter = counter+1;
                    end
                end

                %Watershed again, new fits may merge
                FitMask2 = -bwdist(~FitMask);
                FitMask2 = imimposemin(FitMask2,extendMin);
                FitMask2 = watershed(FitMask2);
                FitMask(FitMask2 == 0) = 0;
                FinalMask = FitMask;
            else
                FinalMask = L;
            end

            %Add detected object boundaries to the figure
            if mode == 1
                %detect objects only
                %adjustbrightness
                maxBright = max(im2double(focusedProcessed(:)));
                imshow(focusedProcessed*(1/(maxBright)));

                if get(Smoothingbox,'Value')==1 %if elipse-fitting, get measurements
                    [B,L,N,A] = bwboundaries(FinalMask);

properties=regionprops(L,focused,'Area','Centroid','MajorAxisLength','MinorAxisLength','Eccentricity
','Perimeter');
```

```
                    propsEx=struct2cell(properties);
                    objIdx = find([properties.Area] < maxObjSize & [properties.Area] > minObjSize &
[properties.Eccentricity] < eccenLimit);
                    allIdx = linspace(1,size(properties,1),size(properties,1));
                else %else take sorted properties from before
                    propsEx = propsExOld;
                    propsExAreas = cell2mat(propsEx(1,:));
                    propsExEccen = cell2mat(propsEx(5,:));
                    objIdx = find(propsExAreas < maxObjSize & propsExAreas > minObjSize &
propsExEccen < eccenLimit);
                    allIdx = linspace(1,size(propsEx,2),size(propsEx,2));
                end

                %exclude low eccentricities, min/max object sizes
                objIdxRemove = nonzeros(~ismember(allIdx,objIdx).*allIdx);
                propsEx=struct2cell(properties);
                propsEx(:,objIdxRemove) = [];
                B(objIdxRemove,:) = [];

                hold on
                for k=1:length(B)
                    jetColourMap = hsv(length(B));
                    boundary_Master = B{k};
                    line(boundary_Master(:,2), boundary_Master(:,1),...
                    'color',[jetColourMap(randi(length(B)),1) jetColourMap(randi(length(B)),1)
jetColourMap(randi(length(B)),3)],'LineWidth',1,'Parent', h.h_im_cont_p_ax);
                end
                hold off;

                set(h.h, 'pointer', 'arrow')
                set(display_label_button,'Enable','on');
            else
            %% myMode = 2. Collate object measurements & Export .csv

               if get(Smoothingbox,'Value')==1
                   [B,L,N,A] = bwboundaries(FinalMask);

properties=regionprops(L,focused,'Area','Centroid','MajorAxisLength','MinorAxisLength','Eccentricity
','Perimeter');
                    %remove objects outside of constraints (size,eccentricity)
                    objIdx = find([properties.Area] < maxObjSize & [properties.Area] > minObjSize &
[properties.Eccentricity] < eccenLimit);
                    allIdx = linspace(1,size(properties,1),size(properties,1));
                    objIdxRemove = nonzeros(~ismember(allIdx,objIdx).*allIdx);
                    propsExOld=struct2cell(properties);

                    if size(FitRes,1) == size(B,1)
                        propsExOld(:,objIdxRemove) = [];
                        B(objIdxRemove,:) = [];
                        %Use the measurements from the ellipse-fit calculations
                        FitRes(objIdxRemove',:) = [];

                        %Data Export organisation
                        nameList=cell(1,size(FitRes,1));
                        for t=1:size(FitRes,1)
                            nameList(t)=cellstr(myname);
                        end
                        averageRes = zeros(size(FitRes,1),3);
                        averageRes(1,1) = mean(FitRes(:,5));
                        averageRes(1,2) = mean(FitRes(:,6));
                        averageRes(1,3) = mean(FitRes(:,7));
                        averageRes = num2cell(averageRes);
                        propsEx=num2cell(FitRes);
                        nameList = nameList';
                        propsEx2=[nameList propsEx];
                        propsEx2=[propsEx2 averageRes];
                    else
                        propsEx2 = cell(1,11);
                        for q = 1:11
                            propsEx2{1,q} = 'Ellipse Fit Error';
                        end
                    end
                else
                    %Data without Elipse Fitting
                    %remove objects outside of constraints (size,eccentricity)
                    propsExOld = propsExOld';
                    objSizes = cell2mat(propsExOld(:,1));
                    objEccens = cell2mat(propsExOld(:,5));
                    removeValues = find(objEccens > eccenLimit | objSizes > maxObjSize | objSizes <
minObjSize);
                    propsExOld(removeValues',:) = [];
                    B(removeValues',:) = [];
                    %Names
                    nameList=cell(1,size(propsExOld,1));
                    for t=1:size(propsExOld,1)
                        nameList(t)=cellstr(myname);
                    end
                    propsEx2=[nameList' propsExOld];
```

```
                end

                if allDataCounter == 1 % first sheet -> put run settings
                        kernelSizeActual=str2double(get(KS_edit,'String'));
                        EccenCutoffActual=str2double(get(Eccentricity,'String'));
                        offsetActual=str2double(get(offset_edit,'String'));
                        size1Actual=str2double(get(sizeFilter1_edit,'String'));
                        size2Actual=str2double(get(sizeFilter2_edit,'String'));
                        runSettings = cell(size(propsEx2,1),6);
                        runSettings{1,1} = EccenCutoffActual;
                        runSettings{1,2} = kernelSizeActual;
                        runSettings{1,3} = offsetActual;
                        runSettings{1,4} = size1Actual;
                        runSettings{1,5} = size2Actual;
                        runSettings{1,6} = str2double(get(ScaleBox_edit,'String'));
                        propsEx2 = [propsEx2 runSettings];
                        if get(Smoothingbox,'Value') == 1
                            testExport=cell2table(propsEx2,'VariableNames',{'Image_Name' 'Centroid_x'
'Centroid_y' 'Axis_1' 'Axis_2' 'Aspect_Ratio' 'Area' 'Rotation' 'Av_AR' 'AV_Area' 'Av_Rot'
'Settings1' 'Settings2' 'Settings3' 'Settings4' 'Settings5' 'Scale'});
                        else
                            testExport=cell2table(propsEx2,'VariableNames',{'Image_Name' 'Area'
'Centroid' 'MajorAxisLength' 'MinorAxisLength' 'Eccentricity' 'Perimeter' 'Settings1' 'Settings2'
'Settings3' 'Settings4' 'Settings5' 'Scale'});
                        end
                        propsEx2 = propsEx2(:,1:(size(propsEx2,1)-size(runSettings,1)));
                else
                     if isnan(propsEx2{1,1}) == 1
                         errCell = cell(1,1);
                         testExport=cell2table(errCell);
                     else
                         if get(Smoothingbox,'Value') == 1
                             testExport=cell2table(propsEx2,'VariableNames',{'Image_Name'
'Centroid_x' 'Centroid_y' 'Axis_1' 'Axis_2' 'Aspect_Ratio' 'Area' 'Rotation' 'Av_AR' 'AV_Area'
'Av_Rot'});
                         else
                             testExport=cell2table(propsEx2,'VariableNames',{'Image_Name' 'Area'
'Centroid' 'MajorAxisLength' 'MinorAxisLength' 'Eccentricity' 'Perimeter'});
                         end
                     end
                end
                %Save Data - code settings on first sheet
                excelFileName = strcat(erase(lif_name,'.lif'),'_Analysis');
                lif_string = strcat(pathstr,erase(lif_name,'.lif'));
                mkdir(strcat(erase(lif_name,'.lif'),'_Analysis'));

writetable(testExport,strcat(strcat(lif_string,'_Analysis\'),excelFileName,'.xlsx'),'sheet',strrep(c
har(myname),'/','-'));

                 %% export images on Run All if box checked
                 % export images with detected objects labelled & scale bar
                 if get(imOut_edit,'Value') == 1
                     figure('Visible','off')
                     temp = imshow(focusedProcessed, 'Parent', h.h_im_cont_p_ax);

                     img=getframe(h.h_im_cont_p_ax);
                     %add the scale bar - bot left always and 200um
                     if get(ScaleBar,'Value') == 1 && isempty(get(ScaleBox_edit,'Value')) == 0
                        imWithScaleBar = addScaleBar(focusedProcessed,'gray');
                        imshow(imWithScaleBar, 'Parent', h.h_im_cont_p_ax);
                     else
                        imWithScaleBar = focusedProcessed;
                     end

                     counter = 1;
                     if get(Smoothingbox,'Value') == 0
                         propsExOld = propsExOld';
                     end
                     for k = 1:size(propsExOld,2)
                         boundary_Master = B{k};
                         eccen = propsExOld{5,k};
                         if eccen < eccenLimit & propsExOld{1,k} < maxObjSize & propsExOld{1,k} >
minObjSize
                             line(h.h_im_cont_p_ax,boundary_Master(:,2), boundary_Master(:,1),...
                             'color','r','LineWidth',1);
                             text(h.h_im_cont_p_ax,propsExOld{2,k}(1), propsExOld{2,k}(2),
sprintf('%d', counter),'FontSize', 20, 'Color', 'white','FontWeight','Bold');
                             counter = counter + 1;
                         end
                     end
                 end
                 % write images
                 imgFinalWrite=getframe(h.h_im_cont_p_ax);

imwrite(imgFinalWrite.cdata,strcat(strcat(erase(lif_name,'.lif'),'_Analysis\'),strrep(char(name),'/'
,'_'),'_',mat2str(allData),'.png'));

                % print progress to command window
```

```
                progressString = sprintf('%d/%d complete',allDataCounter,endImRun)
                waitbar(allData/size(data,1),progress);
                unFreezeInterface;
                set(disco_button,'Enable','off');
            end
        end
        if mode == 2
            if isvalid(progress)
                close(progress)
            end
        end
    end

    %Close the progess bar window
    function closeWindowMode(~,~)
        % delete window
        delete(h.h)
    end
end
```

Supporting Functions.

Ellipse Fitting

```
function [z, a, b, alpha] = fitellipse(x, varargin)
%FITELLIPSE   least squares fit of ellipse to 2D data
%
%   [Z, A, B, ALPHA] = FITELLIPSE(X)
%       Fit an ellipse to the 2D points in the 2xN array X. The ellipse is
%       returned in parametric form such that the equation of the ellipse
%       parameterised by 0 <= theta < 2*pi is:
%           X = Z + Q(ALPHA) * [A * cos(theta); B * sin(theta)]
%       where Q(ALPHA) is the rotation matrix
%           Q(ALPHA) = [cos(ALPHA), -sin(ALPHA);
%                       sin(ALPHA), cos(ALPHA)]
%
%       Fitting is performed by nonlinear least squares, optimising the
%       squared sum of orthogonal distances from the points to the fitted
%       ellipse. The initial guess is calculated by a linear least squares
%       routine, by default using the Bookstein constraint (see below)
%
%   [...]            = FITELLIPSE(X, 'linear')
%       Fit an ellipse using linear least squares. The conic to be fitted
%       is of the form
%           x'Ax + b'x + c = 0
%       and the algebraic error is minimised by least squares with the
%       Bookstein constraint (lambda_1^2 + lambda_2^2 = 1, where
%       lambda_i are the eigenvalues of A)
%
%   [...]            = FITELLIPSE(..., 'Property', 'value', ...)
%       Specify property/value pairs to change problem parameters
%          Property                 Values
%          ================================
%          'constraint'             {|'bookstein'|, 'trace'}
%                                   For the linear fit, the following
%                                   quadratic form is considered
%                                   x'Ax + b'x + c = 0. Different
%                                   constraints on the parameters yield
%                                   different fits. Both 'bookstein' and
%                                   'trace' are Euclidean-invariant
%                                   constraints on the eigenvalues of A,
%                                   meaning the fit will be invariant
%                                   under Euclidean transformations
%                                   'bookstein': lambda1^2 + lambda2^2 = 1
%                                   'trace'    : lambda1 + lambda2     = 1
%
%           Nonlinear Fit Property   Values
%           ================================
%           'maxits'                 positive integer, default 200
%                                    Maximum number of iterations for the
%                                    Gauss Newton step
%
%           'tol'                    positive real, default 1e-5
%                                    Relative step size tolerance
%   Example:
%       % A set of points
%       x = [1 2 5 7 9 6 3 8;
%            7 6 8 7 5 7 2 4];
%
%       % Fit an ellipse using the Bookstein constraint
%       [zb, ab, bb, alphab] = fitellipse(x, 'linear');
%
%       % Find the least squares geometric estimate
```

```
%       [zg, ag, bg, alphag] = fitellipse(x);
%
%       % Plot the results
%       plot(x(1,:), x(2,:), 'ro')
%       hold on
%       % plotellipse(zb, ab, bb, alphab, 'b--')
%       % plotellipse(zg, ag, bg, alphag, 'k')
%
%   See also PLOTELLIPSE

% Copyright Richard Brown, this code can be freely used and modified so
% long as this line is retained
error(nargchk(1, 5, nargin, 'struct'))

% Default parameters
params.fNonlinear = true;
params.constraint = 'bookstein';
params.maxits     = 200;
params.tol        = 1e-5;

% Parse inputs
[x, params] = parseinputs(x, params, varargin{:});

% Constraints are Euclidean-invariant, so improve conditioning by removing
% centroid
centroid = mean(x, 2);
x        = x - repmat(centroid, 1, size(x, 2));

% Obtain a linear estimate
switch params.constraint
    % Bookstein constraint : lambda_1^2 + lambda_2^2 = 1
    case 'bookstein'
        [z, a, b, alpha] = fitbookstein(x);

    % 'trace' constraint, lambda1 + lambda2 = trace(A) = 1
    case 'trace'
        [z, a, b, alpha] = fitggk(x);
end % switch

% Minimise geometric error using nonlinear least squares if required
if params.fNonlinear
    % Initial conditions
    z0     = z;
    a0     = a;
    b0     = b;
    alpha0 = alpha;

    % Apply the fit
    [z, a, b, alpha, fConverged] = ...
        fitnonlinear(x, z0, a0, b0, alpha0, params);

    % Return linear estimate if GN doesn't converge
    if ~fConverged
        warning('fitellipse:FailureToConverge', ...'
            'Gauss-Newton did not converge, returning linear estimate');
        z = z0;
        a = a0;
        b = b0;
        alpha = alpha0;
    end
end

% Add the centroid back on
z = z + centroid;

end % fitellipse

% ----END MAIN FUNCTION-----------%

function [z, a, b, alpha] = fitbookstein(x)
%FITBOOKSTEIN   Linear ellipse fit using bookstein constraint
%   lambda_1^2 + lambda_2^2 = 1, where lambda_i are the eigenvalues of A

% Convenience variables
m  = size(x, 2);
x1 = x(1, :)';
x2 = x(2, :)';

% Define the coefficient matrix B, such that we solve the system
% B *[v; w] = 0, with the constraint norm(w) == 1
B = [x1, x2, ones(m, 1), x1.^2, sqrt(2) * x1 .* x2, x2.^2];

% To enforce the constraint, we need to take the QR decomposition
[Q, R] = qr(B);

% Decompose R into blocks
R11 = R(1:3, 1:3);
R12 = R(1:3, 4:6);
```

```
R22 = R(4:6, 4:6);

% Solve R22 * w = 0 subject to norm(w) == 1
[U, S, V] = svd(R22);
w = V(:, 3);

% Solve for the remaining variables
v = -R11 \ R12 * w;

% Fill in the quadratic form
A        = zeros(2);
A(1)     = w(1);
A([2 3]) = 1 / sqrt(2) * w(2);
A(4)     = w(3);
bv       = v(1:2);
c        = v(3);

% Find the parameters
[z, a, b, alpha] = conic2parametric(A, bv, c);

end % fitellipse


function [z, a, b, alpha] = fitggk(x)
% Linear least squares with the Euclidean-invariant constraint Trace(A) = 1

% Convenience variables
m  = size(x, 2);
x1 = x(1, :)';
x2 = x(2, :)';

% Coefficient matrix
B = [2 * x1 .* x2, x2.^2 - x1.^2, x1, x2, ones(m, 1)];

v = B \ -x1.^2;

% For clarity, fill in the quadratic form variables
A        = zeros(2);
A(1,1)   = 1 - v(2);
A([2 3]) = v(1);
A(2,2)   = v(2);
bv       = v(3:4);
c        = v(5);

% find parameters
[z, a, b, alpha] = conic2parametric(A, bv, c);

end



function [z, a, b, alpha, fConverged] = fitnonlinear(x, z0, a0, b0, alpha0, params)
% Gauss-Newton least squares ellipse fit minimising geometric distance

% Get initial rotation matrix
Q0 = [cos(alpha0), -sin(alpha0); sin(alpha0) cos(alpha0)];
m = size(x, 2);

% Get initial phase estimates
phi0 = angle( [1 i] * Q0' * (x - repmat(z0, 1, m)) )';
u = [phi0; alpha0; a0; b0; z0];

% Iterate using Gauss Newton
fConverged = false;
for nIts = 1:params.maxits
    % Find the function and Jacobian
    [f, J] = sys(u);

    % Solve for the step and update u
    h = -J \ f;
    u = u + h;

    % Check for convergence
    delta = norm(h, inf) / norm(u, inf);
    if delta < params.tol
        fConverged = true;
        break
    end
end

alpha = u(end-4);
a     = u(end-3);
b     = u(end-2);
z     = u(end-1:end);


    function [f, J] = sys(u)
        % SYS : Define the system of nonlinear equations and Jacobian. Nested
```

```
        % function accesses X (but changeth it not)
        % from the FITELLIPSE workspace

        % Tolerance for whether it is a circle
        circTol = 1e-5;

        % Unpack parameters from u
        phi   = u(1:end-5);
        alpha = u(end-4);
        a     = u(end-3);
        b     = u(end-2);
        z     = u(end-1:end);

        % If it is a circle, the Jacobian will be singular, and the
        % Gauss-Newton step won't work.
        %TODO: This can be fixed by switching to a Levenberg-Marquardt
        %solver
        if abs(a - b) / (a + b) < circTol
            warning('fitellipse:CircleFound', ...
                'Ellipse is near-circular - nonlinear fit may not succeed')
        end

        % Convenience trig variables
        c = cos(phi);
        s = sin(phi);
        ca = cos(alpha);
        sa = sin(alpha);

        % Rotation matrices
        Q    = [ca, -sa; sa, ca];
        Qdot = [-sa, -ca; ca, -sa];

        % Preallocate function and Jacobian variables
        f = zeros(2 * m, 1);
        J = zeros(2 * m, m + 5);
        for i = 1:m
            rows = (2*i-1):(2*i);
            % Equation system - vector difference between point on ellipse
            % and data point
            f((2*i-1):(2*i)) = x(:, i) - z - Q * [a * cos(phi(i)); b * sin(phi(i))];

            % Jacobian
            J(rows, i) = -Q * [-a * s(i); b * c(i)];
            J(rows, (end-4:end)) = ...
                [-Qdot*[a*c(i); b*s(i)], -Q*[c(i); 0], -Q*[0; s(i)], [-1 0; 0 -1]];
        end
    end
end % fitnonlinear



function [z, a, b, alpha] = conic2parametric(A, bv, c)
% Diagonalise A - find Q, D such at A = Q' * D * Q
[Q, D] = eig(A);
Q = Q';

    % If the determinant < 0, it's not an ellipse
    if prod(diag(D)) <= 0
        %error('fitellipse:NotEllipse', 'Linear fit did not produce an ellipse');
        z = 0;
        a=0;
        b=0;
        alpha = 0;
    else

        % We have b_h' = 2 * t' * A + b'
        t = -0.5 * (A \ bv);

        c_h = t' * A * t + bv' * t + c;

        z = t;
        a = sqrt(-c_h / D(1,1));
        b = sqrt(-c_h / D(2,2));
        alpha = atan2(Q(1,2), Q(1,1));
    end
end % conic2parametric




function [x, params] = parseinputs(x, params, varargin)
% PARSEINPUTS put x in the correct form, and parse user parameters

% CHECK x
% Make sure x is 2xN where N > 3
if size(x, 2) == 2
    x = x';
```

```
end
if size(x, 1) ~= 2
    error('fitellipse:InvalidDimension', ...
        'Input matrix must be two dimensional')
end
if size(x, 2) < 6
    error('fitellipse:InsufficientPoints', ...
        'At least 6 points required to compute fit')
end


% Determine whether we are solving for geometric (nonlinear) or algebraic
% (linear) distance
if ~isempty(varargin) && strncmpi(varargin{1}, 'linear', length(varargin{1}))
    params.fNonlinear = false;
    varargin(1)       = [];
else
    params.fNonlinear = true;
end

% Parse property/value pairs
if rem(length(varargin), 2) ~= 0
    error('fitellipse:InvalidInputArguments', ...
        'Additional arguments must take the form of Property/Value pairs')
end

% Cell array of valid property names
properties = {'constraint', 'maxits', 'tol'};

while length(varargin) ~= 0
    % Pop pair off varargin
    property      = varargin{1};
    value         = varargin{2};
    varargin(1:2) = [];

    % If the property has been supplied in a shortened form, lengthen it
    iProperty = find(strncmpi(property, properties, length(property)));
    if isempty(iProperty)
        error('fitellipse:UnknownProperty', 'Unknown Property');
    elseif length(iProperty) > 1
        error('fitellipse:AmbiguousProperty', ...
            'Supplied shortened property name is ambiguous');
    end

    % Expand property to its full name
    property = properties{iProperty};

    % Check for irrelevant property
    if ~params.fNonlinear && ismember(property, {'maxits', 'tol'})
        warning('fitellipse:IrrelevantProperty', ...
            'Supplied property has no effect on linear estimate, ignoring');
        continue
    end

    % Check supplied property value
    switch property
        case 'maxits'
            if ~isnumeric(value) || value <= 0
                error('fitcircle:InvalidMaxits', ...
                    'maxits must be an integer greater than 0')
            end
            params.maxits = value;
        case 'tol'
            if ~isnumeric(value) || value <= 0
                error('fitcircle:InvalidTol', ...
                    'tol must be a positive real number')
            end
            params.tol = value;
        case 'constraint'
            switch lower(value)
                case 'bookstein'
                    params.constraint = 'bookstein';
                case 'trace'
                    params.constraint = 'trace';
                otherwise
                    error('fitellipse:InvalidConstraint', ...
                        'Invalid constraint specified')
            end
    end % switch property
end % while

end % parseinputs
```

Ellipse Plotting

```
function [X] = plotellipse2(varargin)
%PLOTELLIPSE   Plot parametrically specified ellipse
%
%   PLOTELLIPSE(Z, A, B, ALPHA) Plots the ellipse specified by Z, A, B,
%       ALPHA (as returned by FITELLIPSE)
%
%       A, B are positive scalars, Z a 2x1 column vector, and
%       ALPHA a rotation angle, such that the equation of the ellipse is:
%           X = Z + Q(ALPHA) * [A * cos(phi); B * sin(phi)]
%       where Q(ALPHA) is the rotation matrix
%           Q(ALPHA) = [cos(ALPHA) -sin(ALPHA);
%                       sin(AlPHA) cos(ALPHA)]
%
%   PLOTELLIPSE(..., LineSpec) passes the LineSpec string to the plot
%       command (e.g. 'r--')
%
%   PLOTELLIPSE(Hax, ...) plots into the axes specified by the axes handle
%       Hax
%
%   H = PLOTELLIPSE(...) returns a handle to the created lineseries object
%       created by the plot command
%
%   Example:
%       % Ellipse centred at 10,10, with semiaxes 5 and 3, rotated by pi/4
%       a = 5;
%       b = 3;
%       z = [10; 10]
%       alpha = pi/4;
%       plotellipse(z, a, b, alpha)
%
%   See also FITELLIPSE

% Copyright Richard Brown. This code can be freely reused and modified so
% long as it retains this copyright clause

error(nargchk(4, 6, nargin, 'struct'));
error(nargchk(0, 1, nargout, 'struct'));

% Parse and check inputs
if ishandle(varargin{1})
    hAx = varargin{1};
    varargin(1) = [];
else
    hAx = gca();
end

% Ellipse centre
z = varargin{1};
z = z(:);
if length(z) ~= 2
    error('plotellipse:InvalidCentre', ...
        'Ellipse center must be a 2 element column vector');
end

a = varargin{2};
b = varargin{3};
if ~isscalar(a) || ~isscalar(b) || a < 0 || b < 0
    error('plotellipse:InvalidAxes', ...
        'A, B must be real, positive scalars');
end

alpha = varargin{4};
if ~isscalar(alpha)
    error('plotellipse:InvalidConstant', ...
        'Rotation angle alpha must be a real scalar, in radians');
end
varargin(1:4) = [];

% See if a linespec is supplied
if ~isempty(varargin)
    linespec = varargin{1};
else
    linespec = '';
end

% form the parameter vector
npts = 1000;
t = linspace(0, 2*pi, npts);

% Rotation matrix
Q = [cos(alpha), -sin(alpha); sin(alpha) cos(alpha)];
% Ellipse points
X = Q * [a * cos(t); b * sin(t)] + repmat(z, 1, npts);
```

```
X = round(X,0);
end
```

Smoothing

```
function fitVal = SmoothTest(xData,yData)
%make it equal to n*360 points by random sampling
%as few as 15 deg is accepted
x = xData;
y = yData;
skip = 0;

dLength = floor((size(x,1)/15));
%dLength = 6;
if dLength >= 24
    %dLength = floor((dLength*30)/360)*360;
    dLength = 360;
elseif dLength >= 12
    dLength = 180;
elseif dLength >= 6
    dLength = 90;
elseif dLength >= 3
    dLength = 45;
elseif dLength >= 1
    dLength = 15;
else
    skip = 1;
end

if size(x,1) < dLength
    skip = 1;
end

if skip == 0
    s = RandStream('mlfg6331_64');
    s2 = datasample(s,1:size(x,1),dLength,'Replace',false);
    s2 = sort(s2);

    %normalise data and centre about y=0
    %x data
    f1 = x - mean(x);
    f1 = f1./(max(f1));
    %y data
    f2 = y - mean(y);
    f2 = f2./(max(f2));

    f3 = zeros(dLength,1);

    %360n random samples in order from data
    for i = 1:dLength
        f3(i,1) = f1(s2(i)); %x
        f6(i,1) = f2(s2(i)); %y
    end
    f4 = f3';
    f5 = f6';

    % Define domain
    dx = 1;
    L = dLength/2;
    x = (1:dx:dLength);
    for i = 1:2
        if i == 1
            f = f4;
        else
            f = f5;
        end

        %uncomment(1/2) for figures of fits.
        %figure;
        %plot(x,f,'-','Color','b')
        %xlim([0 dLength])
        %ylim([-1 1])
        %hold on

        % Compute Fourier series
        A0 = sum(f.*ones(size(x)))*dx;
        fFS = A0/2;
        for k=1:3
            A(k) = sum(f.*cosd(180*k*x/L))*dx; % Inner product
            B(k) = sum(f.*sind(180*k*x/L))*dx;
            fFS = fFS + A(k)*cosd(k*180*x/L) + B(k)*sind(k*180*x/L);
            fFSout = fFS./max(fFS);
        end
```

```
        if i == 1
            fFSout1 = fFSout;
        end
        hold on;
    end

    %check GOF
    fitVal = min(goodnessOfFit(f6,fFSout','NRMSE'),goodnessOfFit(f3,fFSout1','NRMSE'));

    %uncomment(2/2) for figures of fits.
    %plot(x,[fFSout; nan(size(x))],'-','Color','r','LineWidth',1.2)
    %[~, objH] = legend({'Object Pixel Position','Fourier
Fit','other'},'Location','northeast','Orientation','vertical','FontSize',14)
    %lgd = legend;
    %lgd.FontSize = 14;
    %set(findobj(objH, 'Tag', 'other'), 'Vis', 'off');
    %pos = get(objH(3),'Pos');
    %GOFstring = ['G.O.F.     ' ' ' ' ' ' ' num2str(round(fitVal,3))];
    %set(objH(3), 'Pos', [0.1 pos(2:3)], 'String', GOFstring);
    %set(gca,'FontSize',14)
    %xticks([0 45 90 135 180])
    %
else
    fitVal = 999;
end
end
```

Stack Projection

```
function MAXPROJimg = maxstack(img)
%Take maximum projection of an imput image array
%compare each image plane and keep maximum values

if ~iscell(img)
    error('Input needs to be cell array of images.')
end

for i = 1:length(img)
    if i == 1
        imNew = img{i,1};
        xRes = size(img{1,1},1);
        yRes = size(img{1,1},2);
    end
    im = img{i,1};
    imNew = reshape(max(imNew(:),im(:)),xRes,yRes);
end


%optional - background subtraction & lumination normalizing
%background element - arbitrary
bKernel = 40;
%img type - 8bit or 16bit only
imClass = class(imNew);
switch imClass
    case 'uint8'
        backSub = true;
        brightnessScalingFactor = 0.9*255;
    case 'uint16'
        backSub = true;
        brightnessScalingFactor = 0.9*65536;
    otherwise
        backSub = false;
end

if backSub == true
    se = strel('disk',bKernel);
    background = imopen(imNew,se);
    imNew = imNew - background;
    imNew = imNew*(brightnessScalingFactor/(max(imNew(:))));
    MAXPROJimg = imNew;
else
    MAXPROJimg = imNew;
end
end
```

Enclosing Boundaries

```
function BWclosedBoundary = closeBoundary(InputIm);
%% Close incomplete simple boundaries
% Input is a binary image, an outline of an arbitrary incomplete hole-boundary
```

```
% function dialates, fills then subtracts original dilation to fill in
% holes in the boundary
% returns an array of pixel co-ordinates for the completed boundary
%
% Peter Johnson Perriman Group 2020
% Copyright Peter Johnson. This code can be freely reused and modified so
% long as it retains this copyright clause
%%

%checks
if islogical(InputIm) == 1 || max(InputIm(:)) == 1
else
    error('Close Boundary Input Img is not binary');
end

%variables
searchSize = 3; %array search size for missing pixels - good for single missing pixels
searchInc = 5; %increase search size

I = InputIm;
xRes = size(I,2);
yRes = size(I,1);
outArr = zeros(xRes,yRes);
BW = im2bw(I);
SE = strel('square',searchSize);
BWfinal = imfill(imdilate(BW,SE),8,'holes') - imdilate(BW,SE);

if sum(BWfinal(:)) == 0
%No dialation - increase dilation size
    SE = strel('square',searchSize+searchInc);
    BWfinal = (imfill(imdilate(BW,SE),8,'holes') - imdilate(BW,SE));

    if sum(BWfinal(:)) == 0
       %still no dilation, increase size again
       SE = strel('square',2*(searchSize+searchInc));
       BWfinal = (imfill(imdilate(BW,SE),8,'holes') - imdilate(BW,SE));
    end
end

BWfinalBoundary = bwboundaries(BWfinal,8,'noholes');

%An error I think if object is very small? Can't do a BWboundary
if isempty(BWfinalBoundary)
    BWclosedBoundary = InputIm;
else
    BWfinalBoundary2 = BWfinalBoundary{1,1};
    BWclosedBoundary = BWfinalBoundary2;
end

% View outlines in a figure
%show original im vs outline
%   C = imfuse(I,outArr);
%   imshow(C);
end
```